

EXPERIMENTAL AND COMPUTATIONAL ANALYSIS OF MIXED  
CONVECTION AROUND IN-LINE CYLINDERS



EXPERIMENTAL AND COMPUTATIONAL ANALYSIS OF MIXED  
CONVECTION AROUND IN-LINE CYLINDERS

By CHRISTOPHER W. HOLLINGSHEAD, B.Eng, M.A.Sc

A Thesis

Submitted to the School of Graduate Studies

In partial Fulfillment of the Requirements for the Degree

Doctor of Philosophy

McMaster University

© Christopher Hollingshead, July 2022

DOCTOR OF PHILOSOPHY (2022)

(Engineering Physics)

MCMASTER UNIVERSITY

Hamilton, Ontario, Canada

Title: EXPERIMENTAL AND COMPUTATIONAL ANALYSIS OF MIXED  
CONVECTION AROUND IN-LINE CYLINDERS

Author: Christopher William Hollingshead, B.Eng, M.A.Sc (McMaster  
University)

Supervisor: Dr. D.R. Novog

Number of Pages: xv, 100

## ACKNOWLEDGEMENTS

I'm very fortunate in that I feel as though I have more people to thank for their time, kindness, and support than I can fit in one page of a strangely formatted thesis, but here's a try with as many inside jokes as I can manage for those keeping score.

To the grad students who've put up with me over the years, Mengmeng, Dion, Feng, Jared, Andrew, Kendal, Mitch, Josh and many others. Thank you for your time and all of the help you provided to me that you knew you didn't have to, but did anyways.

Frank, I just wanted to say thanks. Whether it was hearing me out about some idea involving lasers and dyes, building my CFD computer, or just discussing the latest thread rippers. You always gave me the time of day, which I appreciate greatly.

Jim, let me get the sappy part out of the way. You always seemed to know what I needed more than I did, and always made a few minutes to discuss ideas and designs, even when you were busy. Thank you. Now, shouldn't you be working instead of reading this?

James, thanks for showing me the lab... And for your immense patience teaching me how to use and do just about everything and anything in the lab. I hope that my practice made adequate. And also thanks for the occasional 8-hour Phoenix session.

Alex, you've always been so supportive of me and generous with your time. You've effectively been a 2<sup>nd</sup> supervisor to me for many years now and I've always greatly appreciated it. Thank you so much. Now go pick up your kids.

To all of my friends, whether its my Eng Phys crowd, my old roommates, the Essex collective (yes, this includes you Erin) or anyone else. I can guarantee that I would not have made it this far without you. There were many times were I was less than a bad day away from quitting. On those days, I always managed to get the support I needed from one or all of you. After I considered joining the circus of course. Thank you all.

Garik, there simply is too many things I would have to say, and not enough space. So, I'll simply say thank you for your time, advice, continued help and hope one day I find the right words. Alpaca.

I would also like to thank my PhD committee, Laurence, Nithy and Cotton. Your guidance was greatly beneficial, and though things didn't end up going where we initially planned, we seem to have made the most of it. And if not, I suspect I'll find out shortly.

Dr. Novog, there was one thing I could always count on you for, and that was above all else, being a good person. Thank you for your guidance and support all these years. Twenty-five years to go.

To my family. It takes a lot of things outside of one's own control to successfully do a PhD. I could always count on your love and support. Thank you all.

## ABSTRACT

This work can be viewed in three separate sections, each of which build off of the prior. The first part of this study examined the flow in a 1/16<sup>th</sup> scale calandria test section based on a typical CANDU moderator layout. The experiments utilized forced flow supplied to the vessel and electrical heated rods to mimic the heat flow from calandria tubes. The size of the vessel, flow rates, and power levels were used to scale the experiments such that they provided representative temperature fields. The temperature field inside the vessel was measured and shown to compare well with CFD predictions over a wide range of inlet conditions and power levels. Additionally, this work addressed the scaling distortions in the experiment which occurred due to physical limitations when performing experiments at 1/16 scale (e.g., a smaller number of heater rods with a larger diameter were used in the experiment because at 1/16-scale direct fabrication of 390 fuel channel simulators is not feasible). The work proposed the  $H$  factor addition to the  $Ar$ . This additional scaling criteria was shown to better maintain the flow regimes expected CANDU moderators by taking into account distortions introduced by surface heating instead of volumetric heating in addition to the reduction in total number of tubes. While this work involved forced convective flows at the inlet of the vessel, in some regions of the calandria buoyancy induced forces were sufficiently high such that these phenomena altered the direction and magnitude of the flows as compared to purely forced convective behavior. Hence further work, discussed below, was

initiated to better understand and measure these local phenomena where buoyancy forces are of similar magnitude as those of forced convection. Such local conditions we have terms mixed convection regime for the purposes of this thesis.

The second part of this work further examined the mixed convection between a subset of the CANDU calandria tubes, namely how does a lower tube effect the mixed convection heat transfer of the upper tube in an inline arrangement. To isolate and measure the phenomena with sufficient detail, a small number of tubes was studied and advanced diagnostics such as Particle Image Velocimetry (PIV) and Laser Induced Fluorescence (LIF) were employed. This study combined fluid velocity, temperature and wall temperature measurements with CFD simulations to develop a mechanistic model and understanding of the effect of natural convection plumes from lower elevations on the natural circulation phenomena on an upper cylinder. Superposition of the natural convection phenomena combined with pseudo forced convection effects from the lower elevation cylinder's plume was used to model the mixed convection phenomena. This model was shown to perform well, with nearly all data being predicted to with  $\pm 20\%$  for experiments performed in this work, and experiments in literature.

A major finding from the preceding discussion is the importance of the lower elevation plume velocity on the local phenomena on the upper cylinder. The third section further expanded upon the prior two by replacing the lower cylinder with a

diffuser nozzle which could provide a forced convective component with accurately defined velocities. Such measurements allow for accurate definition of the local  $Ri$  number and allowed full access for instrumentation to observe the velocity fields. The major contribution of this work was a flow regime map that defined the phenomena around a heated cylinder under mixed convection conditions. Additionally, the establishment of a database of fluid temperature and velocity measurements for a wide range of  $Ri$  was also developed and used to further validate CFD predictions.

## Table of Contents

I.	List of Figures .....	xi
II.	List of Tables .....	xv
1	INTRODUCTION .....	1
1.1	Background .....	2
1.2	CANDU Reactors.....	3
1.3	Aim of the Study .....	5
2	LITERATURE REVIEW .....	9
2.1	Heated Flow Around Cylinders.....	10
2.2	Tandem Cylinder Heat transfer: Effect and determination of local conditions.....	14
2.3	Flow Patterns: Moderator of CANDU Reactors .....	16
3	Sensitivity of local Flow Structures to $Ri$ : Transitions in flow around a cylinder vs $Ri$ .....	20
4	Modelling and Predicting Mixed Convection Heat Transfer based on local conditions for Cylinder Pair.....	51
5	Mixed Convective Flow Patterns for CANDU Geometries: Accounting for Scaling Distortions and issues with $Ar$ .....	66
6	CONCLUSIONS.....	81

7	FUTURE WORK.....	86
7.1	Future Moderator Flow Work .....	87
7.1.1	Departure From Nucleate Boiling Tests: .....	87
7.1.2	Simplified Experimental Studies to Confirm $ArH$ .....	88
7.2	Mixed Convection Heat Transfer Studies in cylinders .....	89
7.2.1	Improving the transition to turbulence of a free thermal plume .....	89
7.2.2	Additional Validation Experiments .....	90
7.3	Critical $Ri$ and heated flow around a cylinder.....	91
7.3.1	Additional Experimental data .....	91
7.3.2	Further numerical studies.....	92
7.3.3	Examination to CANDU type Geometry .....	93
8	Bibliography .....	95
9	Appendix.....	100
9.1	Heat Transfer Measurements for upward flow around a cylinder .....	101
9.2	Particle Image Velocimetry Standard Operating Procedure .....	105
9.2.1	General Instructions/Considerations .....	108
9.2.2	Laser Startup Procedure .....	108
9.2.3	Light Arm Alignment Procedure .....	109
9.2.4	Performing Particle Image Velocimetry .....	110

9.2.5	Shutdown Procedure .....	111
9.2.6	Parameters.....	111
9.3	LIF Calibration Curves.....	114
9.3.1	Free Convection LIF.....	114
9.3.2	Mixed Convection LIF Experiments .....	115
9.4	Effect of Refractive Index Change.....	117
9.5	Effect of Angular Tilt.....	119
9.6	Diffuser Nozzle Design/Performance .....	120
9.7	Departure from Nucleate Boiling in Tube Arrays: Literature Review. ....	126
9.7.1	Enhancement Effect .....	146
9.7.2	Diminishment Effect.....	147
9.7.3	Flaws in experimental studies.....	148
9.8	Design Drawings .....	149
9.9	Calibration Documents.....	168

## **I. List of Figures**

Figure 1. Calandria and pressure tubes of a typical CANDU reactor from [1] .....	4
Figure 2. Fuel bundle, pressure tube and calandria tube arrangement for a typical CANDU from [2].....	5

Figure 3. Visualizes the methods by which the calandria and pressure tubes can come into contact in beyond design basis accident events, from Strack [3].....	5
Figure 4. Circumferentially averaged Temperature differences vs Oncoming velocity.....	102
Figure 5. Circumferential Temperature Distribution for $q'' = 8.5\text{kW/m}^2$ .....	102
Figure 6. Circumferential Temperature Distribution for $q'' = 18\text{kW/m}^2$ .....	103
Figure 7. Circumferential Temperature Distribution for $q'' = 25.6\text{kW/m}^2$ .....	103
Figure 8. Circumferential Temperature Distribution for $q'' = 34.1\text{kW/m}^2$ .....	104
Figure 9. Circumferential Temperature distribution normalized to the average for all tested velocities at a heat flux of $25.6\text{kW/m}^2$ .....	104
Figure 10. Calibration curves used for the free-convection cylinder LIF experiments .....	115
Figure 11. Calibration data points captured during the mixed convection LIF experimental campaign .....	116
Figure 12. Seed profile for no angular tilt for 64W for a pure free thermal plume .....	118
Figure 13. Seed profile for a pure thermal plume for 512W .....	119
Figure 14. Effect of the angular tilt at $Y=50\text{mm}$ from the surface of the cylinder .....	120
Figure 15. General design layout for the large diffuser nozzle designed for the single cylinder experiments .....	121

Figure 16. Four 3-d printed parts comprising the diffuser nozzle, top left: Inlet, top right: baffle plate, bottom left: smooth contraction, and bottom right: outlet and flow straightener .....	122
Figure 17. Isometric of the complete assembly of the large diffuser nozzle .....	123
Figure 18. $k-\omega SST$ contour of the centreline of the nozzle for a mass flow of 100g/s .....	124
Figure 19. Raw PIV image of the installed diffuser nozzle .....	125
Figure 20. Experimental facility of Chan and Shoukri [26] .....	127
Figure 21. CHF enhancement/diminishment of a cylinder in a heated array vs unheated [26] .....	129
Figure 22. Experimental facility used by Thibault [27].....	131
Figure 23. Thibault's quenching CHF results as a function of angle and subcooling. Note only 12 circumferential measurements [27].....	133
Figure 24. Thibault's saturated single tube CHF data collected with their steam line. The distance in cm corresponds to the distance from the nozzle to the cylinder [27] .....	134
Figure 25. Tube array quenching CHF data obtained by Thibault [27].....	136
Figure 26. Percent increase in CHF for a tube subjected to boiling from adjacent tubes in the central column. Note that this percent increase is over the heater reaching CHF without the other tubes heated [27] .....	137
Figure 27. CHF data versus mass flux and inlet quality for Cumo et al's [28] experiments.....	139

Figure 28. CHF data gathered by Fujita and Hidako [29] as a function of lower heater power.....	141
Figure 29. Tube array used by Yao and Hwang [30] in addition to a schematic (right) with postulated hydrodynamics. ....	143
Figure 30. CHF data captured by Yao and Hwang [30] for their tube array experiments compared against their correlation and Haramura and Katto's model. ....	144
Figure 31. Three CHF vs quality curves that Leroux and Jensen [31] found from their data.....	145
Figure 32. Isometric for the test section for used in the experiments in section 5 .....	150
Figure 33. Test section front view for section 5 cross-section .....	151
Figure 34. Test section front view for section 5 East side view .....	152
Figure 35. Test section front view for section 5 West side view .....	153
Figure 36: Test section heater used in section 5 and as Heater A in sections 3 and 4.....	154
Figure 37. Front view of “Large” Diffuser Nozzles used in section 5 .....	157
Figure 38. Side view of “Large” Diffuser Nozzles used in section 5 .....	158
Figure 39. Back view of “Large” Diffuser Nozzles used in section 5 .....	159
Figure 40. Front view of “small” diffuser nozzles used in section 5 .....	161
Figure 41. Side view of “small” diffuser nozzles used in section 5 .....	162
Figure 42. Rear view of “small” diffuser nozzles used in section 5 .....	163

Figure 43. Front view of spray headers .....	164
Figure 44. Side view of spray headers .....	165
Figure 45. Isometrics showing the test section orientation for experiments in section 4.....	166
Figure 46. Assembled inlet manifold for section 4 tests.....	166
Figure 47. Inlet Manifold used in section 4 connection piece – 0-degree view .	167
Figure 48. Inlet Manifold used in section 4: 45-degree view .....	167
Figure 49. Isometrics of the test section setup for experiments in section 3. ....	168

## **II. List of Tables**

Table 1: Design and measured values for the test section used in section 5 .....	153
Table 2: Heated assembly specifications .....	154
Table 3. Thermocouple Positioning: Heater B used in section 3 experiments ...	155
Table 4. Thermocouple Positioning: Heater B used in section 4 experiments ...	156
Table 5: Displays measured and design values for the “Large” Diffuser Nozzles .....	160
Table 6: Measured and design values for the “Small” Diffuser Nozzles used in section 5 .....	164
Table 7: Measured and design values for the Spray Headers .....	166
Table 8. Thermocouple Calibration Data.....	169

## 1 INTRODUCTION

*“Don’t worry, don’t be afraid, ever because, its just a ride. And we can change it  
anytime we want. Its only a choice. Between Fear and Love”*

**Bill Hicks**

## 1.1 Background

The Fukushima Daiichi Nuclear Power Plant underwent a magnitude 9.0 earthquake with the resultant Tsunami flooding the stations emergency backup diesel generators. This resulted in a Station Blackout (SBO) event which eventually led to a meltdown of fuel in the core of units 1,2 and 4 and subsequent hydrogen explosions. This has led to a large cleanup effort which is still underway over 10 years later as of writing.

Understandably, this event has led to significant changes for the use of Nuclear Energy, with countries such as Germany in the midst of a complete phase out of nuclear energy as a result. In Canada, this resulted in a re-examination of nuclear response plans and significant research into how Canadian reactors would respond to similar significant events experienced at Fukushima Daiichi and other potentially harmful scenarios, broadly classified as Beyond Design Basis Accidents (BDBA).

The unique features of CANDU reactors can provide additional response time for operators in such events provided that there is sufficient cooling of the fuel channel assemblies, maintaining channel integrity in both Design Basis Accidents (DBA) and BDBA. This work relates to the improvement of the understanding of mixed convection phenomena around horizontal cylinders, which has been studied much less than forced and natural convection. In DBA and BDBA type events, significant

amounts of thermally generated flow will be present, as a result improved mixed convection predictions can aid in assessing fuel channel integrity.

## 1.2 CANDU Reactors

The CANadian Deuterium Uranium reactor, or CANDU for short, is a Pressurized Heavy water reactor. Contrary to Boiling Water Reactors (BWR) and Pressurised Water Reactors (PWR), CANDU's make use of separate heavy water coolant and moderators with a pressure tubes, annular gas insulator, and calandria tube separating the two. This is in contrast to BWRs and PWRs reactor technologies where the coolant and moderator is the same body of water. This is partially visualized in Figure 1 and Figure 2. The large and separate moderator volume provides unique safety features in design basis accidents (DBA) and BDBA as it can allow for additional cooling when pressure tube (PT) and calandria tube (CT) contact is established. For example, a postulated BDBA would result in a rising fuel temperature, causing expansion or sagging of the PT that houses the fuel. Depending on the specific type of accident that occurs and what happens with the pressure in the primary heat transport system, the pressure tube will balloon or sag into contact with the surrounding CT which separates the moderator and the coolant as shown in Figure 3. This contact establishes a heat transfer path whereby decay heat from the fuel and fuel assembly in the pressure tube can transfer into the low-pressure low-temperature moderator. These phenomena can establish a heat sink pathway to the moderator liquid, and given its large mass it can limit the fuel channel assembly temperatures for a period of time which can give reactor

operators and first responders additional time to respond to the situation and halt the accident progression. However, such a heat sink can be sustained as long as the moderator volume is sufficient or is replenished by responders, and that sustained boiling crisis on the calandria tube surface is prevented. In order to aid in the determination of channel integrity, detailed knowledge of the heat transfer, and flow topologies generated by the mixed convective flow generated by this direct heating of the calandria tube is required and is the primary aim of this work.



Figure 1. Calandria and pressure tubes of a typical CANDU reactor from [1]

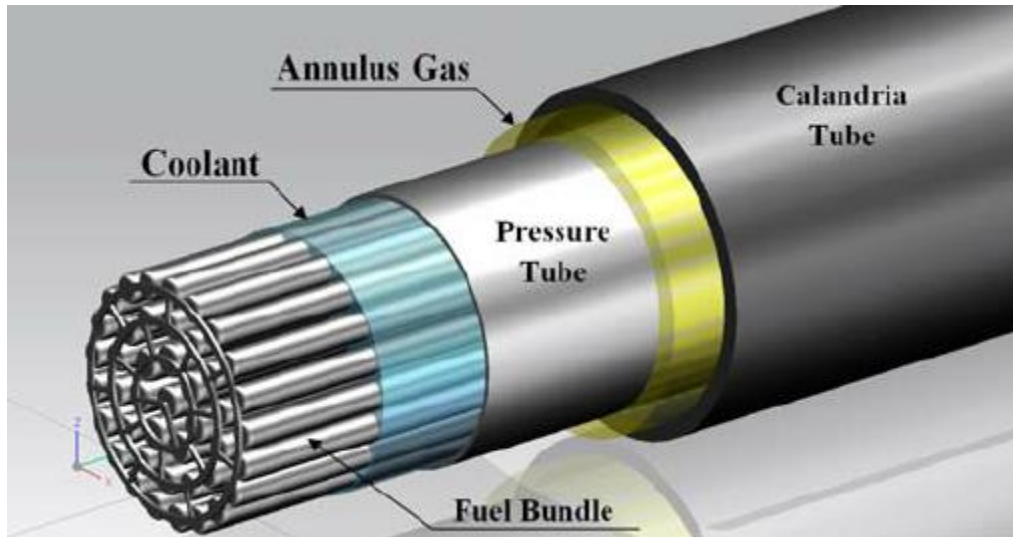


Figure 2. Fuel bundle, pressure tube and calandria tube arrangement for a typical CANDU from [2]

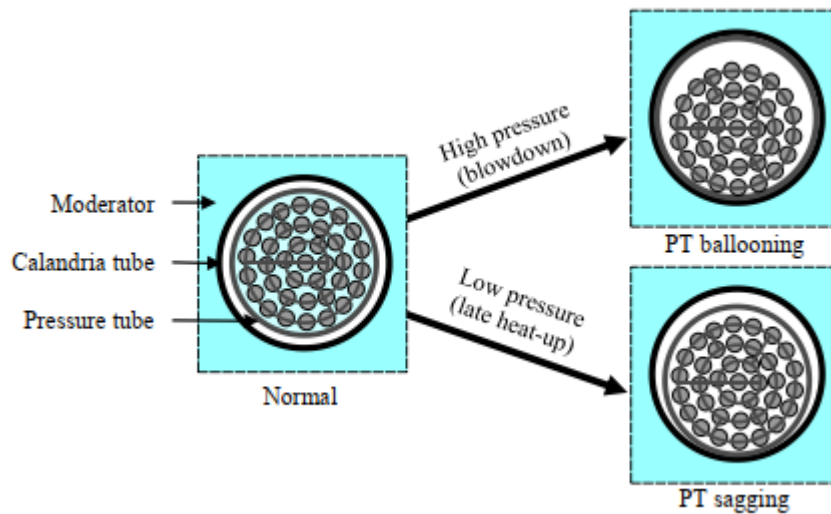


Figure 3. Visualizes the methods by which the calandria and pressure tubes can come into contact in beyond design basis accident events, from Strack [3].

### 1.3 Aim of the Study

The aim of this thesis is to expand and improve the current modelling capability of the Canadian nuclear industry for the local conditions in the CANDU moderator

which are important in DBA and BDBA. More specifically, to improve the understanding of the mixed convective heat transfer expected in these types of events, and the resultant flow topology.

This is to be largely done by expanding on the current knowledge bases in single phase Mixed Convection through a set of separate effects studies examining the interplay of buoyancy and momentum at three different levels. These investigations use a single cylinder, a cylinder pair, and a semi-scale 1/16<sup>th</sup> test rig based on the CANDU moderator flow configuration. This work is most relevant for the ballooning case above given the use of electrical heaters which provide a uniform heat flux in the circumferential direction. This differs from the sagging case as there will be a larger contact area with the calandria tube. This is believed to represent the worst-case scenario, as the sagging case would generate a local hot spot and begin to boil, allowing for steam induced convection to enhance heat transfer.

The key contribution of this work is

- i) the generation of new high-fidelity experimental data to improve the understanding of mixed convection flows around horizontal cylinders,
- ii) validation of CFD against these new experimental data.
- iii) Development of new methods for quantifying the flow topology around the cylinders and for predicting the single phase heat transfer on these cylinders.

The thesis is organized as a compilation of 3 journal papers which each examine the work at different scales. The first examines the integral behaviour inside a complete 1/16-scale calandria vessel. Based on the observed flow patterns and plumes in this experiment, a modified facility with fewer tubes and optical access for PIV and LIF measurements was developed and used for the second paper. The second paper investigated the interaction of the lower plume on the heat transfer around a cylinder at higher elevation. While the CFD results agreed well with the experimental measurements, the experiments in that work could not be used to systematically explore the impact of plume velocity, temperature and diameter because the plumes were driven solely by buoyancy phenomena. In the third paper, the effect of each parameter was isolated by introducing a round jet in replacement of the lower cylinder such that the incoming velocity and temperature field was measured. In the final chapter a summary of the contributions to knowledge is provided as well as the main conclusions from this work.

The intended use of this work is to support the development of tools for predicting local conditions. These local conditions can be critically important for determining fuel channel integrity. The use of this work may look like using model predictions of local temperatures to feed into advanced quenching models like that developed by Dion [4] which determine fuel channel integrity. Additionally, the experiments

and models developed here can be used to further focus and isolate specific phenomena for future simulations and experiments in the mixed convective regime.

## 2 LITERATURE REVIEW

*“When you do things right, people won’t be sure you’ve done anything at all”*

**Robot God**

A complete literature survey has largely already been completed in the introduction section of each of the three papers comprising this thesis. As such, this section will largely focus on the key pieces of literature pertinent to this thesis and examine the deficiencies and opportunities for improvement.

## 2.1 Heated Flow Around Cylinders

Flow around cylinders has been extensively studied isothermally with the wake structures and subsequent von-Karman flow structures well characterized through comprehensive works such as Zdravkovich [5]. Comparatively, flow behind heated cylinders and the effect that heat has on local flow structures has been much less examined in literature.

Typical adiabatic flow around a cylinder contains von-Karman vortices assuming a high enough inlet  $Re$ . Such vortices have characteristic frequencies and alternate from either side of the cylinder. Studies such as [6]-[9] have shown that as heat is added to the cylinder, there is a point whereby the heat addition completely modifies the shedding process to go from a von-Karman shedding process to an eddy pair process. Additionally, as power is further increased, the entire suppression of all types of vortex formation is eventually reached. These critical points are typically reported based on transitions using a critical  $Ri$ , though it must be emphasized here that at least two types of critical  $Ri$  exist, the disruption of pure von-karman shedding, and the elimination of vortex shedding in general. It also must be noted that studies such as Singh et al [6] and Hu and Koochesfahani [7]

have shown that there appears to be a significant difference in the critical  $Ri$  measured for air versus water experiments, with a higher  $Ri$  being required for water experiments in comparison to air experiments at similar  $Re$  ranges. This difference does not appear to have been examined or even acknowledged in previous works. Finally it should be noted that there currently lacks a general approach to attempt to model these critical  $Ri$ .

Using water as a working fluid, Michaux-Leblond and Belorgey [9] examined the wake structure behind a 11.7mm diameter cylinder using Laser Doppler Velocimetry for a geometry where the incident velocity was in the same direction as the buoyancy direction (hereafter described as an aiding geometry). Using these measurements, they determined that at approximately a  $Ri = 0.49$ , the typical von-Karman vortex shedding pattern was replaced by a “standing eddy” pattern. They noted that as power was increased further that this standing eddy pattern was eventually fully suppressed as well. While this study was one of the first found to experimentally report on the transition between pure von-Karman vortices to an Eddy pair type regime, it offered no measurements of when the eddy pair regime disappeared. Additionally, its noted that this first transition was dependent on  $Re$  but only a single critical  $Ri$  was reported.

The study of Hu and Koochesfahani [7] additionally experimentally measured the temperature and velocity fields behind a 4.76mm diameter cylinder in an opposing

flow configuration for a variety of  $Ri$  at a  $Re$  of 135. Hu and Koochesfahani [7] found that when a  $Ri$  of 0.72 was reached, their von-Karman vortices were replaced with what were referred to as smaller wake vortices which appeared to shed at very nearly the same time. These smaller wake vortices were also noted to appear more “Kelvin-Helmholtz” in nature. This was an indication that buoyant effects were beginning to become prevalent in the resultant flow structures. While this study was the first to present detailed velocity measurements coupled with temperature measurements they did not report a  $Ri$  whereby vortex formation was precluded entirely and thermal effects becoming dominant nor were any mechanistic criteria explored.

The study of Kakade et al [8] examined the critical  $Ri$  for square channel type geometries at varying angles to the oncoming flow field in an aiding flow orientation. Using Schlieren interferometry, they measured the critical  $Ri$  vs angle for a relatively tight range of  $Re$ . They found that there exists a strong dependence on angle with it maximized at 20-degrees and then held constant past that point. Of note, when this critical  $Ri$  was reached, vortex shedding was entirely suppressed, meaning that the pair-wise vortex regime was precluded, as noted in earlier mentioned water experiments. This indicates that the regime transitions are not purely  $Ri$  dependent, but that other mechanisms which depend on fluid properties, may also play some role.

Singh et al [6] measured the critical  $Ri$  in a square channel type geometry and a cylinder in air, again using Schlieren interferometry. They noted no significant difference between the value measured for cylinders versus the square channels and like Kakade et al [8] found that at the critical  $Ri$ , vortex generation was suppressed entirely. The magnitude of these values for the cylinder cases were found to be in the range of  $0.12 > 0.15$ , in the  $Re$  range of 85-100, with the critical  $Ri$  increasing with increasing  $Re$  in this range. As mentioned prior, this is significantly lower than the values in water studies.

These most relevant studies summarized above seem to suggest that the critical  $Ri$  has some dependency on fluid properties given the differences observed in air and water. Unfortunately, no examination into these differences or potential reasons why could be found in existing literature. Initial thoughts expanded upon further in section 3 include the significant differences in the relative thicknesses of the thermal and momentum boundary layers in air versus water, as seen in the difference in  $Pr$ . The  $Pr$  dependency may also account for the observed differences in regime transition between working fluids. Additionally, these significant differences in critical  $Ri$  suggest that a mechanistic regime transition criteria can be adopted.

## 2.2 Tandem Cylinder Heat transfer: Effect and determination of local conditions

The impact on heat transfer and local conditions due to the thermal effects of the lower cylinder on the upper cylinder in a tandem pair has been studied in literature due to its key role in commercial heat exchangers and other applications. These studies tended to be experimental in nature and focused solely on heat transfer properties from a single cylinder to develop wide ranged correlations such as Morgan [10] and Ulinskas and Zukauskas [11]. With newer non-intrusive measurement techniques such as PIV and LIF, recent studies have begun examining the interaction between two cylinders and how the lower cylinder effects the properties of the upper cylinder.

From a heat transfer perspective, experiments such as [12-14] have been done for water and air. Generally, for smaller P/D such as 1.5, heat transfer reduction is noted due to the heating effect of the lower cylinder which tends to decrease the local temperature difference between the upper tube surface and fluid. There do appear to be differences between air and water based experiments, with experiments like Sparrow and Niethammer [12] showing much more significant heat transfer degradation for smaller P/D's than the experiments of Grafsonnigen and Jensen [13]. Conversely, for the larger tube spacing, enhancements are found, upwards of 30-40% for P/D = 5 in water from the experiments of Grafsonnigen and Jensen [13].

Examination of the local fluid conditions around the horizontal cylinders has also been studied more recently with techniques such as PIV and LIF. Graftsronnigen et al [15], measured the velocity and temperature field around a 54mm diameter cylinder for  $Ra = 8 \times 10^7$ . Subsequently, Ma and He [16] attempted to validate their Large Eddy Simulation (LES) model with the experimental data of Graftsronnigen et al [15]. This was largely successful as Ma and He [16] quoted a tendency of the LES model to over predict velocity measurements by 15%, thermal predictions were not presented. This approach by Ma and He [16] is particularly useful given the previous failures of modelling the local conditions around a cylinder by other studies such as Graftsronnigen and Jensen [17]. The change in approach that appears to have made Ma and He [16] much more successful is the use of pressure outlet boundaries for the entire domain boundary, much more accurately capturing an “infinite” medium.

Stafford and Egan [19] developed a heat transfer model to predict the heat transfer of the upper cylinder in a cylinder pair versus the power of the lower cylinder for any distance or P/D ratio. This model made use of correlations to calculate the forced convective  $Nu$  and the natural convective  $Nu$ . These two  $Nu$  were combined via a superposition with an exponent of  $n=3$ . The heating effect was handled by evaluating the wall temperature at the local fluid temperature predicted. To obtain the local conditions, Stafford and Egan [19] made use of the laminar point source

model developed by Gebhart et al [20] for velocity, and a temperature model they developed themselves via similarity analysis. While this model appears to be the first to attempt to predict the local conditions of such a geometry and use them in the heat transfer calculation, the underlying relations used for the velocity and temperature predictions had significant limitations, and do not account for phenomenon such as the turbulent transition observed in free thermal plumes at certain distances away from the source. Additionally, the  $Ra$  range used to develop this model is limiting for the application of this model to water based experiments/applications.

These studies seem to indicate that experimental techniques and supporting LES simulations can be used to develop more physical/general criteria. This would allow for the expansion and improvement of models such as Stafford and Egan [19] for a wider  $Ra$  range and for different working fluids, specifically for water.

### 2.3 Flow Patterns: Moderator of CANDU Reactors

Several experimental studies [22-25] have been performed over the years with the intent of developing better experimental data to understand the flow pattern and hence temperature/velocity distribution in the moderator of a CANDU and to develop/enhance prediction methods such as CFD. The accurate prediction of local temperatures and velocities during normal operating conditions and postulated severe accidents is of great importance in safety calculations, to prevent the failure of the calandria tubes and to halt the progression of the postulated accident and

maintain fuel/fission product containment in the primary heat transport system.

Khartibil et al [25] designed and performed experiments on a ¼ scale test facility based on the CANDU-9 design. One key scaling issue discovered was the conservation of the inlet  $Re$  and temperature gradient across the vessel. Due to the decrease in diameter, if the  $Re$  were to be maintained, the temperature gradient would increase to the third power, which can very quickly become unfeasible. To avoid this issue, Khartibil et al [25] made use of the  $Ar$  (equation (1) below) to estimate of the buoyancy force in the vessel to the convective force. Note, this  $Ar$  may be thought of as a “Global”  $Ri$ , as it makes use of the total temperature difference across the vessel, the average inlet velocity into the vessel, and the diameter of the vessel in its formulation. Using this  $Ar$  as their primary consideration for scaling inlet conditions, Khartibil et al [25] suggested that so long as the inlet  $Re$  was large enough to ensure turbulent flow in the inlet of the vessel as found in the full-scale design, flow patterns and non-dimensionalized temperature profiles should be maintained. This approach has been generally accepted by subsequent studies, however it would appear to underestimate the buoyant force via its use of a temperature gradient across the moderator, and not a local temperature near the heated elements/region. Under volumetric heating conditions such differences are likely negligible, but for cases with direct heating of a small number of tubes the local heat flux would generate strongly local temperature gradients around each heater. Additionally, this scaling criteria does

not appear to suggest how to handle the differences in heating arrangement found between scaled facilities (surface heating/electrical) versus the full-scale facility (volumetric/nuclear).

$$Ar = \frac{g\beta\Delta TD}{v_{in}^2} \quad (1)$$

Kim et al [23] experimentally examined the development of a downward secondary jet at the top of a ¼ scale CANDU-6 geometry in isothermal conditions via PIV. While their geometry did include two significant distortions from reality by using air as the working fluid and a simplified nozzle design, they noted that their qualitative jet profile was very similar to prior experiments and experience with water, with the downward magnitude being approximately 50% of the average velocity at the top of the vessel. Using CFD analysis with the  $k-\omega$  SST turbulent model to numerically examine their tests, they observed that their CFD model appeared to under predict dissipation and diffusion, leading to higher velocities predicted than observed. These observations combined with the work of more recent studies such as Ma and He [16] seem to suggest that RANS based CFD models of these types of geometries have a cancellation of errors to some degree, with an over prediction of buoyancy and under prediction of inlet and secondary jet spreading. Given that Kim et al [23] performed their experiments isothermally, the addition of some heated cases from this geometry [23] would have greatly contributed to the understanding of how these two apparent modelling errors affect

temperature and velocity predictions. If subsequent heated experiments were performed using the facility of Kim et al [23] , they are not available in literature as of writing.

Strack [3] examined the temperature fields of a 1/16<sup>th</sup> scale test facility based on the Bruce A moderator configuration experimentally and numerically. It was found that the CFD model using realizable k- $\epsilon$ , tended to over predict temperatures. For qualitative comparisons to the full-scale design, the 1/16<sup>th</sup> facility was found to contain stronger buoyancy forces for similar  $Ar$ . This was largely attributed to the scaling distortions introduced into the 1/16<sup>th</sup> facility such as reduced number of heaters, and surface heating versus volumetric heating. The work of Strack [3] seems to suggest that the change in heating arrangement between scales is not fully reflected in the conventional scaling criteria of the  $Ar$ . This effect appears to be enhanced in the work of Strack [3] as compared to Khartibil et al [25] and Rhee et al [21], which showed that although the total power was scaled correctly, the concentration of this power into a small number of heater rods in the centre of the vessel, increasing the buoyancy strength relative to a larger tube array.

### **3 Sensitivity of local Flow Structures to $Ri$ : Transitions in flow around a cylinder vs $Ri$**

#### **About this Paper:**

#### **Contribution to Knowledge:**

The end goal of this study was to collect temperature and velocity data for upward flow around a cylinder for a wide variety of  $Ri$  to assess the flow structure changes and to develop a wide range of data for subsequent CFD validation. Once this section was completed, the data was arranged in a flow pattern map via visual observations, like the type regularly seen in 2-phase flow studies to quantify the transitions between phase distributions. Using this flow regime map and subsequent simulations, transition criteria were developed based on physical considerations. These transitions included the disappearance of the vortex flow structure routinely associated with momentum dominated flow around a cylinder, and the development of thermal plumes.

Additionally, the significant differences between air and water for vortex suppression identified in literature was briefly examined. Via CFD simulations, the effect of fluid property changes was isolated to examine the physical phenomenological differences for different fluids in aiding flow around a cylinder.

By modifying the specific heat capacity of water, the  $Pr$  was increased and decreased to show that for a thinner thermal boundary layer, a higher  $Ri$  is required. This means that more buoyancy is required to fully suppress all vortices with all other conditions remaining constant for higher  $Pr$  fluids. This work resolved the apparent differences observed in literature which showed different transition regimes occurring for different operating liquids.

One of the main and novel contributions of this thesis was the experimental investigation of the transition phenomena through the natural to mixed convection to forced convection regimes, and the development of mechanistic based transition models capable of working for different fluids.

**Authors Contribution:**

The author (C.W. Hollingshead) was the primary contributor to this study. The CFD/LES model, experimental apparatus and test plan were all developed primarily by Hollingshead with feedback from the co-authors. The experiments were constructed and performed by Hollingshead. Similarly, the analysis and model development work in this study was also primarily done by Hollingshead with guidance from the co-authors. Finally, Hollingshead was responsible for writing the draft paper, with the co-authors contributing significantly in the editing and review process. This paper was submitted to the Journal of Nuclear Engineering and Design on 2022-08-11 and is currently undergoing peer review as of writing.

## **Flow Regime Transitions for Aiding Flow around a heated Cylinder: A Numerical and Experimental Investigation**

C.W. Hollingshead<sup>a</sup>\*, A. Rashkovan<sup>b</sup> and D.R. Novog<sup>a</sup>

<sup>a</sup> Department of Engineering Physics, McMaster University, Hamilton, Ontario, Canada

<sup>b</sup> Nuclear Research Center Negev (NRCN), Beer-Sheva, 84190, Israel

Experiments and numerical simulations were performed to examine the interplay between buoyancy and momentum effects for mixed convection flow around a 13.4mm diameter cylinder in water. PIV and LIF were made to obtain experimental velocity and temperatures over a  $Ri$  range from 0 to 9. LES models were validated against the measured experimental conditions and then used to numerically study the parametric behaviour over a wider range of conditions. The CFD model was found to perform well, with a small tendency to over predict temperature and velocity measurements for higher buoyancy conditions. Using the experimental LIF results, three flow regimes around the cylinder were identified, grouped, and made into a flow regime map. From this, two sets of transition criteria were developed and proposed to predict the collapse of the recirculation zone and the total suppression of vortex formation. This was done via observations from the experimental data and additional CFD simulations to examine the separate effects of fluid properties and incident turbulence levels, both of which were shown to influence vortex suppression significantly. The criteria proposed was found to accurately capture the visually observed flow regimes experimentally in water.

**Keywords:** CFD, LES, PIV, LIF, Mixed convection,  $Ri$ ,

\* Corresponding Author  
E-Mail address: hollincw@mcmaster.ca

## 1 Nomenclature

PIV	Particle Image Velocimetry
LIF	Laser Induced Fluorescence
CFD	Computational Fluid Dynamics
LES	Large Eddy Simulation
$Gr$	Grashof Number
$Ri$	Richardson Number
$Re$	Reynolds Number
$Pr$	Prandtl Number
$St$	Strouhal Number
$C_{pb}$	Base Pressure Coefficient
$k$	Thermal Conductivity [W/mK]
$\beta$	Volumetric thermal expansion coefficient [1/K]
$c_p$	Specific Heat Capacity [J/kgK]
$\mu$	Dynamic Viscosity [Pas]
$\dot{m}$	Mass Flow Rate [kg/s]
$\nu$	Kinematic viscosity [m <sup>2</sup> /s]
$v_\infty$	Average Inlet Velocity [m/s]
$D$	Diameter of vessel [m]
$L$	Length of vessel/heater rods [m]
$g$	Acceleration due to gravity [m/s <sup>2</sup> ]
$T_W$	Cylinder Wall Temperature [K]
$T_{in}$	Nozzle Inlet temperature [K]
$T_i$	Inlet Turbulent Intensity
$q''$	Heat flux [W/m <sup>2</sup> K]
$Q$	Heater Power [W]

## 2 Introduction

Cylinders are the foundational building block of industrial heat exchangers and have a presence in Nuclear Reactor components, such as the horizontal calandria tubes in the moderator of a CANDU reactor. Whilst flow around an adiabatic cylinder has been extensively studied, comparatively less has been done on heated cylinders, more specifically on how the convective and buoyant forces interact, and how the local conditions (temperature, velocity) in mixed convection affect the observed phenomena such as heat transfer. Additionally, with design shifts in Generation IV reactors to passive safety features, understanding the transition between forced, mixed and natural convection phenomena has become more important. The relative strength of buoyancy and momentum can be characterized by the Richardson number ( $Ri$ ) as shown in equation (3) below and is a function of both  $Re$  and  $Gr$ . Generally, forced convection dominates for  $Ri < 0.1$ , and natural convection above  $Ri > 10$  [1]. The region in-between being referred to as Mixed Convection where both effects are present and contribute to heat transfer.

$$Gr_D = \frac{g\beta\Delta TD^3}{v^2} \quad (1)$$

$$Re_D = \frac{\rho v_\infty D}{\mu} \quad (2)$$

$$Ri = \frac{Gr}{Re^2} = \frac{g\beta\Delta TD}{v_\infty^2} \quad (3)$$

An important phenomenon identified in the literature related to mixed convective flows around cylinders is the disappearance of von-Karman Vortices at some critical  $Ri$ . Above the critical  $Ri$  the flow field transitions to a “thermally dominated” regime, which is more stable and begins to behave similarly to that of a free thermal plume. Below this critical transition von-Karman Vortices are observed. This transition has been studied experimentally by studies such as [2-8] with relevant experimental studies summarized in Table 1 with notable differences being observed between experiments with water and air.

Table 1. Shows the critical  $Ri$  from studies in literature

Study	Cylinder Diameter [mm]	Working Fluid	Flow Orientation	$Re$ range	$Ri$ Range	$Ri^1$ crit quoted
Hu and Koochesfahani [2]	4.76	Water	Opposing	135	0-1.04	0.72
Michaux-Leblond and Belorgey [6]	11.7	Water	Aiding	130-327	0-4	0.49
Khashehchi et al. [5]	30	Air	Cross	1000-4000	0-0.2	N/A
Singh et al. [7]	6.2	Air	Aiding	85-92	0-0.18	0.122-0.157

<sup>1</sup> The  $Ri_{crit}$  quoted in these experiments are not consistent and can refer to different phenomena

The study of Michaux-Leblond and Belorgey [6] experimentally examined the wake behind a 11.7mm diameter cylinder in water. Using Laser Doppler Velocimetry, it was determined that at a  $Ri$  of 0.49 a transition occurred and the vortex sheet typically observed for flow around a cylinder was suppressed. When this suppression was first reached, it was found that two simultaneous and approximately symmetric eddies were observed. As heating power was increased further, a secondary flow developed and filled in the momentum deficit region of the wake and suppressed the formation of the two eddies entirely. Hu and Koochesfahani [2] studied the wake of a heated cylinder in opposed flow. Velocity and temperature fields as a function of  $Ri$  were measured employing molecular tagging velocimetry and thermometry in water, respectively. Using a copper tube with a 4.76mm diameter in a working fluid of water it was found that below  $Ri = 0.31$ , no change to the von-Karman vortices was observed. For the values of  $Ri$  between 0.31 and 0.72, it was noted that von-Karman vortices appear to be delayed and began further downstream from the cylinder as compared with the adiabatic case. At  $Ri > 0.72$ , the von-Karman vortices were replaced by smaller wake vortices, generated symmetrically on both sides of the cylinder, and were noted to contain more of a Kelvin-Helmholtz type nature.

Singh et al [7] examined the suppression of vortices for circular and square cylinders in air via Schlieren interferometry. It was reported that above a certain  $Ri$ , vortices were entirely precluded from forming with no mention of a symmetric wake vortices shedding process that were obtained for water (see [2] and [6]). This critical  $Ri$  was noted to be similar for the circular and square cases and was dependent on  $Re$ , with higher  $Re$  yielding higher critical  $Ri$ . The wake behind a square cylinder using Schlieren interferometry at variety of  $Re$  and orientations was also examined by Kakade et al [8]. The general increase in critical  $Ri$  with increasing  $Re$  reported by Singh et al [7] was confirmed. Additionally, when the square cylinder side walls were aligned with the flow path, the critical  $Ri$  was minimized. The critical  $Ri$  was maximized when the angle was increased to 20 degrees and held constant to an angle of 45 degrees (the maximum angle employed). This was suggested to be a result of an increase in the adverse pressure gradient caused by the edges of the square channel. Khashehchi et al. [5] experimentally examined the wake behind a cylinder in a wind tunnel for a  $Ri$  in the range of 0 to 0.22 for a cross-flow orientation. No change was observed to the classical von-Karman shedding flow topology for  $Ri$  up to 0.05. Above  $Ri$  of 0.05, an asymmetry driven by buoyancy began to exist with the upper vortex distorted upwards compared to the adiabatic case. From both experimental studies in air, there was a lack of the transition vortex symmetric shedding phenomena that was observed in water.

Numerical studies of the phenomena in mixed convection over a circular cylinder have also been conducted including [9-13]. Singh et al [9] and Chang and Sa [10] numerically investigated the forced to free convection transition in air at a  $Re$  of 100, and both found a critical  $Ri$  of 0.15. As opposed to the experimental observations in air of Singh et al [9], the transition in the numerical work involved the generation of symmetric eddy pairs. The study of Wan and Patnaik [11] numerically examined the suppression of vortex induced vibrations in cylinders solely by thermal effects using their own code. Using simulations with a cylinder connected to a spring in a channel in a cross-flow, it was noted that as the power to the cylinder was increased in the range of  $Ri$  between 0.1 and 0.2, very little changed in the flow structures around the cylinder, except for a gradual narrowing of the vortex street. For  $Ri$  greater than 0.3, no vortices were detected. Increasing further the  $Ri$ , they found a critical  $Ri$  of 0.8, above which all vibrations were fully

suppressed. Additionally, this critical  $Ri$  was found to be dependent on the free stream velocity.

Previous studies on adiabatic flow around a circular cylinder, such as the one by Feng and Wang [14] experimentally demonstrated in water that the pure von-Karman shedding processes can be interrupted and replaced by a symmetric shedding mode when momentum is introduced into the wake region via jets. The experiments of Fu and Rockwell [15] introduced a slit parallel to the flow direction into the cylinder and varied this slit size using water as the working fluid. They found that for increasing slit size, the von-Karman shedding process was shifted away from the cylinder. Additionally, when the slit reached a critical size (for a fixed  $Re$ ), the rear-wake region of the cylinder appeared to be divided into two separate symmetric regions. Gao et al. [16] also examined the effects of a parallel slit size in a cylinder experimentally in air. Similarly to Fu and Rockwell [15], Gao et al. [16] reported that above a certain size, symmetric vortices begin to compete with the regular von-Karman shedding mode, suppressing the central recirculation zone and appearing to split it into two recirculation zones. These effects were also observed and studied in the experiments of Shi and Feng [17]. Examining the parallel slit geometry numerically, Baek and Karniadakis [18] showed similar results to the experimental studies discussed above. Additionally, it was found that the symmetric vortices shedding process began at a smaller slit size for an inlet  $Re$  of 1000 as compared to  $Re$  of 500. This change in slit size required to introduce the symmetric shedding mode suggests a dependency on the base pressure coefficient of the cylinder. Studies such as Williamson and Roshko [19] have also shown the decrease of rear-base pressure coefficient with  $Re$  in the range examined by Baek and Karniadakis [18], which may partially explain the reduced slit size required in this  $Re$  range. This division of the re-circulation zone also appears to be occurring in heated experiments with momentum induced via buoyancy effects replacing the bypassed flow from the adiabatic slit experiments as evidenced by observations from Hu and Koochesfahani [2] and Michaux-Leblond and Belorgey [6]. This phenomenon is further examined in this study.

The goal of the present study is to present new experimental and numerical analysis to better understand the underlying phenomena behind the transitions observed in mixed convection flows around a heated cylinder. Additionally, modelling efforts which can predict the flow topology around the cylinder are developed and tested against the experimental database and numerical simulations. These models appear to both match the data well and explain the apparent differences in flow topology between air and water that were observed in previous studies.

### 3 Experimental setup and conditions

The aim of the current experimental study was to examine how the oncoming flow velocity and power supplied to a cylinder impact the flow fields around a horizontal cylinder in the mixed convective  $Ri$  regime. To achieve the experimental goals, two separate experimental campaigns were performed.

- Particle Image Velocimetry for velocity measurements
- Laser Induced Fluorescence for fluid temperature measurements

The geometry consisted of a horizontal cylindrical test vessel which was 489.3mm in diameter by 504.7mm in length as used in Hollingshead et al [20] - seen in Figure 1 (left). The heater used was

the same as Heater A as described in Hollingshead et al [20]. This heater had a diameter of 13.4mm and was un-instrumented with the electrical connections on one side to allow for ideal optical access. The heat flux shape was a cosine shape with a heated length of 500mm. Note that all measurements presented are for the central region in the peak heat flux of the heater.

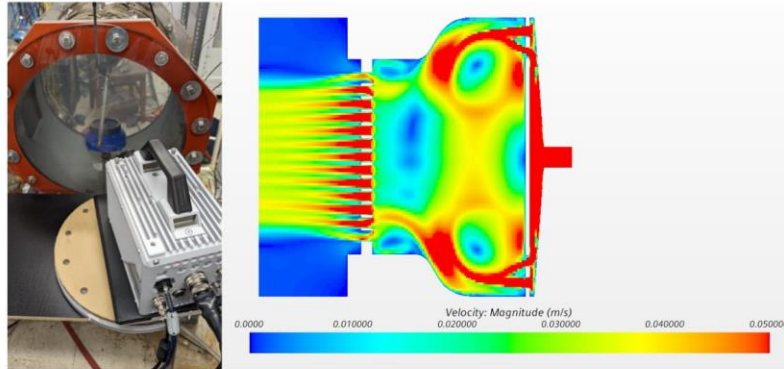


Figure 1. The test section with the nozzle at the bottom of the vessel just below the heater with the PIV/LIF camera in view (left) and instantaneous velocity magnitude contour on a symmetry plane of the diffuser nozzle simulations at 100g/s (right)

### 3.1 Nozzle/Inlet Condition

To adequately control the inlet velocity a 3-D printed nozzle was designed and built. The design was based by CFD calculations employing the  $k-\omega$  SST turbulence model – with the cut-view in Figure 1 (right). The  $k-\omega$  SST turbulence model was used due to its ability to capture salient flow features for early prototypes built and examined via PIV. The velocity profile of the nozzle was measured for a variety of flow rates and can be seen below on Figure 2 with tabulated time and space averaged values shown in Table 2. It should be noted that the flow field outside the nozzle as measured employing the PIV camera system was found to be asymmetrically positioned under the heater with a shift of 6mm. This asymmetry was not correctable due to positioning errors in the assembly of the end plates of the vessel, in addition to potential manufacturing errors in the positioning of the inlet and outlet ports to the vessel. This asymmetry was accounted for in subsequent CFD simulations.

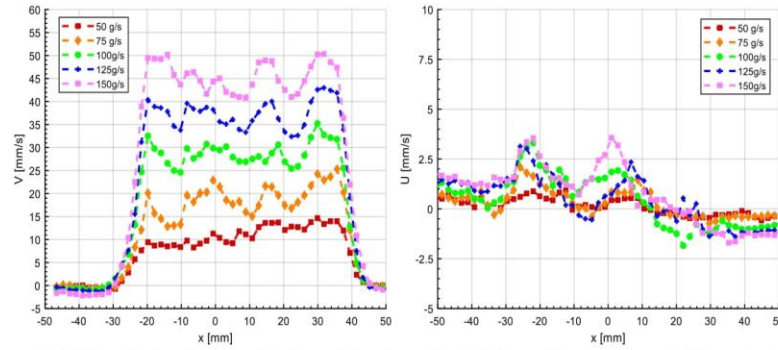


Figure 2. PIV velocity (vertical, left and horizontal, right) profiles measured 20mm below the cylinder for isothermal conditions (note  $x=0\text{mm}$  corresponds to the centre of the heater rod).

Table 2. Nozzle time-averaged parameters versus mass flow

Inlet Flow Rate (g/s)	Measured Average Velocity (mm/s)	Turbulent Intensity	Reynolds Number
$50 \pm 1$	$12.4 \pm 3$	0.2	$187 \pm 40$
$75 \pm 1$	$18.3 \pm 3$	0.34	$275 \pm 40$
$100 \pm 1$	$27.5 \pm 3$	0.27	$414 \pm 40$
$125 \pm 1$	$35.5 \pm 3$	0.3	$534 \pm 40$
$150 \pm 1$	$44.2 \pm 3$	0.31	$665 \pm 40$

### 3.2 Particle Image Velocimetry

The PIV experiments were performed using a Photron SA5 highspeed camera and a ND-YLF pulsed laser. The camera and laser were synchronized via a synchronizer which was set to a capture frequency of 125Hz and a laser pulse delay of  $7800\mu\text{s}$  for a typical pixel displacement of 1-5 pixels. Due to camera buffer limitations, five sets of 400 image pairs were captured for a total time averaging time of 20s. This was used to obtain the time averaged velocity fields. Additionally, the camera was placed on a 10-degree tilt from the imaging plane, as this was found to significantly help with the quality of heated measurements in Hollingshead et al. [20]. Adiabatic tests were done with and without this 10-degree tilt, which showed no impact on the velocity field in the regions reported.

The uncertainty in the PIV measurements was assessed to be 3mm/s via repeatability measurements. This was to account for errors in camera positioning, laser sheet alignment, and process system variability. Additional uncertainty due to pixel displacement ( $\sim 0.1$  pixel) was not included as it was found to be much smaller than the 3mm/s. The laser sheet thickness was approximately 3mm, indicating that all velocity measurements are averaged over this volume.

### 3.3 Laser Induced Fluorescence

In order to clearly observe the thermal plumes and measure the local plume temperatures Rhodamine B dye was added to the water at a concentration of approximately  $1.2 \times 10^{-7}$  mol/L. The LIF measurement procedure, including a 10-degree camera tilt, closely follows the one outlined in Hollingshead et al [20]. Since LIF measurements do not require laser-camera coincident timing, the camera and laser were not synchronized for these measurements to avoid the camera buffer errors mentioned above for the PIV measurements. The laser was operating at a frequency of 1000Hz with the camera at a capture frequency of 125Hz and shutter frequency of 1000Hz. These settings were found to minimize intensity fluctuations in the images.

The error in the LIF temperature measurements was evaluated to be 1.1°C. This was assessed via a contribution of the measured standard deviation in the intensity of a flat temperature field of approximately 1% converted to a temperature and the error in the type T thermocouple used for calibration. Repeatability measurements were also performed but were found to agree well within this 1.1°C error and as such did not contribute to the total error. This improvement in repeatability performance compared to the PIV measurements was directly attributed to the improvement in laser sheet visibility. This was a direct result of the fluorescence of the Rhodamine B.

Sample images from the LIF measurements can be seen in Figure 3 for a variety of inlet flow rates at a fixed power. The change in flow topology vs flow rate is quite noticeable. Starting at 75g/s and 512W, the flow topology appears to largely resemble that of a free thermal plume, qualitatively containing more disturbances than a free thermal plume due to velocity difference between the plume and the small but still significant convective components. As the flow rate is increased to 100g/s, the plume width increases and the length scale of the disturbances appears to increase, though the nature of the disturbances appear to be the same as the 75g/s case. Increasing this flow rate further to 125g/s, the width increased further, and coincident eddies began shedding from the cylinder. Additionally, there no longer appeared to be a contiguous region of hot fluid from the top of the heater to the end of the measurement window as seen for the more thermal 75 and 100g/s cases. When the flow is increased to 150g/s, the width of the rear-wake region is largely unchanged. However, the shedding mode changes, and instead of simultaneous shedding they become asymmetric, appearing to be classic asymmetric von-Karman vortices.

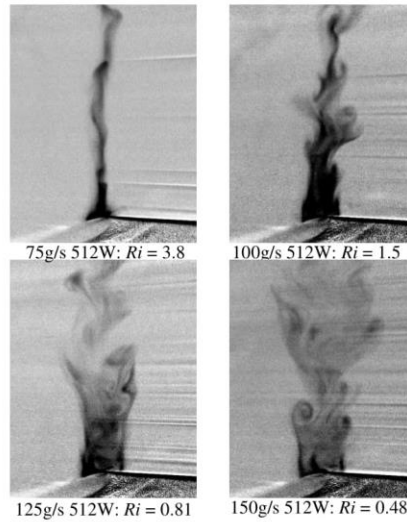


Figure 3. LIF instantaneous intensity fields measured for four mass flow rates at a power of 512W.

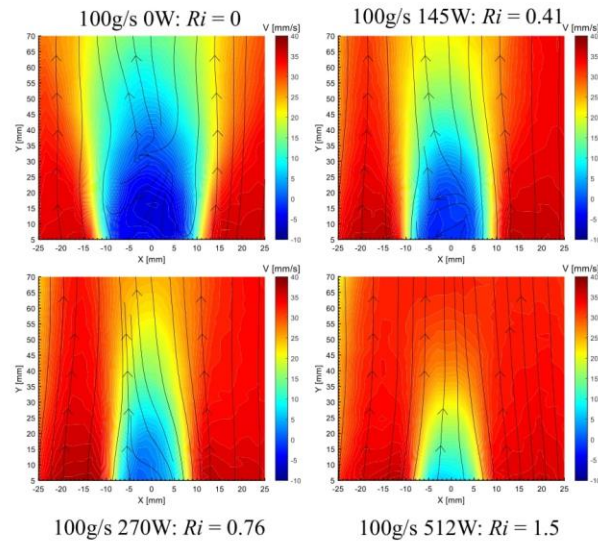


Figure 4. PIV results of the wake behind the cylinder as a function of power (time averaged contours). Note,  $Y=0\text{mm}$  corresponds to the top of the cylinder surface.

## 4 Experimental Results

### 4.1 Velocity Measurements

Selected PIV results showing time-average vertical velocity can be seen in Figure 4 and Figure 5. These figures show the downstream contours of the wake for increasing heat input. A gradual narrowing and eventual disappearance of recirculation zone downstream of the cylinder<sup>2</sup>, in Fig. 4, is observed as the heater power is increased. This is indicative of a transition to buoyancy dominated flow, and the suppression of the von Karman vortex street. This is further illustrated in Figure 5 which shows that for a variety of flow/power combinations the negative velocity in the recirculation zone vanishes for higher ratios of the input powers (buoyancy force) to mass flow rate (momentum). Additionally, as it follows from Figure 5 (b and d), as the power level is increased, a change in curvature is present in the region  $5 < y < 20\text{mm}$ . This change is believed to be associated with an increasing buoyant force and the development of a thermal plume in the flow field.

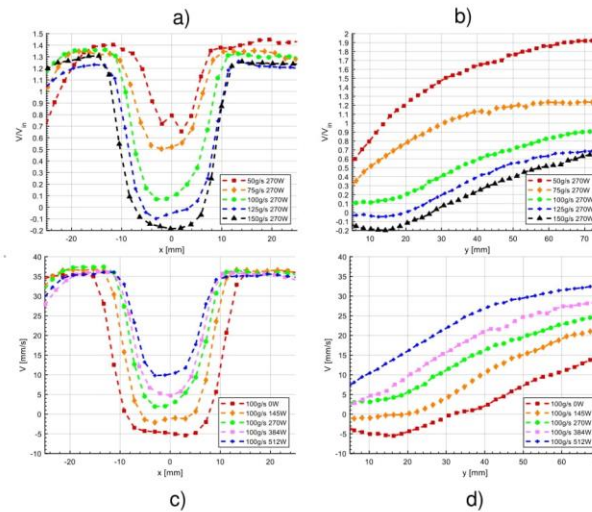


Figure 5. Vertical velocity profile for  $y = 10\text{mm}$  away from the cylinder surface (left) and the centreline  $x=0\text{mm}$  velocities (right)

### 4.2 Fluid Temperature Measurements

Time averaged measurements of local fluid temperature difference relative to the inlet are presented in Figure 6 for a variety of cylinder power levels and inlet flow rates. As the inlet power is increased for a fixed flow rate, there is a gradual thinning of the wake region and an increase in the temperature, indicating the development of a thermal plume. This is consistent with the velocity measurements presented in Figure 5 which also indicate that the region downstream the

<sup>2</sup> The recirculation zone is characterized experimentally as the region of fluid where negative average vertical velocity values are obtained.

cylinder becomes more buoyant in nature. Transient videos and phenomena discussed in subsequent sections also indicate that as the power is increased, or the flow decreased at a fixed power, fewer disturbances are visible in the flow field. This is attributed to the added momentum due to the buoyancy in the wake region. The effect of this thought to increase the average velocity in the wake region. This decreases the velocity gradient between the wake region and convecting fluid thus reducing the primary mode of turbulence generation.

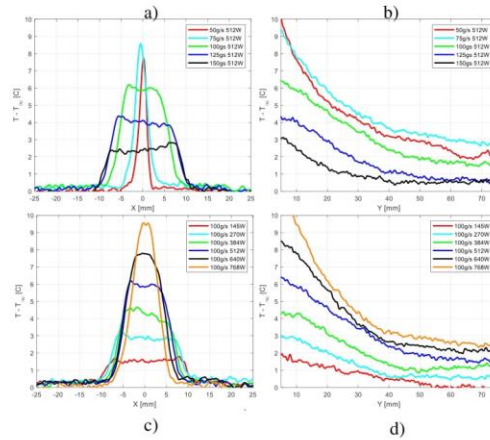


Figure 6. Temperature profiles for a variety of conditions at  $Y = 5\text{mm}$  above the cylinder a) and c), and the centreline profiles away from the cylinder b) and d).

### 4.3 Flow Regime Map

Three regimes were identified to classify the wakes with characteristics observed. These were von Karman vortices (VKV), eddy pair (EP) and thermal dominated flow as identified on Figure 7. Given the unique changes in the turbulent behaviour in the wake of a tube in mixed convection flow observations were collected over a wide range of  $Gr$ ,  $Re$  and  $Ri$ . To organize the data and to narrow the focus for subsequent analyzes, a flow regime map was created based in the experimental observations. The map was based on visual observations from videos generated by the LIF transient data and is presented in Figure 8. Additionally, several lines of constant  $Ri$  are plotted to highlight the range of  $Ri$  conditions measured.

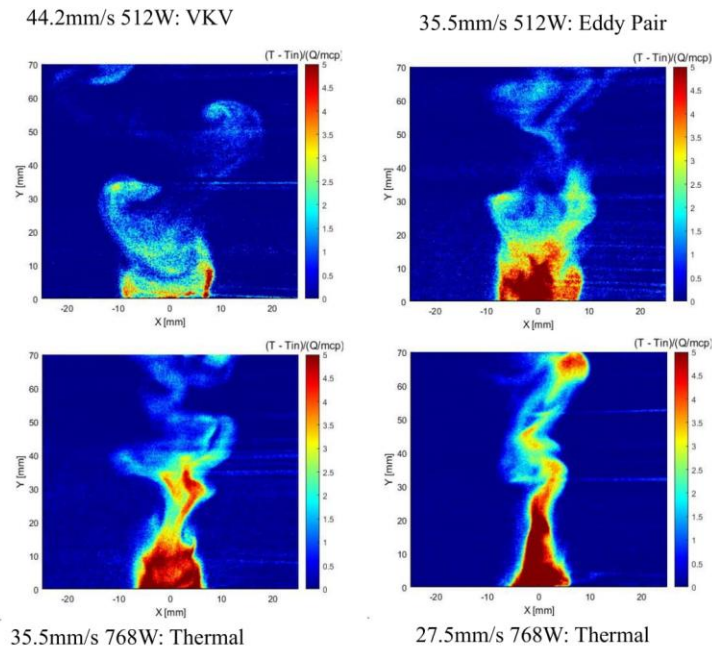


Figure 7. Normalized instantaneous temperature profiles identifying each of the three regimes observed

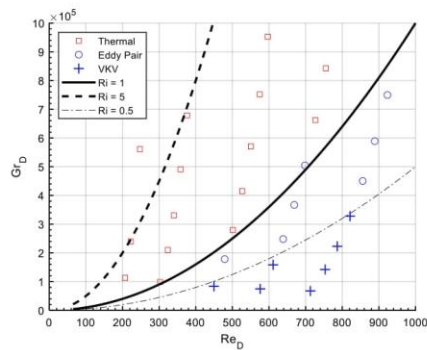


Figure 8. Flow regime map with lines of constant  $Ri$  to indicate approximate buoyancy to force convective strengths

#### 4.3.1 von Karman Vortices Regime

The experiments had an inlet  $Re$  in the 200 to 700 range as shown by Table 2. This range corresponds to boundary of the Transition-in-Wake (TrW) and the Transition in Shear Layers (TrSL) regimes as classified by Zdravkovich [21]. The effects of inlet turbulence intensity on the TrW regime were examined by Aarnes et al [22] up to 25% via DNS simulations. Aarnes et al [22] found that the Strouhal number of this regime decreased slightly at an inlet turbulent intensity of 25% versus none. This indicates that for the current study, the shedding frequencies may be slightly smaller than correlations would predict. Additionally, the lower range of  $Re$  in this study has been examined numerically by Rajani et al [23].

The von-Karman vortices regime, or VKV, is characterized by the traditional von Karman vortex street associated with the TrSL regime visualized in Figure 7 (top left). At these ranges of conditions (blue crosses in Figure 8), the flow field around the heated cylinder is very similar to that of an adiabatic case. This regime of flow around an adiabatic cylinder is largely characterized by one vortex shedding after another in an asymmetric fashion. As power is increased, the length and width of the recirculation zone behind the cylinder monotonically decreases as seen in Figure 9 with little change to the vortex shedding process until the recirculation zone collapses and the Eddy Pair regime discussed in section 4.3.2 is reached. As the power is increased, in the near field at the top of the cylinder, what will be referred to as a precursor plume begins to form. The precursor plume is the hot fluid at the top of the cylinder that forms but is unable to rise from the cylinder surface. This appears to be a result of negative recirculation pressure holding back this hot fluid. This precursor plume tends to wobble from side to side, shedding with the vortices as they are generated from whichever side the precursor plume is currently on. Per the experimental observations of Fu and Rockwell [15], Gao et al [16] and Shi and Feng [17], the transition to the next regime likely occurs when this precursor plume becomes strong enough to divide the momentum boundary layer of the cylinder, with a buoyant plume replacing the physical jets in their adiabatic experiments.

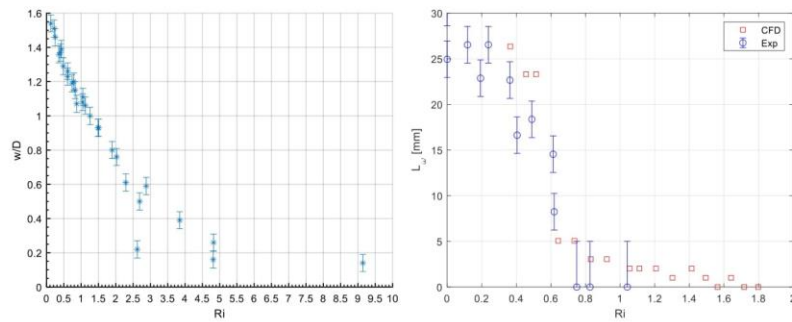


Figure 9. Width of the thermal wake/plume region at a distance of 5mm from the cylinder surface (left) and the length of the recirculation zone as a function of  $Ri$  (right). Note the CFD simulations are for an inlet  $Re$  of 414.

### 4.3.2 Eddy Pair Regime

Once the heat input reaches a certain power level, the fluid on top of the cylinder contains enough buoyancy to partially counteract the recirculating fluid. This appears to alter the vortex shedding process as the vortices begin to shed nearly simultaneously on both sides of the cylinder, as seen in Figure 7 (top right). The precursor plume continues to grow and oscillate from side to side as in the previous VKV regime, except in this case oscillations occur with the simultaneous eddy pair. However the precursor plume is still confined to the wake of the cylinder, though it appears to be larger than at lower powers.

Power Spectral Density (PSD) analysis at the 125g/s flow rate taken at the point  $X=0\text{mm}$ ,  $Y=70\text{mm}$  is shown in Figure 10. The transition from VKV regime appears to increase the  $St$  from 0.20 to approximately 0.25. This increase is attributed to changing dynamic viscosity and density with increasing power, increasing the local  $Re$ . Additionally, the increase could be partially due to the vortices no longer getting “dragged” towards the rear of the cylinder before shedding. This may allow for a subtle increase in shedding frequency and the  $St$ . As the PSD analysis was performed on the LIF data due to the lack of camera buffer issues, no adiabatic data was possible and the direct effect of the turbulent intensity on the shedding frequency was also not available. Though, expanding the general trend backward towards zero power would appear to yield a slight decrease in  $St$ , which would be consistent with the predictions of Aarnes et al [22] for the effect of inlet turbulent intensity on shedding frequency.

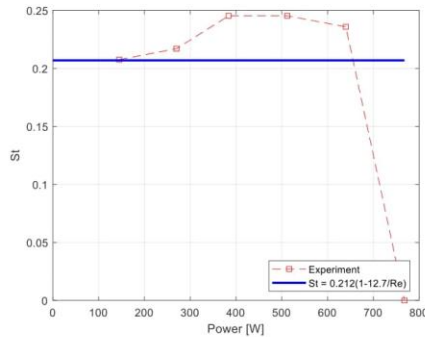


Figure 10. Strouhal number measured from LIF data at 125g/s as a function of heater power versus a correlation for  $St$  via Zdravkovich [21]

The pairwise eddy shedding appears to continue until the buoyant force becomes strong enough to entirely force all fluid in the near-cylinder wake region upward, completely overcoming the recirculation flows that are driving vortex generation. It should be noted that in the experiments of Singh et al [7] and Kakade et al [8] for air, this regime was not observed. This indicates that property differences between air and water appears to be significantly affect regime transition.

### 4.3.3 Thermal Regime

The thermal regime is a broad classification and is first reached when vortices no longer form, or form very infrequently due to occasional disturbances. The size of the plume in this regime varies

greatly, from being near the size of the diameter of the cylinder when first reached to approximately the thickness of a free thermal plume. This is partially visualized in Figure 9, showing the gradual thinning on the wake region vs  $Ri$  which shows that around a  $Ri$  of 4, that the width of the plume/wake region no longer shrinks. Around this  $Ri$ , it is considered to have the flow topology of a free thermal plume.

## 5 LES Modelling

To study the transitions further, obtain more data, and assess the phenomenological differences between fluids, LES modelling of the flows was performed using STAR-CCM+. The computational domain used can be seen below in Figure 11. The domain was 7 cylinder diameters long and 489.3mm in total diameter. The outlet was a 19mm diameter opening at the top of the vessel and in the centre of the domain. The walls of the domain were no-slip walls and a 60mm diameter cut-out was placed 20mm below the cylinder spanning the length of the nozzle to simulate the inlet nozzle. The circular cut out for the inlet condition was offset by 6mm to account for the small asymmetry between the jet and cylinder in the experiments. The inlet velocity boundary condition for the nozzle was matched to the experimentally obtained inlet velocity distributions. The synthetic turbulence on the inlet for the LES simulations was inputted with the turbulent intensity of a given experimental condition with a length scale of 5mm, the diameter of the inlet flow straightener. To handle buoyancy effects the Bousinesq approximation was used. The wall was modelled via the all  $y^+$  wall model.

As was stated previously, the present study spans from the upper transition in wake regime (TrW) to lower subcritical transition in shear layer (TrSL), following Zdravkovich [21] classification of the regimes of flow around the circular cylinder. Of numerous studies on LES modelling of the flow around the circular cylinder in regimes relevant to the present study, including e.g. Rajani et al. [24] in TrSL and Xiyun and Guocan [25] for the  $Re$  characteristic of transition from TrW to TrSL regime, it can be concluded that the dynamic Smagorinsky model is capable of capturing the flow phenomena for the conditions employed in the present study. Furthermore, the simulations of Clifford and Kimber [26] showed exceptional performance of the dynamic Smagorinsky model for natural convection flows in a square cavity.

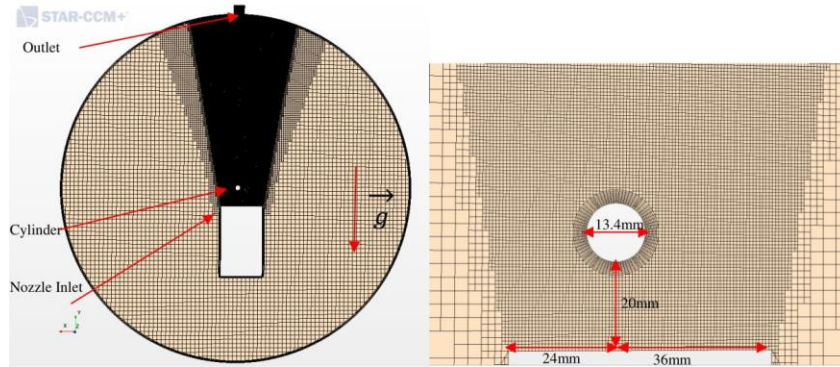


Figure 11. Mesh cross-section for the entire domain and a zoomed in section around the heater

### 5.1 Sensitivities

To ensure the CFD fidelity sensitivity to mesh, timestep and turbulent intensity on the inlet conditions were examined for the 100g/s adiabatic condition. It should be noted that these were performed after ensuring that the computational model was capable of handling >95% of the turbulent kinetic energy, as confirmed by applying the LESIQ proposed by Celik et al [27] to the domain. In general, little sensitivity to mesh and timestep was noted, as seen in Figure 12 below. Owing to this, a mesh base size of 1mm and timestep of 0.1s were chosen for the 100g/s or 27.5mm/s inlet velocity case. For other flow rates, the timestep was varied to assure a maximum CFL value of approximately 3. Over a  $\pm 5\%$  window of the turbulent intensity from the experimentally measured values, no significant difference in velocity profiles was obtained. Additionally, the maximum  $y^+$  on the cylinder wall was found to be 1.8, indicating a proper resolving of the boundary layer. Another sensitivity study was performed for a mesh very similar to the one employed in this study for free thermal plumes in the work of Hollingshead et al. [20] which also showed little sensitivity to mesh or timestep.

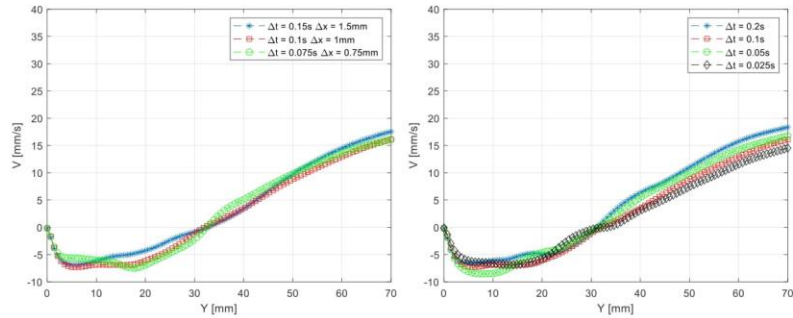


Figure 12. Sensitivity to mesh and timestep for inlet velocity of 27.5mm/s

## 5.2 Validation

To validate the LES modelling a wide range of experimental conditions were chosen covering a  $Ri$  range from 0 to 1.9. These conditions included the following mass flow/power conditions combinations: 100g/s-0W, 100g/s 145W, 100g/s 270W, 100g/s-512W and 75g/s-256W. These ranges of conditions were also chosen to have validation cases for each flow regime identified. The choice of including an adiabatic condition was made to help isolate modelling errors in either the momentum or buoyant fields.

### 5.2.1 VKV Regime Validation: 100g/s 0W and 100g/s 145W

The general performance of the model for the VKV regime can be seen below in Figure 13 a). The strong performance of the thermal field would appear to largely be due to the very small temperature gradients in relation to the error in the LIF measurements of 1.1°C. The performance in the velocity field for the model however is mixed with conflicting indicators. The RMS error indicates a good performing model, yielding a value of 2.31mm/s compared to the measurement uncertainty of 3mm/s. However, this measurement uncertainty captures only 80% of the total predictions. When the added systematic error introduced into the simulations via the inlet condition uncertainty is accounted for, by increasing these error bounds to 5mm/s, 96.4% of the predictions are covered. Additionally, when examining the velocity profiles for the 100g/s 0W case in Figure 14, good agreement is found with nearly all data points lying within measurement error. This level of agreement appears to be consistent with the study of Rajani et al [24] and Xiuyan and Guocan [25].

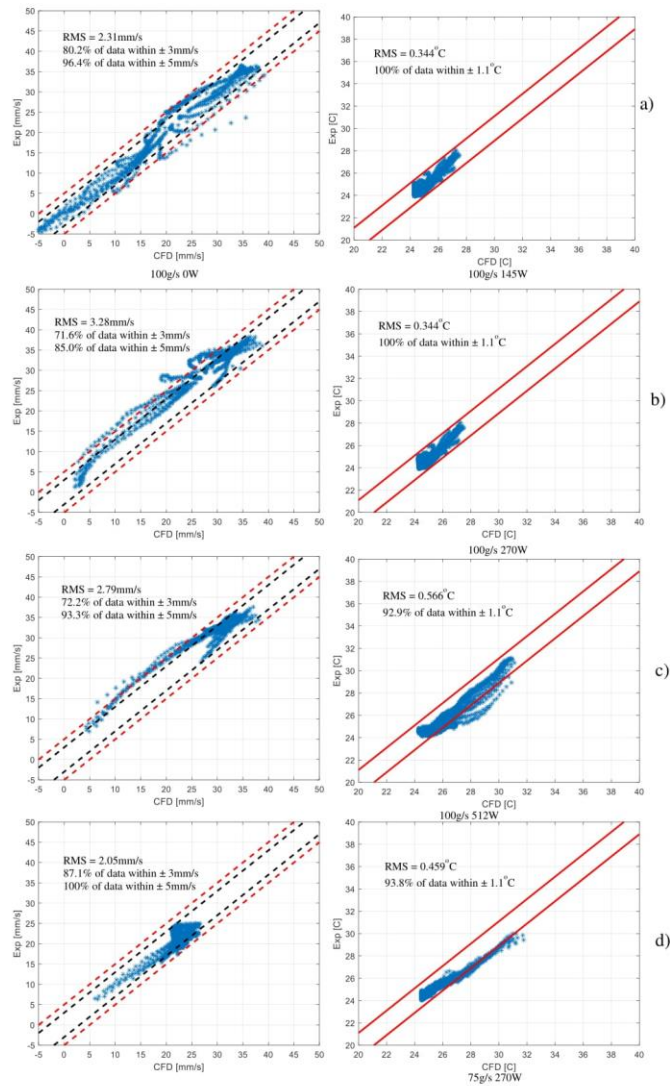


Figure 13. Validation plots for velocity and temperature predictions: Solid red  $\pm 1.1$ °C, dashed red  $\pm 5$ mm/s and dashed black  $\pm 3$ mm/s

### 5.2.2 EP Regime Validation: 100g/s 270W

The performance of the EP regime predictions can be seen in Figure 13 b). The thermal performance for this regime was exceptional, with all the data lying within measurement uncertainty. The performance of the velocity predictions was less so, with only 72.2% of predictions within 3mm/s. This increases to 85% if the bars are expanded to 5mm/s. The main driver for this reduced performance appears to largely be due to a slight difference in slope in the sharp gradient in the  $5 < |X| < 10$ mm region, which appears to occur over a smaller distance than the VKV regime as evidenced by Figure 14. The performance of this model in this regime is considered to be strong aside from this region, nearly all data along the centreline agreeing with experiment as shown in Figure 14. This is further evidenced by an RMS error of 3.28mm/s, slightly error than the measurement error. Additionally, the predicted temperature field agrees very well with experiment as shown in Figure 15.

### 5.2.3 Thermal Regime Validation: 100g/s 512W and 75g/s 270W

As the flow topology becomes increasing thermal, performance characteristics identified by Ma and He [28] and also seen in Hollingshead et al [20] become apparent. Ma and He [28] found that for LES simulations for natural convection around a circular cylinder there was a tendency to over-predict velocities by 15% and under predict  $Nu$  relative to experiment. In Figure 13 c) and d), the model begins to over predict the local temperatures relative to the experimental results. This level of over-prediction appears to be worse with increasing buoyancy, the 75g/s case tending to over predict the centreline temperature by 2°C as compared to the 100g/s 512W case as seen in Figure 15. Conversely, the level of performance in the velocity predictions appears to be consistent with that of the EP regime, with the velocity predictions largely covered by measurement uncertainty in Figure 14. For the most buoyant condition examined, 75g/s 270W, in the far field of Figure 14 (left), there appears to be the beginning of an over-prediction of the velocity field. This systematic over-prediction is consistent with the results shown by Ma and He [28], and is suspected to get worse with increasing  $Ri$  past this point.

The underlying cause of this apparent over-prediction of buoyancy may result from a combination of the models slight deficiency in predicting the heat transfer and/or issues in the SGS model for highly buoyant conditions. In terms of heat transfer, the under prediction of  $Nu$  as shown by Ma and He [28] may be a contributing factor. This over estimation of wall temperature would yield stronger temperature gradients in the near wall region, as evidenced by the over-prediction of fluid temperatures and velocity predictions for  $Ri = 1.9$ . Conversely, Clifford and Kimber [26] show their LES model is quite capable of capturing the  $Nu$  and show no significant deviation in their velocity predictions as compared to experiment. This puzzling difference in model performance may in part be due to the relative size difference between the characteristic lengths in those studies, and subsequently higher local heat fluxes/larger gradient magnitudes over smaller distances in the study from Ma and He [28]. Clifford and Kimber [26] and Ma and He [28] both used the Dynamic Smagorinsky SGS model, indicating that the difference in performance may be related to geometry scale. This is visible in the characteristic length, being 750mm for Clifford and Kimber [26], 54mm for Ma and He [28] and 13.4mm in the present study. Given the excellent performance at large scales in the work of Clifford and Kimber [26], this seems to suggest that under smaller scale flows the performance may deteriorate somewhat. This would appear to be an underprediction of local turbulence and spreading of thermal plumes, yielding higher temperatures and velocities relative to experiment in works such as Ma and He [28] and Hollingshead et al [20].

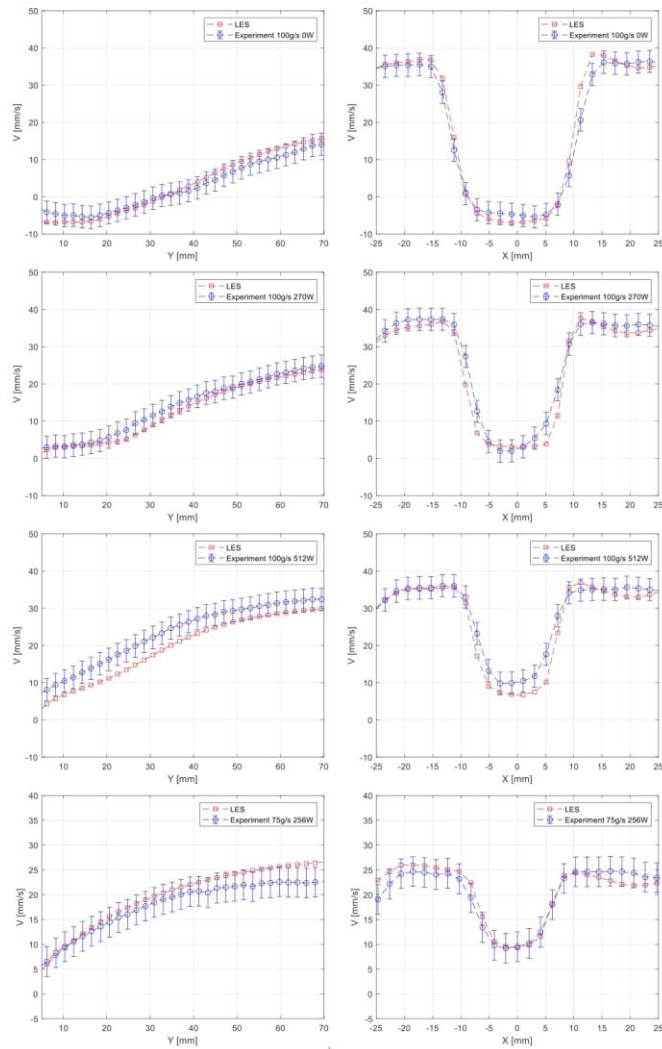


Figure 14. Measured versus predicted velocity profiles for the lines at  $x=0\text{mm}$  (left) and  $y=10\text{mm}$  (right)

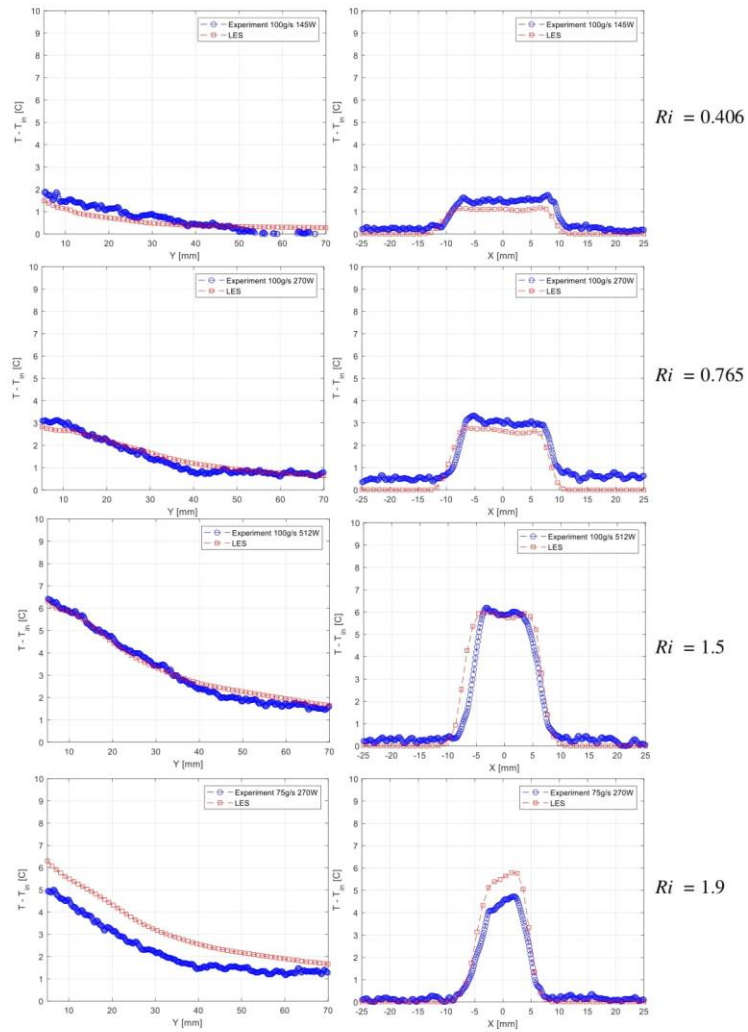


Figure 15. Measured and predicted temperature profiles for the lines  $x=0$ mm (left) and  $y=10$ mm (right) for a variety of conditions

## 6 Regime Transitions

### 6.1 von-Karman Vortices to Eddy Pair Regime

The destruction of the pure von Karman vortex sheet is proposed to be a result of the buoyant force at the top of the cylinder reaching a point where it is sufficiently strong to counteract the low pressures in the recirculation region. This would be analogous to the slit size in the experiments of Gao et al [16], Fu and Rockwell [15] and Shi and Feng [17] being large enough to allow sufficient amount of flow through the slit to counteract the suction pressure, which showed a similar transition. This results in a separation of the wake of the cylinder into two re-circulation zones and the transformation of asymmetric von-Karman vortices into symmetric eddy pairs.

To quantify the transition, a force balance is assumed, leading to a critical  $Ri$  of half the base pressure coefficient as shown by equations (4)-(6) below. For the  $Re$  range of experiments conducted, the base pressure coefficient varies from 0.7 to 0.95 as shown by Williamson and Roshko [19] and Norberg [29]. Following the proposed model (equations. 4-6), this indicates that pure von Karman vortices should disappear around a  $Ri$  of 0.35 to 0.425. The force balance approach to the destruction of the von Karman vortices is expected to correspond with the collapse of the recirculation zone in the centre region as it begins to be divided by buoyancy, which can be seen on Figure 9 (right) to occur in  $0.5 < Ri < 0.6$  region, slightly delayed compared to the prediction of the criteria. This is thought to be attributed to the relatively high turbulent intensity measured on the inlet condition and is further details addressed in section 6.4 below. It should be repeated that the Eddy Pair regime has not been observed in experiments using air such as Singh et al [7].

$$F_{suction} = F_{\beta} \quad (4)$$

$$\frac{C_{pb}}{2} \rho v_{\infty}^2 A = \rho g \beta \Delta T_w D A \quad (5)$$

$$Ri_{T1} = \frac{C_{pb}}{2} \quad (6)$$

### 6.2 Eddy Pair to Thermal Regime

The transition from the eddy pair regime to the thermal regime is proposed to be the point whereby buoyancy and buoyant induced flow is strong enough in the entire upper portion of the cylinder to counteract the suction pressure in the momentum boundary layer of the cylinder. This is partially confirmed by the observations of Singh et al [7], who noted an increase in the measured critical  $Ri$  as a function of  $Re$ . One can suggest that this would indicate that the critical  $Ri$  for this regime is dependent on the base pressure coefficient  $C_{pb}$ , which via a force balance would yield a  $Ri_c$  of  $C_{pb}/2$ , as before. The use of  $C_{pb}$  is justified by experimental studies by Achenbach [30], which show the pressure coefficient to be almost uniform over the downstream half of the cylinder. The value of  $C_{pb}$  was obtained from a lookup table generated from the experimental data of Norberg [29] and Williamson and Roshko [19] for a wide range of  $Re$ .

As noted prior, the EP regime has not been observed in experimental studies such as Singh et al [7]. As such the transition for total vortex suppression appears to be different, as partially visible by the significant difference in the critical  $Ri$  for air found by Singh et al [7] (0.122-0.157) compared to water (0.9->1.18) of the present study. There would appear to be a dependency on fluid properties which allows for air to require relatively less buoyant force to completely preclude all eddy formation. The physical rationale for this large difference is thought to be the difference in the ratio of the thermal boundary layer to the momentum boundary layer thicknesses for air and water and is examined further below.

For water at 25°C, the thermal boundary layer is approximately half the thickness of the momentum boundary layer. This means that with the exception of the top portion of the cylinder where the thermal boundary layer flow begins to move upward, the added buoyancy around the cylinder is unable to counteract all of the negative pressure gradient in the momentum boundary layer. Thus while the negative pressure region is divided along the tube center by the plume, regions of negative pressure persist on either side. This mechanism is similar to the observations of Fu and Rockwell [15] who explored cylinder wake control in isothermal flow, and beginning of phenomena identified as the “Eddy Pair” regime here. This regime would then continue until the induced buoyant velocity is strong enough to counteract the negative pressure gradients in the remaining recirculation regions via shear, leading to the thermal regime. It can be suggested that for fluids with thermal boundary layers appreciably thinner than the momentum boundary layers, three flow regimes exist instead of two for the flow around a cylinder based on buoyant strength: von-Karman Vortices, Eddy Pair and Thermal as found in this study for water.

For air, the thermal and momentum boundary layers are roughly the same thickness. The key difference this implies is that the buoyancy of the thermal boundary layer is now able to act on the entire momentum boundary layer. This means that when the buoyancy force is strong enough to match the suction pressure in one region of the boundary layer, it happens in the entire boundary layer. This causes a direct transition from a VKV regime to a thermal regime, skipping the EP regime observed in the present study for water. The VKV to Thermal transition is consistent with the observations of Singh et al. [7].

To examine this phenomena further and over a wide range of  $Pr$ , several  $Pr$  were chosen varying from 0.1 to 50 for additional LES simulations. These simulations were performed at power level and flows that bracket the suppression point of vortices. To isolate one fluid property at a time, the modification in  $Pr$  was achieved by adjusting the specific heat capacity of water to achieve the desired  $Pr$ . All other fluid properties were left constant, to create a fictitious fluid with a different specific heat capacity and all other properties of water constant at 25°C. Additionally, the geometry was modified to remove the 6mm asymmetry as noted above and the inlet turbulent intensity was reduced from 27% to 1%. This was to be inline with typical experiments in literature and to remove/minimize the turbulent intensity contribution. To remove  $Re$  dependencies, all simulations were performed at an inlet velocity of 27.5mm/s, corresponding to  $Re$  of approximately 414. The resulting  $Ri_C$  obtained from observing the LES flow regimes are presented in Figure 16 with the proposed transition criteria being equation (7). Note, this is correlated to the  $Pr$  of the bulk fluid.

$$Ri_{T2} = \frac{C_{pb}}{2}(0.568Pr^{0.719}) \quad (7)$$

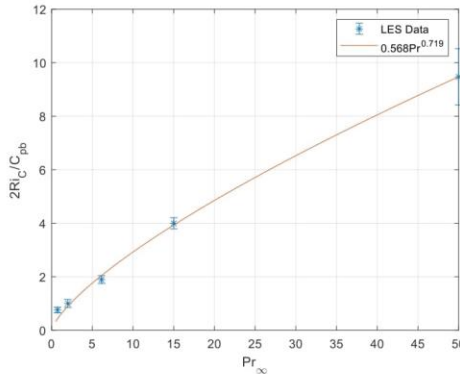


Figure 16. Critical  $Ri$  versus  $Pr$  from LES simulations

### 6.3 Generality of Transition Criteria: Parametric Study

In order to assess the generality of the transition criteria generated by varying  $c_p$ , a parametric study was performed. This was done via simulations of  $Pr=2$  and  $Pr=15$  that modified the dynamic viscosity and thermal conductivity while maintaining the specific heat capacity of water at 25°C. The results of these simulations can be seen below in Table 3, which show no significant difference. Note, when  $\mu$  was modified, the inlet velocity was reduced to ensure the  $Re$  was held constant to avoid changing  $C_{pb}$ .

Table 3. Critical Richardson number vs  $Pr$  via varying other fluid properties

$Pr_\infty$	Parameter Modified	$Ri_c$ Observed via LES	Equation (7)
2	$c_p=1409 \text{ J/kgK}$	$0.48\pm 0.08$	0.444
2	$\mu=3\times 10^{-4} \text{ Pa s}$ ( $Re$ held constant)	$0.45\pm 0.06$	0.444
15	$c_p=10,472 \text{ J/kgK}$	$1.9\pm 0.2$	1.89
15	$k=0.249 \text{ W/mK}$	$2.0\pm 0.2$	1.89

### 6.4 Effect of Inlet Turbulent Intensity

Given the nozzle designed for these experiments yields high inlet turbulent intensities compared to studies existing in literature (20-30% compared to 1%), its effect on flow topology was explored. Figure 17 shows the comparison of two non-dimensional temperature snap shots from LES simulations at the same mass flow/power combination, with and without the inlet turbulent intensity for a  $Ri$  of approximately 1. The case without the turbulent intensity is much more stable and resembles the thermal regime. This indicates that the turbulent intensity is extending the VKV and EP regimes due to the added disturbances, requiring a higher buoyant force to fully suppress them. To take upstream turbulence intensity into account in the regime transitions, a simple multiplier was added to the transition criteria as shown below in equations (8)-(9). The addition

of this multiplier yields criteria which accurately capture the flow regimes identified on Figure 18, while also being applicable to transitions where the upstream turbulence was minimized.

$$Ri_{C1} = Ri_{T1}(1 + T_i) \quad (8)$$

$$Ri_{C2} = Ri_{T2}(1 + T_i) \quad (9)$$

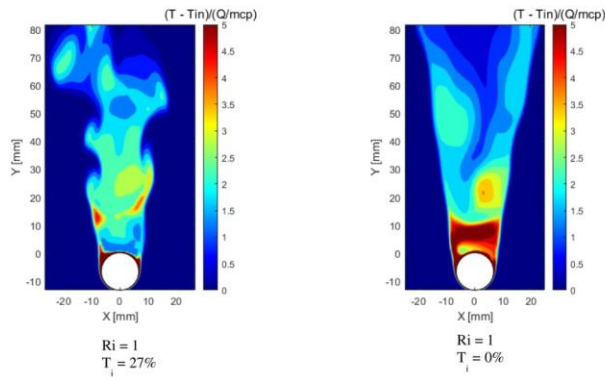


Figure 17. Instantaneous non-dimensional temperature profiles with (left) and without (right) the inlet turbulent intensity at conditions of 100g/s 365W

### 6.5 Performance of Transition Criteria

To test  $Ri_{C2}$ , Table 4 shows the level of agreement between the predictions from the correlation to experimental data currently available for upward flow. Given the limited experimental data, the use of visual observations and the relatively coarse bounds of  $Ri_C$  in the LES simulations the criteria classifies regimes correctly as shown in Figure 18 with few exceptions. Furthermore, it predicts the transitions in the only other relevant study in this configuration as well as all of a parametric variation in  $Pr$  examined via LES. These criteria offer the ability to predict flow topology for a wide range of working conditions. The shaded regions represent the approximate zone over which the transitions cover. This was chosen to cover the data points most difficult to visually identify. This is to account for both the subjective nature of visual observations and that transitions are in reality less abrupt than the criteria suggests.

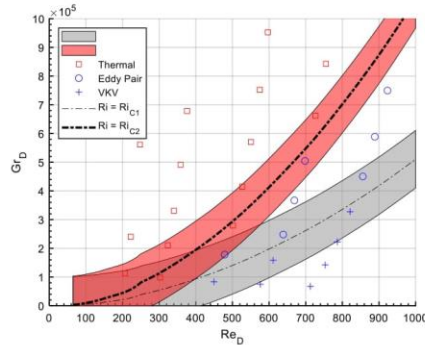


Figure 18. Flow regime map with proposed transition criteria. Shaded regions cover data points difficult to visually identify

Table 4. Performance of the transition criteria from experiments conducted in this work and Singh et al [7]

Study	$Re$	$C_{pb}$	Inlet $T_i$ (%)	$Pr_\infty$	$Ric_{exp}$	$Ric_{Pred}$
Singh et al [7]	94	0.68	N/A	0.73	0.122 <sup>3</sup>	0.154
Singh et al [7]	110	0.75	N/A	0.73	0.157	0.170
Present	414	0.95	27	6.13	0.92±0.2	1.25
Present	590	0.90	30	6.13	1.15±0.1	1.18

## 7 Conclusion

Fluid temperature and velocity measurements from a cylinder in mixed convection flows were presented and examined. A strong dependency of the flow topology behind the cylinder on the inlet velocity and heater power was found. Three distinct flow regimes were identified and used to create a flow regime map. This flow regime map was then divided by transition criteria developed and found to identify the regimes well, with some outliers near transition points.

LES simulations were performed and validated against the experimental data obtained. The performance of the LES model was generally good with RMS error largely agreeing with experimental data to within measurement uncertainty for velocity and temperature predictions respectively. The LES model was found to tend to over predict the velocity and fluid temperature as  $Ri$  increased and the conditions became more buoyant.

Flow regime transition criteria was identified as a function of  $Ri$  and proposed to handle the destruction of pure von Karman vortices, the beginning of a symmetric shedding mode and the removal of all vortex generation. The symmetric shedding mode was found to be analogous to

<sup>3</sup> The error in the points of Singh et al [6] was quoted as 5%, but it was not clear if this is absolute or relative. Errorbars have been left out to avoid confusion.

isothermal slit experiments which split the re-circulation zone with momentum forces instead of buoyancy. Additionally, a strong dependency on the thermal boundary layer thickness or  $Pr$  was found for the removal of all vortex generation with a functional form proposed based on LES simulations. This was found to agree well with the limited data available in literature, the new data collected in this paper, and the set of LES simulations performed over a wide range of conditions. The  $Pr$  dependency in part explains the significant differences between the critical  $Ri$  measured for water and air experiments in existing literature with mechanisms postulated.

#### Acknowledgements

This paper would not have been possible without the generous financial support of the NSERC Industrial Research Chair program and the University Network of Excellence in Nuclear Engineering (UNENE).

#### References

- [1] Y.A.Cengel, "Combined Natural and Forced Convection," in *Heat Transfer. A Practical Approach*, McGraw-Hill, 2002, pp. 486-501.
- [2] H.Hu and M.M.Koochesfahani, "Thermal effects on the wake of a heated circular cylinder operating in mixed convection regime," *Journal of Fluid Mechanics*, vol. 685, pp. 235-270, 2011.
- [3] J.C.Lecordier, L.Hamma and P.Paranthoen, "The control of vortex shedding behind heated circular cylinders at low Reynolds numbers," *Experiments in Fluids*, vol. 10, pp. 224-229, 1991.
- [4] J.C.Lecordier, L.W.B.Browne, S. Masson, F.Dumouchel and P.Paranthoen, "Control of vortex shedding by thermal effects at low Reynolds number," *Experimental Thermal and Fluid Sciences*, vol. 21, pp. 227-237, 2000.
- [5] M.Khashehchi, I. A. Abdi and K.Hooman, "Characteristics of the wake behind a heated cylinder in relatively high Reynolds number," *International Journal of Heat and Mass Transfer*, vol. 86, pp. 589-599, 2015.
- [6] N.Michaux-Leblond and M.Belorgey, "Near-Wake Behaviour of a Heated Circular Cylinder: Viscosity-Buoyancy Duality," *Experimental Thermal and Fluid Science*, vol. 15, pp. 91-100, 1997.

- [8] A.A.Kakade, S.K.Singh, P.K.Panigrahi and K.Muralidhar, "Schlieren investigation of the square cylinder wake: Joint influence of buoyancy and orientation," *Physics of Fluids*, vol. 22, 2010.
- [9] S.Singh, G.Biswas and A.Mukhopadhyay, "Effect of Thermal Buoyancy on the Flow Through a Vertical Channel with a Built-In Circular Cylinder," *Numerical Heat Transfer, Part A*, pp. 769-789, 1998.
- [10] K.S.Chang and J.Y.Sa, "The effect of buoyancy on vortex shedding in the near wake of a circular cylinder," *Journal of Fluid Mechanics*, vol. 220, pp. 253-266, 1990.
- [11] H.Wan and S.S.Patnaik, "Suppression of vortex-induced vibration of a circular cylinder using thermal effects," *Physics of Fluids*, vol. 28, 2016.
- [12] G.Gandikota, S.Amiroudine, D.Chatterjee and G.Biswas, "The Effect of Aiding/Opposing Buoyancy on Two Dimensional Laminar Flow Across a Circular Cylinder," *Numerical Heat Transfer, Part A: Applications*, vol. 58, pp. 385-402, 2010.
- [13] S.Singh and D.Chandar, "Effects of thermal induced buoyancy forces on the vortex shedding of a circular cylinder," *International Communications in Heat and Mass Transfer*, vol. 76, pp. 215-224, 2016.
- [14] L.H.Feng and J.J.Wang, "Circular Cylinder vortex-synchronization control with a synthetic jet positioned at the rear stagnation point," *Journal of Fluid Mechanics*, vol. 662, pp. 232-259, 2010.
- [15] H.Fu and D.Rockwell, "Shallow flow past a cylinder: control of the near wake," *Journal of Fluid Mechanics*, vol. 539, pp. 1-24, 2005.
- [16] D.L.Gao, W.L.Chen, H.Li and H.Hu, "Flow around a circular cylinder with slit," *Experimental Thermal and Fluid Science*, vol. 82, pp. 287-301, 2017.
- [17] X.Shi and L.Feng, "Control of flow around a circular cylinder by bleed near the separation points," *Experiments in Fluids*, vol. 214, 2015.
- [18] H.Baek and G.E.Karniadakis, "Suppressing vortex-induced vibrations via passive means," *Journal of Fluids and Structures*, vol. 25, pp. 848-866, 2009.
- [19] C. Williamson and A. Roshko, "Measurements of base pressure in the wake of a cylinder at low Reynolds numbers," *Z. Flugwiss. Weltraumforschung*, vol. 14, pp. 38-46, 1990.

- [20] C.W.Hollingshead, A.Rashkovan and D.R.Novog, "Mixed convection around two vertically aligned horizontal cylinders: A numerical, experimental, and modeling investigation on the effect of local conditions on heat transfer," *Nuclear Engineering and Design*, vol. 394, 2022.
- [21] M.M.Zdravkovich, *Flow around circular cylinders Vol 1: Fundamentals*, Oxford University Press Inc, 1997.
- [22] J.R.Aarnes, H.I.Andersson and N.E.L.Haugen, "Numerical investigation of free-stream turbulence effects on the transition-in-wake state of flow past a circular cylinder," *Journal of Turbulence*, vol. 19, pp. 252-273, 2018.
- [23] B.N.Rajani, A.Kandasamy and S.Majumdar, "Numerical simulation of laminar flow past a circular cylinder," *Applied Mathematic Modelling*, vol. 33, pp. 1228-1247, 2009.
- [24] B.N.Rajani, A.Kandasamy and S.Majumdar, "LES of Flow past Circular Cylinder at  $Re = 3900$ ," *Journal of Applied Fluid Mechanics*, vol. 9, pp. 1421-1435, 2016.
- [25] L.Xiyun and L.Guocan, "A Large Eddy Simulation of the Near Wake of a Circular Cylinder," *Chinese Journal of Mechanics*, 2002.
- [26] C.E.Clifford and M.K.Kimber, "Assessment of RANS and LES turbulence models for natural convection in a differentially heated square cavity," *Numerical Heat Transfer, Part A: Applications*, vol. 78, pp. 560-594, 2020.
- [27] I. Celik, Z.N., Cehreli and I.Yavuz, "Index of Resolution Quality for Large Eddy Simulations," *Journal of Fluids Engineering*, vol. 127, pp. 949-958, 2005.
- [28] H. Ma and L.He, "Large Eddy simulation of natural convection heat transfer and fluid flow around a horizontal cylinder," *International Journal of Thermal Sciences*, no. 162, 2021.
- [29] C.Norberg, "An Experimental investigation of the flow around a circular cylinder: influence of aspect ratio," *Journal of Fluid Mechanics*, vol. 258, pp. 287-316, 1994.
- [30] E.Achenbach, "Distribution of local pressure and skin friction around a circular cylinder in cross-flow up to  $Re=5 \times 10^6$ ," *Journal of Fluid Mechanics*, vol. 34, pp. 625-639, 1968.

## **4 Modelling and Predicting Mixed Convection Heat Transfer based on local conditions for Cylinder Pair**

### **About this Paper:**

#### **Contribution to Knowledge:**

This paper improves the knowledge base of mixed convection in three primary ways:

1. Generation of additional experimental data (PIV, LIF and Wall temperature measurements) of flow and temperatures around 2 horizontally and in-line cylinders available for subsequent CFD validation and model development.
2. LES simulations of the inline-cylinder natural convection tests were performed and validated. Subsequently, CFD was used to supplement experimental data in the development of local condition prediction methods for fluid temperature and maximum plume velocity as functions of distance from the lower cylinder surface
3. The development of a mixed convection heat transfer model based on physically derived local conditions for water. This was validated against experimental data captured during this study, and data available in literature from the experiments of Grafsronnigen and Jensen [13].

#### **Authors Contribution:**

The author (Hollingshead) was primarily responsible for the all of the experimental work, simulation work, analysis and draft paper writing. The co-authors contributed significantly via guidance at each step of the work, and with their valuable edits.



Contents lists available at ScienceDirect

Nuclear Engineering and Design

journal homepage: [www.elsevier.com/locate/nucengdes](http://www.elsevier.com/locate/nucengdes)



## Mixed convection around two vertically aligned horizontal cylinders: A numerical, experimental, and modeling investigation on the effect of local conditions on heat transfer

C.W. Hollingshead<sup>a,\*</sup>, A. Rashkovan<sup>b</sup>, D.R. Novog<sup>a</sup>

<sup>a</sup> Department of Engineering Physics, McMaster University, Hamilton, Ontario, Canada

<sup>b</sup> Nuclear Research Center Negev (NRCN), Beer-Sheva 84190, Israel

### ARTICLE INFO

**Keywords:**  
Natural Convection  
CFD  
LES  
PIV  
LIF  
Mixed convection

### ABSTRACT

Experimental and numerical studies were performed to assess the effects of buoyancy driven flows from lower cylinders in a tube array on the heat transfer of higher-elevation cylinders. First, PIV and LIF experiments were performed for a single 13.4 mm diameter cylinder submerged in water at atmospheric conditions to measure velocity and temperature fields. Then the effect of buoyancy from a lower heater was studied by arranging two horizontal cylinders at different vertical displacements from each other ( $P/D = 1.5, 2.15, 6.45$ ). Wall temperatures were measured as a function of pitch and power. CFD analysis was performed for the same configurations using an LES model. Using a combination of CFD and experimental measurements, mechanistic models for velocity and temperature behaviour in the plume were developed. These models are used to determine the impact of buoyant plumes from cylinders at lower elevations on heat transfer from heated cylinders at higher elevations. Since the plumes from cylinders at lower elevation are imposed on the natural convection from higher-elevation cylinders there is a combined effect from the momentum and temperature of the lower plume as it interacts with the natural convection phenomena from the upper-elevation heater. A model to predict the  $Nu_D$  of the upper cylinder in the case of horizontal vertically aligned pair of tubes was developed based on superposition of the convection caused by the lower cylinder and the natural convection from the higher-elevation cylinder. This model was found to predict the cylinder  $Nu_D$  with an RMS error of 2.8 and an absolute deviation of 2.31 as compared to the experimental data obtained in this study. It was also found to agree well with independent data available in literature.

### 1. Introduction

The behaviour of heat transfer from a tube array to a surrounding media is an important part of many engineering applications. The fundamental thermalhydraulic study presented in this work is motivated by the need for predictive modelling of the heat transfer from the Calandria tubes in a CANDU nuclear reactor to the surrounding moderator. This heat transfer is an important phenomenon during potential accident conditions where the moderator fluid can act as a temporary heat sink allowing heat to flow from the Calandria tube array to the moderator. Under such circumstances natural circulation phenomena from tubes at lower elevation in the tube array interact with the natural circulation phenomena around tubes at higher elevations.

Natural Convection heat transfer for horizontal cylinders has been

studied extensively over the years [e.g., References (Morgan, 1975; Sparrow and Niethammer, 1981; Grafsonnigen et al., 2011; Marsters, 1972; Kuehner et al., 2015; Atmane et al., 2003; Kuelner et al., 2012; Park et al., 2019)]. Studies such as Morgan (1975) primarily reported experimental results used to generate correlations for the Nusselt number, typically as a function of  $Gr$  or  $Ra$  numbers.

$$Ra = GrPr \quad (1)$$

$$Gr = \frac{g\beta\Delta TD^3}{\nu^2} \quad (2)$$

More recently studies have focused on measuring the local temperature and velocity fields using modern experimental techniques supplemented with prediction methods such as Computational Fluid Dynamics (CFD). Grafsonnigen et al. (2011) experimentally studied the buoyant plume velocity in the near-field region of a 54 mm diameter

\* Corresponding author.

E-mail address: [hollincw@mcmaster.ca](mailto:hollincw@mcmaster.ca) (C.W. Hollingshead).

<https://doi.org/10.1016/j.nucengdes.2022.111823>

Received 26 October 2021; Received in revised form 16 May 2022; Accepted 22 May 2022

Available online 2 June 2022

0029-5493/© 2022 The Authors. Published by Elsevier B.V. This is an open access article under the CC BY license (<http://creativecommons.org/licenses/by/4.0/>).

Nomenclature			
PIV	Particle Image Velocimetry	$\nu$	Kinematic viscosity [m <sup>2</sup> /s]
LIF	Laser Induced Fluorescence	$v_p$	Plume velocity profile [m/s]
CFD	Computational Fluid Dynamics	$D$	Diameter of vessel [m]
LES	Large Eddy Simulation	$P$	Pitch [m]
$P/D$	Pitch-to-tube-diameter ratio	$H$	Closest spacing of cylinders [m]
$Nu$	Nusselt Number	$L$	Length of vessel/heater rods [m]
$Nu_D$	Single Cylinder Natural Convection Nusselt Number	$L_{Crit}$	Critical turbulent transition length [m]
$Nu_F$	Forced Convection Nusselt Number	$n$	Superposition exponent
$Nu_{apparent}$	Apparent Nusselt Number	$g$	Acceleration due to gravity [m/s <sup>2</sup> ]
$Nu_{Du}$	Upper Cylinder Nusselt Number	$T_{Loc}$	Local temperature at upper cylinder [K]
$Gr$	Grashof Number	$T_p$	Plume temperature [K]
$Ra$	Rayleigh Number	$T_{inf}$	Bulk fluid temperature [K]
$Re$	Reynolds Number	$q'$	Heat flux [W/m <sup>2</sup> K]
$Pr$	Prandtl Number	$h$	Heat transfer coefficient [W/m <sup>2</sup> K]
$\beta$	Volumetric thermal expansion coefficient [1/K]	$h_{du}$	Heat transfer coefficient upper cylinder [W/m <sup>2</sup> K]
		$Y$	Vertical distance above lower cylinder surface [m]

horizontal cylinder in water. Velocity measurements were made using Particle Image Velocity (PIV) for  $Ra_D$  from  $2 \times 10^7$  to  $8 \times 10^7$ . Surface temperature measurements were made using thermocouples welded to the cylinder surface and were found to agree with correlations in literature. Graftsronnigen and Jensen (2012) also performed simultaneous temperature and velocity measurements using the same geometry as in Graftsronnigen et al. (2011) for  $Ra_D = 8 \times 10^7$  employing Laser Induced Fluorescence (LIF). They compared the results against similarity solutions. While these measurements included detailed velocity fields they did not include detailed temperature plots as a function of distance from the heated cylinder.

Since the temperature and velocity fields in natural circulation from a cylinder are affected by the transition to turbulence, the latter has been studied extensively, with relevant studies including Forstrom and Sparrow (1966), Jr and Gebhart (1975), Noto et al. (1999), Elicer-Cortes et al. (2000), summarized in Table 1. Typically, these studies have found a dependency on average  $Gr$ , or local  $Gr$  (i.e., a  $Gr$  number calculated as a function of centreline plume temperature) for the transition. Forstrom and Sparrow (1966) using temperature measurements determined that the beginning of the transition regime was at a  $Gr$  of  $5 \times 10^8$  and ended at a  $Gr$  of  $5 \times 10^9$ . Similarly, Jr and Gebhart (1975) studied plumes from horizontal wires using thermocouples and interferometers. They found the critical  $Gr$  to be  $1.1 \times 10^9$  and  $7.9 \times 10^9$  respectively. Jr and Gebhart (1975) noted that discrepancies in comparison to Forstrom and Sparrow (1966) were likely due to differences in their criteria used in evaluating the turbulent transition. Noto et al. (1999) performed spectral analysis on data from thermocouples at several elevations in the plume region of a horizontal wire. With visual observations and spectral analysis, it was determined that the turbulent transition began at  $Gr$  of  $2 \times 10^8$  and ended at  $Gr$  of  $2 \times 10^9$ . Using ultrasound measurements, Elicer-Cortes et al. (2000) measured the turbulent intensity and turbulent transition of thermal plumes from a short disc. Using this method, they found that for different wall temperatures the transition points varied slightly with local  $Gr$  numbers ranging from  $1$  to  $2 \times 10^8$  for the beginning and  $3.5$ – $4.5 \times 10^8$  for the end of the transition to turbulence.

**Table 1**  
Relevant studies for the transition to turbulence for free thermal plumes in air.

Study	$Gr_{start}$	$Gr_{end}$	Diameter[mm]
Forstrom and Sparrow (1966)	$5 \times 10^8$	$5 \times 10^9$	1
Jr and Gebhart (1975)	$1.1 \times 10^9$	$7.9 \times 10^9$	0.0635–0.3429
Noto et al. (1999)	$2 \times 10^8$	$2 \times 10^9$	0.435
Elicer-Cortes et al. (2000)	$1 \times 10^8$	$4.5 \times 10^8$	80

In addition to the above experimental studies, numerical studies (Ma and He, 2021; Graftsronnigen and Jensen, 2017; Graftsronnigen and Jensen, 2012; Pelletier et al., 2016) of the phenomena of free convection from single horizontal cylinder have also been conducted. Ma and He (2021) performed Large Eddy Simulations (LES) and Reynolds Averaged Navier-Stokes (RANS) simulations of the experiments of Graftsronnigen et al. (2011) for a  $Ra_D$  of  $1 \times 10^7$ . Ma and He (2021) improved on the work of Graftsronnigen and Jensen (2017) and used a pressure inlet and outlet boundary conditions as opposed to periodic boundary conditions for the side walls. The model proposed by Ma and He (2021) was found to predict the centreline velocity to within 15%. In addition, the model predictions for the beginning and the end of the transition to turbulence were found to be  $Gr$  of  $1.5 \times 10^8$  and  $7 \times 10^9$  respectively, which aligns with the range found experimental studies in literature shown in Table 1.

Free convection from tubular-arrays of vertically aligned horizontal cylinders has been studied as summarized in Table 2. This geometry exhibits different behaviours compared to the single tube geometry since the buoyant plume generated by the lower cylinder can positively (via enhancement of mixed convection) or negatively affect (via thermal heating of the surrounding fluid) the heat transfer characteristics of the upper cylinder. Graftsronnigen and Jensen (2012) performed

**Table 2**  
Studies for arrays of Horizontal Cylinders.

Study	Rayleigh Range	Working Fluid	Diameter [mm]	P/D tested
Pelletier et al. (2016)	$1.7 \times 10^6$ – $5.3 \times 10^6$	Water	30	2–4
Graftsronnigen and Jensen (2012)	$1.8 \times 10^7$ – $2.55 \times 10^8$	Water	54	1.5–5
Persoons et al. (2011)	$1.8 \times 10^6$ – $5.5 \times 10^6$	Water	30	2–4
Sparrow and Niethammer (1981)	$2 \times 10^4$ – $2 \times 10^5$	Air	37.87	2–9
Stafford and Egan (2014)	$1 \times 10^4$ – $1 \times 10^5$	Air	25	2–10
Marsters (1972)	$Gr, 750$ – $2000$	Air	6.35	2–20
Kitamura et al. (2016)	$5 \times 10^2$ – $1 \times 10^3$	Air	8.4, 14.4, 20.4	1.176–18.9
Tokura et al. (1983)	$4 \times 10^4$ – $4 \times 10^5$	Air	22, 28.5	1.1–40
Reymond et al. (2008)	$2 \times 10^5$ – $6 \times 10^6$	Water	30	1.5–3

experiments for two vertically aligned cylinders, each with a diameter of 54 mm and each at the same power. They reported the Nusselt number of the upper cylinder as a function of the pitch to tube diameter ratio ( $P/D$ ). A 10% reduction in heat transfer coefficient was reported for  $P/D = 1.5$ , whereas for  $P/D = 5$  an enhancement of 30–40% was observed. Similar trends were found by Pelletier et al. (2016) who noted a 5% decrease for small  $P/D$  ratios and an 11% increase at higher  $P/D$ . Raymond et al. (2008) measured the angular dependence of Nusselt number over the surface of a single cylinder and two horizontal cylinders with  $P/D = 1.5, 2$  and  $3$ . They found that the bottom cylinder heat transfer coefficient was unaffected by the upper cylinder irrespective of upper cylinder heating. Additionally, they found that bottom 60-degree portion of the upper cylinder was enhanced relative to the single cylinder case for all  $P/D$  tested. The upper section of the top cylinder was found to be comparable to the single cylinder case. Sparrow and Niethammer (1981) examined how changing the temperature of the bottom cylinder affects the temperature of the upper cylinder for  $P/D$  ratios ranging from 2 to 9 in air. For an increase of the bottom cylinder temperature it was found that the wall temperature of the upper cylinder increased for  $P/D$  smaller than 5.

Stafford and Egan (2014) performed experiments in air and developed a model to predict natural convection heat transfer for two horizontal cylinders spaced vertically and horizontally. For horizontally aligned cylinders at the same elevation, little to no effect was noted until the spacing was within twice the thermal boundary layer thickness. For cylinder spacing smaller than this value heat transfer was impaired. For the cylinders arranged in a vertical array Stafford and Egan (2014) suggested a superposition model to combine the natural convection effect of the upper cylinder with forced convection induced from heating the cylinders at lower elevations. Their model adds a forced convective contribution (arising from the incoming fluids' momentum from the lower cylinder) to that of a single cylinder undergoing free convection with a superposition factor  $n$  as shown in equation (3). The local temperature  $T_{loc}$  used in calculating the natural convection component was based on the thermal plume from the lower cylinder and was used instead of the bulk temperature  $T_{\infty}$  in evaluating the wall temperature. The use of a new local temperature was to account for the heating effect that the lower cylinder creates on the fluid surrounding the upper heater. To close this model, relations for the plume velocity and plume temperature were developed. For velocity predictions, Stafford and Egan (2014) made use of the laminar point source plume model developed by Gebhart et al. (1970). Plume temperatures were based on a profile developed from similarity analysis. Their model was noted to have predicted  $Nu_D$  of the upper cylinder within the measurement uncertainty for a superposition exponent of  $n = 3$ . This model was developed for a  $Ra_D$  range of  $10^4$  to  $10^5$  in air and was shown to predict  $Nu_D$  from their own experiments and other experiments using air well.

$$Nu_{Du} = (Nu_u^n + Nu_l^n)^{1/n} \quad (3)$$

$$T_w = \frac{q''D}{Nu_D k} + T_{Loc} \quad (4)$$

$$Nu_{Apparent} = Nu_{Du} \left( \frac{T_w - T_{\infty}}{T_w - T_{Loc}} \right) \quad (5)$$

$$T_{w_s} = \frac{q''}{h} + T_{Loc} \quad (6)$$

The aim of this study is to develop a comprehensive single-phase heat transfer model for a cylinder that is affected by natural circulation from surrounding cylinders. It expands upon the body of work discussed above by providing new experiments in these configurations, CFD simulations, and a new mechanistically based model. Validation for this new model has also been performed on datasets captured with several increments in power in the lower cylinder. The end goal of this work is the development of a model capable of capturing the trends in the upper

cylinder's heat transfer for a wide range of bottom cylinder powers or  $Ra_D$  in water.

## 2. Experimental setup and conditions

Three sets of experiments were performed in this work:

1. A Particle Image Velocimetry study (PIV) to measure the steady and time variant plume velocity field from a single heated cylinder.
2. A Laser Induced Fluorescence study (LIF) to measure the steady and time variant plume temperature field.
3. Heat transfer experiments for two horizontal cylinders positioned in an inline arrangement. The lower elevation heater powers were controlled separately from the main test cylinder to vary the plume behaviour and study the effects of lower cylinder plumes. Three  $P/D$  ratios (1.5, 2.15 and 6.45) were tested to observe the effect of heater spacing on the measurements.

The experimental facility used is the same as described in Hollingshead et al. (2020) with the addition of a central cylindrical heater of diameter 13.4 mm which contained several internal thermocouples for measuring wall temperatures. The test vessel is 489.3 mm in diameter and 504.7 mm long. Polycarbonate plates are used on the front and side of the vessel to allow for optical access of the laser measurement techniques. A very low amount of flow was provided at the bottom of the test vessel to control the surrounding temperature in the heat transfer experiments. An inlet manifold distributed this flow along the bottom of the vessel to ensure no significant velocity impinges on the centre region of vessel that contains the heater. To control the water temperature,  $T_{\infty}$ , in the vessel and to reduce the stratification in the tank, an inlet flow rate of 0.1 kg/s was applied. This trace flow was selected based on full scale RANS CFD of the experimental vessel which showed that impact of such an inlet flow rate, combined with the inlet manifold resulted in the forced convective velocity to be less than 2 mm/s. This is in comparison to the measured plume velocities which were in the range of 10–20 mm/s. Measurements were taken at two target values of  $T_{\infty}$  (25 and 50 °C) with an operating margin of  $\pm 1$  °C measured with type T thermocouples.

The test vessel and cylindrical heaters are shown in Fig. 2 for a two-heater geometry. Two types of heaters were used for these studies which are referred to as heater A and B. Heater A was used for the PIV and LIF tests. It was also used as the lower heated cylinder in the heat transfer experiments. Heater B is the fully instrumented cylindrical heater used to measure wall temperatures as part of the heat transfer experiments.

Heater A is a 13.4 mm diameter rod with a heated length of 500 mm. The heater is composed of an outer layer of Stainless steel that is 2 mm thick. The heat flux follows a cosine shaped profile, with the peak maximum being 1.4 times the average heat flux. The diameter of Heater B is 13.4 mm with a 340 mm heated length. Heater A was designed to mimic the profiles found in full-scale CANDU reactors and was used in the experiments of Hollingshead et al. (2020). Conversely, the more localised heat flux shape of Heater B was chosen to more accurately capture the heat profile expected from damaged fuel channels during postulated beyond design basis accidents. The heat flux profiles of both heaters are shown in Fig. 1. Heater B also contains internal thermocouples embedded into the heater internal Boron Nitride insulation under a 2 mm stainless steel sheath. External wall temperatures are calculated based on the internal temperature measurements by solving the 1-dimensional conduction problem through the 2 mm sheath. Power was supplied to the heaters through independent REGATRON DC power suppliers capable of 128 kW with calibrated current and voltage sensors.

### 2.1. Particle image Velocimetry study

Particle Image Velocimetry (PIV) was used to obtain non-intrusive velocity measurements. This method works by tracking the

C.W. Hollingshead et al.

Nuclear Engineering and Design 394 (2022) 111823

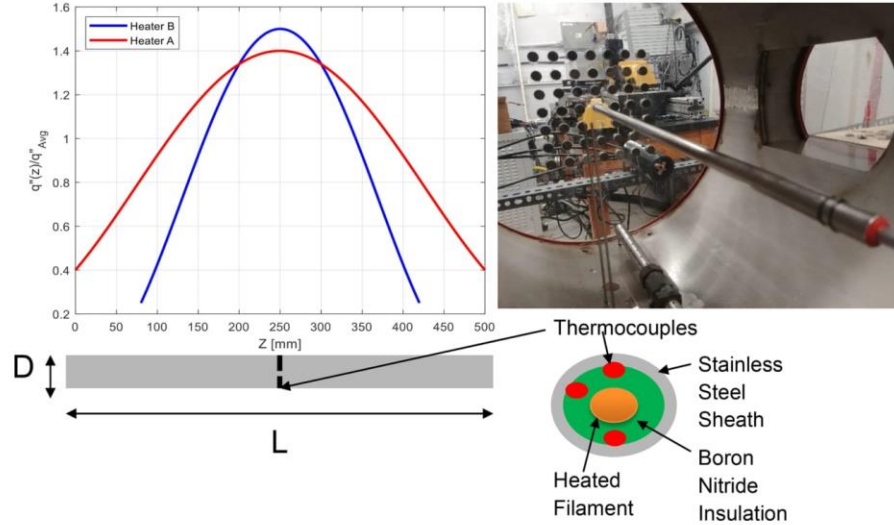


Fig. 1. Heat flux profiles of heater A and B (top left) and the positions of the thermocouples in heater B (bottom right).

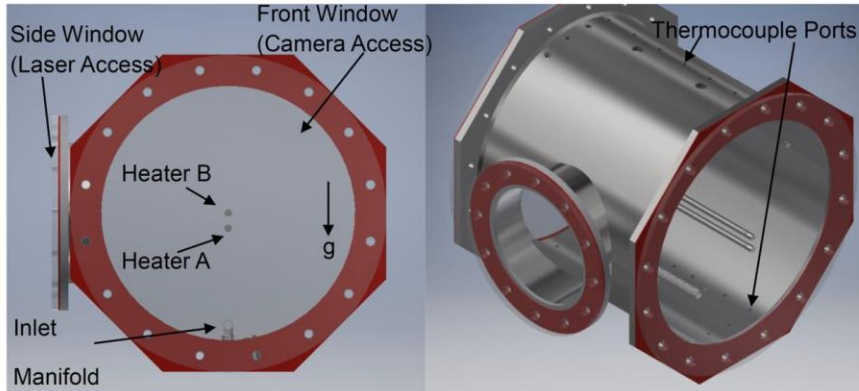


Fig. 2. Schematic of the test vessel, laser access ports, manifold and heater positions.

displacement of tracer particles in the flow field as they traverse through a laser sheet. The laser is periodically pulsed so that the frequency of the laser illumination can be used, along with the measured particle displacement, to infer the local velocities. The tracer particles for this study were hollow glass spheres with diameter of approximately  $10\ \mu\text{m}$ . The laser sheet was generated by a pulsed ND-YLF laser. The displacement of particles was captured by a Photron SA5 camera. The camera and the laser were synchronized such that the system frequency was 60 Hz. These parameters were chosen to ensure a  $\sim 3\text{--}5$ -pixel displacement of the seed particles was observed between image frames. INSIGHT 3G software was used to perform cross correlation of the particle displacements to obtain the velocity field.

For these types of very low velocity measurements the camera in the

PIV system had to operate at its slowest possible frame rate to allow the seed particles in the sheet to move the 3–5 pixels between frames. This is unlike typical PIV applications where the shutter and laser pulse frequencies are typically much faster. The low frequency mode of operation allows background light from sources such as laser reflections to pollute the image and reduces image quality. Some of these issues were resolved by removing an average background image with post-processing. Additionally, density gradients generated near the cylinder caused optical aberrations that could not be reduced or corrected. As a result, data captured at distances  $>20$  mm from the cylinder are included in this work. Additionally, this effect significantly distorts the observed seed positions in the plume above a power level of 512 W.

The reflected light pollution caused by the low capture frequency,

C.W. Hollingshead et al.

Nuclear Engineering and Design 394 (2022) 111823

time dependent density changes in the plume, and the stochastic 3-dimensional movement of the plume in and out of the measurement plane lead to some poor-quality datasets. The datasets where there was a lack of continuity in the maximum velocity at each elevation were discarded. This can be seen below in Fig. 3 which shows two PIV measurements at the same operating conditions time averaged over 6 s. The left shows a poor-quality measurement where the plume centerline was not aligned with the PIV laser sheet and the profile was not monotonic and continuous. This indicates that portions of the plume were out of the laser sheet during this acquisition. This misalignment is expected given the 3D and unsteady nature of the plume wherein the plume itself may meander into and out of the laser sheet. Plume-laser alignment was achieved by taking several measurements at the same conditions, as shown on the right for the same conditions. As a result, data obtained with discontinuities in the velocity field are not included in the analysis. It should also be noted that depending on the test, the plume centerline could curl to the left, right, or be vertical with no systematic plume trajectory was observed.

Due to memory buffer limitations in the camera system, PIV measurements were performed using 5 separate measurement windows of 6 s each (total measurement time was 30 s). Repeatability measurements were performed during selected tests. Velocity measurement uncertainty was then established by considering laser sheet alignment errors, camera angle errors and spatial calibration errors. This was done by comparing repeatability measurements where the laser and camera position were adjusted and then moved back to as close as possible and a spatial calibration was retaken. Overall, the PIV measurement uncertainty via these repeatability measurements was estimated to be 3 mm/s or approximately 20% of a typical plume centerline velocity. Additional error considerations such as error in pixel displacement were not included given their comparatively small size to the quoted 3 mm/s value.

For this study, the most important information from the velocity measurements are the plume centreline velocities since it affects the heat transfer from any higher elevation tubes that are impacted. In prior studies e.g. (Grafsronnigen et al., 2011), plume data is taken from the vertical centreline directly above the heater and time averaged. However, since the plume is inherently 3-dimensional and transient there are times where it will deviate from this centre and give a velocity lower than that at the true centre of the plume. This is evident in Fig. 2 which shows the significant deviations in plume trajectory from pure vertical behaviour. To ensure the plume centerline velocity was consistently extracted from the PIV results, the maximum velocity at

each elevation was extracted. The results of this maxima averaging can be seen in Fig. 13 (right) in section 5.1of the present study.

## 2.2. Laser induced Fluorescence measurements

Temperature measurements were obtained by adding Rhodamine B, a fluorescent dye with emission intensity proportional to the temperature, to the water in the tank at a concentration of approximately  $1 \times 10^7$  mol/L. When excited, Rhodamine B emits light at 543 nm (Sigma Aldrich, 2021). The LIF measurements used the same laser and camera from the PIV measurements with a 545 nm filter lens on the camera such that Rhodamine B emission is the primary contribution to the image. To improve thermal imaging a  $10^\circ$  tilt was applied to the receiving camera. This was to minimize light refraction due to the temperature gradients in the vessel and was found to greatly improve the LIF signal strength. The camera was operated at 250 Hz and 5000 images were captured per run. Additionally, smaller sets of data were taken, at the same frequency and compared to the larger datasets to assess the effect of sampling time on the thermal images. No significant difference was observed.

Thermal images were calibrated using isothermal tests where the vessel was slowly heated and the LIF temperatures were calibrated against thermocouples in the tank. In this study, a type T thermocouple near the cylinder was used and the entire tank volume was heated over a range of temperatures from 25 to 60 °C. A calibration curve of temperature vs intensity was made for all the datasets captured on a given day, with a separate calibration curve being generated for each day of testing. The specific calibration curves were required due to small variations found during repeat tests of the calibration curve. These small changes were accompanied by visible changes in the water quality and Rhodamine concentrations over the course of the testing campaign. Hence daily calibration was performed. The differences in predictions of these calibration curves differed by upwards of 1 °C at temperatures higher than 40 °C. Temperatures of this magnitude were only measured in the  $Y < 5$  mm region, which was omitted from analysis due to laser reflection effects effecting this region.

The processed image and calibrated temperature field at a given instant in time are shown in Fig. 4. In the image, several striations appear in the reconstruction. Prior studies removed these in post-processing (Grafsronnigen and Jensen, 2012), however such artifact removal is not performed in this work as it was not found to significantly affect the plume centerline temperature measurement or its uncertainty. As done in the PIV measurements, processing was performed to extract the peak plume centerline temperature as a function of elevation. The

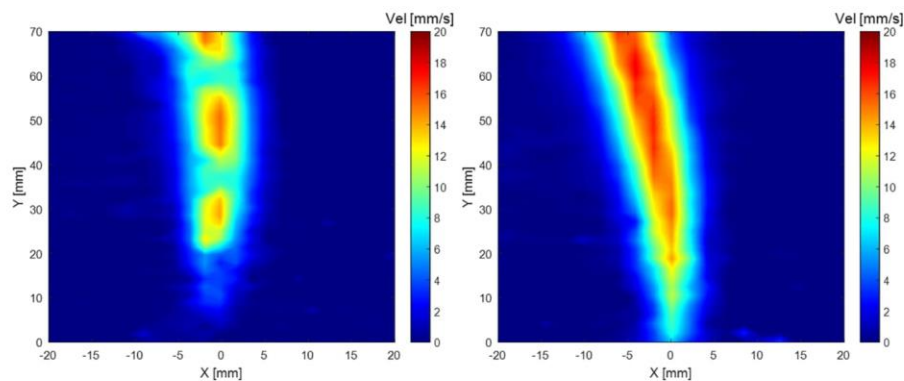


Fig. 3. Accepted (right) and rejected (left) quality dataset from the PIV measurements time averaged over 6 s. Power/heat flux of 128 W/8.5 kW/m<sup>2</sup>Note, Y = 0 mm corresponds to the upper surface of the cylinder and × indicates the distance from the tube centerline.

C.W. Hollingshead et al.

Nuclear Engineering and Design 394 (2022) 111823

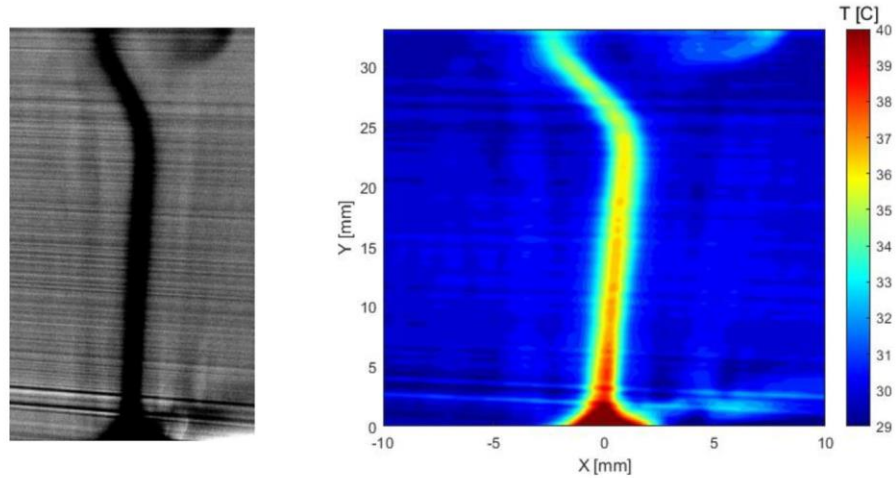


Fig. 4. Normalized LIF image (left) and the resultant instantaneous temperature field (right) for 800 W/53.1 kW/m<sup>2</sup> case,  $T_{\infty} = 29$  °C.

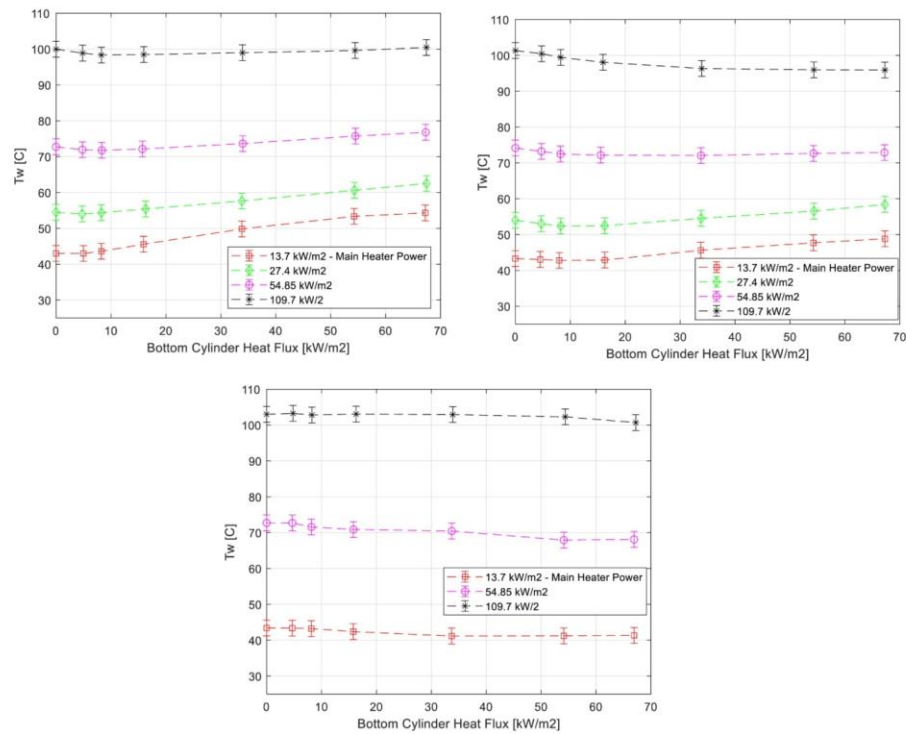


Fig. 5. Upper wall temperatures versus bottom cylinder heat flux for  $P/D = 1.5$  (left),  $P/D = 2.15$  (right) and  $P/D = 6.45$  (bottom) with  $T_{\infty} = 25$ C.

results can be seen in Fig. 13(left) in section 5.1 of the present study. Repeatability measurements were also performed during the test program and the combined repeatability and uncertainty in the plume temperature measurements was assessed to be 2 °C.

### 2.3. Heat transfer experimental results

Heat transfer coefficients were calculated based on the input power and measured wall temperatures on the instrumented heater using the bulk temperature  $T_{\infty}$  as the reference temperature. Consistent with other studies the measured Nusselt number behaves non-monotonically with tube pitch. The natural convection at the lower heater induces a liquid velocity around the upper cylinder which tends to improve the heat transfer. However, the thermal plume from the lower cylinder also acts to increase the local temperature surrounding the upper cylinder which lowers heat transfer. The experimental results from the tests with varying heaters power levels for the three P/D's of 1.5, 2.15 and 6.45 are summarized in Fig. 5 and Fig. 6. As expected, at lower P/D values, the heating effect dominates and higher wall temperatures are observed for the upper cylinder. Conversely, at higher P/D values the plume cools due to diffusion and advection which leads to the convective effect dominating. This leads to lower wall temperatures as illustrated in Fig. 6. Furthermore, as the power to the upper heater increases the impact of heating effect due to the lower cylinder is less observable. For example, Fig. 5 (left) shows that at 13.7 kW/m<sup>2</sup> there is an increase in wall temperature of approximately 10 °C, whereas the 109.7 kW/m<sup>2</sup> case shows no change. At high P/D, the opposite effect is observed on Fig. 5 (bottom), with the higher heater powers resulting in a similar cooling effect, with a 3.5 °C for 109.7 kW/m<sup>2</sup> and 2°C for 13.7 kW/m<sup>2</sup>.

## 3. Numerical study

### 3.1. Model description

CFD in this work is first validated against the experimental measurements and then is used to supplement the experimental information in domains where measurements could not be obtained (E.g., near the heater assembly are in the far field outside of the PIV measurement window). The CFD approach used in the present study extends the earlier work of Ma and He (2021). The computation domain used in STAR CCM+ along with the closeup view of the mesh around the heated cylinder wall is presented in Fig. 7. The domain size was chosen to be 30D by 20D by 4D, to be consistent with the relative domain size used by Ma and He (2021). The top and the bottom of the computational domain were modeled as pressure boundaries while the axial ends of the domain were modeled as periodic boundaries. The lateral side walls were

modeled as slip walls. The standard mesh used in this study had a base size of 1.5 mm and the boundary layer was treated using a prism layer mesh with a total thickness of 3.35 mm, a stretching factor of 1.1, and 16 layers – see boundary layer mesh details in Fig. 7 (right). To handle the density variations, simulations were performed using the Boussinesq approximation while the dynamic viscosity was varied using properties from Engineering Toolbox (Engineering Toolbox, 2021). For the turbulence modeling, LES was chosen with the all  $y^+$  wall model. The highest  $y^+$  recorded was 0.75. Per the suggestions of Ma and He (2021), the dynamic Smagorinsky method was chosen. Mesh refinement, time step and grid resolution sensitivity studies were performed and showed converged results as discussed in 4.1.1. The total domain size was also increased to examine the effects of the boundary conditions on simulations as shown in Fig. 9. Results less than 2 mm from the surface of the cylinder were omitted. This was due to the maxima averaging at every elevation line leading to a “sudden jump” in this region. This was a result of being close enough to the cylinder that this type of averaging as it would begin to take values in the boundary layer of the cylinder, to the right and left of the plume region.

#### 3.1.1. Single cylinder CFD results

Given the inherent unsteadiness of the free thermal plumes, sensitivities to time step and averaging time are expected. These effects were examined while maintaining a constant data sampling time of 0.25 s. The results of mesh and domain depth sensitivity studies are presented in Fig. 8 and Fig. 9. Note that over the range of mesh and time steps used the CFL number ranged from 5 to 0.75. This can be shown to have little effect on the data as shown in Fig. 8 (right). In the range tested, the sensitivity of the centerline velocities is small, with mesh having the largest effect, on the order of 2–3 mm/s and moving the position of the peak velocity further upstream. Considering this, all subsequent time-averaged results are obtained for a runtime of 400 s with an output time step of 0.25 s and base size of 1.5 mm.

To ensure good quality LES, the LESIQ or the Large Eddy Simulation quality index proposed by Celik et al. (2005) was calculated. The LESIQ indicates the percentage of energy contained in resolvable eddies for a given domain. Values of 75–85% considered good quality (Celik et al., 2005). For a mesh size of 2 mm and 1.5 mm at a time step of 0.25 s, the LESIQ for this domain was found to be >95% for the highest (and most turbulent) power level. Indicating that the LES is of good quality.

Comparison of the calculation results obtained with LES model versus experiment can be seen in Fig. 10. The CFD performance is generally good with velocities and temperatures being over predicted by 2 °C and 3–5 mm/s, respectively, while the trends are consistently captured. This level of predictive accuracy appears to be consistent with the results of Ma and He (2021). Given the limitations of the velocity

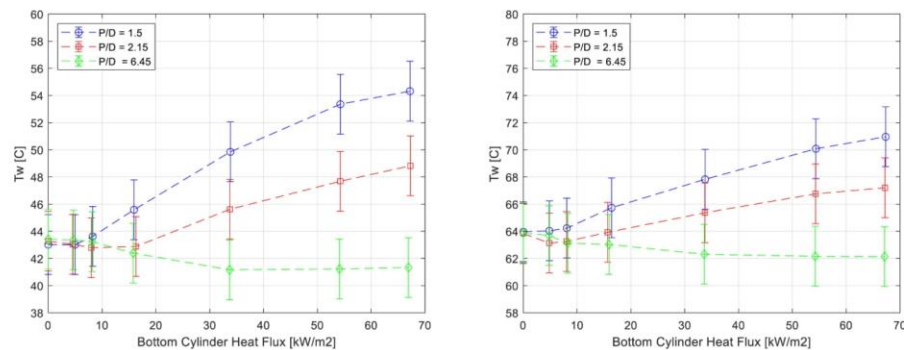


Fig. 6. Wall temperatures measured vs bottom cylinder heat flux for an upper heat flux of 13.7 kW/m<sup>2</sup> with  $T_{\infty} = 25$ C left and 50C right.

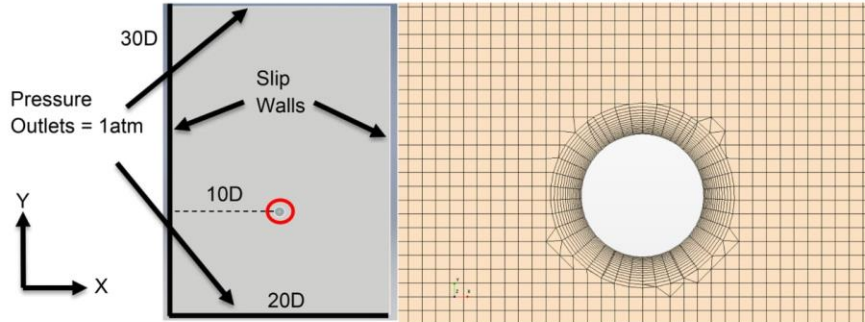


Fig. 7. Computational domain (left) and mesh in the highlighted region in the vicinity of the heated cylinder (right).

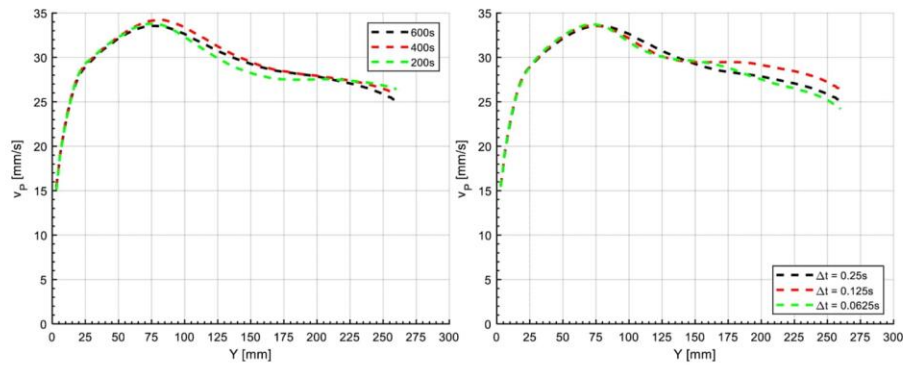


Fig. 8. Sensitivity to time step (right) and total averaging time (left).

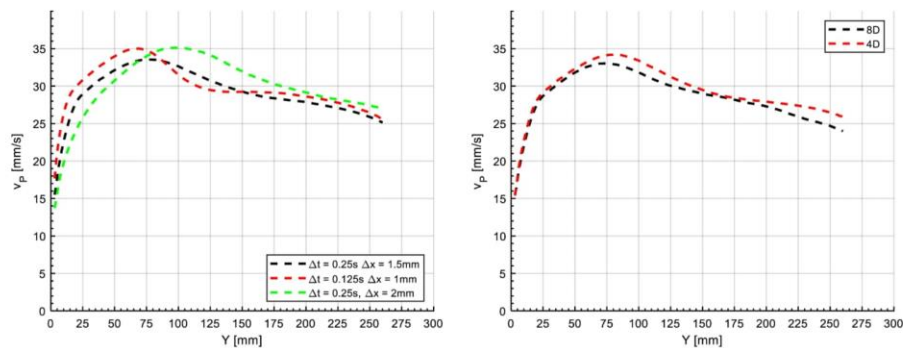


Fig. 9. Sensitivity to mesh (left) and domain depth size (right).

measurements near the heater surface and for large heater powers, the LES simulations are used to supplement the experimental results in the far-field (at high elevations from the lower heater) where limited optical access prevented detailed measurements and where thermal gradients precluded reliable measurements.

#### 4. Model development

The mechanistic model developed below extends the framework proposed by Stafford and Egan (2014). As shown in equations (3)-(8), the influence of the lower cylinder momentum and thermal plume is

C.W. Hollingshead et al.

Nuclear Engineering and Design 394 (2022) 111823

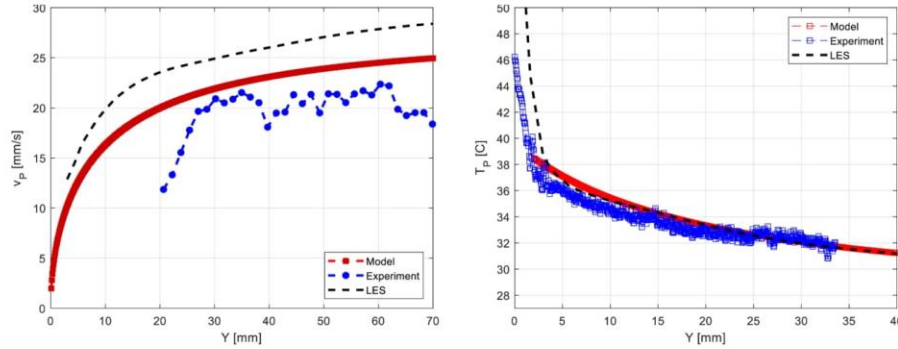


Fig. 10. Comparison between the LES calculation, experiment, and proposed model for the 512 W case.

superimposed on the natural convection of the upper cylinder in the proposed model. These equations suggest that the  $Nu_D$  of the upper cylinder is that of a free single cylinder with an additional forced convective contribution generated by the momentum in the plume from the cylinder below. Additionally, a heating effect from the lower cylinder's thermal plume is captured by evaluating the heat transfer around the upper cylinder using a local temperature  $T_{loc}$  based on the plume temperature, instead of using  $T_{\infty}$ . In other words, the upper cylinder becomes engulfed with moving fluid at a temperature higher than  $T_{\infty}$ . Phenomenologically this implies that the heat transfer may increase or decrease relative to that of a single cylinder case depending upon the bottom cylinder plume, i.e. the induced local velocity,  $v_{loc}$ , and temperature,  $T_{loc}$ . Consistent with the definitions from Stafford and Egan (2014), two distinct Nusselt numbers,  $Nu_{Di}$  and  $Nu_{apparent}$  are considered in the following discussion.  $Nu_{Di}$  is the Nusselt number obtained from the model equation (1) using a purely local set of conditions  $v_{loc}$  and  $T_{loc}$ .  $Nu_{apparent}$  is obtained via evaluating the upper cylinder at the unaffected bulk temperature,  $T_{\infty}$ . Since many of the prior studies in literature did not measure the local temperature in the plume, the distinction proposed by Stafford and Egan (2014) allows for comparing the model to

results in literature. Additionally, it allows for the comparison of the heating and cooling effects as a function of elevation and power. For consistency and later comparisons of the model performance versus past experiments,  $Nu_{apparent}$  will be reported in the current study. The fluid properties are evaluated at the film temperature (defined as an average between the wall and the local fluid temperature  $T_{loc}$ ). A flow chart showing the calculation steps of this model is presented in Fig. 12 and the general geometry with labels is shown in Fig. 11. The details of the model are discussed in the subsequent sections.

$$T_{loc} = \frac{1}{D} \int_H^{H+D} T_p(y) dy \quad (7)$$

$$v_{loc} = \frac{1}{D} \int_H^{H+D} v_p(y) dy \quad (8)$$

#### 4.1. Plume temperature model

The plume temperature is an important parameter in the model and captures the influence of the lower elevation heater on the local thermal boundary layer of the upper heater. Equation (9) shows the plume

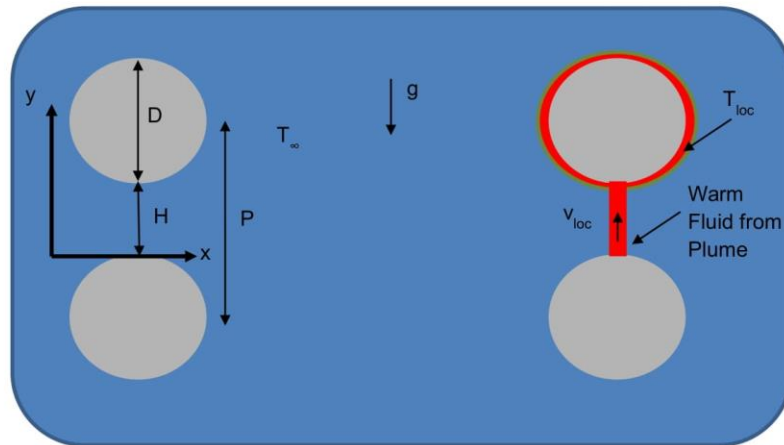


Fig. 11. Shows the geometry used with labelled parameters.

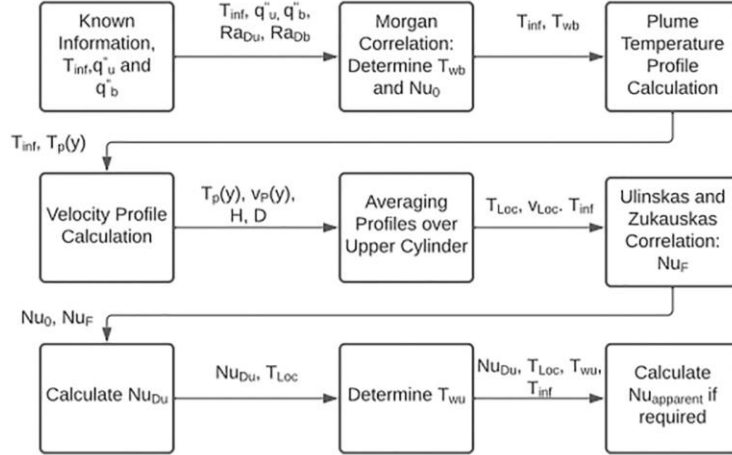


Fig. 12. The progression of the calculations in the model presented with the variables passed on from step to step.

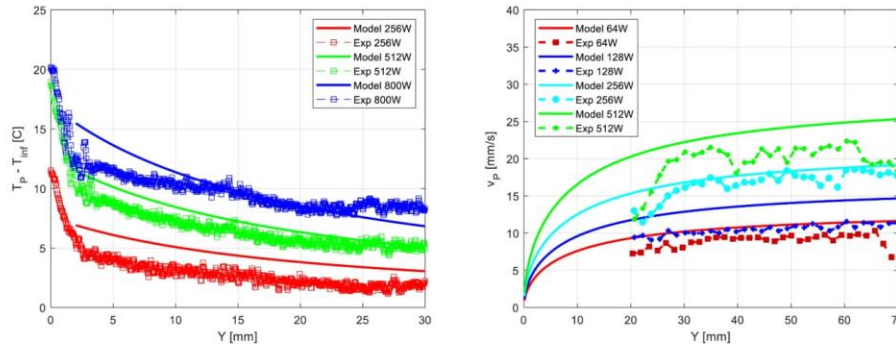


Fig. 13. LIF plume centreline temperature (left) and PIV centreline velocity (right) as a function of power for the developed models (The 64 and 128 W cases were omitted from the temperature figure for clarity).

temperature model used in this work and is based on the observations of [Grafsronnigen and Jensen \(2012\)](#) which suggests the exponent of  $-1$ . Given that the lower cylinder is not a point source, a virtual origin added to account for the finite size of the tubes. The correlating coefficient of 0.7 and virtual origin of 1.5 were found from a least-squares regression to the LIF measurements discussed in the previous sections. Though such a simplistic correlation provides non-physical behaviour for temperatures immediately adjacent to the heater tube and below the virtual origin, it was found to perform well just outside the thermal boundary layer of the cylinder.

$$T_p - T_\infty = 0.7(T_w - T_\infty) \left( \frac{y}{D} + 1.5 \right)^{-1} \quad (9)$$

#### 4.2. Velocity model

The influence of the momentum generated by the lower heater on the upper cylinder's heat transfer is also an important characteristic of the two cylinders configuration. The velocity model for the laminar portion

of the plume is based on an energy balance, e.g. the expression from [White \(2011\)](#). It must be noted that this simple energy balance neglects viscous and turbulent dissipation, and as such is expected to overpredict the local velocity. Equation (10) provides an estimate of the maximum plume velocity as a function of the local plume temperature and the distance from the lower heater surface. While the model is simple, it can capture the local velocity within 2–3 mm/s of measured values with very few fitting parameters – see [Fig. 13](#) (right). The thermal expansion coefficient in equation (10) is evaluated at the bulk temperature  $T_\infty$ . It must be noted that the model is very sensitive to the choice of reference temperature for the thermal expansion coefficient. The choice of the bulk temperature representing the bulk fluid expansion behaviour agreed best with the experimental data.

$$v_p = \sqrt{g\beta(T_p(y) - T_\infty)y} \quad (10)$$

##### 4.2.1. Transition to turbulence

In literature, the transition to turbulence for a free plume is usually based on the value of  $Gr$ . Studies such as [\(Forstrom and Sparrow, 1966;](#)

C.W. Hollingshead et al.

Nuclear Engineering and Design 394 (2022) 111823

Jr and Gebhart, 1975; Noto et al., 1999; Elicer-Cortes et al., 2000) have provided estimates for the critical  $Gr$  for the initial onset and the end of the transition region. The beginning of the transition to turbulence reported in literature ranges from  $2 \times 10^8$  to  $1 \times 10^9$  and the end of the transition ranges from  $2 \times 10^9$  to  $7 \times 10^9$ . For the model in the present study, a value of  $Gr_{crit}$  of  $2 \times 10^8$  was chosen to be consistent with Noto et al. (1999). This is consistent with the transitions observed in the LES simulations, as shown in Fig. 14. It should be noted that due to limited optical window access the transition to turbulence occurred outside of the field of view in most measurements, hence the transition model relies solely on the LES results.

Once  $Gr_{crit}$  is reached, the velocity profile begins to decay as turbulent mixing increases, as observed in Pham et al. (2005). This occurs at a distance  $L_{crit}$  from the surface of the cylinder. The turbulent dissipation of the plume centerline velocity decay is modeled with  $-1/3$  exponent, consistent with both Pham et al. (2005) and with the present LES simulations. Therefore, for all  $y > L_{crit}$  the velocity follows Equation (12). Coefficients  $A$  and  $B$  in Equation (12) are quadratic terms to ensure a smooth transition between the fully laminar and fully turbulent regimes.  $L_{crit}$  was chosen instead of the diameter to nondimensionalize distance in this equation to account for the impact of the transition to turbulence on the flow field changes.  $L_{crit}$  is calculated as the distance  $y$  from the surface of the cylinder when  $Gr_y$  is equal to  $Gr_{crit}$ .  $Gr$  is calculated using properties evaluated at the film temperature ( $T_f = T_w/2 + T_\infty/2$ ).

$$Gr_{crit} = 2 \times 10^8 \quad (11)$$

$$v = Av_{LAM} + Bv_{max} \left( \frac{y}{L_{crit}} \right)^{-1/3} \quad (12)$$

$$B = 1 - \left( \frac{L_{crit}}{y} \right)^2 \quad (13)$$

$$A = \left( \frac{L_{crit}}{y} \right)^2 \quad (14)$$

The performance of the model versus LES simulations is presented in Fig. 14. As mentioned above, the transition criteria of Noto et al. (1999) of  $Gr_{crit} = 2 \times 10^8$  was chosen as it captured the position of the peak velocity and slope after transition for a majority of conditions. The velocity magnitudes agree to within 3–5 mm/s for the entire range of the experimental conditions of the present study. Comparisons of the LES to the model predictions with  $Gr_{crit} = 2 \times 10^8$  for different power levels are shown in Fig. 15. Again, the performance of the model is within 3–5 mm/s over a wide range of test conditions. However, for lower power cases, the prediction of the peak velocity value i.e. the transition to

turbulence is not predicted well with the  $Gr$ -based criteria adopted here.

#### 4.3. Correlations

To predict the base  $Nu_D$  of the upper cylinder, correlations using the local condition relations developed in equations (9) and (12) are needed. For this purpose, the Morgan (1975) correlation for single cylinder natural convection, and Zukauskas and Ulinskas (1988) for external forced convection over a cylinder were selected as shown below. These correlations were chosen as they cover wide ranges of  $Ra$  and  $Re$ .

Morgan, 1975	
$Nu_D = 0.675Ra_D^{0.058}$	$10^{-10} \leq Ra_D < 10^{-2}$
$Nu_D = 1.02Ra_D^{0.148}$	$10^{-2} \leq Ra_D < 10^2$
$Nu_D = 0.85Ra_D^{0.188}$	$10^2 \leq Ra_D < 10^4$
$Nu_D = 0.48Ra_D^{0.25}$	$10^4 \leq Ra_D < 10^7$
$Nu_D = 0.125Ra_D^{0.333}$	$10^7 \leq Ra_D < 10^{10}$

Zukauskas and Ulinskas, 1988	
$Nu_D = CRe^m Pr^n \left( \frac{Pr}{Pr_s} \right)^{1/4}$	$n = 0.37$
$C = 0.75, m = 0.4$	$1 \leq Re_D < 40$
$C = 0.51, m = 0.5$	$40 \leq Re_D < 1000$
$C = 0.26, m = 0.6$	$1000 \leq Re_D < 200,000$
$C = 0.076, m = 0.7$	$200,000 \leq Re_D < 10^6$

#### 4.4. Superposition exponent

As mentioned previously, the base natural convection heat transfer from the upper cylinder is superimposed on the effect of the plume coming from lower elevations. The superposition exponent chosen by Stafford and Egan (2014) used in equation (1) was  $n = 3$ . For the current study, it was found that a value of 2 provided the best level of agreement with the experimental data. A higher exponent tends to increase the impact of temperature from the lower plume whereas a lower exponent leads to momentum effects dominating. The difference between  $n = 3$  from Stafford and Egan (2014) and  $n = 2$  for the present study is thought to be a combination of different working fluid (water in the present tests to air used in literature) and diameter of the heaters.

#### 5. Model performance

The performance of the model provided in equations (1–6) is quantitatively presented in Fig. 16. Generally, the performance is good with

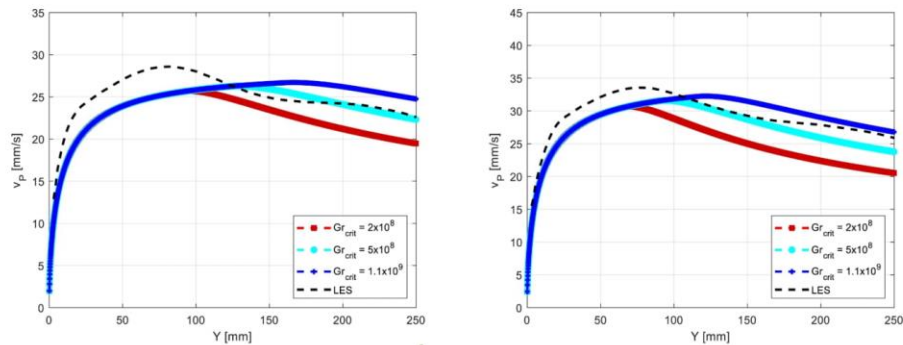


Fig. 14. The performance of the velocity model with different transitions to turbulence against Large Eddy Simulations (512 W left, 800 W right).

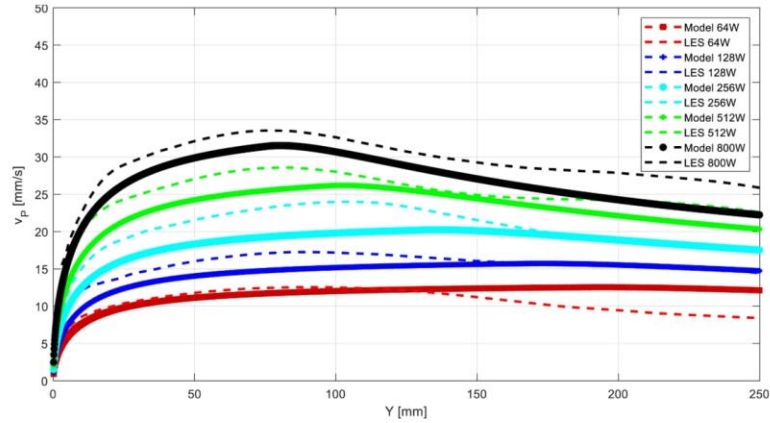


Fig. 15. Model performance using the Noto et al. (1999) criteria for several power levels compared with LES simulations.

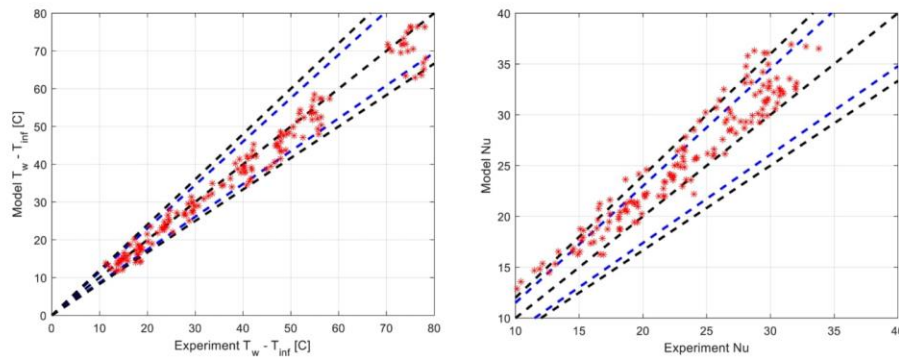


Fig. 16. The performance of the experiment versus the present model with  $\Delta T$  (left) and  $Nu$  (right) with bars representing  $\pm 15\%$  (blue) and  $\pm 20\%$  (black). (For interpretation of the references to colour in this figure legend, the reader is referred to the web version of this article.)

93.51% of the wall temperature data lying within 15% of experiment. This corresponds to an RMS error of 3.42 °C and an absolute deviation of 2.27 °C. The model tends to overpredict the  $Nu_D$  in comparison to experiment, with 75.6% of the data falling within  $\pm 15\%$ . This increases to 85.71% of data within  $\pm 20\%$ . There is also a clear overprediction in  $Nu_D$ , most notably for  $P/D = 6.45$  and at higher powers. This systemic overprediction of  $Nu_D$  may in part be due to the three instrumented thermocouples on the heater. Two of these three thermocouples are located on the upper section of the heater as shown in Fig. 1. Due to the developing thermal boundary layer from the bottom of the cylinder to the top, the upper side generally has higher temperatures (measured to be 1 to 2°C higher than the lower thermocouples). This very likely contributes to lower  $Nu_D$  observed compared to the model predictions. Furthermore, it is believed that the plume velocity model and the turbulent transition may also be contributors to this systematic overprediction of  $Nu_D$ . This is due to the PIV measurements unable to resolve anything beyond  $y = 70$  mm. For  $P/D = 6.45$ , the plume will extend to  $y > 85$  mm. Knowing this, it is possible that the model magnitude and turbulent transition are different than what the model predicts in this region.

To validate the model for a wider range of conditions it was compared to the independent results available from Grafssonigen and Jensen (2012). Their experiment, also performed with water and employed cylinders that were 54 mm in diameter compared to the 13.4 mm used in the present study. Only  $Nu_D$  were reported and experimental conditions were such that the upper and lower cylinders were always at the same heat flux or  $Ra_D$ . The comparison can be seen in Fig. 17, and the performance is good with a  $Nu_D$  RMS error of 7.46 and an absolute deviation of 6.53. This corresponded to 100% of model predictions within 20% of Grafssonigen and Jensen (2012). Additionally, 82.6% of the data lies within 15% of the model predictions.

## 6. Conclusion

Heat transfer measurements from a pair of vertically aligned horizontal cylinders at three  $P/D$  values were presented. These measurements were made over a range of powers from 128 W to 1000 W. It was found that at  $P/D = 1.5$ , the heating effect from the lower cylinder caused a reduction in the heat transfer in the upper cylinder due to the change in the local boundary layer temperatures. Conversely, at  $P/D =$

C.W. Hollingshead et al.

Nuclear Engineering and Design 394 (2022) 111823

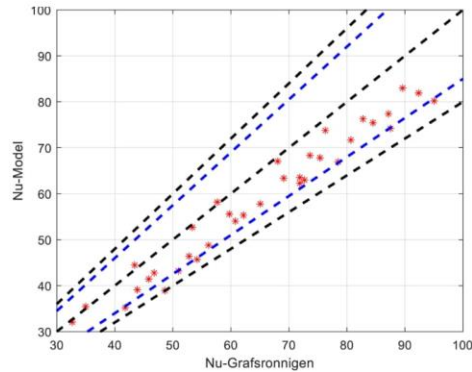


Fig. 17. Nu predictions versus the experiments of Grafronnigen and Jensen (2012) with error bars of  $\pm 15\%$  (blue) and  $\pm 20\%$  (black). (For interpretation of the references to colour in this figure legend, the reader is referred to the web version of this article.)

6.45 the convection effects, i.e., the velocity induced from the lower heater, largely dominated which increased heat transfer and decreased the wall temperature. At  $P/D = 2.15$ , both enhancement and diminishment were measured, depending on the local conditions.

LES simulations were performed and validated with both temperature and velocity measurements using a framework similar to the one used by Ma and He (2021). The LES model over predicted plume velocity measurements by  $\sim 5$  mm/s whereas plume temperatures were much more accurately captured. After validation, the LES simulations were used to expand the information used to develop the plume velocity model to include a turbulent transition which could not be observed in the experiments. The turbulent transitions were found to agree best with the criteria proposed by Noto et al. (1999).

A model capable of predicting the heat transfer of the upper cylinder in a vertically aligned cylinder pair was developed and tested. Unlike the model developed by Stafford and Egan (2014), the underlying velocity and temperature models are based on experimental data where possible and LES simulation to fill in gaps in the velocity measurements. The model includes the effects of the local temperature changes caused by the lower heater as well as the induced momentum from the buoyant plume below. The model is based on well established relationships in literature and was found to be generally accurate with an RMS error of 2.8 and absolute deviation of 2.31 in  $Nu_D$  of the upper cylinder. When comparing the model to the experiments of Grafronnigen and Jensen (2012) an RMS error of 7.46 and absolute deviation of 6.53 in  $Nu_D$  are obtained. The model predictions captured all the experimental data of Grafronnigen and Jensen (2012) to within 20%.

#### CRedit authorship contribution statement

**C.W. Hollingshead:** Data curation, Formal analysis, Project administration, Software, Visualization, Writing – original draft, Writing – review & editing. **A. Rashkovan:** Methodology, Resources, Writing – review & editing. **D.R. Novog:** Conceptualization, Funding acquisition, Methodology, Project administration, Resources, Supervision, Writing – review & editing.

#### Declaration of Competing Interest

The authors declare that they have no known competing financial interests or personal relationships that could have appeared to influence the work reported in this paper.

#### Acknowledgements

This paper would not have been possible without the generous support of the NSERC Industrial research chair and the University Network of Excellence in Nuclear Engineering (UNENE).

#### References

- Morgan, V., 1975. The overall convective heat transfer from smooth circular cylinders. *Adv. Heat Transfer* 11, 199–264.
- Sparrow, E.M., Niethammer, J.E., 1981. Effect of vertical separation distance and cylinder-to-cylinder temperature imbalance on natural convection for a pair of horizontal cylinders. *J. Heat Transfer* 103, 638–644.
- Grafronnigen, S., Jensen, A., Reif, B.A.P., 2011. PIV investigation of buoyant plume from natural convection heat transfer above a horizontal heated cylinder. *Int. J. Heat Mass Transf.* 54, 4975–4987.
- Marsters, G.F., 1972. Arrays of heated horizontal cylinders in natural convection. *Int. J. Heat Mass Transf.* 15, 921–933.
- Kuehner, J.P., Hamed, A.M., Mitchell, J.D., 2015. Experimental investigation of the free convection velocity boundary layer and plume formation region for a heated horizontal cylinder. *Int. J. Heat Mass Transf.* 58, 78–97.
- Atmane, M.A., Chan, V.S.S., Murray, D.B., 2003. Natural Convection around a horizontal heated cylinder: the effects of vertical confinement. *Int. J. Heat Mass Transf.* 46, 3661–3672.
- Kuehner, J., Pflug, J.R., Jr, F.A.T., Hamed, A.M., Marin, F., 2012. Velocity measurements in the free convection flow above a heated horizontal cylinder. *Int. J. Heat Mass Transf.* 55, 4711–4723.
- Park, H., Park, J., Jung, S.Y., 2019. Measurements of velocity and temperature fields in natural convective flows. *Int. J. Heat Mass Transf.* 139, 193–302.
- Grafronnigen, S., Jensen, A., 2012. Simultaneous PIV/LIF measurements of a transitional buoyant plume above a horizontal cylinder. *Int. J. Heat Mass Transf.* 55, 4195–4206.
- Forstrom, R.J., Sparrow, E.M., 1966. Experiments on the buoyant plume above a heated horizontal wire. *Int. J. Heat Mass Transf.* 10, 321–331.
- Jr, R., Gebhart, B., 1975. The transition of plane plumes. *Int. J. Heat Mass Transf.* 18, 513–526.
- Noto, K., Teramoto, K., Nakajima, T., 1999. Spectra and critical grashof numbers for turbulent transition in a thermal plume. *J. Thermophys Heat Transfer* 13 (1), 82–90.
- Elice-Garcia, J., Fuentes, J., Valencia, A., Baudet, C., 2000. Experimental study of transition to turbulence of a round thermal plume by ultrasound. *Exp. Therm. Fluid Sci.* 20, 137–149.
- Gebhart, B., Pera, L., Schorr, A.W., 1970. Steady laminar natural convection plumes above a horizontal line heat source. *Int. J. Heat Mass Transf.* 13, 161–171.
- Ma, H., He, L. 2021. Large Eddy simulation of natural convection heat transfer and fluid flow around a horizontal cylinder. *Int. J. Therm. Sci.* (162).
- Grafronnigen, S., Jensen, A., 2017. Large eddy simulations of a buoyant plume above a heated horizontal cylinder at intermediate Rayleigh numbers. *Int. J. Therm. Sci.* 112, 104–117.
- Grafronnigen, S., Jensen, A., 2012. Natural Convection heat transfer from two horizontal cylinders at high Rayleigh numbers. *Int. J. Heat Mass Transf.* 55, 5552–5564.
- Pelletier, Q., Murray, D.B., Persoons, T., 2016. Unsteady natural convection heat transfer from a pair of vertically aligned horizontal cylinders. *Int. J. Heat Mass Transf.* 95, 693–708.
- Reymond, O., Murray, D.B., O'Donovan, T.S., 2008. Natural Convection heat transfer from two horizontal cylinders. *Exp. Therm Fluid Sci.* 32, 1702–1709.
- Persoons, T., O'Gorman, I.M., Donoghue, D.B., Byrnel, G., Murray, D.B., 2011. Natural convection heat transfer and fluid dynamics for a pair of vertically aligned isothermal horizontal cylinders. *Int. J. Heat Mass Transf.* 54, 5163–5172.
- Stafford, J., Egan, V., 2014. Configurations for single-scale cylinder pairs in natural convection. *Int. J. Therm. Sci.* 84, 62–74.
- Kitamura, K., Mitsuishi, A., Suzuki, T., Kimura, F., 2016. Fluid Flow and heat transfer of natural convection induced around a vertical row of heated horizontal cylinders. *Int. J. Heat Mass Transf.* 92, 414–429.
- Tokura, I., Saito, H., Kishinami, K., Muramoto, K., 1983. An experimental study of free convection heat transfer from a horizontal cylinder in a vertical array set in free space between parallel walls. *J. Heat Transfer* 105, 102–107.
- Hollingshead, C.W., Rashkovan, A., Strack, J.M.V., Novog, D.R., 2020. An experimental and numerical investigation into scaling considerations for moderator circulation experiments. *Nucl. Eng. Des.* 369.
- Sigma Aldrich, Sigma Aldrich, [Online]. Available: <https://www.sigmaaldrich.com/catalog/product/sigma/83689?lang=en&region=CA#:~:text=Rhodamine%20B%20is%20a%20xanthene,is%20bright%20red%20in%20color.> [Accessed 2021].
- Engineering Toolbox, 2021. [Online]. Available: <https://www.engineeringtoolbox.com/>. [Accessed 2021].
- Celik, I., Cehreli, Z.N., Yavuz, I., 2005. Index of resolution quality for large eddy simulations. *J. Fluids Eng.* 127, 949–958.
- White, F.M., 2011. *Viscous Fluid Flow*. McGraw Hill.
- Pham, M.V., Ploaude, F., Kim, S.D., 2005. Three-dimensional characterization of a pure thermal plume. *J. Heat Transfer* 127, 624–636.
- Zukauskas, A., Ulinskas, R. 1988. Heat transfer in tube banks in crossflow.

## **5 Mixed Convective Flow Patterns for CANDU Geometries: Accounting for Scaling Distortions and issues with $Ar$**

### **About this Paper:**

#### **Contribution to Knowledge:**

This paper added additional experimental and simulation data to further characterize the performance of CFD for CANDU geometries in an integral test facility. This was in the continued effort to improve the prediction of local conditions important in the determination of fuel channel integrity in DBA and BDBA events. This paper analyzed various scaling distortions introduced by a  $1/16^{\text{th}}$  scaling via CFD simulation and suggested key features of the geometry whereby minimization of these distortions could be achieved. Additionally, the performance of the  $Ar$  on the non-dimensional temperature field was assessed. While the  $Ar$  was found to yield the same temperature distribution in well-mixed regions of the tank, flow pattern was found to be a stronger factor. Consequently, a modification factor  $H$ , based on the heat flux areas of the ideal vs built case was proposed in an attempt to correct for the increase in buoyant force when fewer heaters are present or heated. Thus the novelty of this work, beyond the experimental data generated and CFD validation performed, was in the

development of an additional scaling parameter needed to assure mixed convection similarity in smaller scale facilities.

**Authors Contribution:**

The primary author (Hollingshead) performed all of the draft writing, analysis and experimentation for this study. The CFD simulations for this work were primarily performed by Rashkovan under the direction of Hollingshead for choice of heating arrangement,  $Ar$  and other factors. The initial design of the test vessel used was performed by Strack. Funding, support and guidance was provided by Novog. All co-authors contributed significantly to the editing of the document.



Contents lists available at ScienceDirect

## Nuclear Engineering and Design

journal homepage: [www.elsevier.com/locate/nucengdes](http://www.elsevier.com/locate/nucengdes)



### An experimental and numerical investigation into scaling considerations for moderator circulation experiments



C.W. Hollingshead<sup>a,\*</sup>, A. Rashkovan<sup>b</sup>, J.M.V. Strack<sup>a</sup>, D.R. Novog<sup>a</sup>

<sup>a</sup> Department of Engineering Physics, McMaster University, Hamilton, Ontario, Canada

<sup>b</sup> Nuclear Research Center Negev (NRCN), Beer-Sheva 84190, Israel

#### ARTICLE INFO

**Keywords:**  
CANDU  
Moderator  
CFD  
Archimedes  
Scaling

#### ABSTRACT

The moderator system in a CANDU reactor provides the unique ability to provide emergency cooling to the fuel in postulated severe accidents during the early phases of the transient. A key criteria which dictates the effectiveness of heat removal during these events is the integrity of the fuel channel assembly. This in turn relies on the prevention of dryout on the calandria tube. The main tool used to demonstrate adequate margins to dryout on the calandria tubes is Computational Fluid Dynamics (CFD). While several experimental datasets are available for validation of these tools, the historical facilities lack the specific geometrical features present in some of the older CANDU designs. The historic tests were typically scaled based on the so-called Archimedes number and non-dimensional heat flux. To extend the validation database two unique 1/16th scale (based on vessel diameter) experiments are performed which include features found in the moderator systems of two operating CANDU designs. The primary goal of these new experiments was to generate thermohydraulic data for validation of CFD codes, but several additional tests were performed to examine the potential impact of scaling on the results. This paper demonstrates a consistent conservative bias in the CFD predictions with respect to maximum temperature in the experiments over the range of conditions tested. The combination of CFD and experimental observations concludes that the likely cause of the bias is due to CFD's over prediction of inlet jet dissipation leading to less cold fluid penetration in the heated core of the test section. In terms of scaling, a combination of experimental evidence and supporting CFD simulations indicate that the historical scaling parameters do provide some level of qualitative similarity in the mixed-convection regimes in the vessel, but some revision to account for geometrical and flow pattern deviations may be necessary.

#### 1. Introduction

The CANDU reactor is a pressure tube (PT) reactor which uses natural uranium as its fuel and a low-pressure heavy water moderator. In each fuel channel, high temperature and high-pressure coolant flows within a pressure tube which is surrounded by an insulating annulus gas (CO<sub>2</sub>) and a calandria tube (CT) with spring spacers separating the two tubes. Under normal operating conditions, approximately 5% of the total reactor power is deposited into the moderator through gamma ray heating and the thermalization of neutrons. Hence, the moderator of a CANDU contains its own low-pressure cooling circuit.

In beyond design basis accidents such as a loss of coolant accident (LOCA) with subsequent loss of emergency core cooling (ECC), the PTs can balloon or sag into contact with the surrounding CTs. This establishes a pathway for heat generated in the fuel to be rejected to the heavy water moderator. This heat sink can provide additional cooling

to the fuel giving operators and responders time to establish a longer-term heat sink. However, heat removal through the PT-CT walls to the moderator may be limited by the Critical Heat Flux (CHF) or "dryout" at the CT-moderator surface. Sustained dryout at the CT surface could result in its structural failure, which in turn would result in progression of the accident sequence. The CHF occurrence has been shown to depend upon the local moderator sub-cooling (Nitheanandan et al., 1998). Hence, detailed prediction of moderator temperature within the Calandria is required in the safety analysis. The next sections provide a review of previous studies and methods into the measurement and prediction of CANDU moderator conditions.

Measurements of real reactor moderator and scaled experimental facilities have been performed by several groups to understand both the temperature and velocity fields see e.g. (Sion, 1983; Khartabil et al., 2000; Atkins et al., 2017; Kim et al., 2017; Huguet et al., 1989; Rhee et al., 2013). The experiments of Sion (1983) were done on Unit 3 of the

\* Corresponding author.

E-mail address: [hollincw@mcmaster.ca](mailto:hollincw@mcmaster.ca) (C.W. Hollingshead).

<https://doi.org/10.1016/j.nucengdes.2020.110829>

Received 12 February 2020; Received in revised form 3 June 2020; Accepted 26 August 2020

Available online 12 September 2020

0029-5493/ © 2020 The Authors. Published by Elsevier B.V. This is an open access article under the CC BY license

(<http://creativecommons.org/licenses/by/4.0/>).

Nomenclature			
$A_{exp}$	Surface area of 52 heater rods [m <sup>2</sup> ]	$Gr$	Grashof number
$A_{predict}$	Surface area of all 120 rods [m <sup>2</sup> ]	$L$	Length of vessel/heater rods [m]
$Ar$	Archimedes number	LPM	Litres per minute [L/min]
CT	Calandria tube	LOCA	Loss of coolant accident
ECC	Emergency core cooling	$Nu$	Nusselt number
PT	Pressure tube	$q''$	Heat flux [W/m <sup>2</sup> K]
$\beta$	Volumetric coefficient of expansion [1/K]	$Re$	Reynolds number
$D$	Diameter of vessel [m]	$T_{excess}$	Non-dimensional temperature
$g$	Acceleration due to gravity [m/s <sup>2</sup> ]	$\Delta T$	Temperature difference across test section [°C]
		$U_i$	Average inlet nozzle velocity [m/s]

Bruce Generating Station. In these in-reactor tests a probe equipped with K-type thermocouples and RTDs was inserted in place of a shut-down rod to assess the radiation impacts associated with measuring temperatures in-core for RTDs and thermocouples. Khartabil et al. (2000) performed tests on a 1/4 scale facility based upon the CANDU-9 design to gather experimental temperature and velocity data over a 3-dimensional domain. In attempt to accurately scale the facility to capture the important features present in the full-sized reactor, Khartabil et al. (2000) examined the feasibility of maintaining the inlet Reynolds number ( $Re$ ) and heat load. They found that due to the reduction in vessel diameter, the temperature difference across the test section would need to increase to the third power if  $Re$  was to be maintained. This can quickly become unfeasible from a power viewpoint. As an alternative, they maintained the buoyancy to inertial forces ratio in the tank described by the Archimedes ( $Ar$ ) number shown in Eq. (1). It should be noted that the  $Ar$  defined in that work is very similar to Richardson number, however for consistency with previous literature the  $Ar$  defined in Eq. (1) is used in the present study. Using this as their primary scaling factor they argued that the flow and temperature fields should be largely similar as long as  $Re$  was large enough to ensure turbulent flow in the moderator inlets.

$$Ar = \frac{g\beta\Delta TD}{U_i^2} \quad (1)$$

The goal of using the  $Ar$  number was to replicate the qualitative flow structure inside the vessel. Three of the commonly observed flow topologies are shown in Fig. 1 where buoyancy forces can cause changes from the pure momentum dominated behaviour (left drawing in Fig. 1) and Buoyancy influenced (right side of Fig. 1). Rhee et al. (2013) examined the validity of the scaling analysis outlined by Khartabil et al. (2000) by comparing CFD simulations of the 1/4 scale test facility based on a CANDU-6, to those of the full-scale reactor. Here, scaling was performed based on the  $\Delta T$  and  $Ar$ . It was noted that 1/4

scale facility was unable to replicate the moderator flow characteristics of the CANDU-6 based on comparisons of CFD results. This was attributed to the 1/4 scale facility making use of direct heating as opposed to volumetric heating in real-size reactor model, resulting in larger buoyancy forces near the heater surfaces, which were characterized using the Grashof ( $Gr$ ) number. In the small-scale test the  $Gr$  was shown to be four orders of magnitude larger than the full-scale reactor. Another issue was the lack of Reynolds number scaling of the inlets, since complete scaling of inlets was not possible. This was thought to have contributed to experimental inlet nozzle jets not reaching the top of the vessel as they do in the CANDU-6 simulations. Such a conclusion is also supported by the work shown in the experiments in the following section.

Kim et al. (2017) examined the downward secondary jet developed from the interaction of two upward facing inlet jets in a 1/4 scale CANDU-6 test section under isothermal conditions using particle image velocimetry (PIV). This facility contained two significant scaling distortions as air was used as a working fluid and featured a different inlet nozzle geometry and configuration. Kim et al. (2017) showed that the use of air and altered inlet geometry still resulted in the development of the secondary downward jet from the top of the vessel. It was determined that the same qualitative jet profile was obtained when compared to previous experiments using water and a more accurate inlet geometry. The downward jet profile at the top of the vessel was noted to have a downward magnitude of approximately 50% the average inlet velocity. This was further reduced to 15% in the centre of the vessel. Kim et al. (2017) also performed CFD simulations on their geometry to assess the ability to computationally predict important flow features. Using the  $k-\omega$  SST turbulence model, they noted an apparent under-prediction of the dissipation and diffusion of the secondary jet due to greater peak velocities in the simulations than those observed experimentally.

Mixed convection around calandria tubes was recently studied by

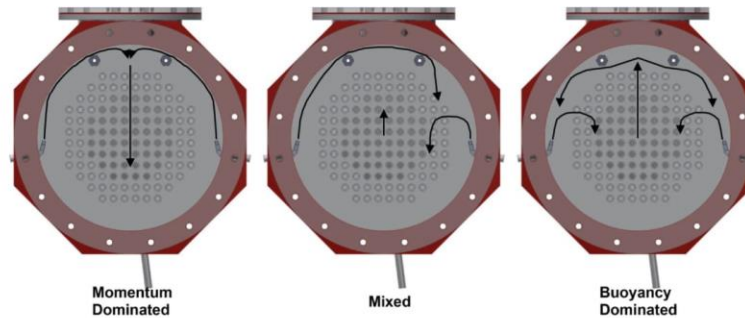


Fig. 1. Shows the momentum, mixed and buoyancy dominated flow patterns present in CANDU moderators depending primarily on the inlet flow rate and total power.

Atkins et al. (2017). They used the same test section as Kim et al. (2017) and examined the heat transfer from the calandria tubes in the centre of the vessel where the secondary jet loses its vertical momentum. Temperatures were measured using an instrumented tube with a single K-type thermocouple. To get circumferential measurements, a rotary table was used to rotate the instrumented tubes to measure circumferential distributions of the Nusselt ( $Nu$ ) number. They first measured the natural circulation  $Nu$  profile for a single tube, and then performed the measurements for selected tube rows in the centre of the vessel for various inlet  $Re$  conditions. It was shown that  $Nu$  was largest for the tubes at the top of the vessel and gradually decreased with jet velocity approaching the natural convection profile for the tubes in lower rows.

Validation studies for computer codes used to predict moderator conditions include among others (Kim et al., 2017, 2006; Carlucci et al., 2000; Yoon et al., 2002; Strack, 2019). The study performed by Carlucci et al. (2000) used the industry standard CFD code MODTURC\_CLAS to compare results against the measurements obtained in the 1/4 scale facility of Khartabil et al. (2000). It was determined that the overall level of agreement between experiment and simulation was good, with the temperature field typically being under predicted in the bottom region of the vessel. This was attributed to an underprediction of the inlet nozzle jets entrainment and the porous media approximation used in the MODTURC\_CLAS code which replaces the CT tubes of the reactor with a suitably selected porous media.

The study of Strack (2019) examined the similarity of a 1/16th test section to a full-scale reactor experimentally and numerically using  $Ar$  to scale test parameters. Strack (2019) found the scaled down facility capable of reproducing flow features found in the full-scale reactor primarily through CFD simulations using STAR-CCM+. It was noted that buoyancy forces were found to be stronger in the small-scale test section compared to the full scale calandria. This was thought to have been a result of the reduction in the number of tube elements (~120 as opposed to ~400) which meant that the local heat flux from a given tube was a factor of 4 higher than the full scale case. It was also found that the CFD model tended to overpredict temperatures by upwards of 4 °C using the realizable  $k-\epsilon$  turbulence model. In addition, it was noted that for higher  $Ar$  the comparison between the model and experiment improved.

The present study seeks to add more experimental data to assist in the continued validation efforts for CFD codes of the 3-dimensional temperature and velocity fields of a CANDU moderator with the construction of two 1/16th facilities based upon two distinct CANDU moderator designs. In addition, the use of the  $Ar$  number as the main scaling criterion is further investigated.

## 2. Experimental programs

The test sections for this study are approximately 1/16th linear scale based on two CANDU reactor designs visualized in Figs. 2 and 3. They will be referred to as 'Phase A' and 'Phase B' tests, respectively. These test sections were constructed with the primary goal of generating experimental data to validate CFD codes such as STAR-CCM+ and FLUENT. The 1/16th linear scaling refers primarily to the diameter of the test section. All other components were also scaled down by a factor of 16 where possible with some exceptions needed due to the significant size reduction. The scaling of these vessels was designed such that they contain the salient flow features found in the actual reactors, with some distortions intentionally added to allow for better measurement access with laser systems and traversable thermocouples. Other significant scaling distortions include a reduced number of calandria tubes and changes to the inlet diameters to try and maintain turbulent flow at the inlets. This study focuses primarily on the results of Phase B. with additional comments and analysis into Phase A being available in the study of Strack (2019).

The uncertainties quoted below are derived using the ISA 67.04 procedure and account for instrument, transmitter, power supply, and

data acquisition uncertainties. Temperature measurements were made using traversable T-type thermocouples accurate to 0.5 °C which were positioned either above/beside a tube element or in-between tubes. The thermocouples would be left in this position for a measurement window of 300 s to obtain time-averaged and standard deviations of the measured temperature. The heat balance for these tests was measured using a flowmeter accurate to with 0.5% on the inlet line in addition to calibrated T-type thermocouples on the inlet and outlet of the test section. The heat balance was found to always be within 2% over any given experiment. The heat balance was closely monitored during the 300 s measurement window and if it was ever found to be 5% or greater, the 300 s window of data was deleted and taken again when the heat balance fell below 5%. These measurements were made for a wide range of power and flow combinations representing conditions for a wide range of  $Ar$ .

Flow in these experiments each inlet was controlled using Alicat LCR flow controllers (AFC). The devices were accurate to within 2% of their full-scale flow reading (5 LPM) and were used in conjunction with more accurate Coriolis flowmeter (0.5%) on the inlet line to ensure that the total flow was within 1% of the desired value for the experiment (note the reported total flow rate is in grams per second). For the Phase A experiments, six of flow controllers were used while eight were used for the Phase B experiments. The total DC current to the heaters was measured using a calibrated shunt resistor accurate to within 0.1%, with the measured electrical power found from the product of the heater voltage and current. The test section heat balance was always within 2% of the measured electrical power.

The heat generated by the test sections was rejected using a heat exchanger attached to a chilled-water supply line shared by the building housing the facility. As a result, the inlet temperature varied slightly from day to day for the same test conditions depending on the temperature of the chilled-water supply line. Several repeatability measurements were taken and found to be within 3%.

### 2.1. Phase A

The Phase A test section consisted of 120 rods and 22 downward facing inlet J-nozzles entering the top of the vessel as shown in Fig. 2. The inner 52 rods were heated, with the remaining 68 outer tubes being unheated acetal rods. The heater rods had a cosine non-uniform power profile and were powered uniformly (all 52 heated rods had the same power). A pipe was added to the top of the vessel to allow for optical access for PIV measurements. However, it was found that temperature gradients in the tank lead to large optical distortions and did not allow for this technique to be employed and thus no PIV velocity measurements are presented. Limited velocity measurements within the tube bank regions were made using Laser Doppler velocimetry (LDV), which

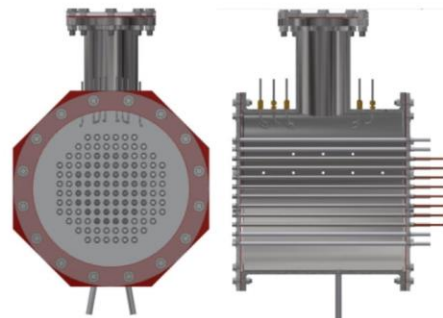


Fig. 2. Phase A Test section front and side views.

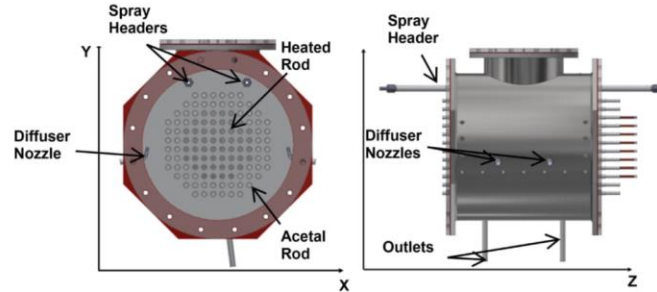


Fig. 3. The Phase B geometry front (left) and side (right) views.

are presented in Strack (2019).

### 2.2. Phase B

The Phase B test section which is visualized in Fig. 3 reuses the same rod elements and rod placement as the Phase A tests, but contains different inlet flow configurations. These include two spray headers located in the top section of the vessel and four fan-shaped diffuser nozzles located near the mid-plane of the vessel pointed upward. The total flow of the facility was divided such that 70% of the total flow would be delivered equally from the four diffuser nozzles, with the remaining 30% coming from the two spray headers (each header fed from both sides). A total of eight flow controllers were used; flow from each individual diffuser nozzle was controlled by a single flow controller while flow from each spray header was controlled by a flow controller at each end. Flow exited the vessel through two drains at the base of the vessel at a 7° angle from the vertical, giving front-to-back symmetry. Note that the heaters were reused from the Phase A tests in the same positions. The laser access port in the Phase B test section was designed to be much larger than Phase A, allowing for additional thermocouple penetrations from the top of the vessel. This facilitated additional temperature measurements in the top region of the vessel.

Two nozzle designs were used for this facility to assess the impact of the inlet condition on the temperature field measured inside the tank. These two nozzle types are termed 'large' and 'small', with the 'large' nozzles referring to a 1/10th scaling (each dimension 1/10th of the full-scale value) and the 'small' nozzles referring to a 1/16th scaling of the real-size facility. The use of both 'large' and 'small' nozzles was chosen to allow for CFD model validation across a wider range of flow patterns and also to experimentally investigate the impact of small changes in inlet configuration. Relevant dimensions of the facility can be found in Table 1 to be used in conjunction with Fig. 4.

### 2.3. Scaling distortions

In both Phase A and Phase B, the primary scaling distortion that was introduced involved the reduction of the total number of calandria tubes present in the vessel (from 390 total in full-scale CANDU to 120 in the two experimental facilities employed in the present study). In addition, only the central 52 rods were heated electrically which attempted to mimic the radial power distribution in a real moderator system where power levels on the periphery of the core are at much lower power than the central region. As a consequence of the direct electrical heating and a reduced number of calandria tubes it was recognized that local buoyancy forces may be higher in the experiments as opposed to the actual reactors. Other distortions include: a) no internal reactivity control devices or guide tubes were included, b) to allow for optical access an extension pipe was added to the top of the vessel and

c) in some cases the scaling was modified in the inlets such as to attempt to retain turbulent flow at the scaled mass flux.

#### 2.3.1. Phase A

For Phase A, the hydraulic diameter of the inlet nozzles was reduced to approximately a 1/20th linear scale. This intentional deviation from

Table 1  
Displays relevant geometric information for the Phase B test Experiment.

Component	Comment	Value	
Vessel/Tank	Inner Diameter of vessel [mm]	489.4	
	Outer Diameter of vessel [mm]	498.6	
	Tube-bank pitch [mm]	29.1 ± 0.1	
	Rod Element outer diameter [mm]	13.6 ± 0.02	
	Length of Vessel [mm]	505 ± 1	
	Drain Port Angle [degrees]	7	
	Drain Port Length [mm]	152.4	
	Spacing Between Nozzles [mm]	194.4 ± 0.9	
	Distance from Drain to Drain [mm]	283.2 ± 0.2	
	Inner Diameter of Laser Access Port [mm]	15.7	
	Height of Laser Access Port from Vessel OD [mm]	244.4	
	Height of Laser Access Port from Vessel OD [mm]	75.8	
Spray Headers	Spray Header to Spray Header Distance [mm]	187.8	
	Spray Header Height from centre [mm]	201.4	
	Inner Diameter of Ports [mm]	1.59	
	Pitch of Banks of Holes [mm]	63.9	
	Angle for holes off of centre [degrees]	45	
	Inner Diameter of Spray Header [mm]	13.87	
Small Diffuser Nozzle	Entry Length to First bank of Holes [mm]	185.5	
	ID	Inner Diameter of Nozzle [mm]	11.1 ± 0.04
	OD	Outer Diameter of Nozzle [mm]	19.0 ± 0.01
	L <sub>1</sub>	Entry Length to Divider Wall [mm]	90.8
	L <sub>2</sub>	Length of transition [in]	9.65
	L <sub>3</sub>	Length of Diffuser section from transition [mm]	25.6
	L <sub>4</sub>	Length of Diffuser section from tube [mm]	25.6
	L <sub>5</sub>	Nozzle face height [mm]	7.08
	H <sub>1</sub>	Height of Nozzle Flow area [mm]	5.23 ± 0.04
	H <sub>2</sub>	Height of Nozzle Flow area [mm]	5.23 ± 0.04
W <sub>1</sub>	Width of Nozzle Flow area [mm]	9.82 ± 0.08	
W <sub>2</sub>	Width of Nozzle Flow area [mm]	8.80 ± 0.1	
t <sub>p</sub>	Thickness of Nozzle Walls on outlet face [mm]	1.10 ± 0.02	
θ <sub>n</sub>	Bend Angle of Nozzle [degrees]	147.639	
θ <sub>1</sub>	Angle of 2nd and 3rd Nozzle Slots [degrees]	24.572	
θ <sub>2</sub>	Angle of 1st and 4th Nozzle Slots [degrees]	24.857	
t <sub>w</sub>	Thickness of Dividing Wall [mm]	1.00	

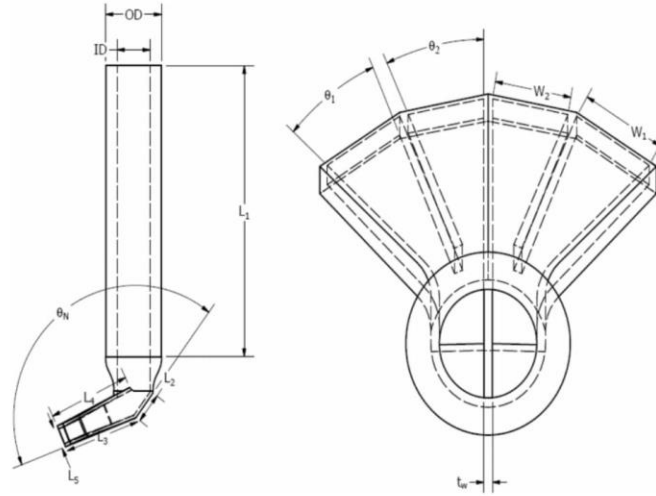


Fig. 4. Displays labels of relevant design parameters for the small diffuser nozzles to be used with Table 1.

1/16 scaling was implemented in order to ensure fully turbulent inlet flows under the scaled mass flow rates selected for these tests.

### 2.3.2. Phase B

For some CANDUs, approximately 1/3 of the moderator flow enters the calandria tube from many sprays at the top of the vessel while 2/3 of the flow enters from fan-shaped diffusers located on the curved sidewalls of the vessel. Similarly, for Phase B, some distortions to the inlet geometry were made. The full-scale reactor configuration includes 12 inlet fan-shaped inlet diffusers (6 on each side) that are directed

upwards. Furthermore, in the operating reactor the 12 nozzles are divided into 3 sizes. Using 12 inlets in the scaled facilities would require very small nozzles and in such case manufacturing tolerances would cause a very high uncertainty in the flow area. Instead, the 12 inlets were replaced by 4 equally sized inlets (2 on each side) such that the nozzle dimensions are more easily fabricated and where the manufacturing tolerances would not be significant. Since these deviations may lead to changes in flow topology, inlet diffusers constructed at both 1/16th and 1/10th scale were investigated. The moderator spray inlets at the top of the vessel were replaced by 2 headers with 21 small spray

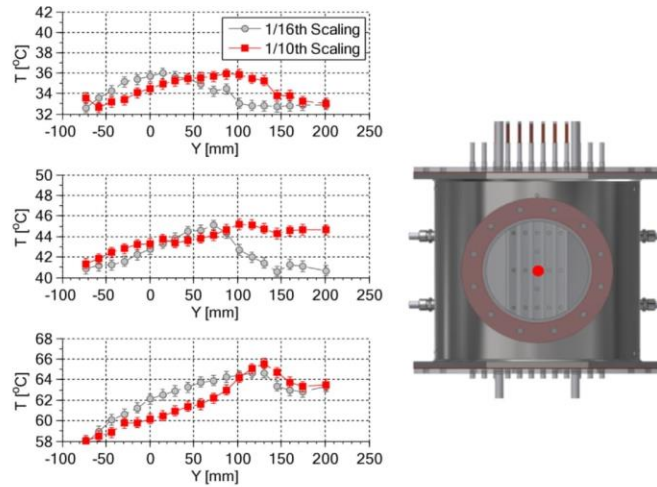


Fig. 5. Comparison of thermal measurements between inlet diffuser nozzle size with a mass flow rate of 500 g/s and 10 kW (top), 20 kW (middle) and 38 kW (bottom).

holes in each header. Flow was fed from both sides of each headers to minimize the flow changes amongst the 21 sprays. They were placed in tank in the top region of the vessel as shown in Fig. 3.

### 3. Experimental results

A detailed analysis of the Phase A experimental results can be found in Strack (2019). This paper will focus solely on Phase B.

In addition to the reported temperatures, the temperature measurement results are also normalized to the test section  $\Delta T$  as shown in Eq. (2). Note that the overbars in Eq. (2) refer to time averages of a given temperature measurement. This value is termed the excess temperature as it is a fraction of the integral water temperature rise across the test section. This normalization is useful for examining data which were obtained on different test days where the inlet temperatures are marginally different. As a result, results compared at the same experimental conditions have been modified by taking the inlet temperature difference and adding that value to the results from the appropriate data set. This allows for a fair comparison without introducing the extra error that would be associated with  $T_{excess}$ . No extra error is introduced as this difference was 2 °C or less and any differences in the specific heat of water over this range are considered to be negligible.

$$T_{excess} = 100 \times \frac{\bar{T} - \bar{T}_{in}}{\bar{T}_{out} - \bar{T}_{in}} \quad (2)$$

#### 3.1. Impact of inlet nozzle size

A comparison of the vertical temperature profiles measured at the centre of the vessel for each nozzle size is presented in Fig. 5 for the power levels of 10, 20 and 38 kW. A key feature observed in historical work was the interaction of the opposing jets from either side of the vessel which form a secondary downward jet. At 10 kW, the higher temperatures measured at the top of the vessel in the 1/10th case suggest that the secondary jet formed at the top of the vessel but did not penetrate as far into the tube bank region in comparison to 1/16th nozzles. At the highest power conditions (38 kW), the similarity between the measured temperature fields in the upper regions of the vessel for both nozzle sizes suggested that buoyancy effects precluded the formation of this secondary jet.

#### 3.2. Archimedes number comparison

Several experiments were performed by varying the power and flow combinations whilst maintaining  $Ar$ . Fig. 6 left presents all temperature data obtained for 5 kW, 275 g/s and 20 kW, 500 g/s - these conditions both correspond to  $Ar = 0.017$ . This figure shows that 87.6% of the

total points lie within the 20% error bars. While the agreement in the temperature field is good, it is also shown that the low flow, low power case systematically resulted in higher non-dimensional temperatures for the same  $Ar$ . Three thermocouple positions were chosen to determine the nature of this difference as shown Fig. 7. The results in Fig. 7 clearly indicate that the low flow, low power condition results in higher excess temperatures in the top region of the vessel, with close agreement in the lower sections. The higher excess temperatures in the top region of the vessel for the low flow low power case are thought to be a result of the reduction in the mass flow rate and the associated drop in inlet momentum. This is thought to prevent the formation of the secondary downward jet which was observed in an isothermal CFD simulation. However, even considering the change in flow topology at the same  $Ar$  number, nearly 90% of the data still falls within 20% for tests with a 50% reduction in flow rate and 400% reduction in heater power. This indicates that the  $Ar$  does provide some level of scaling, at least for cases where geometry is fixed and only test conditions are altered. Fig. 6 (right) shows the comparison for this low-flow low power case compared to a near double  $Ar$  of 0.036. Surprisingly, this comparison is much more favorable, with 97.7% of all data lying within the 20% error bars. This improvement is thought to have been a result of the effect of the increased buoyancy on the overall flow topology, in particular the effect it had on the secondary jet. For an  $Ar$  of 0.036 the buoyancy in the vessel is strong enough to prevent a secondary jet formation at the top of the vessel. As a result the flow pattern would appear more similar to that of the low-flow low power case as evidenced by the temperature profiles in Fig. 7. This was also evident in similar comparisons to this low-flow low power case with the 1/10th scale nozzles. This suggests that maintaining  $Ar$  is not sufficient to ensure accurate non-dimensional behaviour in scaling cases. The secondary jet behaviour must be examined and well-understood in order to obtain the best level of agreement.

### 4. Numerical study

A numerical study was performed using the realizable  $k-\epsilon$  turbulence model with the all  $y+$  wall treatment model in FLUENT. This was done for two distinct reasons. First it was to determine the performance of CFD codes at predicting temperatures for geometries similar to a CANDU reactor. The second study was to examine the impact of scaling distortions present in the 1/16th scale facility that are not present in the full-scale facility. These distortions included the use of surface heating (as opposed to volumetric heating in the full-scale reactor), a reduction in the number of tube bank elements from 390 to 120, changes in nozzle scaling, and the addition of the instrumentation access volumes at the top of the vessel.

The model used to simulate the Phase B experiments can be seen

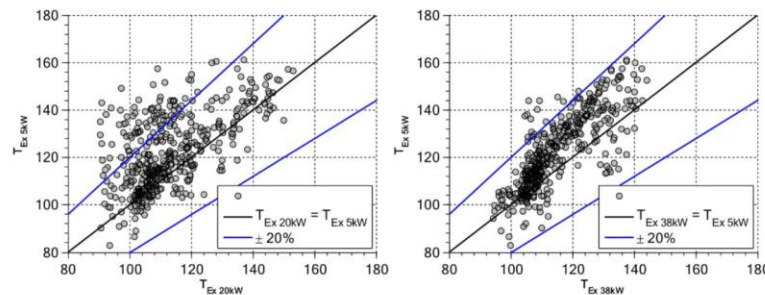


Fig. 6. Excess Temperature comparison for the 5 kW 275 g/s test condition to the 20 kW 500 g/s left ( $Ar = 0.017$  for both) and to the 38 kW 500 g/s ( $Ar = 0.036$ ) test on right.

C.W. Hollingshead, et al.

Nuclear Engineering and Design 369 (2020) 110829

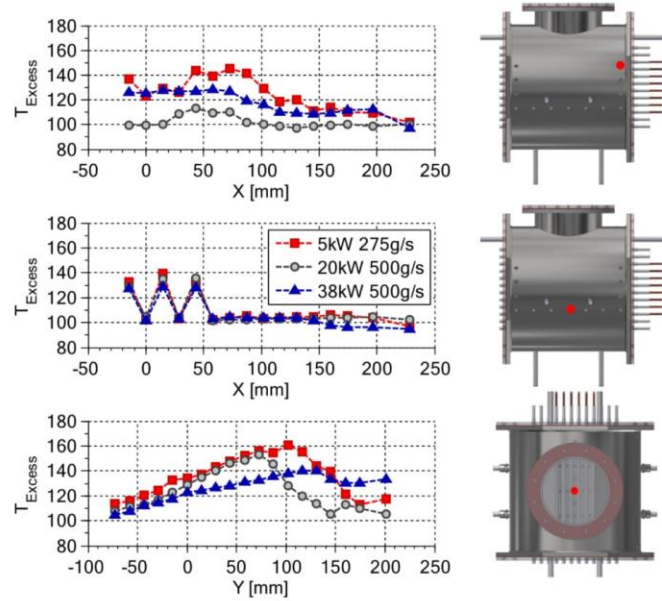


Fig. 7. Small diffuser nozzles at three positions in the tank for three power/flow combinations.

below in Fig. 8. All simulations were run using the realizable  $k-\epsilon$  turbulence model coupled with the all  $y+$  wall treatment model as done in Strack (2019). The all  $y+$  wall model was chosen as the vessel contains regions of high and very low flow. Grid independence was

established for each simulation by systematically increasing the mesh size until the simulated temperatures became invariant with grid size in a steady-state simulation. After an appropriate grid was selected the transient CFD simulations were performed for each test case.

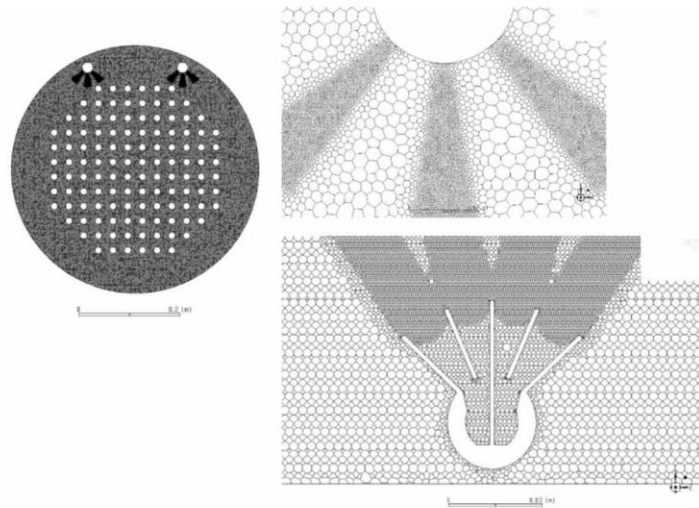


Fig. 8. Computational grid used for validation study, a) full vessel mesh (left), b) grid structure around sprays and spray header (top-right) and c) mesh near the fan-shaped diffuser.

C.W. Hollingshead, et al.

Nuclear Engineering and Design 369 (2020) 110829

4.1. Effect of surface heating

While the moderator is heated volumetrically in the full-scale case, surface heating was employed in the small-scale for practical reasons. To assess the impact of the use of surface heating, simulations of the small-scale facility were performed for both volumetric and surface heating cases at the same power and flow rate. The volumetric heat generation rate was chosen to be constant in the radial direction and to follow the same cosine shape axially as the heaters used in the experiment. The heated volume was chosen to be a cylinder surrounding the inner 52 heated rods.

Fig. 9 shows a comparison of the temperature and velocity contours at the center plane ( $z = 250$  mm) for the 20 kW 500 g/s test condition. It can clearly be seen that the volumetric heat flux case results in a lower temperature at the top of the vessel than compared to the surface heating case. This results from stronger local gradients in the surface heating case at the heater surfaces, which leads to greater buoyancy forces. These stronger buoyancy forces are seen to weaken the strength of the cold downward jet. This gives higher temperatures at the top of the vessel for the surface heating case as compared to the volumetric heating case.

4.2. Effect of laser access volume

Compared to the full-scale vessel, a volume of fluid was added to the

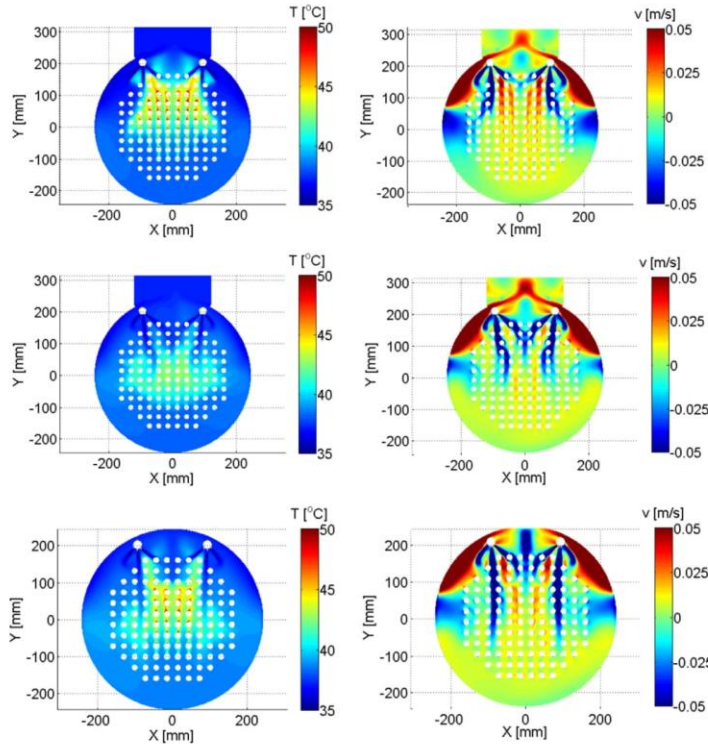


Fig. 9. Velocity and temperature contours at the axial mid-plane for a) surface heating (top), b) volumetric heating (middle) and c) surface heating without the laser access volume at the top of the vessel (bottom) for the 20 kW 500 g/s ( $Ar = 0.017$ ) test condition at the axial centre of the vessel.

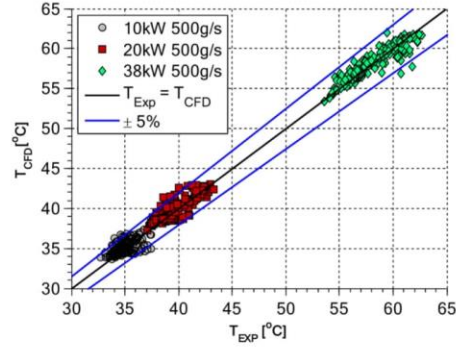


Fig. 10. Predicted versus measured temperature with a mean  $T_{CFD}/T_{EXP}$  of 0.9976 and standard deviation of 0.0186.

top of the experimental facility to allow optical access for velocity measurements. CFD models with and without this window were created to assess its impact on the flow field. Fig. 9 shows a comparison of the velocity and temperature contours at  $z = 250$  mm for the 20 kW 500 g/

s test condition. The distortion introduced by the window can be seen in Fig. 9 (bottom), and it can be seen to have resulted in a weaker downward flow in the top region of the vessel. This additional open volume of water above the tube bank allowed the inlet jets to interact and spread upward instead of being confined by the curvature of the top of the calandria vessel. This resulted in relatively weaker downward secondary jet at the top of the 1/16th scale facility compared to results that would be expected without the optical access volume.

#### 4.3. Performance of CFD model

In general, the simulations performed in FLUENT with the realizable  $k-\epsilon$  turbulence model and the all  $y+$  wall model performed very well as shown in Fig. 10, with 97.6% of all predicted temperatures falling within 5% of the experimental values. This improves to 99.0% of data only the highest-powered data are considered. The level of agreement and trend in these predictions is consistent with those found in the study of Strack (2019).

To examine the detailed behaviour in the vessel three thermocouple positions are compared against experiment in Fig. 11 for the 20 kW 500 g/s test condition. Deviations between the experimental and simulation results appear largest at the top region of the vessel where the temperature field is sensitive to the formation of the secondary jet. These differences would appear to indicate that the CFD results show a weaker secondary jet than the experiments (i.e., less cold secondary jet penetration into the tube array). To test this, the experimental results for thermocouples at the top of the vessel are compared against the corresponding simulation results at multiple power levels in Fig. 12. This shows qualitatively that as the power is increased, the agreement between the CFD model and experiment begins to improve. For the case at the maximum power buoyancy forces are so large that both the experiments and CFD show limited secondary jet penetration into the heated region. The intermediate power level experiments show that

secondary jet penetration increases with decreasing power but CFD shows higher temperatures indicating less jet penetration. This suggests that the jet dissipation from the inlet nozzles is over predicted. Finally, under the lowest power condition the simulated temperatures appear monotonic which indicates downwards flow is predicted in this plane, while the experimental trends indicate mixed convection still persists in this plane.

#### 4.4. Comparison to the full-scale facility

To determine if the small-scale facility contains flow features consistent with then full-scale reactor, additional comparisons to literature were performed. Simulations of a full-scale CANDU-6 reactor were previously performed by Sarchami (2011). The CANDU-6 geometry is similar to the design the 1/16th test section is based on with the main exception being the inlet spray headers at the top of the vessel. For a fair comparison, a simulation with the flow out of the headers was turned off was performed. Comparison of these results to simulations of the small-scale facility are presented in Fig. 13. In addition, Table 2 shows relevant experimental condition values compared to those estimated for the full-scale reactor from Sarchami (2011).

The level of agreement of predicted flow field of the present 1/16th facility to that of the real-size reactor is qualitatively very good, with poorest agreement at the top of the vessel as seen in Fig. 13. This is in large part due to the summation of scaling distortions in the 1/16th facility. The features thought to cause the differences are the outer two rows of unheated rods, the presence of the spray header tubes and the laser access window volume at the top of the vessel. The most significant effect would appear to be a result of the laser access window. As previously discussed, the presence of the laser access window does not allow the inlet jets to strongly interact in the proper way in the upper regions of the vessel above the tube bank.

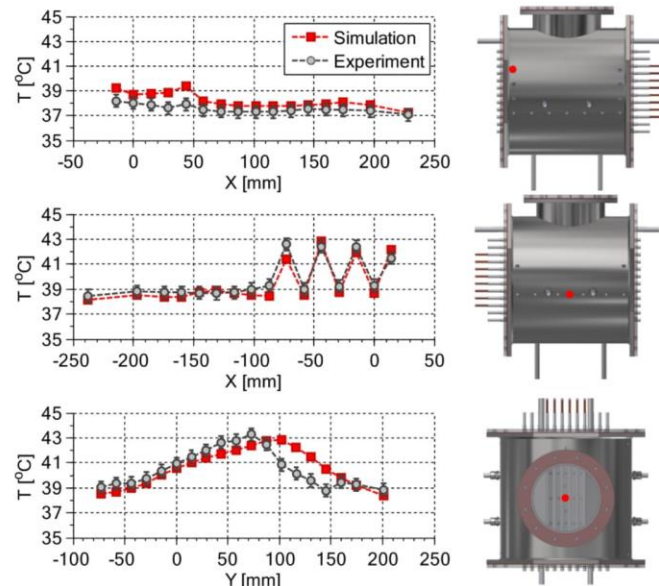


Fig. 11. Calculated and measured temperature profiles. Power of 20 kW and flow of 500 g/s.

C.W. Hollingshead, et al.

Nuclear Engineering and Design 369 (2020) 110829

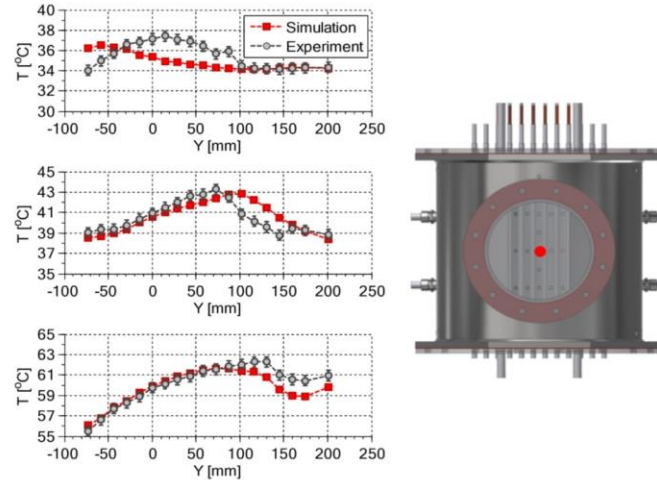


Fig. 12. Calculated and measured temperature profiles at the centre of the vessel for 10 kW (top), 20 kW (middle) and 38 kW (bottom) mass flow rate of 500 g/s.

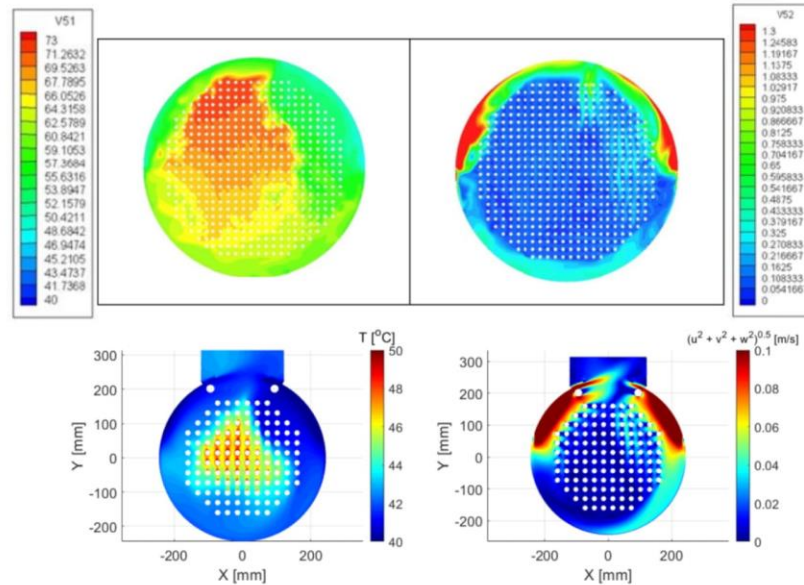


Fig. 13. Comparison of CFD full-scale (top) from Sarchami (2011) to 1/16th Phase B (bottom) facility: temperature (left) and velocity field (right) for an Ar of 0.017.

### 5. Modifications to the Ar

As previously noted, the  $Ar$  defined in Eq. (1) is very similar to the Richardson number ( $Ri$ ) and can in some ways be thought of as a “global”  $Ri$  as the length, temperature and velocity scales are taken as the vessel diameter, temperature change over the entire vessel and the inlet velocity. Some ambiguity over the velocity scale may exist,

however traditionally the CANDU industry has relied on the  $Ar$  to assess moderator buoyancy effects. In this study the average inlet velocity was chosen to be consistent with the studies of Khartabil et al. (2000), Carlucci et al. (2000) and Kim et al. (2006) in addition to its relative ease to measure/estimate. Another potential option for this velocity scale would be to use the magnitude of the secondary jet of cold liquid at the top of the vessel, however this can be very difficult to determine.

**Table 2**  
Displays relevant experiment parameters for the 1/16th scale facility compared to the full scale.

Geometry	Mass Flow Rate [kg/s]	Average Nozzle Velocity [m/s]	Total Power [kW]	Volume to Mass Flow Rate [m <sup>3</sup> /kg/s]	Volume to Power [m <sup>3</sup> /kW]
PhaseB Small Nozzle	0.5	0.902	10	0.206	0.0206
	0.5	0.902	20	0.206	0.0103
	0.5	0.902	38	0.206	0.0054
	0.4	0.721	20	0.257	0.0128
	0.275	0.496	5	0.374	0.0748
Phase B Large Nozzle	0.5	0.573	10	0.206	0.0206
	0.5	0.573	20	0.206	0.0103
	0.5	0.573	38	0.206	0.0054
Estimated Full Scale (from (Sarchami, 2011))	948	N/A	129,000	0.318	0.0020

Khartabil et al. (2000) suggested the use of the inlet velocity was justified so long as the inlet velocity remained high enough to ensure turbulence. Kim et al. (2006) took this one step further developing a flow regime map based on the inlet  $Re$  and the  $Ar$ , also based on the inlet velocity which was shown to agree well with experiment. This choice is also consistent with the study of Atkins et al. (2017) that showed experimentally that the heat transfer of the central column of a similar configuration depends strongly on the inlet  $Re$  or velocity.

The choice of inlet velocity for the  $Ar$  is also thought to be a reasonable estimate of the global convective effect for these geometries as the strength of the downward flow of cold water (or lack thereof) will depend on the inlet velocity and is relatively easy to measure/estimate given mass flow rate or inlet  $Re$  information compared to the secondary jet. This can be seen if we examine the case of decreasing the inlet velocity. The reduction in inlet velocity would also result in a weakening of the secondary jet, and depending on the level of reduction completely preclude its formation. This would lead to flow field to have more upward flow in the top central region of the vessel, appearing more buoyant in nature, which would be consistent with an increase in the  $Ar$  based on the change in inlet velocity.

### 5.1. Buoyancy effects

While  $Ar$  has been shown in section 4.2 to be useful in maintaining a non-dimensional temperature profile within a fixed geometry, scale reductions such as a 1/16th reduction often require modifications to the geometry. For example, in the 1/16th facility only 52 surface heaters were present when in the full-scale, the heat is added via a heated volume of around 390 fuel channels because fabrication of 390 calandria tube heaters at 1/16 scale (i.e., less than 1 mm diameter) was unfeasible. This distortion leads to a higher heat flux on each of the 52 rods as compared to case where 390 rods are heated. Thus, the local water temperature near each heater, and hence buoyancy force, will be greater in the 52 heater experiment than that which would occur in a 390 heater case. The increase in the buoyant force will therefore distort the scaling based on  $Ar$  somewhat, with a general trend of reducing the  $Ar$  number in the 52 heater experiment providing more similarity to the full scale/geometry case.

To account for these effects additional scaling based on imposed heat flux, an  $H$  factor, is proposed. This factor is intended to account for the effect of increased surface heat flux due to the reduced total number of heated tubes. This is to recognize that by heating fewer tubes with the same overall power that the buoyancy forces will be stronger, but

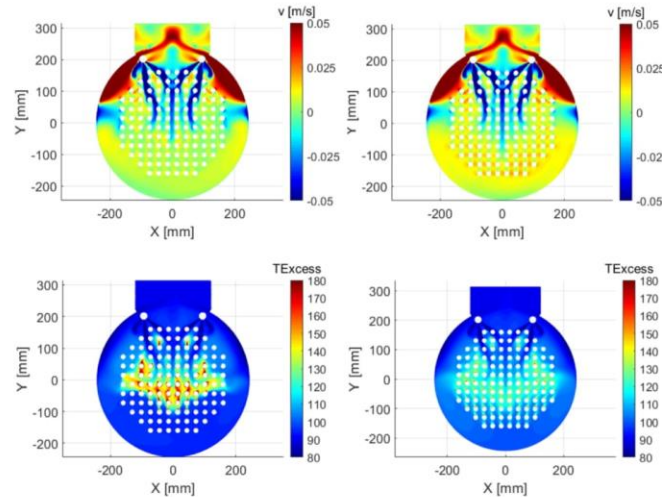


Fig. 14. Velocity and  $T_{Excess}$  contours at the center of the vessel for the standard test geometry (left) for  $Ar = 0.0074$  (500 g/s 11.24 kW) and a modified geometry to have all 120 rod elements heated (right) for  $Ar = 0.017$  (500 g/s 20 kW) with  $ArH$  maintained.

the global  $Ar$  would remain the same. Scaling the  $Ar$  in the current test facility by this factor results in an increase by approximately a factor of 8, all other parameters being equal. Thus, in comparing the results of the experiment to full scale one should look at experiments where the uncorrected  $Ar$  is about 1/8 of the full-scale system. It must be noted that this does not taken into account the inherent difference in buoyancy strength observed between surface and volume heating discussed previously.

To test the  $H$  factor two simulations were performed, one on the standard test geometry and one with all unheated rods converted into heaters with the power spread uniformly amongst all 120 rods. The 120-heater simulation was performed at an  $Ar = 0.017$  which corresponded to a mass flow rate of 500 g/s and a power of 20 kW. Then using the  $H$ -factor  $ArH$  was calculated and the power for the standard test geometry was lowered until  $ArH$  for both cases matched, this corresponded to a total power of 11.24 kW for the central 52 heaters at a mass flow of 500 g/s. The normalized temperature and velocity contours at the centre of the vessel for these simulations can be seen below in Fig. 14. This clearly shows that the  $H$ -factor helps to ensure similar flow features by accounting for the distribution of power in the test section. This is also evidenced by comparing Fig. 14 (right) to Fig. 9 (top) which occur at the same  $Ar$  and the same test conditions and vary only by heater arrangement. This indicates that flow field and temperature field similarity is obtained better using this  $H$  factor. This is a result of the full-strength of buoyancy being accounted for as it normally is not in the standard  $Ar$  definition based on global parameters.

$$Ar_{Mod} = ArH \quad (3)$$

$$H = \frac{q_{exp}^{\prime\prime}}{q_{predict}^{\prime\prime}} \quad (4)$$

$$\frac{q_{exp}^{\prime\prime}}{q_{predict}^{\prime\prime}} = \frac{A_{predict}}{A_{exp}} = \frac{\pi DLN_{predict}}{\pi DLN_{exp}} = \frac{390}{52} \quad (5)$$

### 5.2. Secondary flow effects

As previously stated, the full-scale reactor case has a characteristic secondary jet in the top region of the vessel, while the formation of such a secondary flow is dependent on the conditions of each experiment. In Fig. 6, it was shown that just matching  $Ar$  does not guarantee similarity of secondary jet flow, even for the same test geometry. A single “catch-all” factor to account for secondary flow behaviour and its differences between cases is very difficult to develop. This is largely because it is either is or is not present, depending on parameters such as inlet  $Re$ , tube spacing, and local heat fluxes. For scaling geometries with different configurations and flow phenomenon, it is suggested that the best way to ensure proper flow behaviour for all test cases would be an a priori CFD examination of a potential test-section to ensure similarity. This concept of “CFD-informed scaling” would determine some level of the effectiveness of the scaling used and identify potential flaws before manufacturing the experiment. Validation of those CFD results would still need to be performed.

#### 5.2.1. Fan-nozzle spacing

For this type of nozzle geometry, a significant amount of the flow out of the nozzle can interact with flow from an adjacent nozzle. Given that these nozzles are pointed towards the top of the vessel, this interaction will increase the strength or possibility of a secondary jet. For the 1/16th test section, if the spacing were reduced this interaction would have been stronger and have resulted in a stronger secondary jet and a more favorable comparison to the full-scale reactor.

#### 5.2.2. Fan-nozzle sizing/flow area

The physical size of the inlet fan-nozzle can drastically impact the

secondary jet as evidenced by Fig. 5. As a result, it may be advantageous in some cases to reduce the size of the inlet geometry to obtain stronger inlet jets. The effect of stronger inlet jets would be to increase the velocity of the potential core of the jets, thereby increasing its distance of travel. This would increase the chance of developing the proper secondary jet and potentially improve overall similarity to the full-scale even if it is no longer is a perfect linear scale model.

#### 5.2.3. Inlet momentum

For every test section, there is a finite amount of momentum required for a jet to reach the top of the vessel, if this amount is not supplied, a secondary jet will not develop as evidenced by the low-flow low-power test condition in this study. In scaling a test section, the size may be linearly scaled (by a factor of 1/16 in this case) but the inlet momentum may not. This is partially due to the ambiguity in the choice of power and flow that maintaining  $Ar$  allows. This can also be evidenced by the kinetic energy of the inlet jet. As such, care must be taken in choosing the inlet flow rates of these jets to avoid the situation of improper jet behaviour even under isothermal test conditions.

## 6. Conclusion

In comparing the results of the CFD model to experiment, it was shown that the simulations can predict the temperature field within an accuracy of 5% for 97.6% of all points and is visualized in Fig. 10. The qualitative agreement of the model to experiment can also be seen in Figs. 11 and 12 and is noted to improve with higher powers which is consistent with Strack (2019). This is thought to be a result of the turbulence model overpredicting the dissipation of the jet, which would lead to higher CFD-predicted temperatures at the top of the vessel as compared to the measured quantities.

The distortions of the current experimental facilities were also examined. It was shown that the introduction of the laser access port at the top of the vessel partially reduced the strength of the secondary jet in Fig. 9. This was a result of this additional volume at the top of the vessel allowing the jet to travel further upward and diffuse over a larger area. Additionally, it was shown that the scaling distortion of using surface heat sources instead of the more realistic volumetric heat source also resulted in a further reduction in the secondary jet. Due to this and the unheated rows and spray headers, the flow pattern in the top region of the 1/16th scale facility differed from the full-scale reactor, but remains similar in most locations in the vessel.

It was also proposed that  $Ar$  should contain a correction factor for experiments where perfect geometrical similarity cannot be maintained. This factor was proposed to be the ratio of the experimental heat flux to that for a case with perfect geometrical similarity and shown to perform well in CFD simulations. This factor was deemed necessary for this facility to account for the increase in buoyancy forces that resulted from reducing the total heated area and thereby increasing the local temperature gradients around heated tubes. In comparing this modified  $Ar$  number to the  $Ar$  number of the full-scale reactor, it was seen that the same flow phenomena do exist, despite the additional scaling distortions of the facility altered the secondary jet strength.

### CRediT authorship contribution statement

**C.W. Hollingshead:** Validation, Software, Formal analysis, Data curation, Writing - original draft, Writing - review & editing, Visualization, Project administration. **A. Rashkovan:** Software, Methodology, Resources, Writing - review & editing. **J.M.V. Strack:** Conceptualization, Methodology, Writing - review & editing, Project administration. **D.R. Novog:** Conceptualization, Methodology, Resources, Writing - review & editing, Supervision, Project administration, Funding acquisition.

C.W. Hollingshead, et al.

Nuclear Engineering and Design 369 (2020) 110829

#### Declaration of Competing Interest

The authors declare that they have no known competing financial interests or personal relationships that could have appeared to influence the work reported in this paper.

#### Acknowledgements

The funding for this research was provided by CANDU Owners Group and the Natural Science and Engineering Research Council under the Collaborative Research and Development (CRD) Program.

#### References

- Atkins, M., Rossouw, D., Boer, M., Kim, T., Rhee, B.W., Kim, H.T., 2017. Mixed Convection around calandria tubes in a 1/4 scale CANDU-6 moderator circulation tank. *Nucl. Eng. Des.* 316, 151–162.
- Carlucci, L., Agronati, V., Waddington, G., Khartabil H., Zhang, J., 2000. Validation of the MODTURC-CLAS Moderator Circulation Code for CANDU 9 Steady-State and Transient Conditions. In: Canadian Nuclear Society 21st Nuclear Simulation Symposium, Ottawa, Ontario, Canada, September 24–26.
- Huget, R., Szymanski, J., Midvidy, W., 1989. Status of Physical and Numerical Modelling of CANDU Moderator Circulation. In: CNS 10th Annual Conference, Ottawa, Ontario, Canada, June 4–7.
- Khartabil, H.F., Inch, W., Szymanski, J., Novog, D., Tavasoli, V., Mackinnon, J., 2000. Three-Dimensional Moderator Circulation Experimental Program for Validation of CFD Code MODTURC-CLAS. In: Canadian Nuclear Society 21st Nuclear Simulation Symposium, Ottawa, Ontario, Canada, September 24–26.
- Kim, H., Rhee, B.W., Im, S., Sung, H.J., Atkins, M., Rossouw, D., Kim, T., 2017. The iso-thermal-fluidic field of a secondary moderator jet in a 1/4 scale CANDU-6 reactor model. *Nucl. Eng. Des.* 323, 394–406.
- Kim, M., Yu, S., Kim, Y., 2006. Analyses on fluid flow and heat transfer inside Calandria vessel of CANDU-6 using CFD. *Nucl. Eng. Des.* 236, 1155–1164.
- Nitheendandan, T., Tiede, R., Sanderson, D.B., Fong, R., Coleman, C., 1998. Enhancing the Moderator Effectiveness as a Heat Sink During Loss-Of-Coolant Accidents in CANDU-PHW Reactors Using Glass-Peened Surfaces. [Online]. Available: [https://inis.iaea.org/collection/NCLCollectionStore/\\_Public/31/031/31031654.pdf](https://inis.iaea.org/collection/NCLCollectionStore/_Public/31/031/31031654.pdf).
- Rhee, B.W., Kim, H.T., Park, S.K., Cha, J.E., Choi, H.-L., 2013. A Scaling Analysis of a CANDU-6 Moderator Tank Scaled-Down Test Facility. In: Proceedings of the 2013 21st International Conference on Nuclear Engineering, Chengdu, China, July 29–August 2.
- Sarchami, A., 2011. Investigation of Thermal Hydraulics of a Nuclear Reactor Moderator (PhD Thesis), University of Toronto, Toronto.
- Sion, N., 1983. In-core moderator temperature measurements within CANDU reactors. *Nucl. Instrum. Methods* 206, 527–536.
- Strack, J., 2019. A Study of the Thermal-Hydraulic Behaviour of the Bruce A CANDU Moderator Using a Small-Scale Model (PhD Thesis), McMaster University, Hamilton.
- Yoon, C., Rhee, B.W., Min, B., 2002. Validation of a CFD Analysis Model for Predicting CANDU-6 Moderator Temperature against SPEL Experiments. In: 10th International Conference on Nuclear Engineering, Arlington, Virginia, USA, April 14–18.

## 6 CONCLUSIONS

*“We are here to laugh at the odds and live our lives so well that Death will tremble to take us”*

**Charles Bukowski**

The combined efforts of this thesis expand the understanding of mixed convection and buoyant induced flows. Specific conclusions for each study are found in each paper, this section will rather focus on the greater impact of the combined works.

A primary contribution of these works is the ability to determine the “global” flow pattern in a CANDU-moderator type geometry via CFD and the associated experimental validation in section 5. This can be coupled with the “local” heat transfer and flow topology information from sections 3 and 4 which measure the specific interactions between buoyancy and forced convection in the near-field around each tube. The combination of this information allows for a deeper understanding of how the local conditions around calandria tubes are formed based on macroscopic calandria-wide behaviour, and the impact on heat transfer, flow topology and local condition predictions for fuel channel integrity calculations.

Additionally, the corrections and models presented provide a basis from assessing the applicability of experimental results to actual in-core predictions or to design a test campaign involving mixed convection phenomena. For example, to assess the applicability of previous experiments to a given mixed convection design and/or to assess scaling behaviour, one would utilize the traditional macroscopic scaling assessed in section 5 based on important non-dimensional parameters, but to ensure similarity of local behaviour one would want to ensure coverage of the same flow topologies (and transitions) as discussed in section 3. Given the success of CFD

validation in all three papers, potential use of URANS based CFD models of the full core could be used to ensure both the macro and local flow features are represented in a given experiment.

A consistent finding amongst all of the studies conducted was an apparent small over-estimation of buoyant effects in CFD simulations relative to experiment which may have resulted from either larger buoyancy forces, or an underprediction of turbulent dissipation which would act to reduce the buoyant plume features. While in general CFD did quite well in all aspects of the studies, it is important to reflect on the causes of the systematic behaviour in the simulations. This was found irrespective of modelling approach (RANS vs LES) and was consistent with prior literature where available. While this result seemed to be partially due to over-stated jet spreading in the RANS simulations, this is not believed to be the case for the LES simulations (since LES models do not involve the same approximations used in RANS that lead to jet spreading issues). Given that the over-prediction of buoyancy appeared to only worsen with increasing power, it appears to be caused by the Boussinesq approximation itself, and/or in the case of LES the applied sub-grid scale modelling. In spite of this, the predictive ability of these models was found to be quite strong for local velocity and temperatures. However, the systematic trend of over-stated buoyant effects must be considered when examining the simulations presented in this thesis, and future simulations.

A key finding during the process of these works was the importance of CFD simulations as a design tool for experiments. This was initially done to assess the impact of design decisions on the flow topology of the 1/16<sup>th</sup> scale facility post-experiment. While pre-test simulations were performed a combination of approximations in the simulations (both physical and CFD turbulence modelling based) made the outputs and test specification non-ideal. Specifically the role of the optical access ports in the flow topology at the macro-scope level was not observed, the impact of density gradients on the laser velocity measurements was not realized ahead of time, and thermocouple locations were not always optimal. In other areas of the work pre-test simulations proved extremely valuable such as in the design of the diffuser nozzle via CFD simulation for the local flow topology study. This study required a very flat velocity field in order to achieve the desired experimental conditions and a fine control of the  $Ri$ . CFD was also valuable in addressing comments from Journal Reviewers for issues related to tank size, uncertainty in thermal field measurements, and time dependency of the overall solutions. As such, it is highly recommended in the design phase to not only utilize CFD, but to minimize the deviations from the intended experiment to the greatest extent practical.

In summary, this work provides a look at both the macro and microscopic behaviors of mixed convection flows in a complex CANDU calandria geometry. This work also highlights the importance of local conditions to mixed convective heat transfer

and local flow topology. This leaves behind an improved understanding of these effects, which can be used to better predict local flow phenomena and conditions around calandria tubes. This information can aid in fuel channel integrity calculations for DBA and BDBA type events.

## 7 FUTURE WORK

*“When we are no longer able to change a situation – we are challenged to change ourselves”*

**Viktor Frankl**

## 7.1 Future Moderator Flow Work

### 7.1.1 Boiling Tests:

As this work sought out to improve methods to predict local conditions to assess fuel channel integrity, experiments examining the effect of such local conditions on the Departure from Nucleate Boiling (DNB) would be greatly beneficial. As described in section 9.7, DNB depends greatly on the local conditions which can either enhance or diminish DNB. An experiment designed with great care, capable of determining local temperature, velocity and void fraction would have the potential to develop a semi-mechanistic model of DNB. Early attempts at such experiments in this work failed due to the rapid temperature excursions on the test sections which damaged the experiments. This could potentially have a similar form to the model proposed in section 4 and would provide valuable data to improve fuel channel integrity calculations.

Additionally, the effect of lower heaters on the nucleate boiling phenomena of the upper heater would also provide valuable insight into the fuel channel integrity issue. Specifically, buoyant plumes carry warm fluid towards a heater which may increase nucleation, and may provide some additional convective enhancement. Preliminary studies of these phenomena showed the improvements, if any, were negligible relative to the high- $Nu$  nucleate boiling phenomena itself and the impacts of surface aging during the boiling tests. Such findings are consistent with literature

where subcooled boiling effects in forced flow dominate any contributions from the convection velocity and/or temperature of the incoming fluid, however a detailed experimental investigation to prove this is still lacking.

### 7.1.2 Simplified Experimental Studies to Confirm $ArH$

To further examine and prove the  $H$  factor modification to the  $Ar$ , an experimental campaign on a simplified moderator flow type geometry would be greatly beneficial. The geometry would need to be similar to the CANDU geometry in that a down coming jet at the top of a vessel would be required to simulate the secondary jet which is the primary indication of the type of flow regime for a given set of conditions. With an appropriately sized tube/diffuser nozzle at the top of the vessel to simulate this, the remainder of the geometry would simply be heaters in an inline tube array geometry at the standard  $P/D = 2.15$  indicative of a CANDU reactor. From there, the physical number of tubes could be modified from the simplest case of 1 tube, all the way to an array of  $7 \times 7$  heaters (based on the total number of heaters from experimental campaigns in this study), or more, number of heaters limiting. Using PIV and LIF measurements, the flow regime of these simplified geometries could be identified and using  $H$  to scale heater powers (or mass flow rate) from one set of conditions to another experimental proof of whether or not the added  $H$  factor maintains flow regime could be gathered. This would also have the added benefit of developing more relatively high fidelity validation datasets for CFD simulations,

further improving the reliability of local condition predictions for moderator flow conditions.

## 7.2 Mixed Convection Heat Transfer Studies in cylinders

### 7.2.1 Improving the transition to turbulence of a free thermal plume

The model developed for mixed convection heat transfer in this thesis was found to be sensitive to the velocity predictions. A key component of those predictions was the transition to turbulence, which begins to decrease the velocity as it begins to spread much faster. The current modelling approach for this  $Gr_{crit}$  is based on prior experimental studies in air. LES simulations of a free thermal plume in water as a function of power indicated that this current approach lacks generality and could be improved upon. To improve this, additional PIV measurements of a free thermal plume in water for a variety of powers would be greatly beneficial. Specifically, measurements that are able to capture the “far field” where this transition occurs, as the experimental measurements in this work were limited to the near field due to the limited size of the measurement window. Additional measurements in the far field would be capable of developing a correlation or mechanistic approach that takes into account heater effects, and replaces the currently used constant  $Gr_{crit}$ . This may take the form of a modification to the current criteria presented to include a power component of the cylinder to account for the observation that higher heater powers appear to cause the transition to occur closer to the cylinder surface than the current model predicts.

### 7.2.2 Extension to more complex geometries

The framework for the mixed convection model focuses solely on a tandem cylinder pair. Additional experiments on bigger columns of cylinders to expand the local condition prediction methods presented here would be greatly beneficial. This would allow the extension of the model presented to begin to represent the effect of the additional cylinders above or below and make the model more physically realistic for the CANDU case.

### 7.2.3 Additional thermal plume simulation and experiments

To identify the root cause of the apparent over-statement of buoyancy in the LES simulations of this work, additional experimentation and simulation would be greatly beneficial. More specifically, experiments and simulations of free thermal plumes around cylinders that are similar in  $Ra$  but different size scales would be of the greatest interest (i.e. 13.4mm and 35mm). This would examine what appears to be the main driving factor, length scale. Examining specially the size of thermal gradients would be useful for not only identifying this issue further, but potentially for generating improvements to the models.

### 7.2.4 Additional Validation Experiments

The mixed convection heat transfer model would be improved upon with additional validation cases. Specifically, ones that change the diameter of the heater relative to the cases already examined i.e. 13.4 and 54mm, and perhaps more importantly

examine different working fluid combinations, perhaps most importantly using air. This would help establish the generality of the model developed, as its possible that the velocity and temperature relations established to close the model may fail for other working fluids. Additionally, it may be possible that the exponent  $n$  may be correlated depending on the working fluid, given that Stafford and Egan [19] developed a similar model for air but found a value of 3 to work instead of the value of 2 for the current work. For this, further experiments with varying working fluids would be required to increase generality via this method.

### 7.3 Critical $Ri$ and heated flow around a cylinder

#### 7.3.1 Additional Experimental data

More experimental data examining the flow regimes around cylinders would be greatly beneficial. This would allow for further examination of the transition criteria proposed in this thesis experimentally, which is currently based on very limited available data. Additionally, these experiments ideally would provide more information on the effects of turbulent intensity and  $Pr$  which were explored numerically in this study. A suggestion for these experiments would be to use water at a variety of inlet temperatures, instead of 25°C as done in this work. This would allow some exploration into the effect of  $Pr$  experimentally, from ~6 to a lower and higher value. This of course would be limited by the onset of boiling, and the upper limit for inlet temperatures would need to be selected with this in mind and the ability to still achieve powers that will dampen all vortices. Additionally, further

LES studies into fictitious fluids of varying  $Pr$  would greatly enhance the understanding of the differences identified in this work and could be used to improve the developed criteria further.

### 7.3.2 Further numerical studies

One of the key contributions of this present work was the relatively strong performance of the LES model employed in predicting the velocity and temperature fields in comparison to experiment. Similar models could be used and further simulations examining the effects that were not able to be examined in this current work could be performed. This would include simulation campaigns to confirm the base pressure coefficient dependency in the transition criteria's and additionally, simulations to develop further transition criteria that potentially identifies the point whereby buoyancy is strong enough to re-form a flow topology that closely mimics a free thermal plume, which was observed experimentally. Additionally, more simulations examining the interplay of the boundary layer thicknesses and their impact on the flow regime transitions would be greatly beneficial. The hope being that work presented in this document may allow future works to narrow their focuses.

### 7.3.3 Downward flow case

Future experiments making use of a downward flow type geometry would be of great value for CANDU type geometries. This would ideally lead towards the development of another flow regime map and transition criteria. This would be

most useful in the upper sections of the CANDU geometry where a significant amount of downward flow exists in normal operation conditions. Additionally, this could be coupled with the existing upward flow map to aid in verifying flow similarity. Furthermore, this work could be coupled with additional heat transfer measurements to extend the mixed convection model further.

#### 7.3.4 Application to CANDU type Geometry

As shown in section 5, the true CANDU facility simulations showed a significant amount of tube-tube interaction with a tremendous amount of upward flow for the more buoyant conditions. Applying the flow regime mapping approach from section 3 would result in potentially different flow regimes in different elevations of the facility. This would be due to the changing  $Pr$  with elevation due to the change in bulk fluid temperature. Numerical simulations and experimental studies focusing on a column of several heaters would be greatly beneficial to examine this effect, and to modify the local condition models proposed in this work to potentially further analyze this phenomenon in these types of flow facilities.

Additionally, the use of mapping flow regimes around individual calandria tubes in full-scale simulations could be employed as a scaling verification tool. The intent would be to ensure that similar flow topologies exist for the scaled vessel as compared to the full-scale and could be visualized by plotting all of the tube elements on a flow regime map. This approach would ensure similar local flow topology between scales, or identify mismatch regions i.e. more or less buoyant

regions. This would also identify what conditions may need to be changed to ensure better agreement between scales. Early attempts at this using results from CFD simulations in section 5 indicate that the flow regimes around cylinders in the upward flow region of the experimental facility were very thermal. However, this is in part expected due to the increased heater size relative to the perfect scaled case, and the reduced number of heaters. Both of these effects contribute to higher local buoyant forces.

## 8 Bibliography

- [1] Canadian Nuclear Safety Commission, [Online]. Available: <http://nuclearsafety.gc.ca/eng/reactors/power-plants/nuclear-power-plant-safety-systems/index.cfm>. [Accessed 20 June 2022].
- [2] L.Grande, W.Peiman, S.Mikhael, B.Villamere, A.Rodriguez-Prado, L.Allison and I.Pioro, "Thermal Aspects of Using Uranium Nitride in Supercritical Water cooled Nuclear Reactors," in *ICONE18*, Xi'an, 2010.
- [3] J. Strack, "A Study of the Thermal-Hydraulic Behaviour of the Bruce A CANDU Moderator Using a Small-Scale Model (PhD Thesis)," McMaster University, Hamilton, 2019.
- [4] A.Dion, *A Model to Predict Fuel Channel Failure*, Hamilton: McMaster University, 2016.
- [5] M.M.Zdravkovich, *Flow around circular cylinders Vol 1: Fundamentals*, Oxford University Press Inc, 1997.
- [6] S.K.Singh, P.K.Panigrahi and K.Muralidhar, "Effect of buoyancy on the wakes of circular and square cylinders: a schlieren-interferometric study," *Experiments in Fluids*, vol. 43, pp. 101-123, 2007.
- [7] H.Hu and M.M.Koochesfahani, "Thermal effects on the wake of a heated circular cylinder operating in mixed convection regime," *Journal of Fluid Mechanics*, vol. 685, pp. 235-270, 2011.

- [8] A.A.Kakade, S.K.Singh and P.K.Panigrahi, "Schlieren investigation of the square cylinder wake: Joint influence of buoyancy and orientation," *Physics of Fluids*, vol. 22, 2010.
- [9] N.Michaux-Leblond and M.Belorgey, "Near-Wake Behaviour of a Heated Circular Cylinder: Viscosity-Buoyancy Duality," *Experimental and Fluid Science*, vol. 15, pp. 91-100, 1997.
- [10] V. Morgan, "The Overall Convective Heat Transfer from Smooth Circular Cylinders," *Advances in Heat Transfer*, vol. 11, pp. 199-264, 1975.
- [11] A.Zukauskas and R.Ulinskas, Heat transfer in tube banks in crossflow, 1988.
- [12] E.M.Sparrow and J.E.Niethammer, "Effect of Vertical Separation Distance and Cylinder-to-Cylinder Temperature Imbalance on Natural Convection for a pair of Horizontal Cylinders," *Journal of Heat Transfer*, vol. 103, pp. 638-644, 1981.
- [13] S.Grafsronnigen and A.Jensen, "Natural Convection heat transfer from two horizontal cylinders at high Rayleigh numbers," *International Journal of Heat and Mass Transfer*, vol. 55, pp. 5552-5564, 2012.
- [14] T.Persoons, I.M.O'Gorman, D.B.Donoghue, G.Byrnel and D.B.Murray, "Natural convection heat transfer and fluid dynamics for a pair of vertically aligned isothermal horizontal cylinders," *International Journal of Heat and Mass Transfer*, vol. 54, pp. 5163-5172, 2011.

- [15] S.Grafsronnigen, A.Jensen and B. A. P. Reif, "PIV investigation of buoyant plume from natural convection heat transfer above a horizontal heated cylinder," *International Journal of Heat and Mass Transfer*, vol. 54, pp. 4975-4987, 2011.
- [16] H. Ma and L.He, "Large Eddy simulation of natural convection heat transfer and fluid flow around a horizontal cylinder," *International Journal of Thermal Sciences*, no. 162, 2021.
- [17] S.Grafsronnigen and A.Jensen, "Large eddy simulations of a buoyant plume above a heated horizontal cylinder at intermediate Rayleigh numbers," *International Journal of Thermal Sciences*, vol. 112, pp. 104-117, 2017.
- [18] S.Grafsronnigen and A.Jensen, "Unsteady Reynolds averaged Navier-Stokes simulations of a buoyant plume above a cylinder," *Engineering and Computational Mechanics*, vol. 168, pp. 35-42, 2015.
- [19] J.Stafford and V.Egan, "Configurations for single-scale cylinder pairs in natural convection," *International Journal of Thermal Sciences*, vol. 84, pp. 62-74, 2014.
- [20] B.Gebhart, L.Pera and A.W.Schorr, "Steady Laminar Natural Convection Plumes above a Horizontal Line Heat Source," *International Journal of Heat and Mass Transfer*, vol. 13, pp. 161-171, 1970.
- [21] B.W.Rhee, H.T.Kim, S.K.Park, J.E.Cha and H-L.Choi, "A Scaling Analysis of a CANDU-6 Moderator Tank Scaled-Down Test Facility," in *Proceedings*

*of the 2013 21st International Conference on Nuclear Engineering,*  
Chengdu,China, July 29-Augst 2, 2013.

- [22] M. Atkins, D. Rossouw, M.Boer, T.Kim, B.W.Rhee and H.T.Kim, "Mixed Convection around calandria tubes in a 1/4 scale CANDU-6 moderator circulation tank," *Nuclear Engineering and Design*, vol. 316, pp. 151-162, 2017.
- [23] H. Kim, B.W.Rhee, S.Im, H.J.Sung, M. Atkins, D. Rossouq and T.Kim, "The isothermal-fluidic field of a secondary moderator jet in a 1/4 scale CANDU-6 reactor model," *Nuclear Engineering and Design*, vol. 323, pp. 394-406, 2017.
- [24] N. Sion, "In-core Moderator Temperature Measurements within CANDU Reactors," *Nuclear Instruments and Methods*, vol. 206, pp. 527-536, 1983.
- [25] H.F.Khartabil, W. Inch, J.Syzmanski, D.Novog, V.Tavasoli and J.Mackinnon, "Three-Dimensional Moderator Circulation Experimental Program for Validation of CFD Code MODTURC\_CLAS," in *Canadian Nuclear Society 21st Nuclear Simulation Symposium*, Ottawa, Ontario, Canada, September 24-26, 2000.
- [26] A. Chan and A. Shoukri, "Boiling Characteristics of Small Multitube Bundles," *Journal of Heat Transfer*, vol. 109, pp. 753-760, 1987.
- [27] J. Thibault, "Boiling Heat Transfer Around A Horizontal Cylinder and in Tube Bundles," McMaster University, Hamilton, 1978.

- [28] M.Cumo, G. Farello, J.Gasiorowski, G. Iovino and A. Naviglio, "Quality Influence on the Departure from Nucleate Boiling in Cross Flows through Bundles," *Nuclear Technology*, 1979.
- [29] Y. Fujita and S. Hidaka, "Effect of Tube Bundles on Nucleate Boiling and Critical Heat Flux," *Heat Transfer - Asian Research*, vol. 27, no. 4, 1998.
- [30] S. Yao and T.Hwang, "Critical Heat Flux on horizontal tubes in an upward crossflow of Freon-113," *Int. J Heat Mass Transfer*, 1989.
- [31] K. Leroux and M. Jensen, "Critical Heat Flux in Horizontal Tube Bundles in Vertical Crossflow of R113," *Journal of Heat Transfer*, vol. 114, pp. 179-184, 1992.
- [32] S. Dykas and M. Jensen, "Critical Heat Flux on a Tube in a Horizontal Tube Bundle," *Experimental Thermal and Fluid Science*, vol. 5, pp. 34-39, 1992.
- [33] M. Jensen and H. Tang, "Correlations for the CHF Condition in Two-Phase Crossflow Through Multitube Bundles," *Journal of Heat Transfer*, vol. 116, pp. 780-783, 1994.
- [34] P. Symolon, W. Moore and D. Wolf, *Critical Heat Flux Experiments in a Heated Rod Bundle with Upward Crossflow of Freon 114*, KAPL Atomic Power Laboratory, 1997.

## 9 Appendix

*” Finally, from so little sleeping and so much reading, his brain dried up and he went completely out of his mind”*

**Miguel de Cervantes**

## 9.1 Heat Transfer Measurements for upward flow around a cylinder

Using heater B, instrumented with 8 thermocouples, heat transfer measurements were performed at a target  $T_{\text{inf}} = 25^{\circ}\text{C} \pm 1^{\circ}\text{C}$  for a time averaging period of 5 minutes. The thermocouples<sup>1</sup> were placed in the peak heat flux region at the centre of the vessel. As the heat flux shape between heater A and B is different, a correction was applied to the total power used in the measurements using Heater A in the PIV and LIF measurements to obtain the same local heat flux at the axial centre of the heater. This gives a good approximation of the wall temperature for the uninstrumented heater used for the PIV and LIF measurements. Additionally, PIV measurements were performed using the same local heat flux to test for differences in velocity due to heat flux shape. No significant difference was observed.

The results of these measurements can be seen below in Figure 4 to Figure 9. A strong dependency on velocity is apparent. In addition, Figure 4 seems to indicate that there may exist a lower bound on the velocity, below which, no enhancements to the heat transfer are possible. Additionally, the temperature distribution was normalized to the average for a heat flux of  $25.6\text{kW}/^2$  in Figure 9 to view how the distribution changes with the flow regimes identified in section 3. This indicates that when the critical  $Ri$  is first reached, and the flow topology begins to become thermally dominated, no significant change to the temperature profile is observed. As the power is increased further past this point however, the profile begins to

---

<sup>1</sup> Note that -180 degrees corresponds to the top of the heater and 0-degrees corresponds to the bottom

transform into the “truly” thermal case when no flow is applied. This change in the profile shape may offer more information for subdividing the thermal regime.

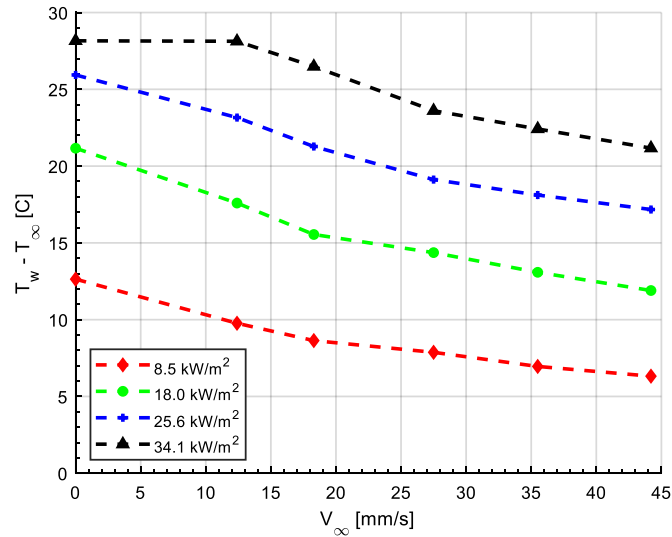


Figure 4. Circumferentially averaged Temperature differences vs Oncoming velocity

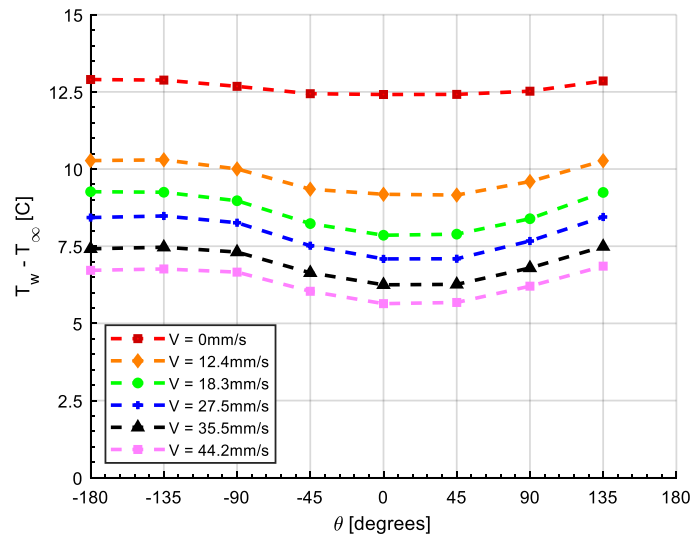


Figure 5. Circumferential Temperature Distribution for  $q'' = 8.5\text{kW/m}^2$

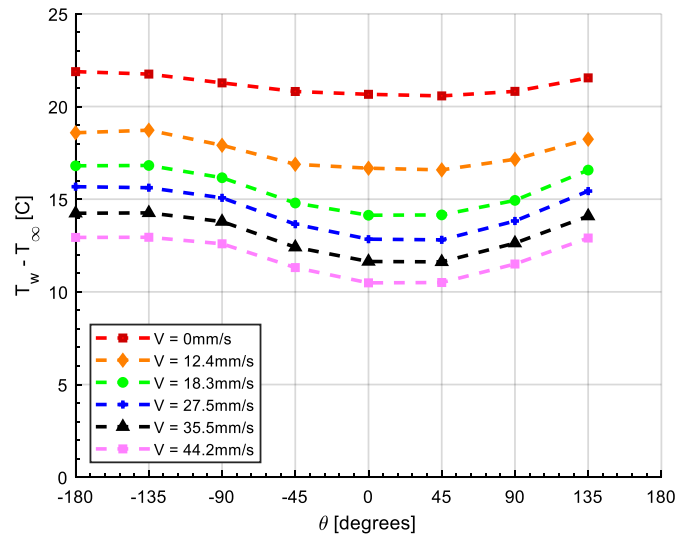


Figure 6. Circumferential Temperature Distribution for  $q'' = 18\text{kW/m}^2$

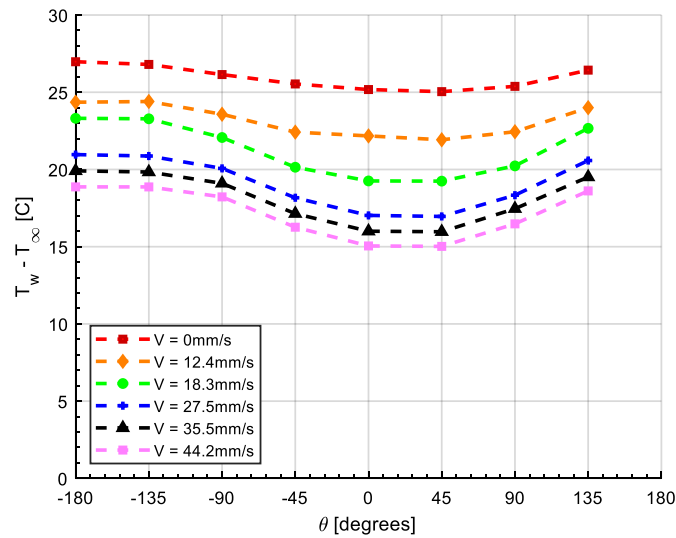


Figure 7. Circumferential Temperature Distribution for  $q'' = 25.6\text{kW/m}^2$

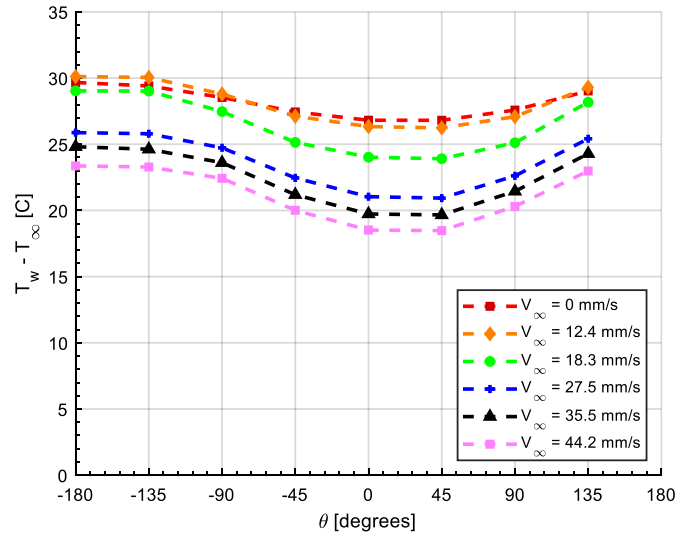


Figure 8. Circumferential Temperature Distribution for  $q'' = 34.1 \text{ kW/m}^2$

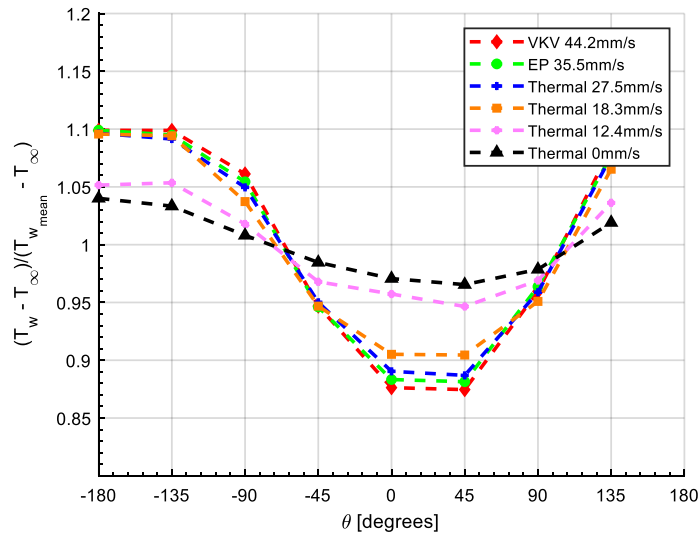


Figure 9. Circumferential Temperature distribution normalized to the average for all tested velocities at a heat flux of  $25.6 \text{ kW/m}^2$

## 9.2 Particle Image Velocimetry Standard Operating Procedure

<b>Name of SOP</b>	150W (Pulsed) Class 4 PIV Laser Operating Procedure								
Effective Date									
Author	Christopher Hollingshead								
Reason for SOP	<p>Check All that Apply:</p> <table border="0"> <tr> <td style="border: 1px solid black; text-align: center; width: 20px; height: 20px;">X</td> <td>Procedure/Process could cause critical injury.</td> </tr> <tr> <td style="border: 1px solid black; text-align: center; width: 20px; height: 20px;"></td> <td>Procedure/Process could cause occupational illness.</td> </tr> <tr> <td style="border: 1px solid black; text-align: center; width: 20px; height: 20px;"></td> <td>Procedure/Process could cause environmental impairment<sup>2</sup>.</td> </tr> <tr> <td style="border: 1px solid black; text-align: center; width: 20px; height: 20px;"></td> <td>Procedure/Process could damage University property</td> </tr> </table> <p>If none of the boxes are checked (criteria is not met) then the Committee will decline to review the SOP.</p> <p>Provide Details:</p>	X	Procedure/Process could cause critical injury.		Procedure/Process could cause occupational illness.		Procedure/Process could cause environmental impairment <sup>2</sup> .		Procedure/Process could damage University property
X	Procedure/Process could cause critical injury.								
	Procedure/Process could cause occupational illness.								
	Procedure/Process could cause environmental impairment <sup>2</sup> .								
	Procedure/Process could damage University property								
Approved by (supervisor)	David Novog								
Date reviewed by JHSC	April 11 <sup>th</sup> , 2018								
Date Last Reviewed									

### Definitions

---

2 i.e. Procedure/Process involves potentially hazardous materials.

Terms	
Acronyms	RMM – Risk Management Manual JHSC - Joint Health and Safety Committee EOHSS - Environmental and Occupational Health Support Services EPA – Environmental Protection Act OHSa – Occupational Health and Safety Act PIV- Particle Image Velocimetry

### Requirements

<b>Applicable OHSa regulations and / or codes of practice.</b>  1. RMM #101 - McMaster University Risk Management System
<b>Training and Competency</b>  1. Laser Safety Training provided by EOHSS 2. Laser Safety Lecture by Engineering Physics department 3. Onsite training by competent individuals familiar with equipment

Description of the Task

<b>Location and time of work</b>	<b>NRB B115, B119 during normal working hours</b>
<b>Individuals involved</b>	<b>Graduate student researchers and Undergraduate Summer Students</b>
<b>Equipment and supplies required</b>	<b>Light Arm, High speed camera and Alan Key set</b>
<b>Personal protective equipment required</b>	<b>Safety goggles designated for the laser</b>

## **Sequential Steps to Complete the Work Safely**

### **9.2.1 General Instructions/Considerations**

1. Do not look into the laser
2. Ensure windows are blacked out before starting laser
3. Ensure appropriate signage is placed on the exterior of lab door before operating, lock laboratory door to ensure access is restricted
4. Wear the appropriate safety goggles/glasses whenever the laser is powered
5. Ensure laser is not directed at reflective surfaces i.e. mirror/metallic surfaces
6. Keep work area around laser clean
7. The laser goggles used for this laser have a tendency to fog if worn for an extended period of time (20-30 minutes). If this begins to occur turn the laser off in the front panel display in addition to closing the shutter in the front panel display and wait until they are clear before proceeding.
8. At low powers during alignment, the beam can be quite hard to see thru the laser goggles. To avoid turning the laser up to higher powers than necessary, use a camera (a cell-phone camera or CCD available in the lab should suffice) to view the beam.

### **9.2.2 Laser Startup Procedure**

1. Ensure all people in the room are briefed on laser safety and have completed the required EOHSS training. Unlock and flip the breaker connected to the PIV laser power supply.
2. Twist the Emergency stop button such that it “pops” out and is able to be pushed back in. This enables the emergency stop. This action should power-on the display.

3. Using the front panel controls, select SYSTEM and switch it from OFF to ON. Do this for PUMP as well. This will turn on the pump inside the PIV laser supply and should be heard.
4. The system requires time to chill the coolant water in the PIV laser supply, once the water reaches the required temperature, the system will beep, this indicates that the laser is now ready for use.
5. Ensure that all windows in the room are blocked and that appropriate signage is placed on the exterior of the door(s). Lock the exterior door to prevent accidental entry to the room while the laser is in use.

### **9.2.3 Light Arm Alignment Procedure**

1. With the laser in off position, and the light arm not attached to the laser, inspect the lenses for dirt and grease. Clean as necessary.
2. Ensure that the laser is pointed away from any windows or reflective surfaces and that there is a beam stop in front of the laser.
3. Ensure that the System power is at 20% and that the Energy 1 and 2 dials are turned down (Counter-Clock wise) all the way. Having both Energy dials turned all the way down will ensure that the laser is not lasing.
4. Place an alignment block in front of the laser. This is to be used with the level adjusters on the laser feet (attachment to rail) to ensure the laser is firing straight thru the alignment block.
5. Ensure the proper safety goggles are on.
6. Using the front panel, turn LASER ON and set SHUTTER to OPEN. The laser is now lasing, but the beam should not be visible due to the Energy dials.
7. As both beams should be aligned internally (if not contact TSI), only one beam need be used. Slowly turn the “Energy1” dial clockwise until the laser beam is barely visible.
8. Adjust the laser feet until the laser beam is travelling straight thru the alignment block into the beam stop. It is recommended that only the front or back feet are adjusted at this step to make future steps easier.
9. Turn the laser off.
10. Move the alignment block onto the end of the laser rail, move the beam stop if necessary.
11. Ensure goggles are on, then turn the laser on. Adjust the laser feet until the beam goes straight thru the alignment block.
12. Turn the laser off.

13. The lightarm consists of a “box” attached to a long arm that the beam exits. Place the box squarely in the centre of the rail and tighten the wing nuts to firmly attach it to the rail. Ensure that there is a beam stop in front(exit) of the end of the light arm.
14. Ensure goggles are on and then turn the laser on. If the beam is not visible on the beam stop thru the light arm, loosen the three bolts on the top of the lightarm box and move the top piece until the beam is visible. Once it is, tighten them down and turn the laser off.
15. Next, attach the “cross-hairs” attachment onto the end of the lightarm and insert two appropriately sized alan keys into the lightarm box. This is to adjust mirrors in the lightarm box to ensure the beam is properly travelling thru the lightarm. Turn the laser on. Once the mirrors are in the proper place, a perfect circle with two crosses thru it vertically and horizontally should be visible. Turn the laser off. The lightarm is now properly aligned and ready for use.
16. If it is not possible to achieve the perfect cross-hairs, go back to steps 11 and attempt it once more.
17. If it still is not possible to obtain the perfect cross-hairs, turn the laser off. Decouple the light arm from the laser so there is no possibility of lasing through the light arm. Inspect the lens and clean as necessary. Go back to Step 13.

#### 9.2.4 Performing Particle Image Velocimetry

1. Place the nozzle/target in the desired position.
2. Setup the camera stand and place the PIV camera on the stand. Ensure that the camera is level.
3. Using the PFV (camera program) software set on low light mode (ensure camera aperture is fully open) adjust camera position until the nozzle/target is in the desired position in the cameras line of sight.
4. Move the lightarm into an approximate location such that it will shine near the flow field under measurement, and place a beam stop behind the test area. Under no circumstance is the laser or lightarm to be pointed in the direction of a work station or doorways/windows.
5. Ensure the beam stop is in correct position .

6. Add 6-8 scoops of seed particles to the flow (Hollow glass spheres). This amount may need to be modified to allow for 3-6 seed particles visible per grid spacing in the PIV software (INSIGHT 3G)..
7. Turn the laser energy dials (two of them) all of the way down such that they are both at zero. Ensure appropriate safety goggles are in place.
8. On the front panel display turn “laser” on and “shutter” open. The laser is now on.
9. In the INSIGHT3G software select “Laser On” and “Capture”. You should now be able to see a black screen in the software as the energies are too low to be seen.
10. Turn one dial up slowly until the beam is barely visible in the software. (There is some delay in the software sensing the laser beam, proceed slowly to minimize overshoot).
11. Move the lightarm until the beam appears in the desired plane. Ensure that the beam is as perpendicular to the camera orientation as possible.
12. If the beam appears too thick (i.e., covers too thick a region of the measurement field (more than 1 or 2 mm) it may mean that the lightarm is not aligned properly. One should stop measurements, turn off the laser and repeat the lightarm alignment.
13. Turn up both laser energy dials to the maximum.
14. Adjust the camera aperture and focus such that there is no glare in the images seen on the computer screen, and the seed particles are clearly visible.
15. Select the option in the insight software which cycles between frames and adjust the laser energies until each frame appears as close as possible in brightness.

### 9.2.5 Shutdown Procedure

1. When the laser is no longer needed, ensure the laser is turned off and the shutter is closed using the front panel settings.
2. Allow the PIV laser power supply chilling system to run for an additional 15-20 minutes after step 1 to allow the system to cooldown.
3. After the cooldown period, turn the pump off on the front panel display and then turn the system off also on the front panel display. Then push the red E-stop button on the front of the PIV laser power supply.
4. Flip the breaker powering the PIV laser power supply to the closed position and lock the switch out.

### 9.2.6 Parameters

Water flow rate: 4.0 GPM

Cooling water temperature: 22C  
System Power at alignment: 20%  
System Power during data capture: 70-80%

### Contingency Plan and Reporting

#### **Accident / injury response**

1. Apply first aid as needed
2. Notify the supervisor Dr. David Novog (905-525-9140 ext 24904) and the Engineering Physics department (905-525-9140 ext 24545) immediately
3. Complete an Injury/Incident Report

#### **In the Case of Serious/Critical Injuries**

1. Shutdown the laser and any other equipment that may also be on
2. Call Security at (905) 522-4135 to arrange for medical and emergency services immediately
3. Apply first aid as needed
4. Notify the supervisor Dr. David Novog (905-525-9140 ext: 24904) and the Engineering Physics department (ext: 24545) immediately
5. Notify EOHSS immediately (ext: 24352)

#### **Equipment Malfunction**

**If an equipment malfunction occurs, press in the red E-stop button on the front of the PIV laser power supply. This will immediately shutdown the laser.**

**In the event of the E-stop button not working, flip the breaker powering the PIV laser power supply to ensure a shutdown state.**

**If any of the steps in the above procedure are unsuccessful, turn off the laser, turn off the breaker and lock it in the off position. Contact Dr. Novog for further instructions.**

#### **Equipment shutdowns**

To turn the laser off one must:

1. Turn LASER to off in the front panel and turn SHUTTER to CLOSED in the front panel
2. Turn PUMP and SYSTEM to OFF from ON in the front panel display
3. Push the red E-stop button
4. Turning off the power breaker and lock it out

### Environmental Responsibility

#### **Waste disposal procedures**

N/A

#### **Building air quality**

N/A

### References

1. OSHA/ regulations
2. EPA and Municipal environmental regulations
3. RMM #100 McMaster University Environmental Health and Safety Policy
4. Material Safety Data Sheets (MSDS)
5. RMM #300 Safety Orientation and Training Program
6. RMM #301 Standard Operating Procedures
7. RMM #310 Eye Protection Program
8. RMM #703 Laser Safety Program

### Distribution

1. Faculty of Engineering JHSC (for review)
2. Occupants of NRB B115 and NRB B119

### **Legal Disclaimer**

The Standard Operating Procedures on this website are provided for the use of the McMaster University employee and/or student community. The procedures outlined in the above referenced document are intended to reflect best practices in this field; as such they are provided to the community for guidance and/or direction. However, these recommendations should not be construed as legal advice. used.

## 9.3 LIF Calibration Curves

### 9.3.1 Free Convection LIF

For the free-convection LIF measurements, a calibration curve was generated for each day of experimental data over the range of temperatures expected, and in some cases beyond. Each dataset was processed with the calibration curve generated during the day that dataset was captured and can be seen below on Figure 10. Note, the slope in these curves shifted slightly downward with each day, this was attributed to the accelerated oxidation in the Aluminum in the test section observed with the Rhodamine B in the vessel, potentially causing the concentration to reduce slightly with time.

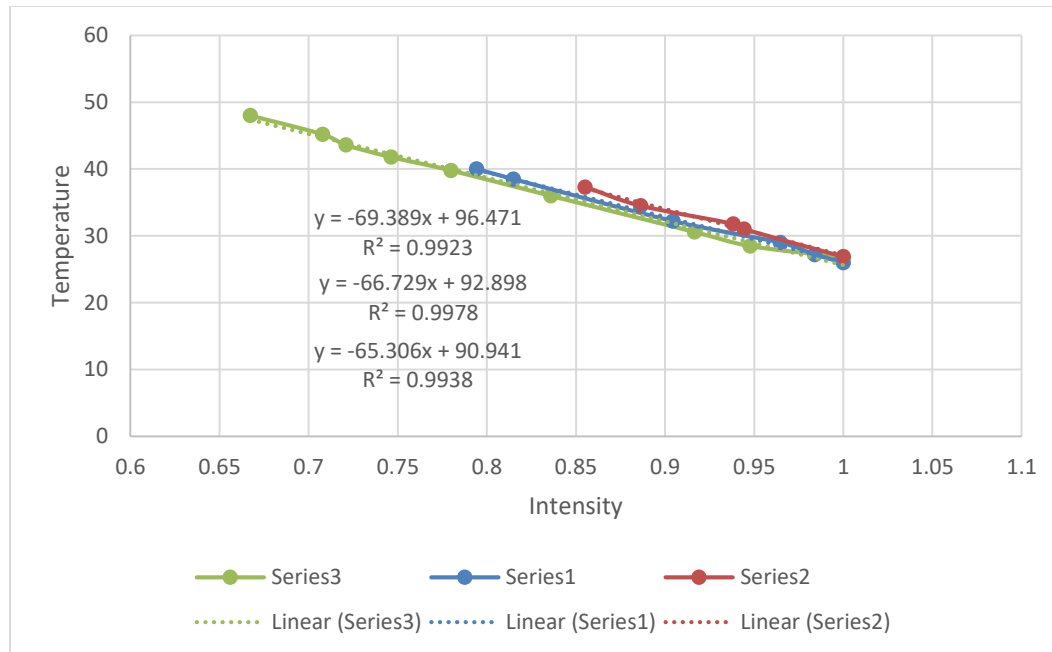


Figure 10. Calibration curves used for the free-convection cylinder LIF experiments

### 9.3.2 Mixed Convection LIF Experiments

The calibration curve for the mixed convection experiments was handled slightly differently. All of the calibration points were plotted on a single curve and then fit to a single line to obtain the slope as in Figure 11. This slope was then plugged into equation (A1) for a more general form of the calibration curve and to allow for reference images to be used just prior to the data acquisition, which helped image quality over longer experimental days. The errors and errorbars are discussed in the body of the paper.

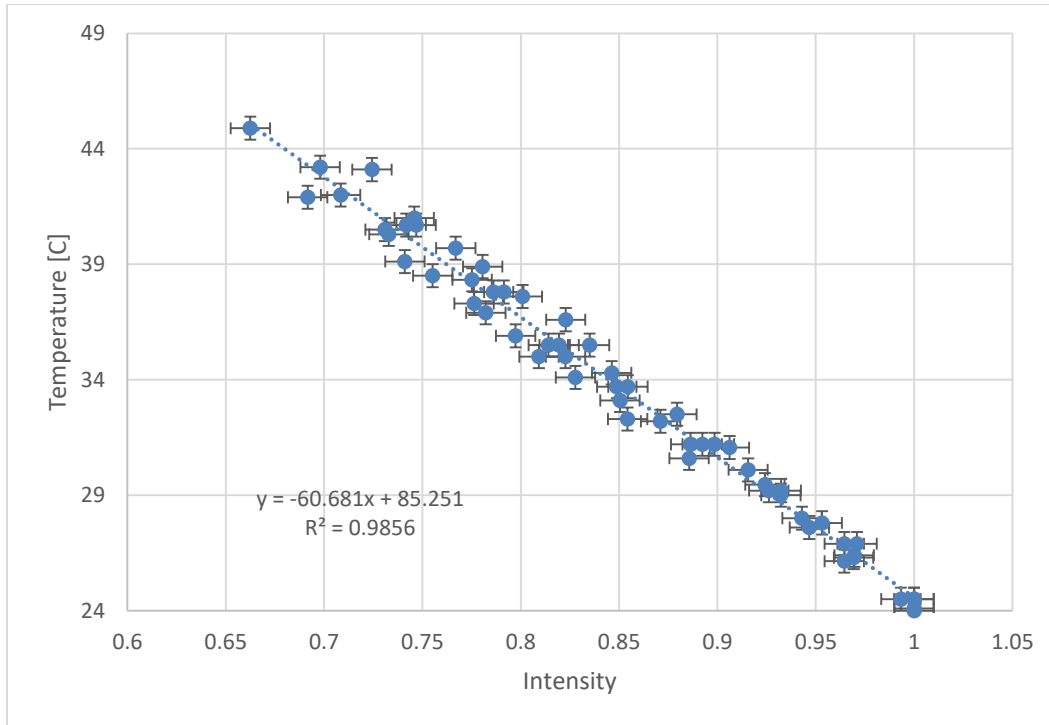


Figure 11. Calibration data points captured during the mixed convection LIF experimental campaign

$$T_{image} = T_{Ref} - 60.681(1 - I_{image}) \quad (A1)$$

Additionally, due to the camera and laser being unsynchronized fluctuations in the intensity profile relative to the reference image was measured. This was minimized by the camera setting employed, but resulted in background temperatures that deviated from the measured inlet temperature. This deviation was not due to stratification effects, given a type T thermocouple was in the tank and agreed approximately with the inlet temperature reading. To account for this, a correction to the image was applied via equation (A2) below. This correct takes the lines at  $x = \pm 25\text{mm}$  and averaged the raw measured temperatures at all  $y > 0\text{mm}$ . This value

gets compared to the inlet temperature and generates a correction factor to apply to the entire domain. This factor was typically 0 to 1.5°C.

$$T_{correct} = T_{image} - (T_{back} - T_{inlet}) \quad (A2)$$

#### 9.4 Effect of Refractive Index Change

The effect of the refractive index change on the seeding profile with no tilt can be seen via Figure 12 and Figure 13. For these free-thermal conditions, all data above 512W fully distorted the seed in the plume region, rendering the measurements in this region and effectively the entire dataset useless.

This effect was found to be significantly reduced by adding a 10-degree tilt to the camera in subsequent tests, and for significant heating experiments in water, is the suggested course of action for the best quality data. This does however result in some distortions of the velocity field, but this is shown to be manageable in a certain region of interest in section 9.5.

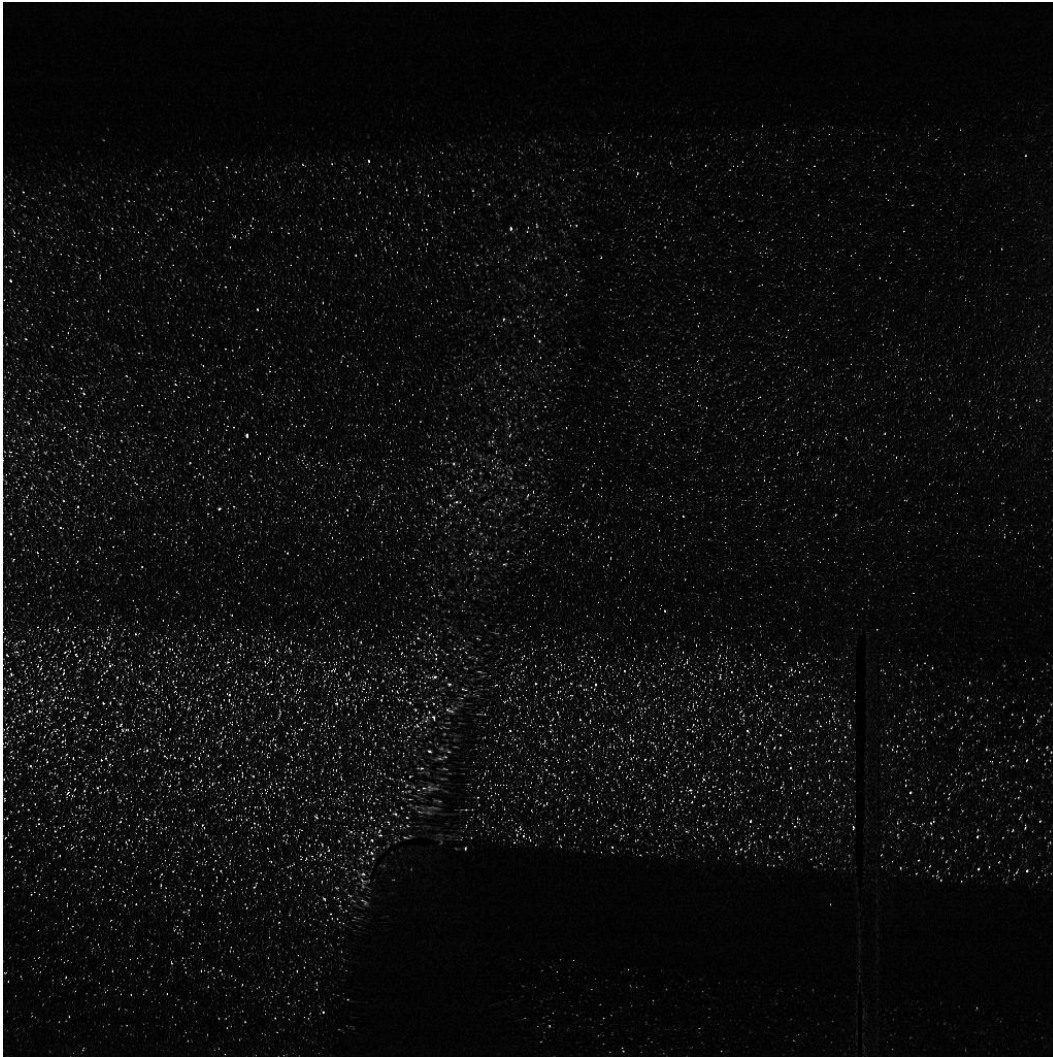


Figure 12. Seed profile for no angular tilt for 64W for a pure free thermal plume

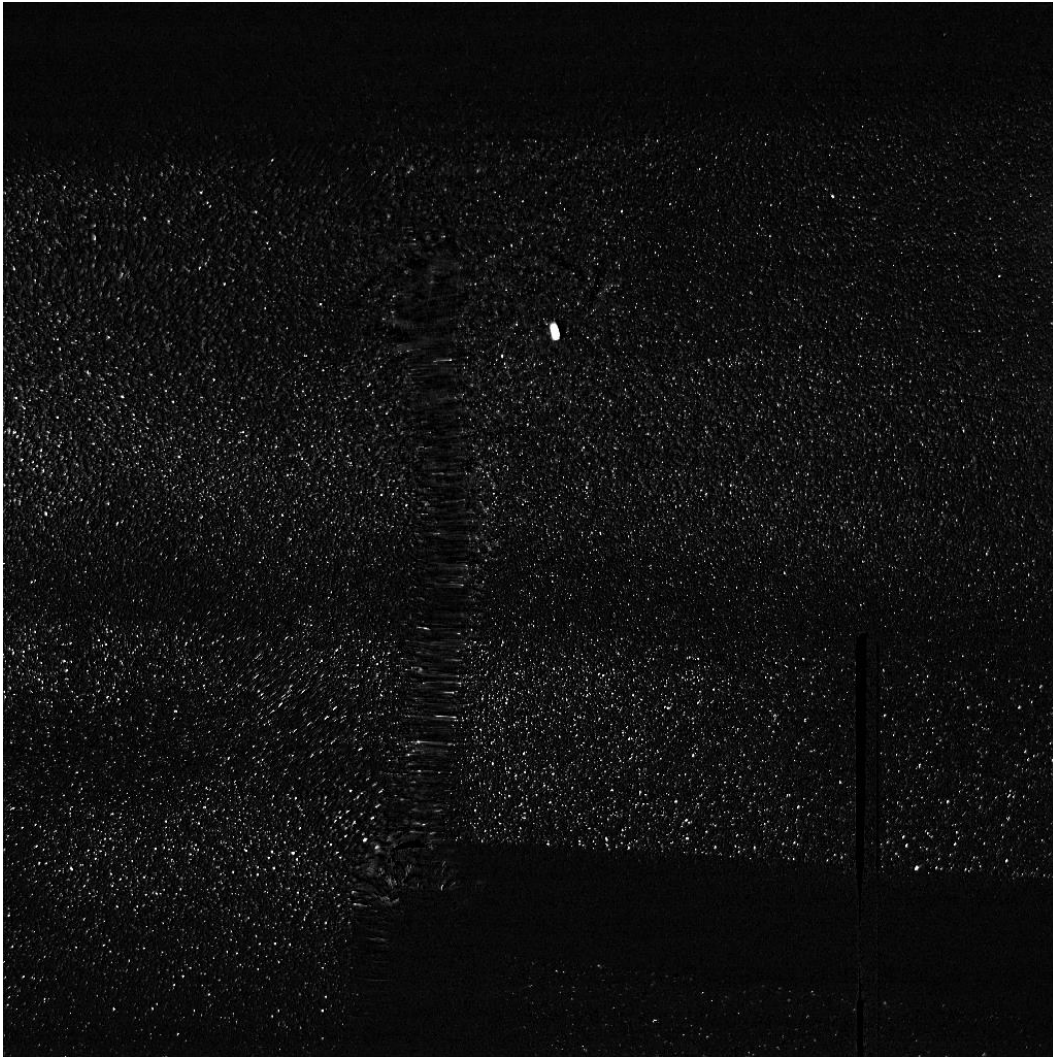


Figure 13. Seed profile for a pure thermal plume for 512W

### 9.5 Effect of Angular Tilt

The effect of the angular tilt introduced in the PIV measurements of the third study in this thesis was explored. This was achieved by comparing isothermal velocity fields containing the 10-degree tilt, and with the ideal setup without the tilt. As shown on Figure 14 below, no significant effect is observed in the  $-25 < x < 25$  mm region. Outside of this region, tilt effects can be seen to cause a pseudo acceleration

effect, as the  $x > 25\text{mm}$  region is closer to the laser sheet, causing the distortion in pixel size to become significant. As a result, all data not in the  $-25 < x < 25\text{mm}$  region was not considered for subsequent analysis or use in the validation cases. This region was extended to the LIF data as well.

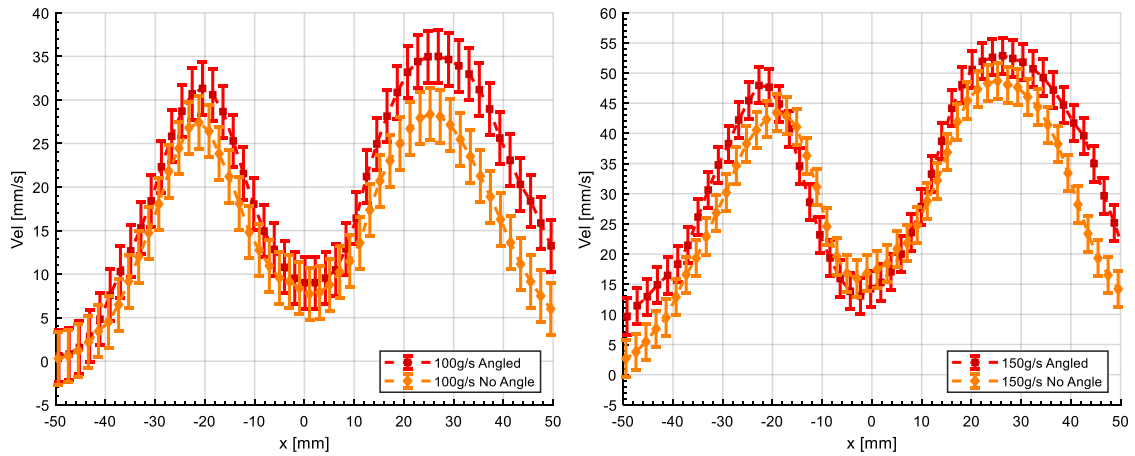


Figure 14. Effect of the angular tilt at  $Y=50\text{mm}$  from the surface of the cylinder

## 9.6 Diffuser Nozzle Design/Performance

The design of the large diffuser nozzle used for the single cylinder experiments can be visualized in Figure 15. The goal of this nozzle was to reduce the inlet velocities from the 12.7mm inlet line from the 1-3m/s range to a range similar to that of a free thermal plume, or 10-40mm/s. Additionally, it was desired to make this nozzle as large with as flat of a velocity profile as reasonably achievable to help with experimental alignment.

This design was based in part on a smooth contraction nozzle with baffle plates to re-direct the flow to more accurately mimic this type of nozzle design and to spread

the incoming high velocity fluid across the entire nozzle inner diameter. A flow straightener was placed near the outlet of the cylinder to reduce inlet turbulence. The nozzle was designed using the  $k-\omega SST$  turbulence model and a contour of this nozzle can be seen on Figure 18. This was chosen as the general flow topology using other RANS based models tended to over predict the total spreading of the nozzle. This was noted in early prototypes which were much smaller, but yielded velocities approximately twice the size of predictions from realizable  $k-\epsilon$ .

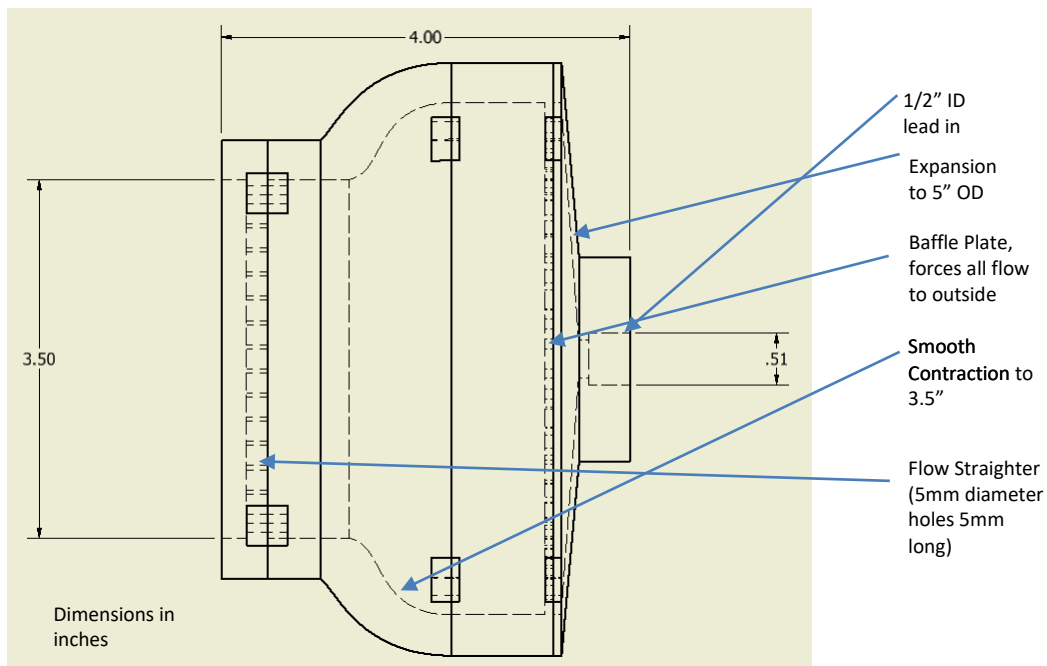


Figure 15. General design layout for the large diffuser nozzle designed for the single cylinder experiments



Figure 16. Four 3-d printed parts comprising the diffuser nozzle, top left: Inlet, top right: baffle plate, bottom left: smooth contraction, and bottom right: outlet and flow straightener

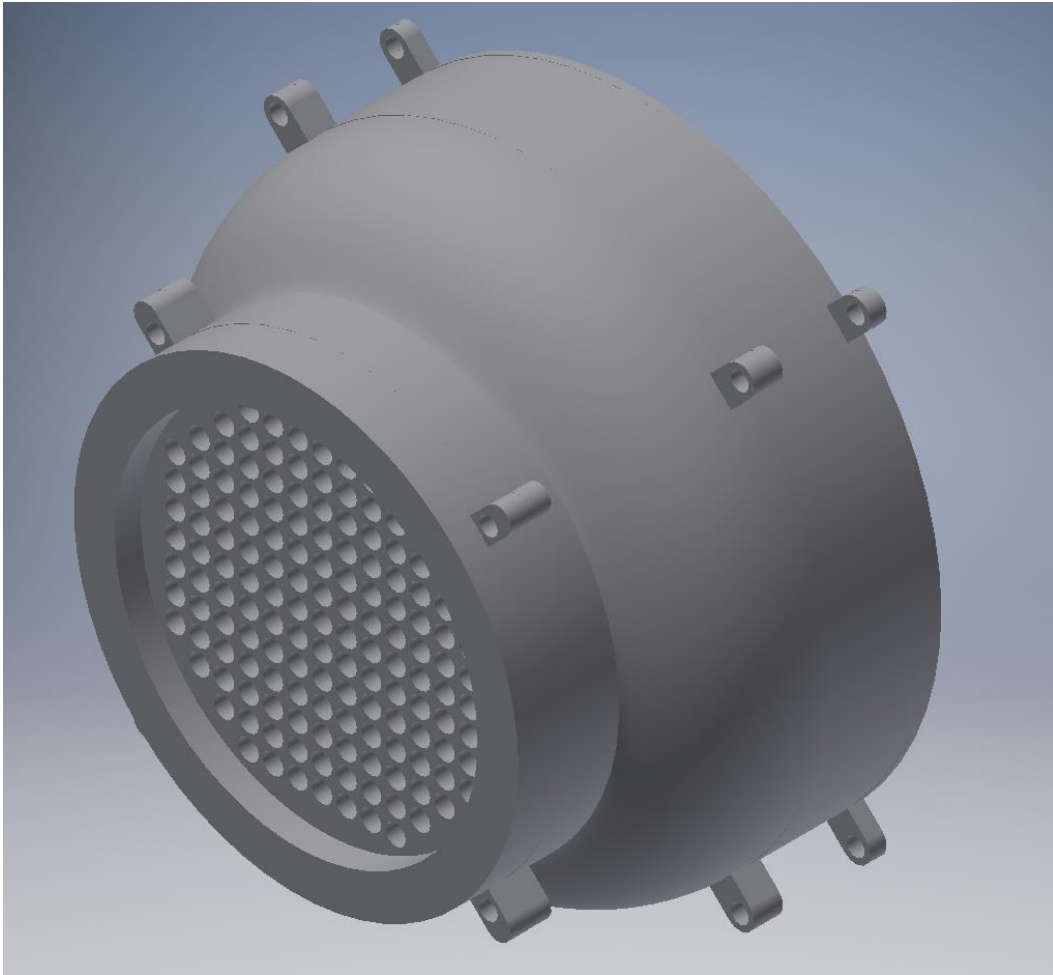


Figure 17. Isometric of the complete assembly of the large diffuser nozzle

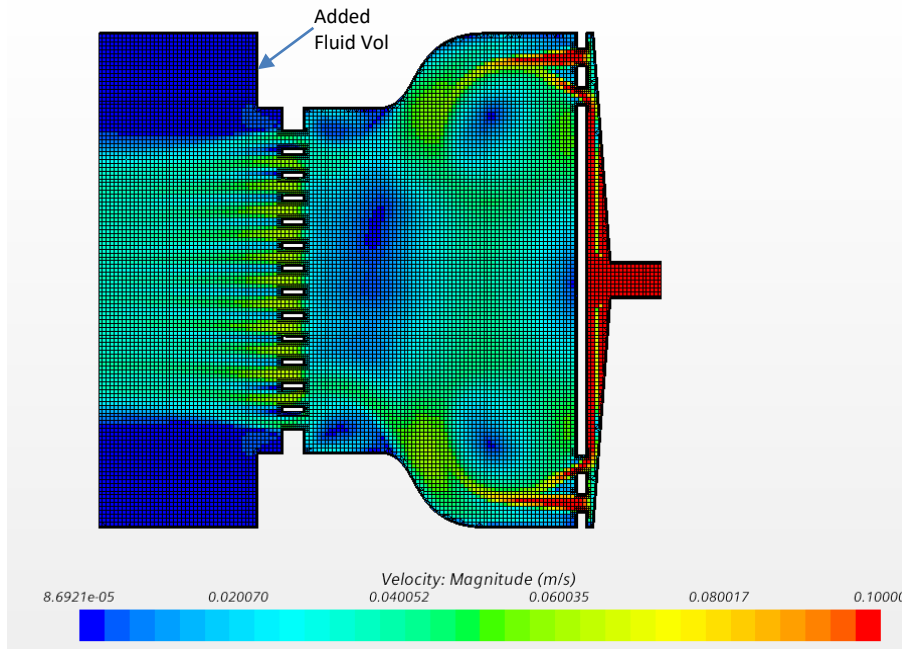


Figure 18.  $k-\omega$  SST contour of the centreline of the nozzle for a mass flow of 100g/s

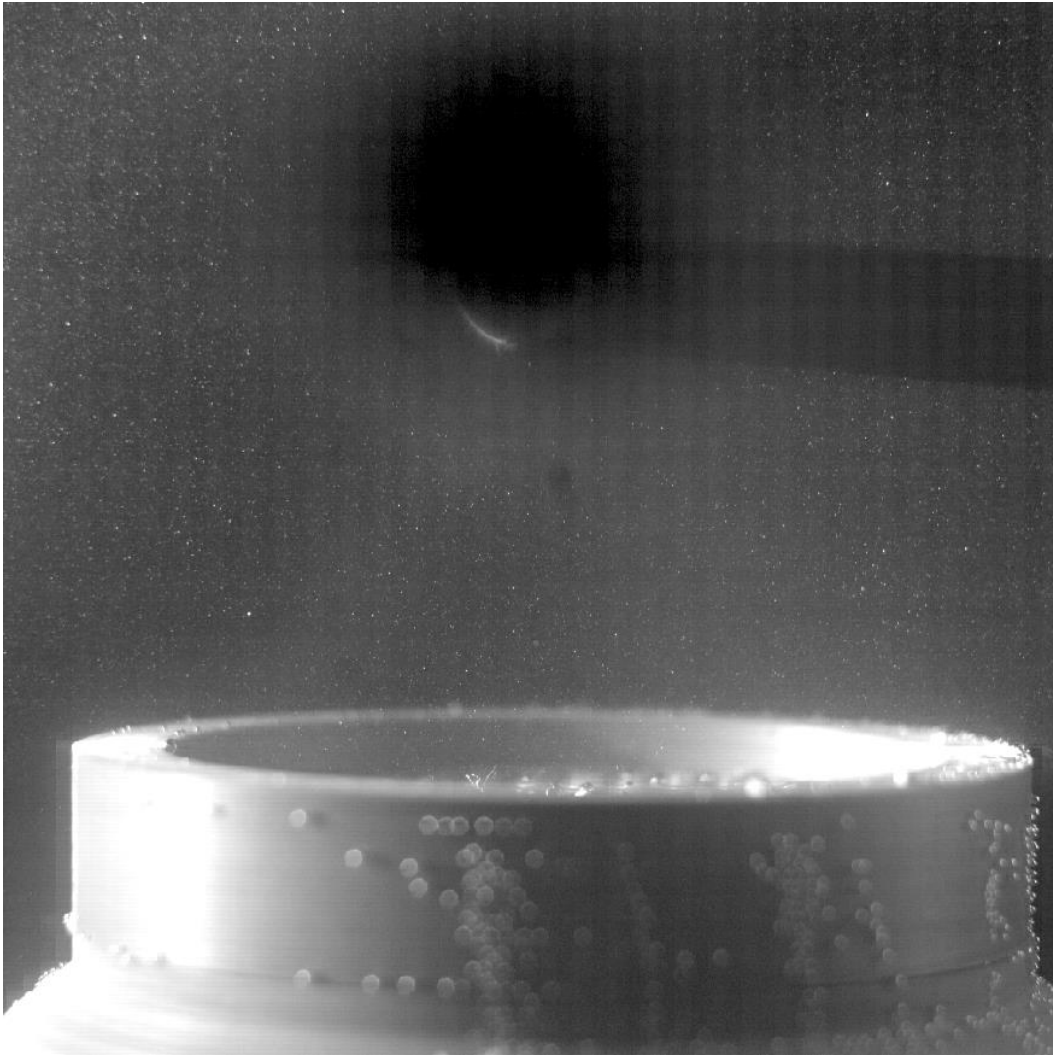


Figure 19. Raw PIV image of the installed diffuser nozzle

## 9.7 Departure from Nucleate Boiling in Tube Arrays: Literature

### Review

Compared to the study of horizontal cylinders in a cross flow, tube arrays are relatively untouched. Key features of the studies that are about to be outlined is that nearly all of the experimental studies are for refrigerants as their working fluid in addition, only one study to date has reliable void fraction measurements.

Tube arrays can be arranged in many ways however they can be defined by three parameters. The number of cylinder elements, the Pitch to Diameter ratio (P/D) and the pattern of the arrangement (Rectangular/Inline or Triangular/Staggered).

Using R-113, Chan and Shoukri [26] examined the boiling characteristics for a single tube, 3x3 inline array in addition to a 3x9 array. They examined and compared the CHF characteristics for a single tube to a 3x3 array, and examined the effect position of their primary heater CHF value in addition to the impact of adding heat to other heaters in the central column (either above, below, or in some cases both). They also obtained void fraction measurements using a Gamma Densitometer. It should be noted that these void fractions were stated to be averaged over the region above a heater due to their beam size. Their test section was purely pool boiling and can be seen below in Figure 20. Chan and Shoukri [26] describe two competing effects modifying the CHF of a cylinder in a tube array versus a single cylinder in an infinite medium. Namely, a two-phase generated convective effect that acts to enhance CHF via recirculation and a vapor blanketing effect

caused by an increase in flow resistance and less space for vapor to escape, diminishing CHF.

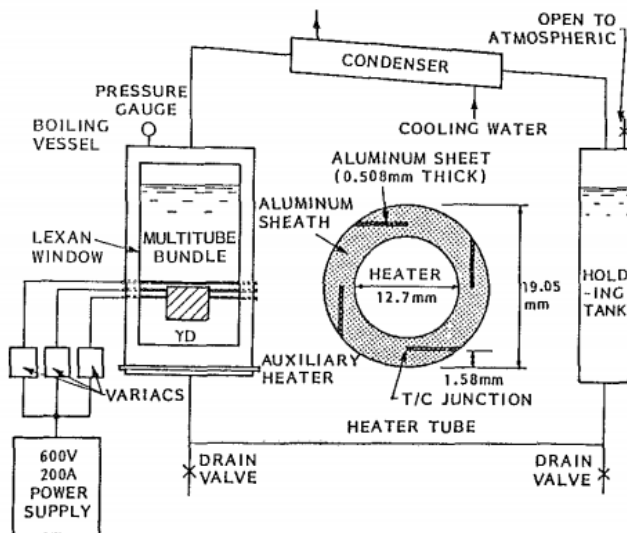
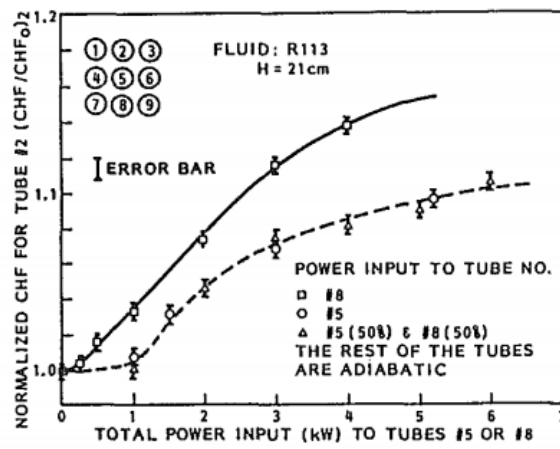


Fig. 1 Schematic of experimental setup

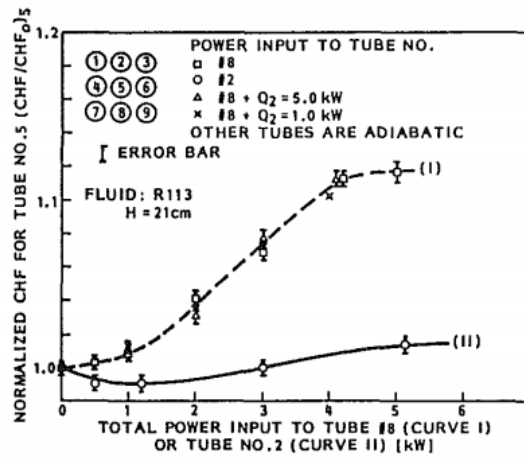
Figure 20. Experimental facility of Chan and Shoukri [26]

The main results of Chan and Shoukri [26] can be seen below in Figure 21. It is worth clarifying that the ratio is not the tube bundle CHF to a single cylinder case, but rather the tube bundle CHF measured with heat addition above/below the primary cylinder compared to the case without any heat addition to adjacent cylinders. The main takeaways from this series of tests is that for their geometry, the enhancement effect appears to be stronger than the diminishment effect. Their results are also consistent with the thought that the CHF enhancement effect is strongest for cylinders higher up in the tube array, with the lowest CHF being recorded for the bottom cylinder. Their results also would seem to indicate that after a certain level

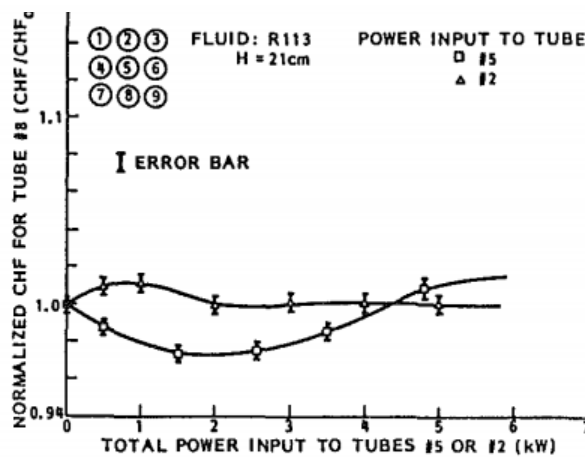
of void being generated below the primary heater, a maximum enhancement is reached, as evidenced by the gradual slow down in the curves which appears to be logarithmic in nature. Finally, they note that the CHF for cylinders in an array is ~10% smaller than that for their single cylinder experiments under similar conditions. This coupled with their enhancement data (upwards of 15%) would seem to indicate that under the best possible conditions, some cylinders in the upper section of a tube array will have their CHF occur at a very similar value to that of a single cylinder.



(a)



(b)



(c)

Figure 21. CHF enhancement/diminishment of a cylinder in a heated array vs unheated [26]

Thibault [27] performed quenching experiments with a heat flux meter on 127mm diameter copper tubes for both single cylinder and 3x5 arrays with a P/D of 2.18 for water. Given the size of these copper rods, an oven was used and the assembly was then dropped into a dousing tank. Heat flux was measured using a “heat flux meter” that they developed and calibrated. It should be noted that part of the calibration process was to conduct quenching tests individually for each cylinder in the array separately (i.e. single tube CHF), and any changes were judged from that single tube CHF value (for each cylinder). They also assessed how a steam injection line at the bottom of their tank affected their quenching CHF values. In addition, steady state experiments on a 3x4 array (same P/D) with Heptane were also performed using steam as a heat source. Diagrams of the test facility for the quenching tests can be seen on Figure 22.

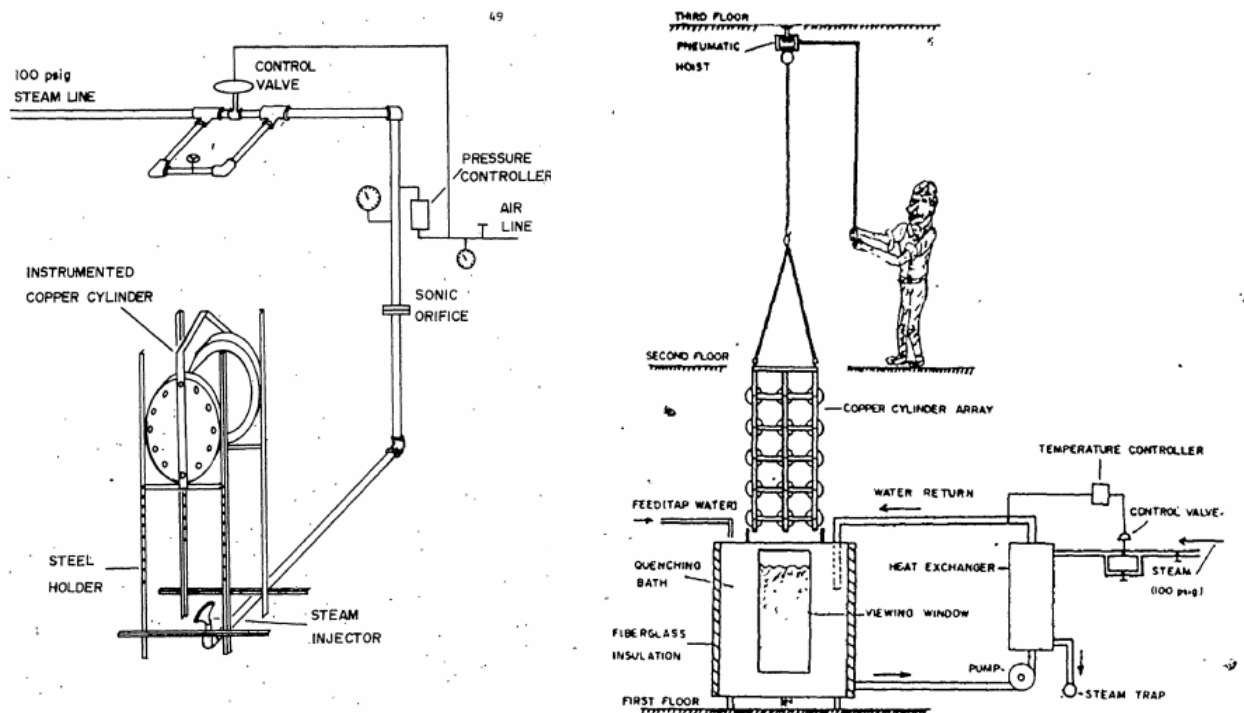


Figure 22. Experimental facility used by Thibault [27]

Thibault's [27] results for CHF as a function of circumferential position and subcooling for a single cylinder can be seen on Figure 23 below. On this figure, it can be clearly seen that for most of the conditions that the minimum CHF value occurs on the upper half of the cylinder at the 30-degree point. Thibault [27] states that great care was taken to make sure that this was not an effect of part of the cylinder quenching first and state that visual observations proved this. They state that this effect is most likely a hydrodynamic effect and correspond roughly to their visual observations of viewing steam separate off the cylinder at approximately this 30-degree point on either side of the cylinder. Thibault [27] also provided a linear

fit to relate his saturated data to his subcooled data shown below as equation (A3). They also generated data for a single cylinder at saturated pool boiling conditions with varying steam line pressures and distances impinging upward onto the cylinder as it is being doused, seen in Figure 24. While there appears to be no consistent pattern, Thibault's [27] data for these cases does indicate that the hydrodynamics play a significant role in the CHF value at a given circumferential position.

$$\frac{q''_{M_{Sub}}}{q''_{M_{SAT}}} = 1.0 + 0.0437\Delta T_{SUB} \quad (A3)$$

100

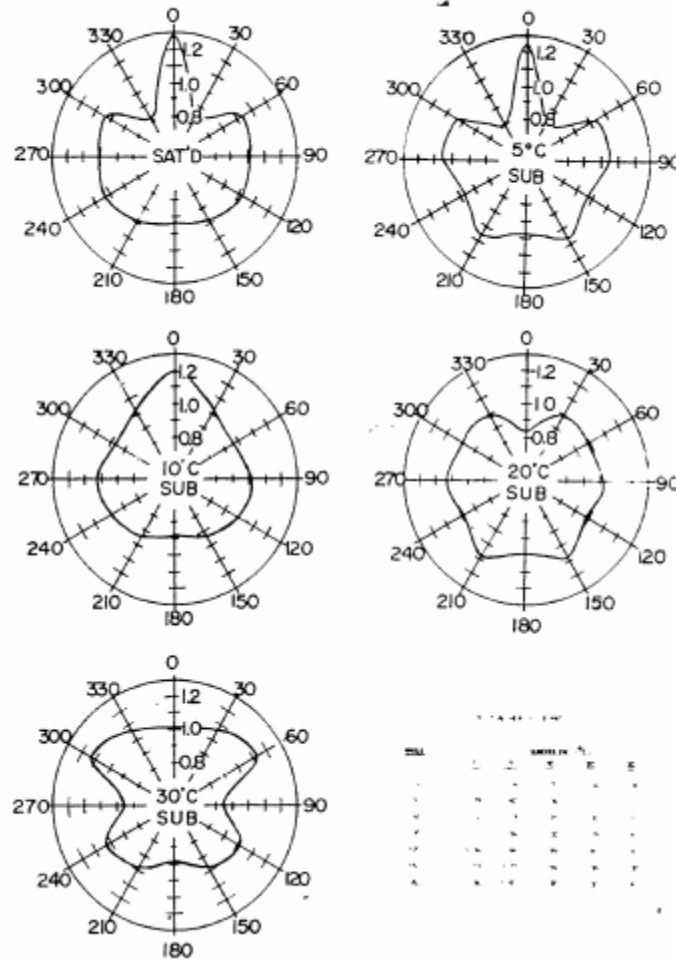


Figure 23. Thibault's quenching CHF results as a function of angle and subcooling. Note only 12 circumferential measurements [27]

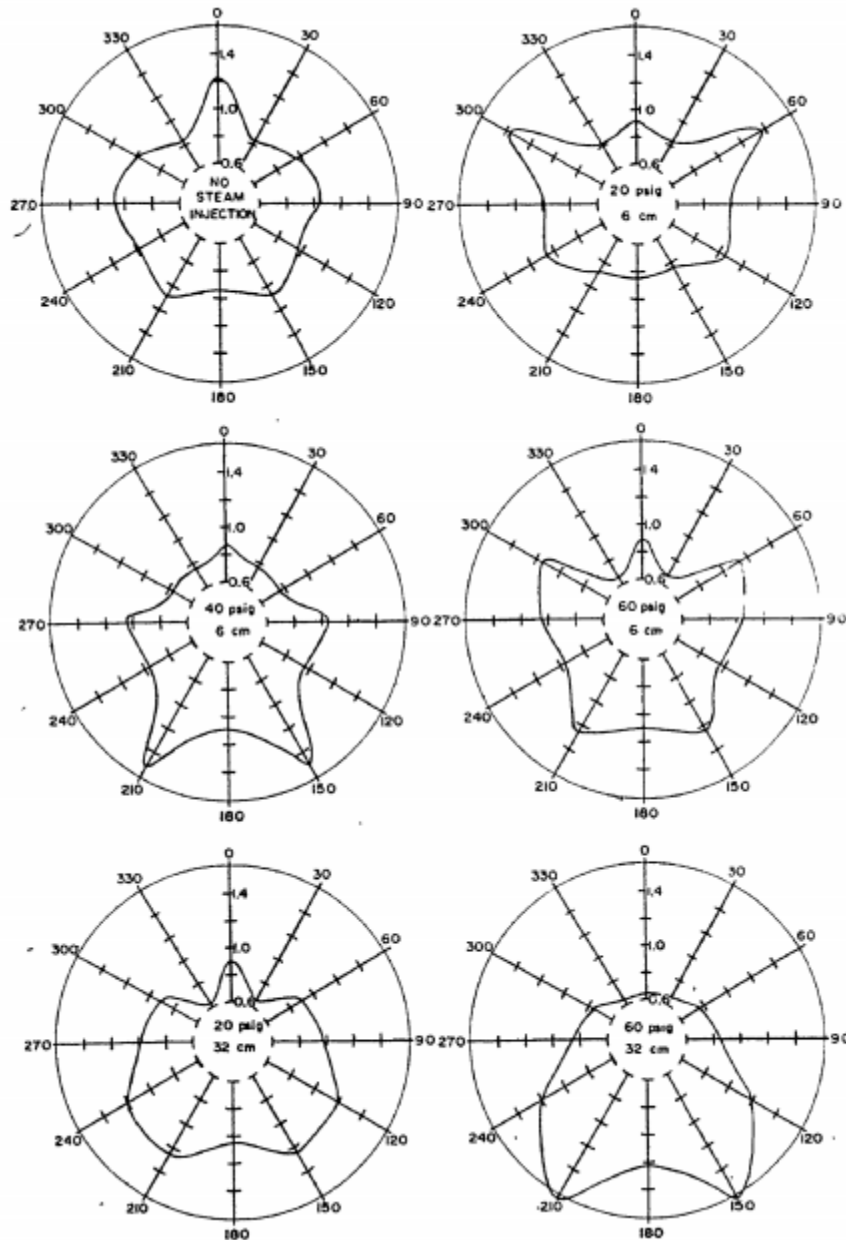


Figure 24. Thibault's saturated single tube CHF data collected with their steam line. The distance in cm corresponds to the distance from the nozzle to the cylinder [27]

A table from Thibault's [27] thesis summarizing his tube bundle quenching experiments can be seen below as Figure 25. Using the single tube CHF value for

each tube in the array as a reference value, Thibault [27] showed that under most cases CHF for the downward facing heat flux meter was almost always increased in the array compared to the single cylinder case. Some decreases are noted for the 90-degree and 0-degree positions with some steam injection. Thibault [27] notes that it was generally considered that additional void flowing from the bottom should decrease CHF, not increase it. The fact that his data largely saw an increase with this effect was attributed to the relatively large P/D of 2.18 used compared to most experiments done with heat exchangers in mind, not CANDU reactors (1.5->1.25 typically). Thibault also suggests that the relatively large pitch in a CANDU and his tests allowed for vapour to flow freely between the channels and mostly avoid the vapor blanketing mechanism that acts to reduce CHF. The relatively different increases in CHF for the 5 tubes is partially explained by boiling and CHF being reached on the lower tubes first. Thibault [27] noted that boiling always started on 1 first (due to being dropped in), followed by 2 and 3 and the same time, then 4 and 5 at the same time. This means that there is likely some systematic error due to the dropping process in the enhancement results. They also note that their test may not exactly model a CANDU in a postulated severe accident as its unlikely that all of the pressure tubes in a region contact the calandria tube at the same time.

TABLE 6.1

AVERAGE % INCREASE OF CHF IN MULTIPLE CYLINDER ARRAY

POSITION IN BUNDLE	1	2	3	4	5
BLOCK NUMBER	12	13	9	17	20
OVERALL CHF WHEN CALIBRATED AS A SINGLE COPPER CYLINDER ( $w/cm^2$ )	105.2	113.3	117.2	117.7	96.5
	% INCREASE				
SATURATION ( $\beta = 180^\circ$ )	0.7	52	128	37	108
20°C SUBCOOLING ( $\beta = 180^\circ$ )	—	145	105	92	63
STEAM INJECTION (60 psig, $\beta = 180^\circ$ )	—	47	109	36	67
STEAM INJECTION (100 psig, $\beta = 180^\circ$ )	—	94	116	69	36
STEAM INJECTION (100 psig, $\beta = 90^\circ$ )	11	32	5	-33	30
STEAM INJECTION (100 psig, $\beta = 0^\circ$ )	-18	10	36	-13	-3

Figure 25. Tube array quenching CHF data obtained by Thibault [27]

For Thibault's [27] steady state experiments with the 3x4 P/D = 2.18 (OD = 2.67cm) and Heptane, it was found that the CHF was ~80% of the value obtained using Zuber's model. For the 12 tube array, Thibault found CHF to be ~20% higher than the single tube case. In addition, the CHF value was found to roughly be constant for the entire array (central column). This was thought to indicate that the CHF is strongly dependant on the clearance between tubes (i.e. smaller P/D would cause reduction potentially). Thibault also showed an additional enhancement

effect due to boiling from tubes below the tube of interest and is seen in Figure 26. This enhancement is relative to the cylinder being heated alone in the array and is noted to be relatively independent of the actual heat level of the adjacent tubes. In other words some void generation beyond a minimum threshold was enough to provide an additional enhancement effect.

<u>ACTIVE ROW(S)</u>	<u>% INCREASE IN CHF ON</u>		
	<u>TUBE 2</u>	<u>TUBE 3</u>	<u>TUBE 4</u>
1	18	20	16
2	—	17	21
3	—	—	12
1 and 2	—	22	19
1 and 3	—	—	18
2 and 3	—	—	24
1, 2 and 3	—	—	20

Figure 26. Percent increase in CHF for a tube subjected to boiling from adjacent tubes in the central column. Note that this percent increase is over the heater reaching CHF without the other tubes heated [27]

The study of Cumo et al [28] examined the critical heat flux for a single heated cylinder in a staggered array with outer diameters of 13.6mm and a P/D of 1.25. They measured how CHF in this staggered array was effected by both inlet quality and mass flux. Their data was limited to a maximum inlet quality of 30%. Their data is presented below in Figure 27 and a very clear trend can be seen. Their measured CHF can be seen to clearly increase with small increases in quality and reaches a maximum enhancement effect. The rate at which this maximum is increased appears to reach its maxima quicker with higher mass flux rates. They also gathered data with no inlet quality as a function of mass flux but found a very weak relation on its impact on CHF.

Cumo et al's [28] CHF heater was also instrumented with four thermocouples (N, S, E, W) and data judging where CHF first occurs was also gathered vs mass flux and quality. Very generally, they note that for low quality, low flow experiments, CHF tended to start on the bottom section of the heater. Conversely for high flow, higher qualities (still less than 30% for their study), the CHF location shifted towards the top side of the heater.

Cumo et al [28] proposed a modification to Zuber's hydrodynamic model to account for the added heat removal due to the 2-phase mixture impinging on the cylinder surface, enhancing CHF margin. Their model can be seen below as equation (A4), and it is noted that the constant  $C_2$  is determined via a fit of the experimental data. It was found to predict their data reasonably well for  $C_2=0.002$ ,

although it did not capture the flattening of the enhancement effect clearly visible in their test data.

$$q''_{CHF\_FB} = (q''_{CHF\_PB}{}^2 + C_2 \rho_{TP} \rho_g h_{fg}^2 u_{tp}^2)^{1/2} \quad (A4)$$

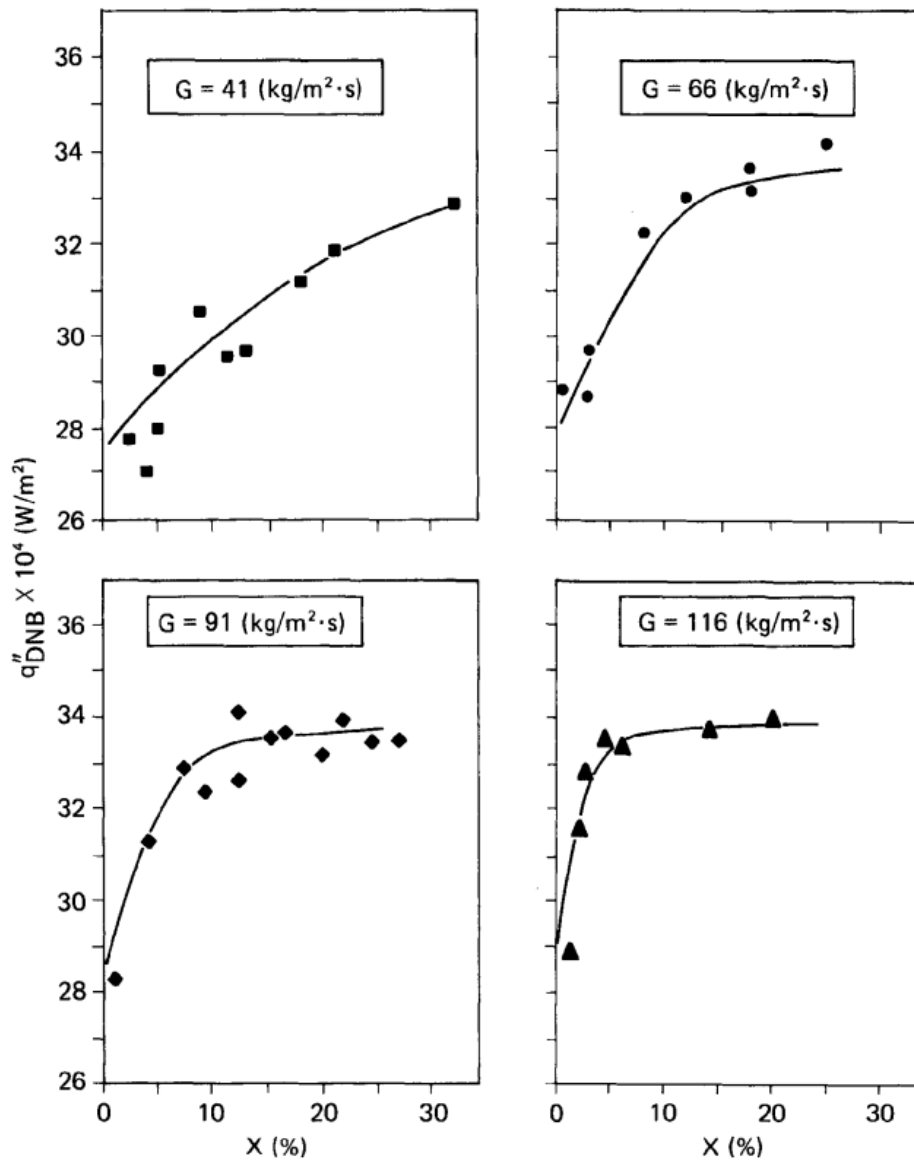


Figure 27. CHF data versus mass flux and inlet quality for Cumo et al's [28] experiments

Fujitita and Hidako [29] examined the effect of tube array geometry on CHF and nucleate boiling characteristics for four test geometries (Staggered and Inline, P/D = 1.3, 1.5). They tried to assess the impact of array geometry on nucleate boiling using the heat transfer coefficient primarily in addition to heating arrangement (entire array vs only central column). They noted that the heat transfer coefficient is highest at the top of the array and lowest at the bottom. Little P/D effect was found for the nucleate boiling regime. They also found that when the modified the oncoming velocity to the array  $U$ , that no significant changes were found (0.022m/s->0.22m/s).

For their CHF measurements, they examined how heating/void generation directly below the CHF heater affected the measured CHF for all four of their geometries. Their data can be seen below on Figure 28. It can be seen clearly that P/D has a significant effect for the staggered array, and appears to have minimal effect on the inline array except for some cases. They also clearly show than additional void generation from below appears to enhance CHF. However, it takes a certain amount of void/power to cause an enhancement in tube array CHF compared to the single tube CHF reported.

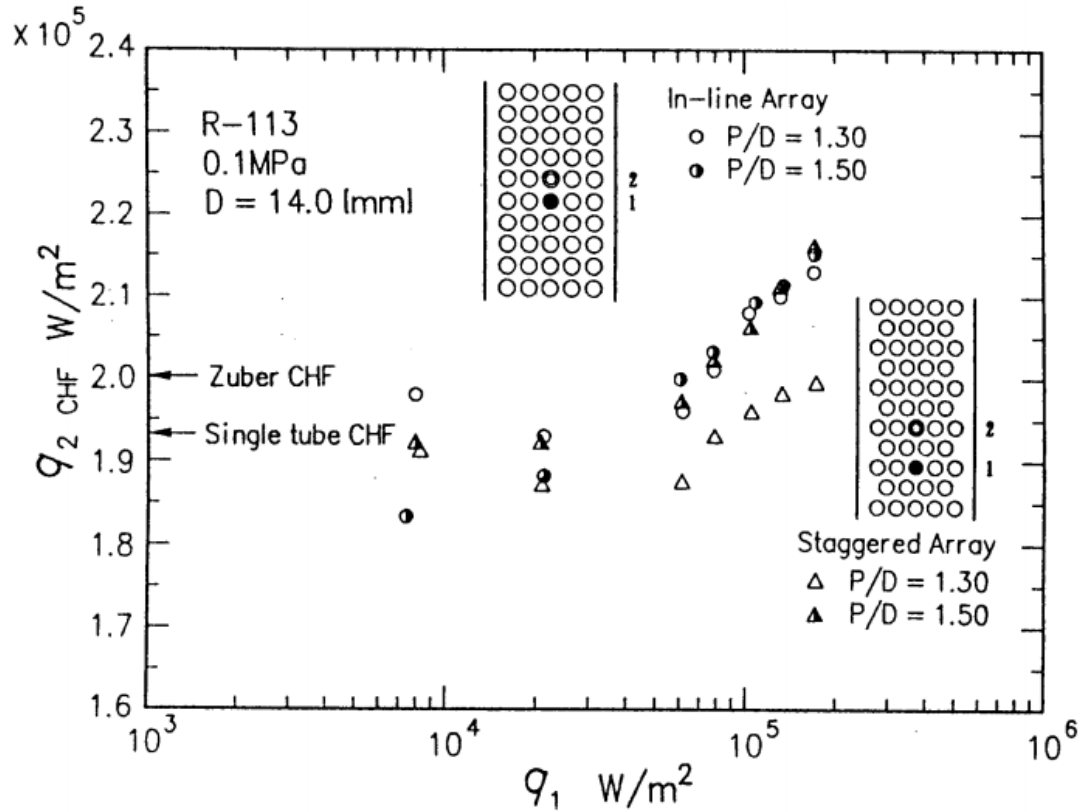


Figure 28. CHF data gathered by Fujita and Hidako [29] as a function of lower heater power.

The study of Hwang and Yao [30] examined the CHF for an inline tube array (3x16,  $P/D = 1.5$ ), a single channel in an infinite medium and a single tube in a finite channel (blockage). Their test geometry for the tube array tests can be seen on Figure 29. They also collected data to assess where the CHF would occur on the circumferential position on the heater in addition to developing a correlation applicable to a single tube in a channel and with some manipulation, using this correlation for tubes in an array. CHF for a variety of mass fluxes was collected.

The highest CHF that Yao and Hwang [30] measured was for their single cylinder in an infinite medium. They also note that for these cases, CHF initiated on the downstream portion of the cylinder (i.e. the top). The rationale being that vapor was getting captured in the wake of the single cylinder. When they moved the single cylinder into a channel, they noted that relatively small channel blockages ( $d/H = 0.25$ ) were resulting in CHF reductions by as much as 30%. They also proposed a modification to the CHF model of Haramura and Katto to account for this, but also developed their own correlation included this factor and is shown below as equation (A6). It is important to note that for their tube array data, it was found that CHF was initiated on the upstream portion of the cylinder instead of the downstream portion as in the single cylinder case. This was thought to have been a result of the wake generated by upstream cylinders in the array causing bubbles to get trapped in the vicinity of the downward facing part of the heated CHF cylinder. This was thought to be analogous to a downward facing flat heated plate.

Its important to note that with the correct choice of spacing using the tube array geometry to replace H in equation 3, they found that this relation did a good job capturing their tube array data, as can be seen in Figure 30. Although, it must be noted that their data is significantly lower than the pool boiling value obtained for the Haramura and Katto model and physical mechanism as to why that may have been the case are not discussed.

$$\frac{q''_{MAX}}{\rho_g h_{fg} U_\infty} = 0.594 W e_g^{-0.476} (1 - x_{loc})^{0.954} (R^*)^{0.36} \left[ 2.25 + \left( \frac{\rho_g}{\rho_f} \right)^{0.15} \right]^{-1} \left[ 1 - \left( \frac{d}{H} \right)^{0.86} \right] \quad (A6)$$

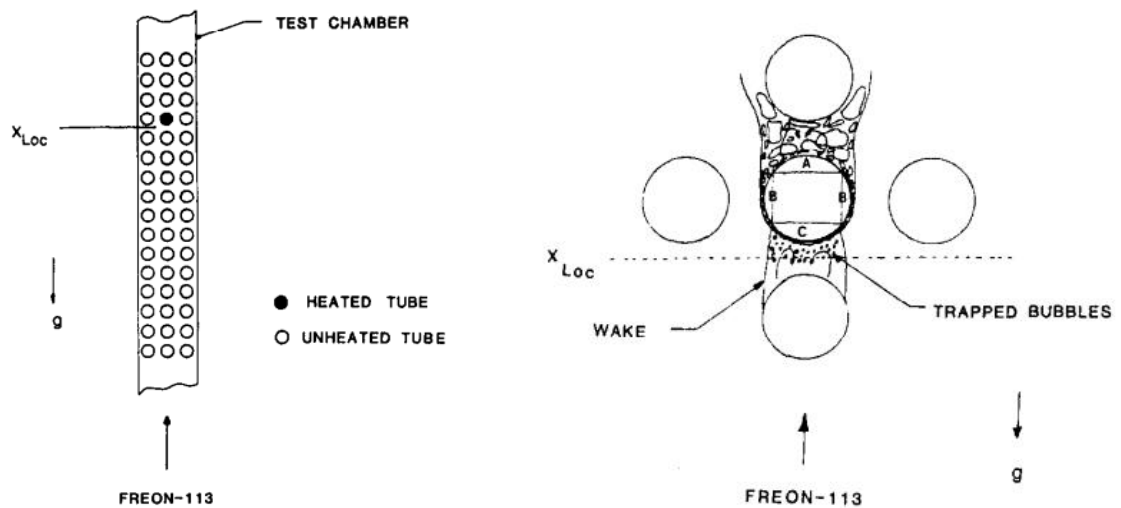


Figure 29. Tube array used by Yao and Hwang [30] in addition to a schematic (right) with postulated hydrodynamics.

Table 1. Comparison of the bundle CHF data

$G$ (kW m <sup>-2</sup> s <sup>-1</sup> )	CHF,† Exp. (kW m <sup>-2</sup> )	CHF,‡ Equation (4) (kW m <sup>-2</sup> )	CHF,§ Katto and Haramura [14] (kW m <sup>-2</sup> )	Percentage error Exp. – Equation (4) Exp.
132	105	111.8	205.8	–6.5
242	108	115	209	–6.5
352	108.6	117	210.6	–7.7
462	114.2	118.7	212	–3.9
560	116.5	120	215.2	–3.0

† CHF data for a tube in an unheated bundle.

‡ Prediction of equation (4) for the bundle CHF ( $H = 2X_T$ ).

§ Prediction of CHF for a single tube in an infinite pool [14].

Figure 30. CHF data captured by Yao and Hwang [30] for their tube array experiments compared against their correlation and Haramura and Katto's model.

The study of Leroux and Jensen [31] examined how CHF varied as a function of mass flux and local quality for four test geometries, three of which were presented in this study, one from a prior study. They examined mass fluxes ranging from 50 to 500 kg/m<sup>2</sup>s, qualities from 0 to near 100%, and their test geometry was a 5x27 array in both staggered and inline geometries with P/D ratios of 1.3 and 1.7 for both. Very generally, they noted that a DNB type CHF occurred for their low mass flux, low quality data, and for higher flow, higher qualities, a dryout type CHF was thought to have occurred.

Leroux and Jensen [31] found three types of CHF vs quality curves depending upon the mass flux and can be seen in Figure 31. The first pattern was thought to correspond to a pure DNB process with the 2<sup>nd</sup> and 3<sup>rd</sup> corresponding to a dryout type CHF at a certain quality, with some sort of transitional mechanism in between.

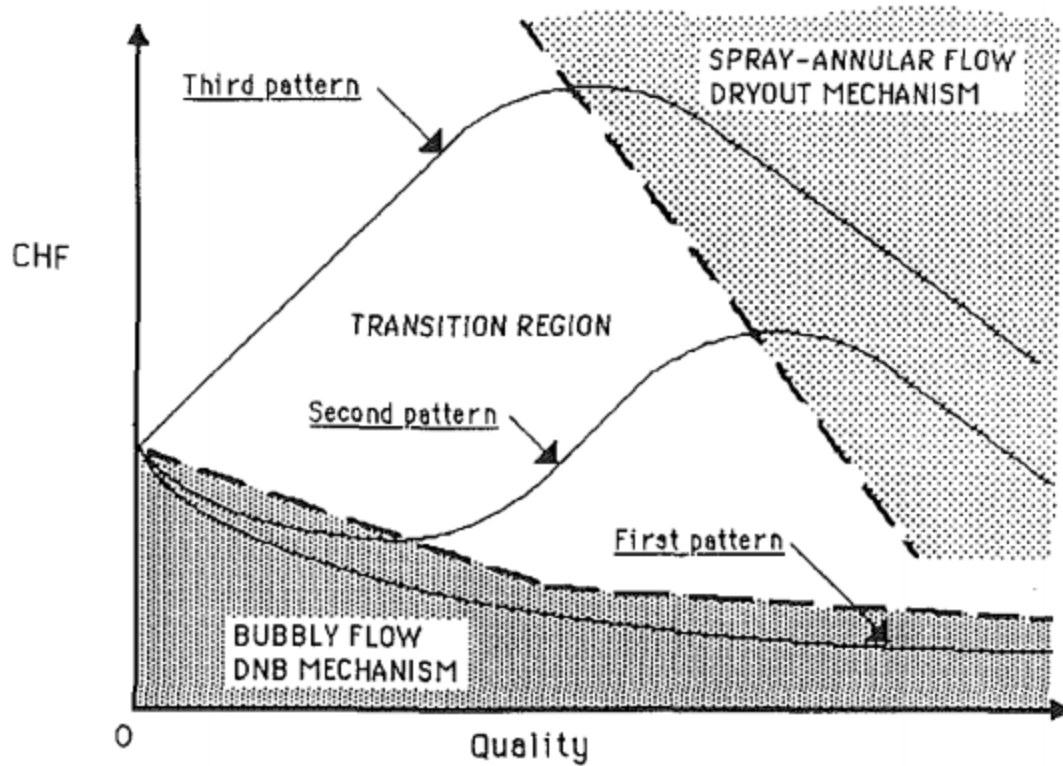


Figure 31. Three CHF vs quality curves that Leroux and Jensen [31] found from their data.

In terms of geometry effects, Leroux and Jensen [31] state that increases in  $P/D$  were found to decrease CHF margin in the case of the inline bundle. For the staggered bundle, they also state that a decrease in CHF was found, but tends to disappear at higher mass fluxes.

The study of Dykas and Jensen [32] examined CHF for a single heated tube in a  $5 \times 27$  inline tube array with a  $P/D$  of 1.3. They noted that upon inspection of their CHF heaters after use, that burn marks were found near the rear stagnation point of their cylinder, indicating that CHF occurred first there. All of the trends previously

described in the Leroux and Jensen [32] section we also found in this paper and these two studies are considered to be companion pieces. They also state that the CHF found for their single heated tests with zero inlet quality are in the range of 10-20% lower than that of the single isolated tube case.

Jensen and Tang [33] used data gathered from the prior studies of Leroux and Jensen [31] and the study of Dykas and Jensen [32] to develop a correlation to cover all three sets of the CHF vs quality curves found in those studies. Their correlation borrowed some transition criteria from Taitel and Dukler (1976) and depended upon whether or not the geometry was a staggered or inline array.

Symolon et al [34] performed CHF tests on a staggered array with a  $P/D = 1.5$ . They varied the mass flux and the inlet qualities and had four instrumented thermocouples on their CHF heater (Three near the top, on facing directly upstream). They noted that they saw CHF occurrence on the top side of their CHF heater and state that their bottom thermocouple was comparatively quiet. They compared their data to that of Leroux and Jensen [31] and to the correlation of Jensen and Tang [33], and found satisfactory agreement.

### 9.7.1 Enhancement Effect

The studies of Chan and Shoukri [26] and Cumo et al [28] both clearly indicate that there is an enhancement effect that can happen for CHF in a tube array when

additional void from below the CHF heater is added. Both experimental studies also indicate that this effect begins to slow down, indicating that some threshold amount of void is enough to get most of the enhancement effect. This is particularly encouraging as both of these studies were for relatively low mass fluxes (zero in Chan and Shoukri's [26] case). Cumo et al [28] attempted to trace this enhancement effect down to an added kinetic energy term based on the 2-phase mixture velocity, adding another method to remove heat for a near-pool boiling CHF process. The idea to add this effect to the pool boiling CHF seems very promising, but their specific attempt failed to capture the tail off in the enhancement effect observed in their CHF data.

### 9.7.2 Diminishment Effect

Chan and Shoukri [26] explained this diminishment effect as a vapor blanketing effect caused by void/void generation above the CHF heater increasing flow resistance. This added flow resistance was thought to trigger a lower CHF as void generated by the heater does not depart the surface/vicinity of the heater as easily. This effect is seen to be lower than the enhancement effect (almost negligible by comparison) in Chan and Shoukri's [26] data and is noted to be completely absent in Thibault's [27] datasets. An added note is that it appears that only the nearest neighbour tube to the CHF cylinder appears to negatively impact CHF. This may indicate that there is some sort of local drag effect due to the neighbouring tube, which becomes much weaker further from the CHF tube, due to the increase in

space and potentially some void drift (i.e. void flowing mostly in the channel between tubes in an inline array).

It is also important to note that most of studies did note a diminishment in CHF for a tube array compared to the single cylinder case. The study of Thibault [27] noted no change, and even an enhancement, but it also appears that his study would always have the enhancement effect on some tubes due to the nature of quenching experiments so the applicability of his findings to this particular effect are unclear. It would appear that there may be two different factors may be at work to reduce CHF in tube arrays, a drag type effect causing vapor to have a harder time leaving the CHF surface due to the immediately neighbouring upward tubes. A secondary factor could be a reduction in the natural circulation of single-phase liquid due to the presence of the tube array itself.

### 9.7.3 Flaws in experimental studies

A major flaw in nearly all of the experimental studies on CHF in tube arrays is a lack of void fraction measurements. The only study that did void fraction measurements was Chan and Shoukri [26], however they did not report any for their CHF measurements. Several of these studies do however show a strong effect of void on CHF, with enhancements compared to the no void case of upwards of 10-15%, although this directly conflicts with the data collected by Leroux and Jensen [31] as their experiments showed that for low mass fluxes only decreases in CHF can be noted.

Another major flaw with all of these studies is a lack of variety in working fluids, most notably a lack of experiments with water. Nearly all of these experimental studies used R-113, with a single study using R-12 and a single study using water. Unfortunately, the water data was obtained via transient CHF experiments and is unclear how directly applicable it is in comparison to the refrigerants data that is all captured via steady state experiments.

Finally, nearly all of these experiments covered the P/D range of 1.3 to 1.5, and used cylinders in the diameter range 8mm-19mm. This means that there is a wide range of test geometries, most notably P/D that need further examination to explain some gaps or inconsistencies in the various studies. Most notably, why does CHF decrease for some of these tube arrays compared to the single tube case and not for the large diameter and pitch case of Thibault [27]? A current theory may perhaps be due to the larger magnitude of the pitch itself in comparison to the most critical wavelength of instability that is predicted via Kelvin-Helmholtz instability. A potential theory could take the form of when the actual value of the pitch is much greater than this value (~30mm for water), no reduction in CHF is observed, as noted by Thibault [27] ( $P = 277\text{mm}$ ). Whereas when the pitch is similar in magnitude as in nearly all other studies, (Chan and Shoukri [26],  $\lambda=11\text{mm}$ ,  $P = 30\text{mm}$ ), a reduction in CHF is noted.

## 9.8 Design Drawings

Note all dimensions are in millimeters unless otherwise stated

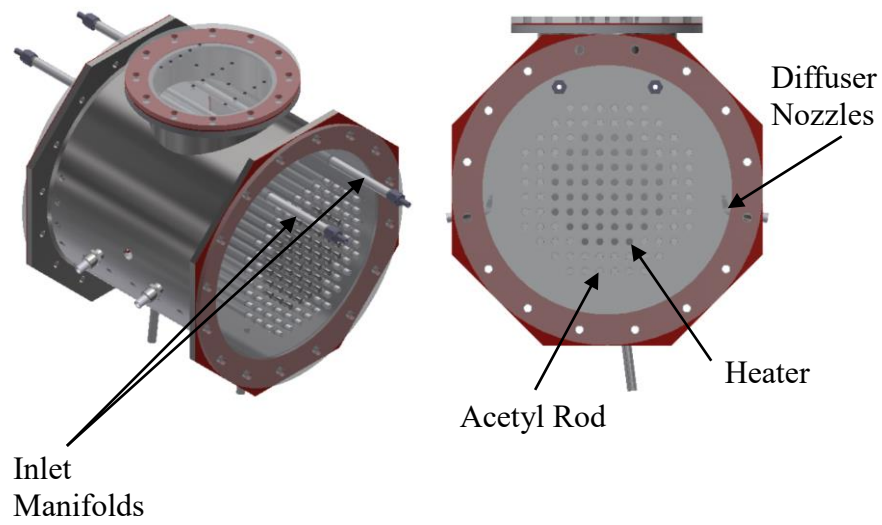


Figure 32. Isometric for the test section for used in the experiments in section 5

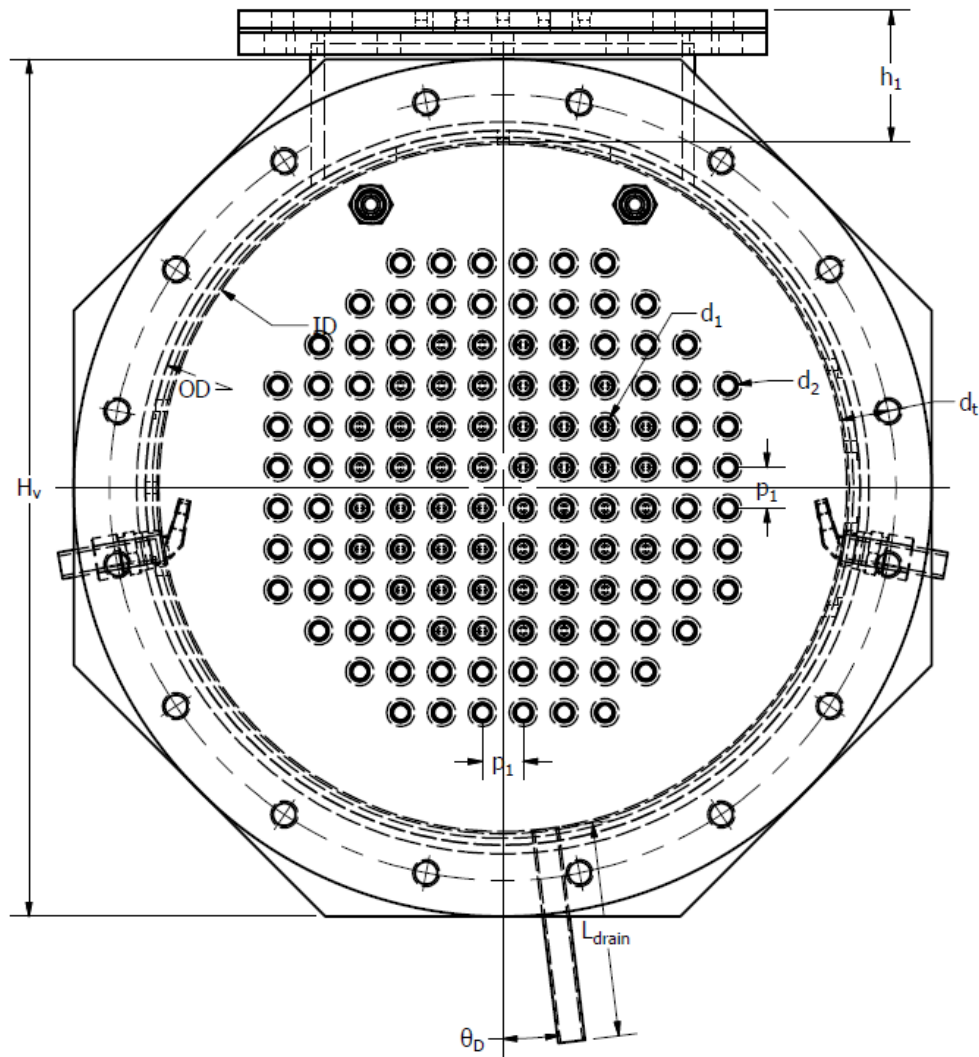


Figure 33. Test section front view for section 5 cross-section

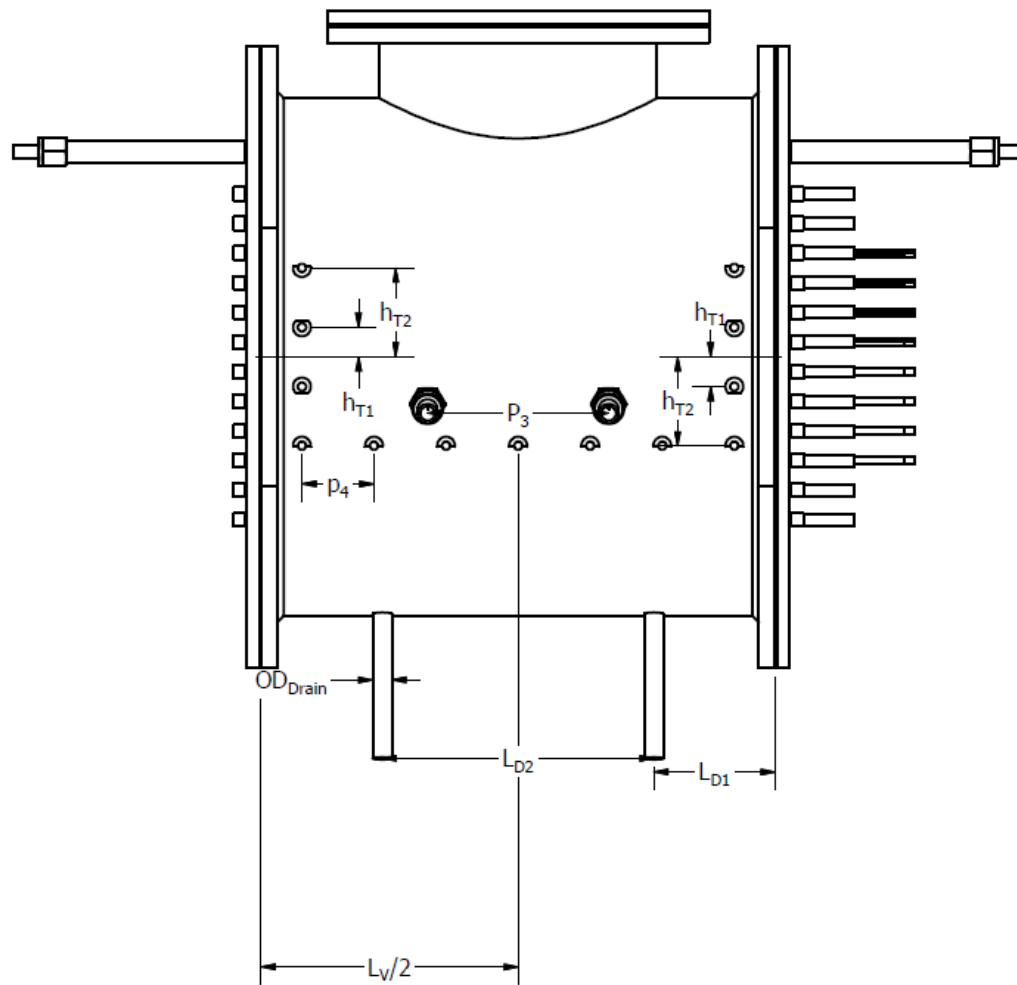


Figure 34. Test section front view for section 5 East side view

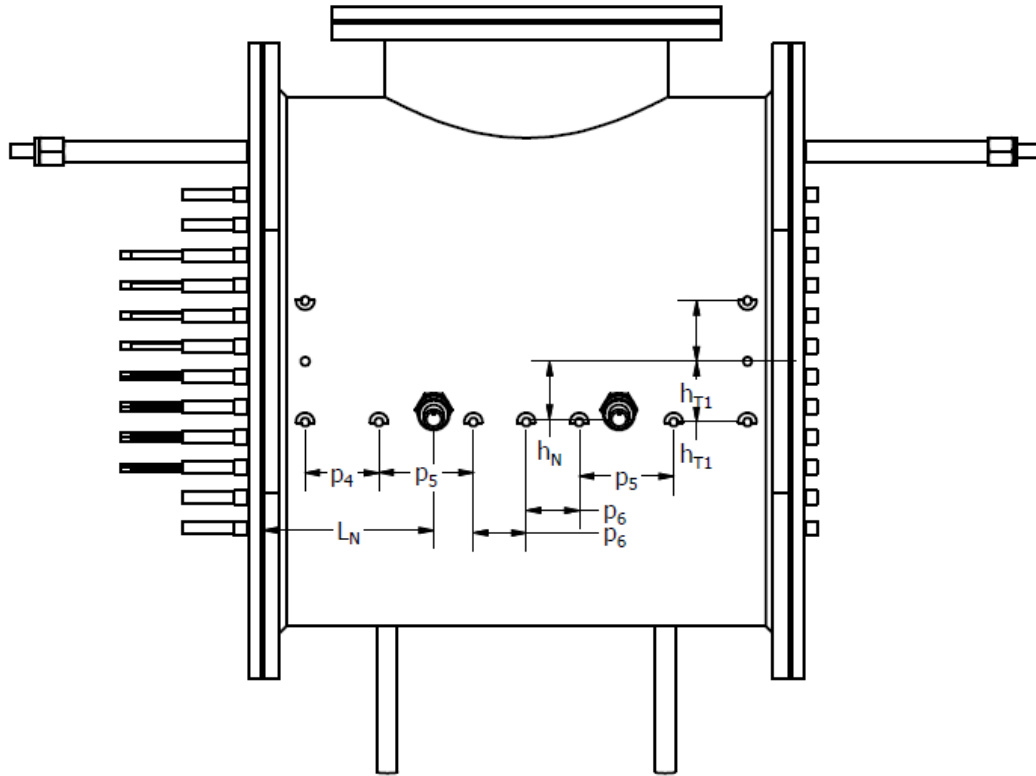


Figure 35. Test section front view for section 5 West side view

Table 1: Design and measured values for the test section used in section 5

Parameter	Value	Comment
ID	19.269	Inner Diameter of vessel [in]
OD	19.630	Outer Diameter of vessel [in]
p1	$1.145 \pm 0.005$	Tube-bank pitch [in]
d1	$0.5337 \pm 0.0008$	Heated rod outer diameter [in]
d2	$0.5336 \pm 0.0012$	Unheated rod outer diameter [in]
d <sub>t</sub>	$1.396 \pm 0.023$	Bolt-hole to inner tank wall distance [in]
h <sub>l</sub>	3.487	Height of Laser Access port [in]
H <sub>V</sub>	23.933	Vessel Flange Height [in]
L <sub>D</sub>	6.000	Drain Port Length [in]
θ <sub>D</sub>	7	Drain Port Angle [degrees]
h <sub>T1</sub>	1.144	Height of Thermocouples from centreline [in]

$h_{T2}$	3.432	Height of Thermocouples from centreline [in]
$p_4$	$2.788 \pm 0.005$	Spacing Between Thermocouples on East Side [in]
$P_3$	$7.036 \pm 0.036$	Spacing Between Nozzles [in]
$OD_{\text{Drain}}$	$0.7535 \pm 0.002$	Outer Diameter of Drains [in]
$L_v$	$19.872 \pm 0.036$	Length of Vessel [in]
$L_{D1}$	$4.731 \pm 0.018$	Distance from Flange to Drain [in]
$L_{D2}$	$10.536 \pm 0.01$	Distance from Drain to Drain [in]
$p_5$	$2.007 \pm 0.003$	Horizontal Spacing of Thermocouples in proximity to Nozzles [in]
$p_6$	$3.572 \pm 0.003$	Horizontal Spacing of Thermocouples in between Nozzles [in]
$h_N$	2.183	Vertical Distance of Nozzles below centreline [in]
$L_N$	6.435	Distance of Nozzles from Flange Face [in]

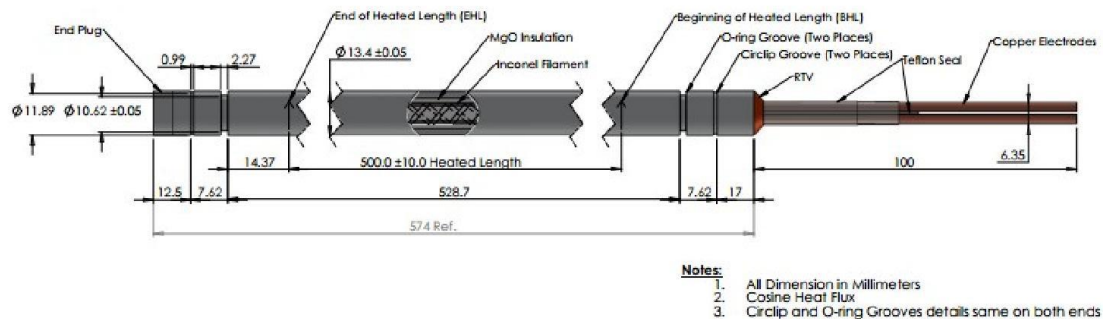


Figure 36: Test section heater used in section 5 and as Heater A in sections 3 and 4.

Table 2: Heated assembly specifications

Parameter	Design specification	Measured value / test condition
Operating pressure (max) [MPa]	1.0	N/A
Nominal power [kW]	1.0	Test dependent
Nominal voltage [V]	20	Test dependent
Nominal current [A]	50	Test dependent
Maximum linear power [kW/m]	2.8	N/A

Average surface heat flux [kW/m <sup>2</sup> ]	47.5	Test dependent
Outside diameter [mm]	13.40 ± 0.05	13.42 ± 0.02
Straightness over 1.0 m [mm]	≤ 1.26	N/A
Heated length [mm]	500 ± 10	N/A
Filament resistance (25°C) [Ω]	0.392 ± 0.020	0.378

Heater B used in section 3 and 4 is geometrically nearly identical to Heater A outlined above with a few key differences. Heater B is a double ended heater design which and contained instrumented thermocouples. Due to Departure from Nucleate Boiling (DNB) experiments in between sections 3 and 4, the heaters used are physically different. Each had the same physical design, with a change to the thermocouple positioning, with all of the thermocouples moved to the central heat flux region for the section 3 tests. Note, in Table 3 and Table 4 an axial position of 170mm corresponds to the centre of the vessel. These are the thermocouples that would have been used for heat transfer measurements with the additional thermocouples being added for the purpose of DNB identification. Additionally, the heater was installed such that thermocouple A would be positioned upward i.e. the highest point of the cylinder.

Table 3. Thermocouple Positioning: Heater B used in section 3 experiments

Thermocouple Identifier	Thermocouple Axial Position (Relative to heat flux shape) [mm]	Thermocouple Angular Position [deg]

A	170	0
B	145	15
C	170	45
D	170	900
E	170	135
F	170	180
G	170	225
H	170	270
I	170	315
J	195	345

Table 4. Thermocouple Positioning: Heater B used in section 4 experiments

Thermocouple Identifier	Thermocouple Axial Position (Relative to heat flux shape) [mm]	Thermocouple Angular Position [deg]
A	170	0
B	120	36
C	170	72
D	145	108

E	195	144
F	170	180
G	220	216
H	120	252
I	170	288
J	220	324

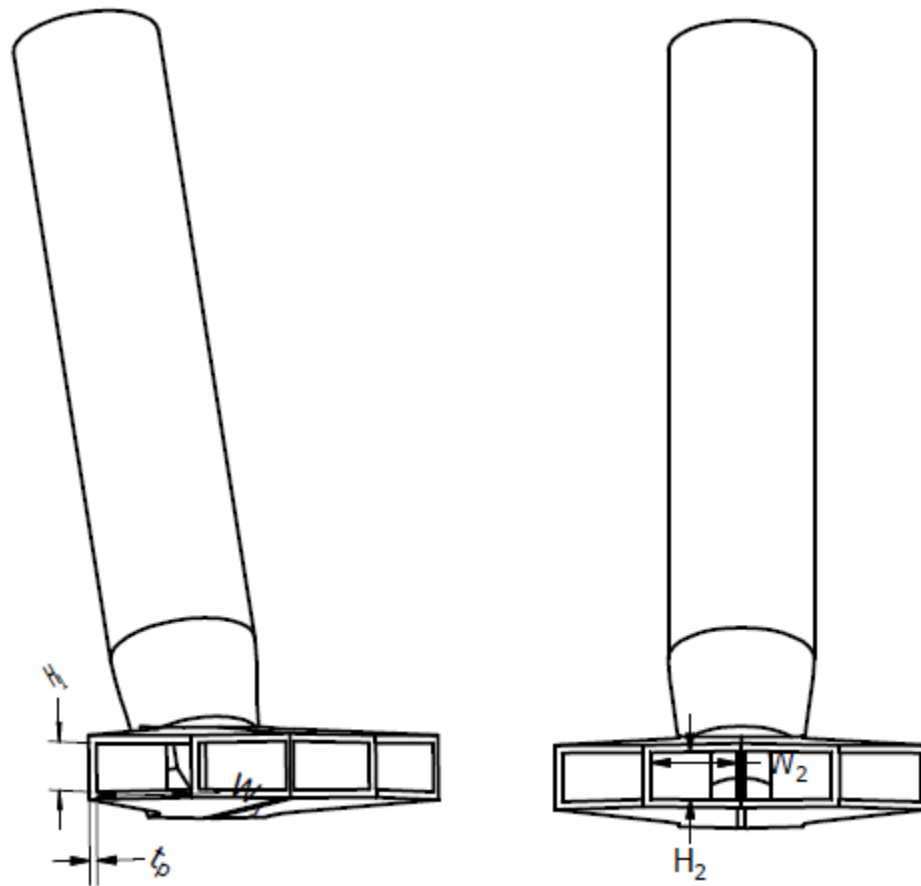


Figure 37. Front view of “Large” Diffuser Nozzles used in section 5

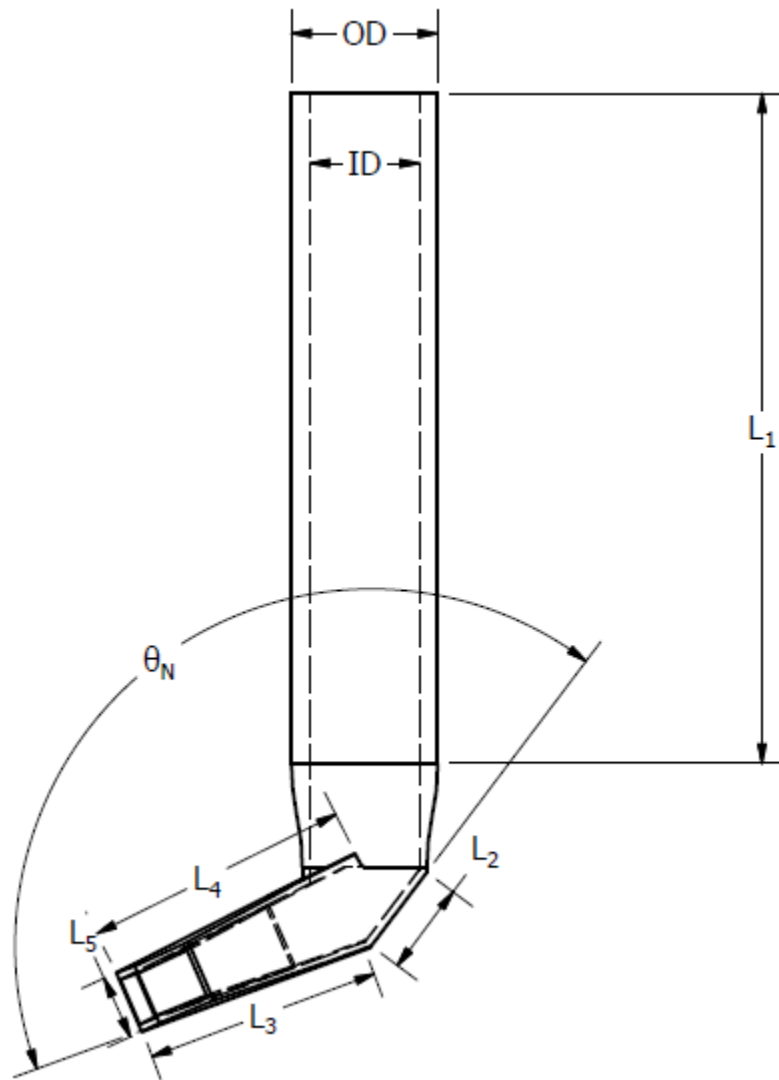


Figure 38. Side view of “Large” Diffuser Nozzles used in section 5

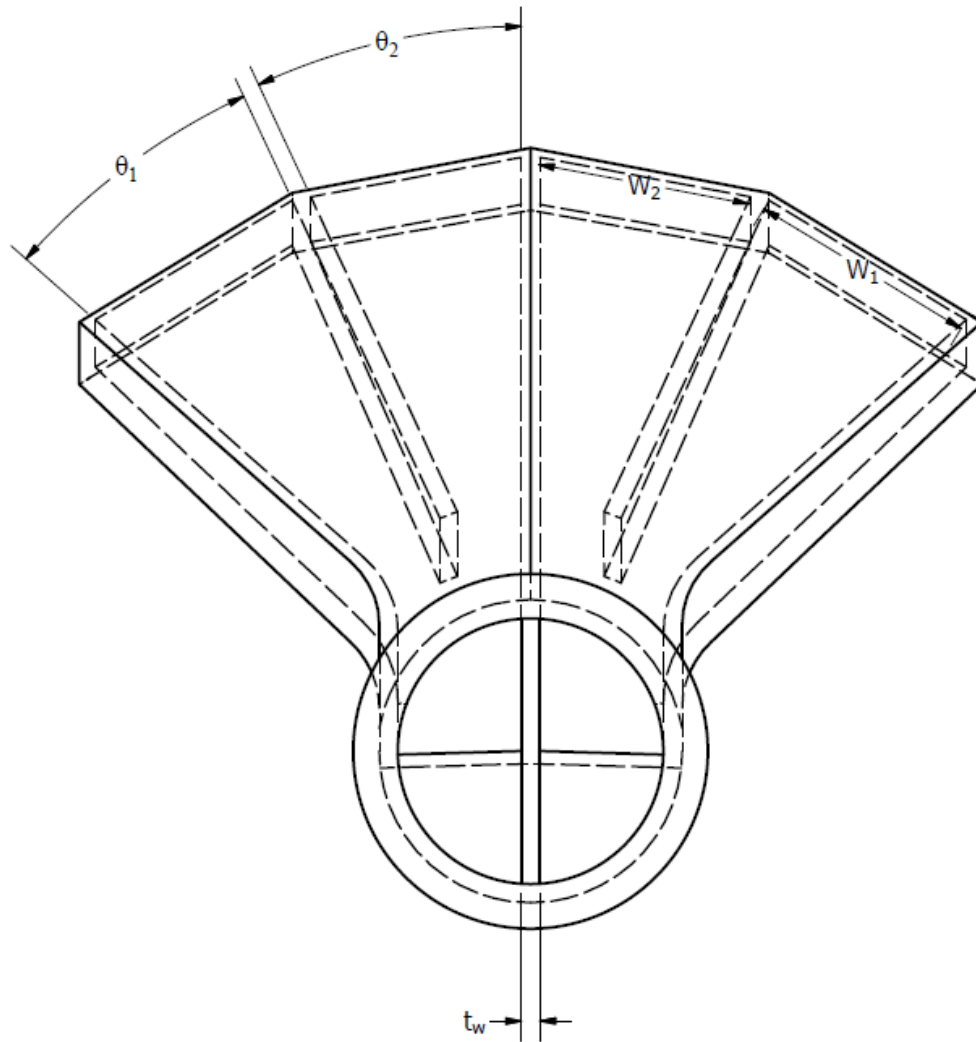


Figure 39. Back view of “Large” Diffuser Nozzles used in section 5

Table 5: Displays measured and design values for the “Large” Diffuser Nozzles

Parameter	Value	Comment
ID	$0.558479 \pm 0.0031$	Inner Diameter of Nozzle [in]
OD	$0.749979 \pm 0.0017$	Outer Diameter of Nozzle [in]
L <sub>1</sub>	3.434	Entry Length to Divider Wall [in]
L <sub>2</sub>	0.473	Length of transition [in]
L <sub>3</sub>	1.215	Length of Diffuser section from transition [in]
L <sub>4</sub>	1.369	Length of Diffuser section from tube [in]
L <sub>5</sub>	0.329	Nozzle face height [in]
H <sub>1</sub>	$0.253797 \pm 0.0034$	Height of Nozzle Flow area [in]
H <sub>2</sub>	$0.248656 \pm 0.0038$	Height of Nozzle Flow area [in]
W <sub>1</sub>	$0.483375 \pm 0.0044$	Width of Nozzle Flow area [in]
W <sub>2</sub>	$0.44375 \pm 0.0029$	Width of Nozzle Flow area [in]
t <sub>p</sub>	$0.043242 \pm 0.0012$	Thickness of Nozzle Walls on outlet face [in]
θ <sub>N</sub>	149.198	Bend Angle of Nozzle [degrees]
θ <sub>1</sub>	23.558	Angle of 2 <sup>nd</sup> and 3 <sup>rd</sup> Nozzle Slots [degrees]
θ <sub>2</sub>	24.967	Angle of 1 <sup>st</sup> and 4 <sup>th</sup> Nozzle Slots [degrees]

$t_w$	0.039	Thickness of Dividing Wall [in]
-------	-------	---------------------------------

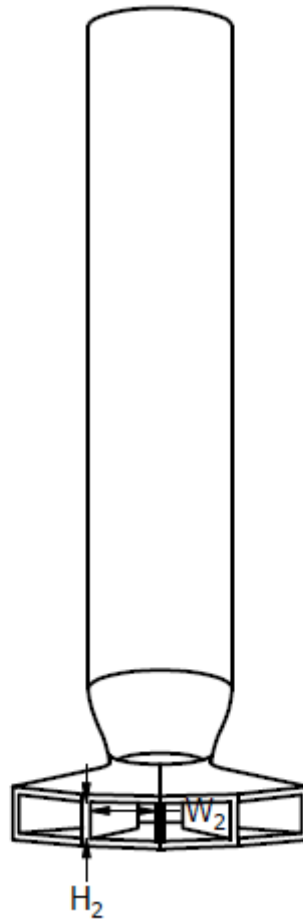


Figure 40. Front view of “small” diffuser nozzles used in section 5

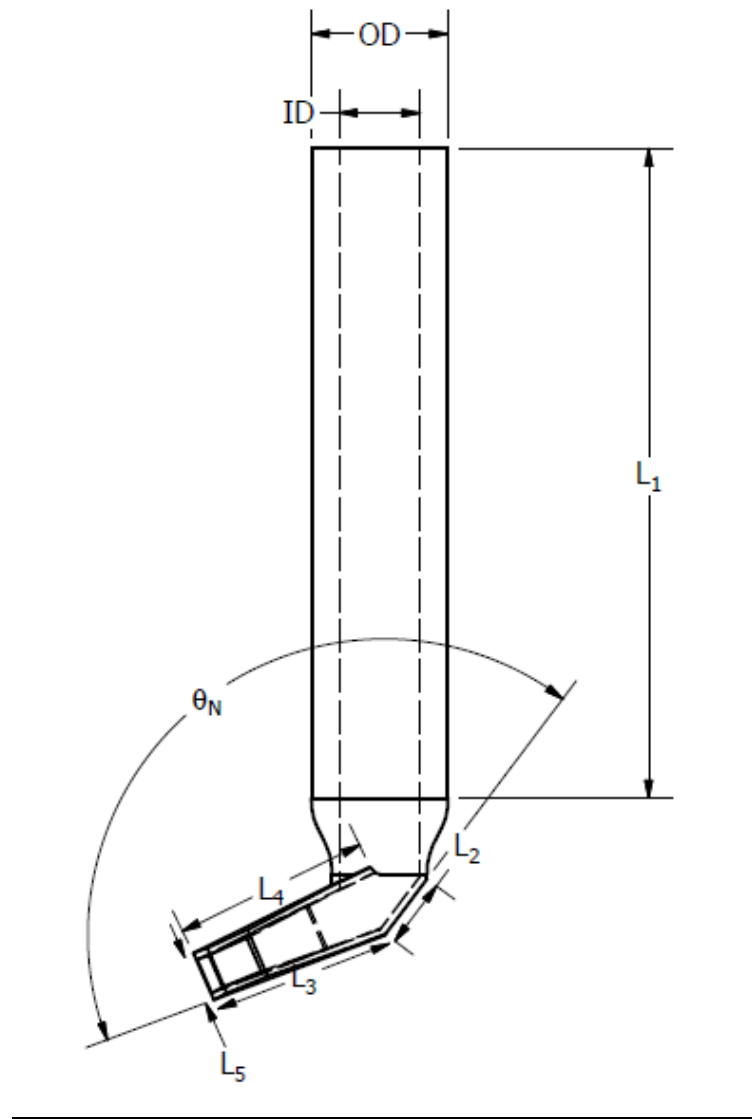


Figure 41. Side view of “small” diffuser nozzles used in section 5

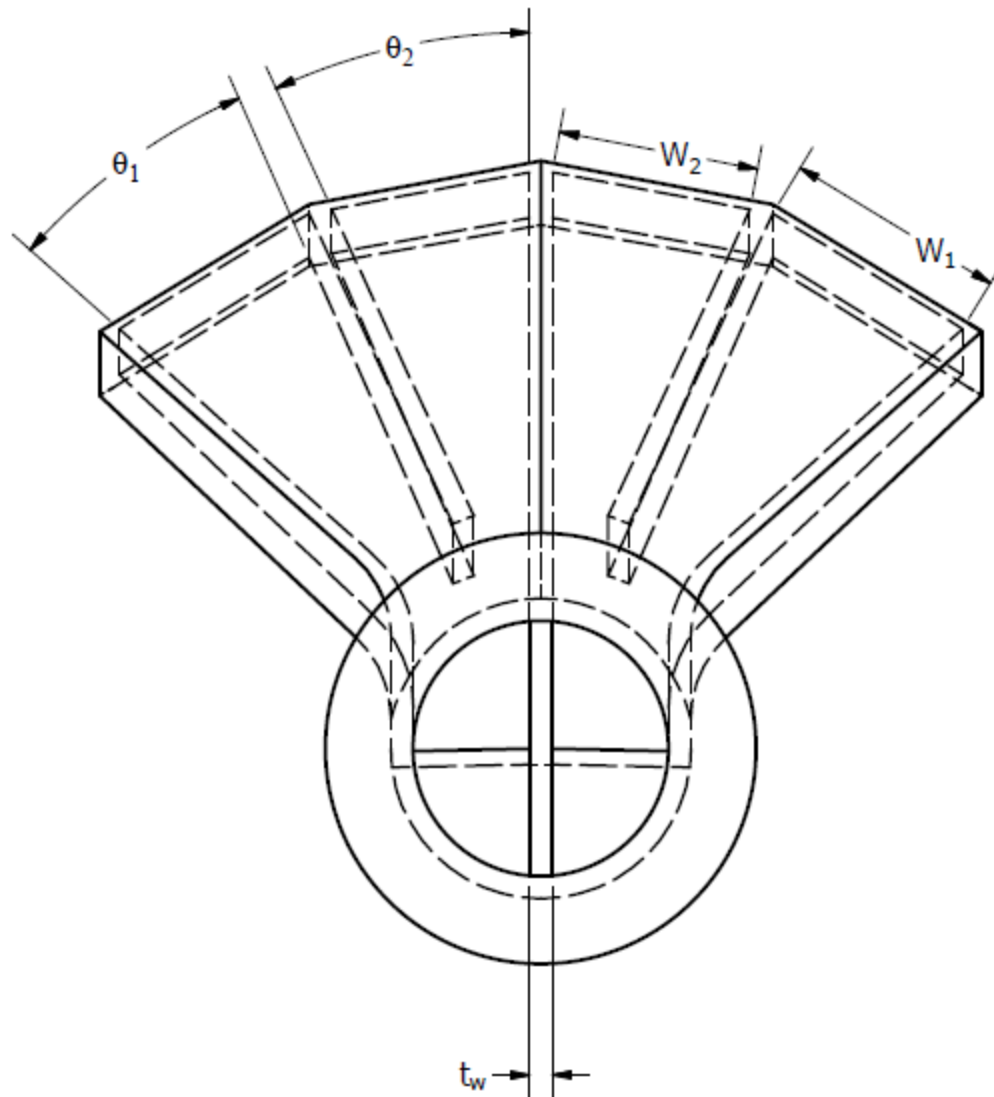


Figure 42. Rear view of “small” diffuser nozzles used in section 5

Table 6: Measured and design values for the “Small” Diffuser Nozzles used in section 5

Parameter	Dimension	Description
ID	$0.4386 \pm 0.0018$	Inner diameter of nozzle [in]
OD	$0.7492 \pm 0.0037$	Outer diameter of nozzle [in]
L <sub>1</sub>	3.574	Entry length to divider wall [in]
L <sub>2</sub>	0.380	Length of transition [in]
L <sub>3</sub>	1.007	Length of diffuser section from transition [in]
L <sub>4</sub>	1.080	Length of diffuser section from tube [in]
L <sub>5</sub>	0.279	Nozzle face height [in]
H <sub>1</sub>	$0.2063 \pm 0.0017$	Height of nozzle flow area [in]
H <sub>2</sub>	$0.2056 \pm 0.0026$	Height of nozzle flow area [in]
W <sub>1</sub>	$0.3867 \pm 0.0030$	Width of nozzle flow area [in]
W <sub>2</sub>	$0.3463 \pm 0.0058$	Width of nozzle flow area [in]
t <sub>p</sub>	$0.0423 \pm 0.0006$	Thickness of nozzle walls on outlet face [in]
θ <sub>N</sub>	147.6	Bend angle of nozzle <small>Error! Bookmark not defined.</small> [degrees]
θ <sub>1</sub>	24.6	Angle of 2 <sup>nd</sup> and 3 <sup>rd</sup> nozzle slots [°]
θ <sub>2</sub>	24.9	Angle of 1 <sup>st</sup> and 4 <sup>th</sup> nozzle slots [°]
t <sub>w</sub>	0.039	Thickness of dividing wall <small>Error! Bookmark not defined.</small> [in]

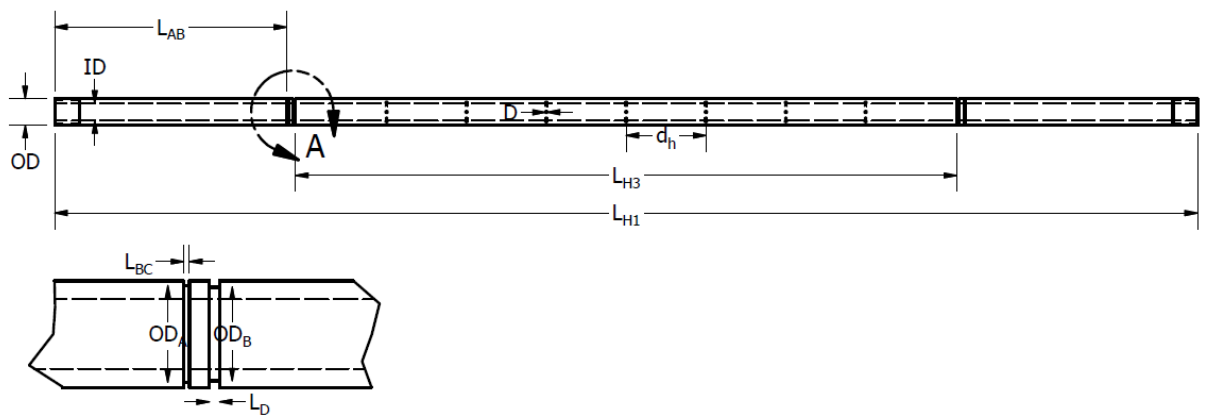


Figure 43. Front view of spray headers

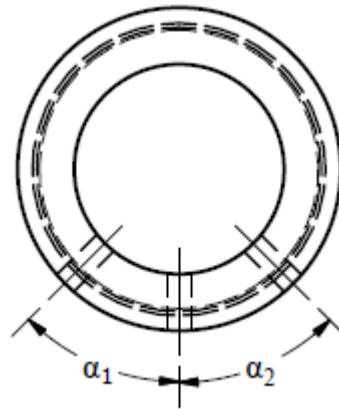


Figure 44. Side view of spray headers

Table 7: Measured and design values for the Spray Headers

Parameter	Dimension	Description
ID	$0.5217 \pm 0.0093$	Inner diameter of spray header [in]
OD	$0.8416 \pm 0.0025$	Outer diameter of spray header [in]
L <sub>AB</sub>	7.304	Length from header end to circlip groove [in]
L <sub>BC</sub>	$0.0474 \pm 0.0005$	Length of circlip groove [in]
L <sub>D</sub>	$0.0803 \pm 0.0006$	Length of O-ring groove [in]
OD <sub>A</sub>	$0.7597 \pm 0.0008$	Outer diameter of circlip section [in]
OD <sub>B</sub>	$0.7394 \pm 0.0004$	Outer diameter of O-ring section [in]
L <sub>H1</sub>	36.0	Total length of spray header [in]
L <sub>H3</sub>	20.828	Inner O-ring to inner O-ring spacing [in]
D	$0.0588 \pm 0.0004$	Diameter of discharge ports [in]
d <sub>h</sub>	$2.5160 \pm 0.0010$	Discharge port spacing [in]
$\alpha_1$	$44.2 \pm 0.3$	Angle of discharge ports from centre [°]
$\alpha_2$	$44.2 \pm 0.4$	Angle of discharge ports from centre [°]

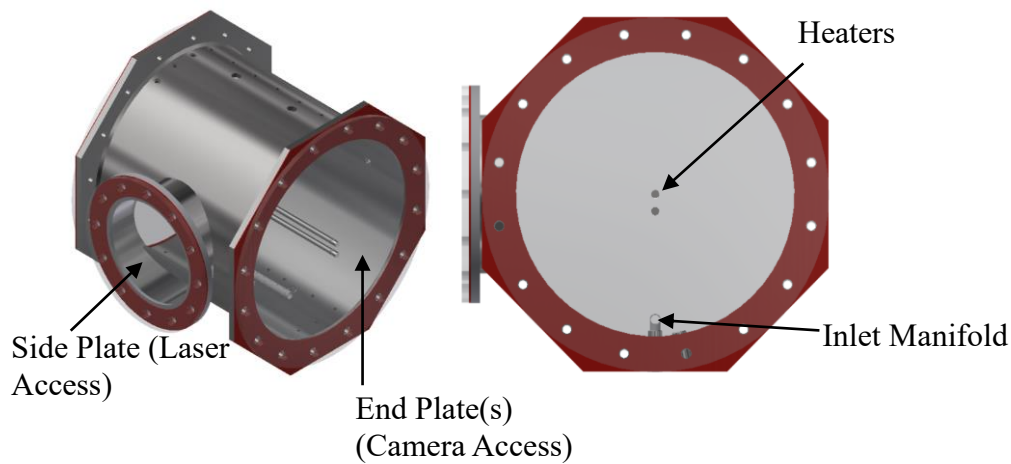


Figure 45. Isometrics showing the test section orientation for experiments in section 4



Figure 46. Assembled inlet manifold for section 4 tests

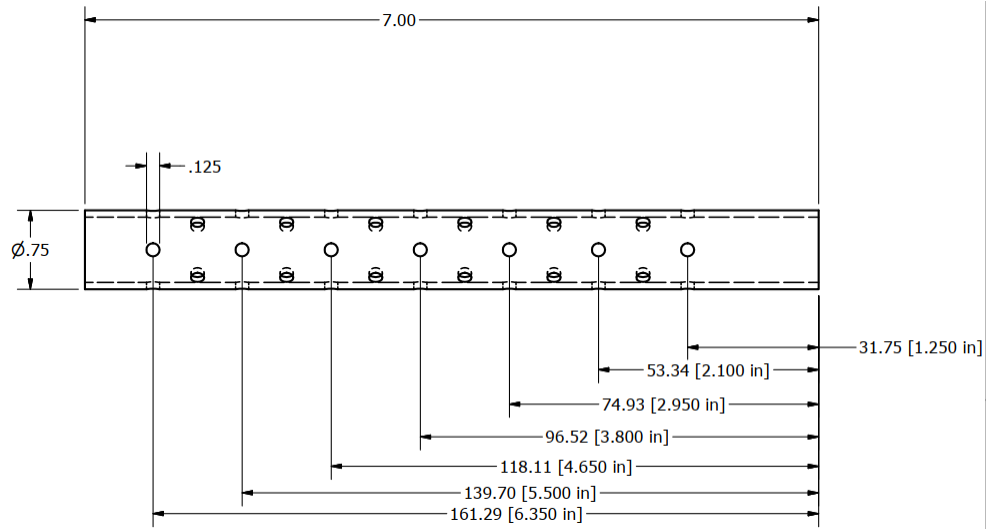


Figure 47. Inlet Manifold used in section 4 connection piece – 0-degree view

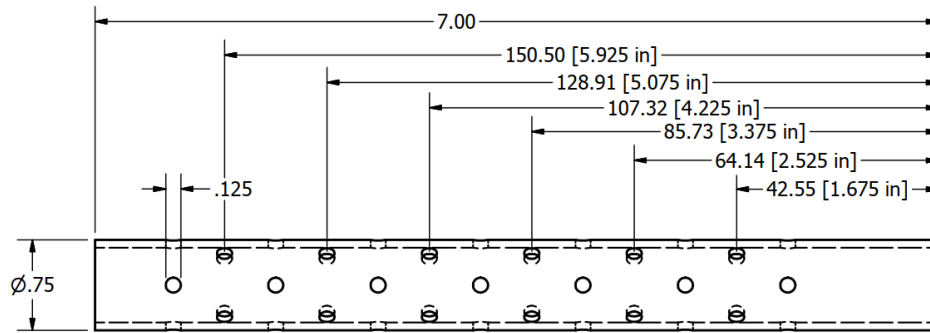


Figure 48. Inlet Manifold used in section 4: 45-degree view

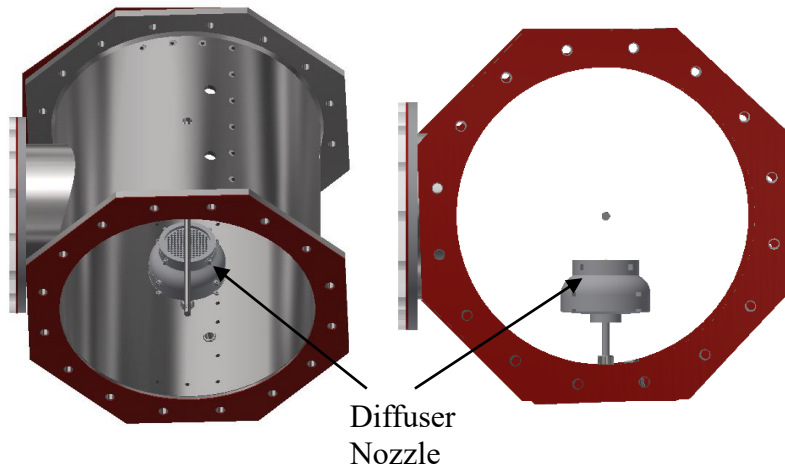


Figure 49. Isometrics of the test section setup for experiments in section 3.

## 9.9 Calibration Documents

Using a hot water temperature bath generously lent by Dr. Cotton, all of the thermocouples used in the 1/16<sup>th</sup> scale vessel experiments and all subsequent experiments were calibrated. This data, and fit coefficients is summarized below in Table 8. In general, none of the thermocouple deviated greater than uncertainty from the RTD temperature in the 25->50C range.

Table 8. Thermocouple Calibration Data

<b>Thermocouple ID</b>	<b>RTD Temperature (°C)</b>	<b>Uncalibrated Temperature (°C)</b>	<b>Calibrated Temperature (°C)</b>
TCT-28	24.98	25.01	24.94
	30.11	30.18	30.09
	35.03	35.16	35.06
	40.03	40.18	40.05
	44.96	45.12	44.98
	50.23	50.39	50.24
	55.13	55.30	55.14
	60.07	60.27	60.09
	64.95	65.14	64.94
	69.94	70.15	69.93
	74.99	75.20	74.96
TCT-29	24.98	25.00	24.96
	30.11	30.18	30.10
	35.03	35.15	35.05
	40.03	40.18	40.05
	44.96	45.14	44.97
	50.23	50.41	50.22

<b>Thermocouple ID</b>	<b>RTD Temperature (°C)</b>	<b>Uncalibrated Temperature (°C)</b>	<b>Calibrated Temperature (°C)</b>
	55.13	55.34	55.11
	60.07	60.34	60.09
	64.95	65.23	64.94
	69.94	70.27	69.95
	74.99	75.34	74.99
TCT-30	24.98	25.04	24.97
	30.11	30.19	30.10
	35.03	35.15	35.04
	40.03	40.18	40.04
	44.96	45.13	44.97
	50.23	50.42	50.23
	55.13	55.33	55.12
	60.07	60.32	60.08
	64.95	65.23	64.96
	69.94	70.22	69.93
	74.99	75.30	74.98
TCT-31	24.98	25.03	24.96
	30.11	30.17	30.10

<b>Thermocouple ID</b>	<b>RTD Temperature (°C)</b>	<b>Uncalibrated Temperature (°C)</b>	<b>Calibrated Temperature (°C)</b>
	35.03	35.12	35.05
	40.03	40.09	40.02
	44.96	45.06	44.98
	50.23	50.33	50.24
	55.13	55.22	55.13
	60.07	60.16	60.06
	64.95	65.06	64.96
	69.94	70.00	69.90
	74.99	75.11	75.01
TCT-32	24.98	24.99	24.95
	30.11	30.15	30.06
	35.03	35.14	35.04
	40.03	40.16	40.04
	44.96	45.10	44.96
	50.23	50.38	50.23
	55.13	55.30	55.13
	60.07	60.27	60.08
	64.95	65.17	64.97

<b>Thermocouple ID</b>	<b>RTD Temperature (°C)</b>	<b>Uncalibrated Temperature (°C)</b>	<b>Calibrated Temperature (°C)</b>
	69.94	70.17	69.96
	74.99	75.22	74.99
TCT-33	24.98	25.04	24.98
	30.11	30.18	30.10
	35.03	35.14	35.03
	40.03	40.18	40.04
	44.96	45.13	44.97
	50.23	50.41	50.22
	55.13	55.33	55.12
	60.07	60.33	60.09
	64.95	65.23	64.96
	69.94	70.22	69.93
	74.99	75.29	74.98
TCT-34	24.98	25.00	24.97
	30.11	30.15	30.09
	35.03	35.13	35.04
	40.03	40.15	40.04
	44.96	45.10	44.97

<b>Thermocouple ID</b>	<b>RTD Temperature (°C)</b>	<b>Uncalibrated Temperature (°C)</b>	<b>Calibrated Temperature (°C)</b>
	50.23	50.39	50.23
	55.13	55.31	55.13
	60.07	60.30	60.09
	64.95	65.19	64.95
	69.94	70.21	69.94
	74.99	75.26	74.97
TCT-35	24.98	25.03	24.94
	30.11	30.19	30.09
	35.03	35.18	35.06
	40.03	40.20	40.06
	44.96	45.14	44.98
	50.23	50.41	50.23
	55.13	55.33	55.13
	60.07	60.30	60.09
	64.95	65.18	64.95
	69.94	70.19	69.94
	74.99	75.24	74.97
TCT-36	24.98	25.02	24.96

<b>Thermocouple ID</b>	<b>RTD Temperature (°C)</b>	<b>Uncalibrated Temperature (°C)</b>	<b>Calibrated Temperature (°C)</b>
	30.11	30.16	30.09
	35.03	35.10	35.03
	40.03	40.14	40.06
	44.96	45.06	44.97
	50.23	50.34	50.24
	55.13	55.24	55.13
	60.07	60.19	60.08
	64.95	65.08	64.95
	69.94	70.06	69.93
	74.99	75.11	74.97
TCT-37	24.98	25.02	24.94
	30.11	30.18	30.09
	35.03	35.16	35.05
	40.03	40.19	40.07
	44.96	45.13	45.00
	50.23	50.37	50.22
	55.13	55.28	55.12
	60.07	60.25	60.08

<b>Thermocouple ID</b>	<b>RTD Temperature (°C)</b>	<b>Uncalibrated Temperature (°C)</b>	<b>Calibrated Temperature (°C)</b>
	64.95	65.14	64.95
	69.94	70.14	69.94
	74.99	75.18	74.97
TCT-38	24.98	25.08	24.97
	30.11	30.24	30.09
	35.03	35.21	35.04
	40.03	40.25	40.05
	44.96	45.19	44.96
	50.23	50.50	50.24
	55.13	55.43	55.14
	60.07	60.40	60.08
	64.95	65.30	64.95
	69.94	70.31	69.94
	74.99	75.36	74.97
TCT-39	24.98	25.11	24.95
	30.11	30.27	30.09
	35.03	35.24	35.04
	40.03	40.28	40.06

<b>Thermocouple ID</b>	<b>RTD Temperature (°C)</b>	<b>Uncalibrated Temperature (°C)</b>	<b>Calibrated Temperature (°C)</b>
	44.96	45.22	44.98
	50.23	50.49	50.23
	55.13	55.41	55.13
	60.07	60.38	60.08
	64.95	65.27	64.95
	69.94	70.28	69.94
	74.99	75.33	74.96
TCT-40	24.98	25.10	24.96
	30.11	30.25	30.10
	35.03	35.22	35.04
	40.03	40.26	40.05
	44.96	45.21	44.98
	50.23	50.47	50.22
	55.13	55.39	55.12
	60.07	60.37	60.07
	64.95	65.28	64.96
	69.94	70.28	69.94
	74.99	75.36	74.99

<b>Thermocouple ID</b>	<b>RTD Temperature (°C)</b>	<b>Uncalibrated Temperature (°C)</b>	<b>Calibrated Temperature (°C)</b>
TCT-41	24.98	25.12	24.94
	30.11	30.27	30.08
	35.03	35.25	35.05
	40.03	40.26	40.06
	44.96	45.19	44.98
	50.23	50.46	50.24
	55.13	55.35	55.13
	60.07	60.31	60.09
	64.95	65.17	64.94
	69.94	70.16	69.93
	74.99	75.20	74.96
TCT-42	24.98	25.13	24.98
	30.11	30.27	30.11
	35.03	35.21	35.03
	40.03	40.23	40.03
	44.96	45.21	44.98
	50.23	50.48	50.23
	55.13	55.39	55.13

<b>Thermocouple ID</b>	<b>RTD Temperature (°C)</b>	<b>Uncalibrated Temperature (°C)</b>	<b>Calibrated Temperature (°C)</b>
	60.07	60.31	60.02
	64.95	65.27	64.97
	69.94	70.27	69.95
	74.99	75.34	75.00
TCT-43	24.98	25.06	24.95
	30.11	30.23	30.09
	35.03	35.19	35.04
	40.03	40.24	40.07
	44.96	45.17	44.98
	50.23	50.44	50.24
	55.13	55.35	55.13
	60.07	60.32	60.08
	64.95	65.21	64.95
	69.94	70.22	69.94
	74.99	75.25	74.96
TCT-44	24.98	24.96	24.98
	30.11	30.09	30.08
	35.03	35.09	35.04

<b>Thermocouple ID</b>	<b>RTD Temperature (°C)</b>	<b>Uncalibrated Temperature (°C)</b>	<b>Calibrated Temperature (°C)</b>
	40.03	40.13	40.05
	44.96	45.10	44.99
	50.23	50.37	50.22
	55.13	55.29	55.11
	60.07	60.29	60.07
	64.95	65.17	64.92
	69.94	70.22	69.94
	74.99	75.32	75.01
TCT-45	24.98	24.96	24.95
	30.11	30.13	30.09
	35.03	35.10	35.04
	40.03	40.14	40.06
	44.96	45.08	44.97
	50.23	50.36	50.24
	55.13	55.28	55.13
	60.07	60.26	60.08
	64.95	65.14	64.95
	69.94	70.15	69.93

<b>Thermocouple ID</b>	<b>RTD Temperature (°C)</b>	<b>Uncalibrated Temperature (°C)</b>	<b>Calibrated Temperature (°C)</b>
	74.99	75.21	74.97
TCT-46	24.98	24.97	25.02
	30.11	30.08	30.13
	35.03	34.99	35.04
	40.03	39.96	40.00
	44.96	44.87	44.91
	50.23	50.19	50.22
	55.13	55.09	55.12
	60.07	60.06	60.08
	64.95	64.94	64.96
	69.94	69.93	69.94
	74.99	75.01	75.01
TCT-47	24.98	24.96	25.01
	30.11	30.10	30.13
	35.03	35.03	35.03
	40.03	40.03	40.00
	44.96	44.95	44.90
	50.23	50.31	50.23

<b>Thermocouple ID</b>	<b>RTD Temperature (°C)</b>	<b>Uncalibrated Temperature (°C)</b>	<b>Calibrated Temperature (°C)</b>
	55.13	55.22	55.11
	60.07	60.23	60.09
	64.95	65.12	64.96
	69.94	70.14	69.96
	74.99	75.20	74.99
TCT-48	24.98	24.95	25.01
	30.11	30.07	30.13
	35.03	34.98	35.03
	40.03	39.97	40.02
	44.96	44.86	44.91
	50.23	50.17	50.22
	55.13	55.06	55.10
	60.07	60.05	60.09
	64.95	64.93	64.97
	69.94	69.91	69.94
	74.99	74.98	75.01
TCT-49	24.98	24.99	25.01
	30.11	30.11	30.12

<b>Thermocouple ID</b>	<b>RTD Temperature (°C)</b>	<b>Uncalibrated Temperature (°C)</b>	<b>Calibrated Temperature (°C)</b>
	35.03	35.01	35.01
	40.03	40.00	40.00
	44.96	44.97	44.96
	50.23	50.25	50.23
	55.13	55.14	55.12
	60.07	60.10	60.08
	64.95	64.97	64.94
	69.94	69.98	69.95
	74.99	75.05	75.01
TCT-50	24.98	24.97	25.01
	30.11	30.12	30.13
	35.03	35.05	35.03
	40.03	40.06	40.01
	44.96	44.98	44.90
	50.23	50.33	50.23
	55.13	55.24	55.11
	60.07	60.25	60.09
	64.95	65.15	64.96

<b>Thermocouple ID</b>	<b>RTD Temperature (°C)</b>	<b>Uncalibrated Temperature (°C)</b>	<b>Calibrated Temperature (°C)</b>
	69.94	70.17	69.95
	74.99	75.25	75.00
TCT-51	24.95	24.98	24.93
	30.05	30.12	30.04
	35.01	35.13	35.02
	40.00	40.16	40.03
	45.10	45.27	45.11
	50.13	50.27	50.09
	54.92	55.12	54.92
	60.02	60.28	60.05
	64.90	65.19	64.94
	70.07	70.31	70.03
	75.04	75.32	75.02
TCT-52	24.98	24.93	24.99
	30.11	30.03	30.05
	35.03	35.03	35.02
	40.03	40.13	40.08
	44.96	45.09	45.00

<b>Thermocouple ID</b>	<b>RTD Temperature (°C)</b>	<b>Uncalibrated Temperature (°C)</b>	<b>Calibrated Temperature (°C)</b>
	50.23	50.36	50.23
	55.13	55.28	55.12
	60.07	60.28	60.08
	64.95	65.18	64.94
	69.94	70.21	69.93
	74.99	75.30	74.99
TCT-53	24.98	24.87	24.97
	30.11	29.98	30.04
	35.03	35.02	35.04
	40.03	40.11	40.09
	44.96	45.06	45.00
	50.23	50.34	50.24
	55.13	55.26	55.12
	60.07	60.25	60.07
	64.95	65.15	64.93
	69.94	70.19	69.93
	74.99	75.28	74.98
TCT-54	24.98	25.12	25.01

<b>Thermocouple ID</b>	<b>RTD Temperature (°C)</b>	<b>Uncalibrated Temperature (°C)</b>	<b>Calibrated Temperature (°C)</b>
	30.11	30.24	30.13
	35.03	35.15	35.03
	40.03	40.13	40.01
	44.96	45.03	44.91
	50.23	50.36	50.23
	55.13	55.24	55.11
	60.07	60.22	60.09
	64.95	65.09	64.96
	69.94	70.08	69.94
	74.99	75.14	75.00
TCT-55	24.98	25.10	25.02
	30.11	30.22	30.11
	35.03	35.15	35.00
	40.03	40.20	40.02
	44.96	45.15	44.94
	50.23	50.48	50.24
	55.13	55.40	55.12
	60.07	60.41	60.10

<b>Thermocouple ID</b>	<b>RTD Temperature (°C)</b>	<b>Uncalibrated Temperature (°C)</b>	<b>Calibrated Temperature (°C)</b>
	64.95	65.29	64.94
	69.94	70.32	69.94
	74.99	75.41	74.99
TCT-56	24.98	25.14	25.01
	30.11	30.23	30.09
	35.03	35.10	34.96
	40.03	40.22	40.08
	44.96	45.15	45.01
	50.23	50.36	50.21
	55.13	55.28	55.12
	60.07	60.23	60.07
	64.95	65.11	64.94
	69.94	70.12	69.94
	74.99	75.18	75.00
TCT-57	24.98	25.18	25.00
	30.11	30.29	30.08
	35.03	35.25	35.01
	40.03	40.34	40.07

<b>Thermocouple ID</b>	<b>RTD Temperature (°C)</b>	<b>Uncalibrated Temperature (°C)</b>	<b>Calibrated Temperature (°C)</b>
	44.96	45.28	44.99
	50.23	50.53	50.20
	55.13	55.46	55.11
	60.07	60.45	60.07
	64.95	65.35	64.94
	69.94	70.38	69.94
	74.99	75.47	75.00
TCT-58	24.98	25.15	24.99
	30.11	30.25	30.09
	35.03	35.18	35.01
	40.03	40.24	40.07
	44.96	45.17	44.99
	50.23	50.39	50.20
	55.13	55.29	55.11
	60.07	60.26	60.07
	64.95	65.13	64.94
	69.94	70.14	69.94
	74.99	75.20	75.00

<b>Thermocouple ID</b>	<b>RTD Temperature (°C)</b>	<b>Uncalibrated Temperature (°C)</b>	<b>Calibrated Temperature (°C)</b>
TCT-59	24.98	25.08	24.99
	30.11	30.13	30.04
	35.03	35.16	35.05
	40.03	40.19	40.07
	44.96	45.11	44.99
	50.23	50.35	50.22
	55.13	55.25	55.11
	60.07	60.23	60.08
	64.95	65.10	64.94
	69.94	70.10	69.93
	74.99	75.17	75.00
TCT-60	24.95	25.02	24.94
	30.05	30.15	30.04
	35.01	35.15	35.01
	40.00	40.17	40.01
	45.10	45.28	45.10
	50.13	50.33	50.13
	54.92	55.16	54.93

<b>Thermocouple ID</b>	<b>RTD Temperature (°C)</b>	<b>Uncalibrated Temperature (°C)</b>	<b>Calibrated Temperature (°C)</b>
	60.02	60.30	60.05
	64.90	65.20	64.92
	70.07	70.34	70.04
	75.04	75.35	75.02
TCT-61	24.95	25.01	24.94
	30.05	30.10	30.04
	35.01	35.08	35.01
	40.00	40.07	40.01
	45.10	45.16	45.10
	50.13	50.19	50.13
	54.92	55.00	54.94
	60.02	60.10	60.04
	64.90	64.98	64.93
	70.07	70.09	70.03
	75.04	75.07	75.02
TCT-62	24.95	25.03	24.94
	30.05	30.13	30.04
	35.01	35.10	35.01

<b>Thermocouple ID</b>	<b>RTD Temperature (°C)</b>	<b>Uncalibrated Temperature (°C)</b>	<b>Calibrated Temperature (°C)</b>
	40.00	40.10	40.01
	45.10	45.19	45.10
	50.13	50.21	50.12
	54.92	55.02	54.93
	60.02	60.13	60.04
	64.90	65.01	64.93
	70.07	70.13	70.04
	75.04	75.11	75.03
TCT-63	24.95	24.99	24.97
	30.05	30.08	30.03
	35.01	35.07	34.99
	40.00	40.08	39.97
	45.10	45.19	45.05
	50.13	50.32	50.16
	54.92	55.16	54.97
	60.02	60.32	60.10
	64.90	65.19	64.94
	70.07	70.30	70.01

<b>Thermocouple ID</b>	<b>RTD Temperature (°C)</b>	<b>Uncalibrated Temperature (°C)</b>	<b>Calibrated Temperature (°C)</b>
	75.04	75.31	74.99
TCT-64	24.95	25.00	24.94
	30.05	30.13	30.02
	35.01	35.12	34.99
	40.00	40.15	39.99
	45.10	45.25	45.07
	50.13	50.31	50.10
	54.92	55.13	54.90
	60.02	60.28	60.03
	64.90	65.19	64.91
	70.07	70.33	70.03
	75.04	75.33	75.00
TCT-65	24.95	25.03	24.94
	30.05	30.13	30.04
	35.01	35.10	35.02
	40.00	40.10	40.01
	45.10	45.19	45.10
	50.13	50.21	50.12

<b>Thermocouple ID</b>	<b>RTD Temperature (°C)</b>	<b>Uncalibrated Temperature (°C)</b>	<b>Calibrated Temperature (°C)</b>
	54.92	55.01	54.92
	60.02	60.13	60.04
	64.90	65.03	64.94
	70.07	70.14	70.04
	75.04	75.12	75.02
TCT-66	24.95	25.01	24.94
	30.05	30.11	30.04
	35.01	35.09	35.01
	40.00	40.08	40.01
	45.10	45.17	45.09
	50.13	50.20	50.12
	54.92	55.01	54.93
	60.02	60.12	60.04
	64.90	65.01	64.93
	70.07	70.12	70.04
	75.04	75.10	75.02
TCT-67	24.95	25.03	24.93
	30.05	30.16	30.04

<b>Thermocouple ID</b>	<b>RTD Temperature (°C)</b>	<b>Uncalibrated Temperature (°C)</b>	<b>Calibrated Temperature (°C)</b>
	35.01	35.16	35.01
	40.00	40.18	40.01
	45.10	45.30	45.10
	50.13	50.36	50.14
	54.92	55.18	54.94
	60.02	60.31	60.04
	64.90	65.23	64.94
	70.07	70.34	70.03
	75.04	75.35	75.01
TCT-68	24.95	25.04	24.93
	30.05	30.18	30.05
	35.01	35.16	35.02
	40.00	40.18	40.02
	45.10	45.29	45.10
	50.13	50.33	50.12
	54.92	55.15	54.92
	60.02	60.28	60.03
	64.90	65.20	64.93

<b>Thermocouple ID</b>	<b>RTD Temperature (°C)</b>	<b>Uncalibrated Temperature (°C)</b>	<b>Calibrated Temperature (°C)</b>
	70.07	70.32	70.04
	75.04	75.33	75.03
TCT-69	24.95	24.98	24.93
	30.05	30.10	30.05
	35.01	35.06	35.01
	40.00	40.07	40.02
	45.10	45.15	45.10
	50.13	50.17	50.12
	54.92	54.97	54.92
	60.02	60.09	60.04
	64.90	64.99	64.93
	70.07	70.09	70.04
	75.04	75.09	75.03
TCT-70	24.95	25.12	24.94
	30.05	30.24	30.04
	35.01	35.23	35.00
	40.00	40.26	40.01
	45.10	45.38	45.11

<b>Thermocouple ID</b>	<b>RTD Temperature (°C)</b>	<b>Uncalibrated Temperature (°C)</b>	<b>Calibrated Temperature (°C)</b>
	50.13	50.42	50.12
	54.92	55.24	54.92
	60.02	60.38	60.03
	64.90	65.31	64.93
	70.07	70.44	70.04
	75.04	75.45	75.03
TCT-71	24.95	25.10	24.94
	30.05	30.21	30.04
	35.01	35.17	35.01
	40.00	40.18	40.02
	45.10	45.27	45.10
	50.13	50.28	50.12
	54.92	55.09	54.92
	60.02	60.20	60.04
	64.90	65.10	64.93
	70.07	70.20	70.04
	75.04	75.19	75.03
TCT-72	24.95	25.05	24.94

<b>Thermocouple ID</b>	<b>RTD Temperature (°C)</b>	<b>Uncalibrated Temperature (°C)</b>	<b>Calibrated Temperature (°C)</b>
	30.05	30.19	30.05
	35.01	35.16	35.00
	40.00	40.20	40.01
	45.10	45.32	45.10
	50.13	50.37	50.13
	54.92	55.20	54.93
	60.02	60.33	60.04
	64.90	65.23	64.91
	70.07	70.39	70.05
	75.04	75.40	75.03
TCT-73	24.95	25.14	24.93
	30.05	30.27	30.05
	35.01	35.26	35.01
	40.00	40.29	40.03
	45.10	45.37	45.08
	50.13	50.44	50.13
	54.92	55.26	54.93
	60.02	60.39	60.04

<b>Thermocouple ID</b>	<b>RTD Temperature (°C)</b>	<b>Uncalibrated Temperature (°C)</b>	<b>Calibrated Temperature (°C)</b>
	64.90	65.31	64.93
	70.07	70.43	70.04
	75.04	75.44	75.03
TCT-74	24.95	25.09	24.93
	30.05	30.23	30.05
	35.01	35.22	35.02
	40.00	40.25	40.02
	45.10	45.31	45.06
	50.13	50.41	50.14
	54.92	55.23	54.93
	60.02	60.36	60.04
	64.90	65.27	64.93
	70.07	70.41	70.05
	75.04	75.40	75.01
TCT-75	24.95	25.10	24.93
	30.05	30.23	30.03
	35.01	35.24	35.02
	40.00	40.28	40.04

<b>Thermocouple ID</b>	<b>RTD Temperature (°C)</b>	<b>Uncalibrated Temperature (°C)</b>	<b>Calibrated Temperature (°C)</b>
	45.10	45.38	45.11
	50.13	50.38	50.10
	54.92	55.23	54.92
	60.02	60.37	60.04
	64.90	65.30	64.95
	70.07	70.40	70.03
	75.04	75.41	75.02
TCT-76	24.95	24.95	24.94
	30.05	30.07	30.03
	35.01	35.07	35.01
	40.00	40.11	40.02
	45.10	45.21	45.09
	50.13	50.28	50.13
	54.92	55.12	54.95
	60.02	60.26	60.06
	64.90	65.18	64.95
	70.07	70.28	70.02
	75.04	75.29	75.00

<b>Thermocouple ID</b>	<b>RTD Temperature (°C)</b>	<b>Uncalibrated Temperature (°C)</b>	<b>Calibrated Temperature (°C)</b>
TCT-77	24.95	24.95	24.95
	30.05	30.05	30.02
	35.01	35.05	35.00
	40.00	40.10	40.01
	45.10	45.20	45.09
	50.13	50.27	50.14
	54.92	55.11	54.95
	60.02	60.25	60.07
	64.90	65.16	64.95
	70.07	70.26	70.02
	75.04	75.26	75.00
TCT-78	24.95	24.96	24.95
	30.05	30.09	30.05
	35.01	35.09	35.02
	40.00	40.08	39.99
	45.10	45.21	45.09
	50.13	50.25	50.11
	54.92	55.10	54.93

<b>Thermocouple ID</b>	<b>RTD Temperature (°C)</b>	<b>Uncalibrated Temperature (°C)</b>	<b>Calibrated Temperature (°C)</b>
	60.02	60.25	60.06
	64.90	65.15	64.93
	70.07	70.29	70.05
	75.04	75.29	75.02
TCT-79	24.95	24.92	24.96
	30.05	30.01	30.02
	35.01	35.01	34.99
	40.00	40.05	40.01
	45.10	45.15	45.07
	50.13	50.25	50.15
	54.92	55.09	54.96
	60.02	60.24	60.09
	64.90	65.12	64.94
	70.07	70.22	70.01
	75.04	75.23	74.99
TCT-80	24.95	24.92	25.24
	30.05	29.74	30.00
	35.01	34.66	34.86

<b>Thermocouple ID</b>	<b>RTD Temperature (°C)</b>	<b>Uncalibrated Temperature (°C)</b>	<b>Calibrated Temperature (°C)</b>
	40.00	39.71	39.85
	45.10	44.74	44.82
	50.13	50.22	50.24
	54.92	55.07	55.04
	60.02	60.23	60.13
	64.90	65.15	64.99
	70.07	70.26	70.04
	75.04	75.26	74.98
TCT-81	24.95	24.94	24.95
	30.05	30.06	30.04
	35.01	35.05	35.00
	40.00	40.07	39.99
	45.10	45.15	45.05
	50.13	50.29	50.16
	54.92	55.12	54.96
	60.02	60.27	60.09
	64.90	65.16	64.94
	70.07	70.27	70.03

<b>Thermocouple ID</b>	<b>RTD Temperature (°C)</b>	<b>Uncalibrated Temperature (°C)</b>	<b>Calibrated Temperature (°C)</b>
	75.04	75.26	74.99
TCT-82	24.95	24.98	24.96
	30.05	30.07	30.02
	35.01	35.08	35.01
	40.00	40.11	40.01
	45.10	45.22	45.09
	50.13	50.26	50.11
	54.92	55.11	54.93
	60.02	60.26	60.06
	64.90	65.16	64.93
	70.07	70.30	70.04
	75.04	75.30	75.02
TCT-83	24.95	24.93	24.93
	30.05	30.05	30.03
	35.01	35.04	35.00
	40.00	40.08	40.02
	45.10	45.18	45.09
	50.13	50.25	50.14

<b>Thermocouple ID</b>	<b>RTD Temperature (°C)</b>	<b>Uncalibrated Temperature (°C)</b>	<b>Calibrated Temperature (°C)</b>
	54.92	55.09	54.95
	60.02	60.23	60.07
	64.90	65.14	64.95
	70.07	70.22	70.01
	75.04	75.23	75.00
TCT-84	24.95	24.94	24.93
	30.05	30.07	30.03
	35.01	35.09	35.03
	40.00	40.12	40.03
	45.10	45.22	45.11
	50.13	50.22	50.09
	54.92	55.07	54.92
	60.02	60.22	60.04
	64.90	65.14	64.95
	70.07	70.25	70.03
	75.04	75.27	75.03
TCT-85	24.95	24.75	25.17
	30.05	29.82	30.14

<b>Thermocouple ID</b>	<b>RTD Temperature (°C)</b>	<b>Uncalibrated Temperature (°C)</b>	<b>Calibrated Temperature (°C)</b>
	35.01	34.70	34.93
	40.00	39.57	39.71
	45.10	44.60	44.65
	50.13	50.41	50.35
	54.92	55.26	55.11
	60.02	60.41	60.17
	64.90	65.33	65.00
	70.07	70.43	70.01
	75.04	75.46	74.94
TCT-86	24.95	25.06	24.97
	30.05	30.16	30.04
	35.01	35.15	35.00
	40.00	40.15	39.97
	45.10	45.23	45.04
	50.13	50.39	50.17
	54.92	55.20	54.96
	60.02	60.36	60.08
	64.90	65.21	64.91

<b>Thermocouple ID</b>	<b>RTD Temperature (°C)</b>	<b>Uncalibrated Temperature (°C)</b>	<b>Calibrated Temperature (°C)</b>
	70.07	70.39	70.07
	75.04	75.33	74.98
TCT-87	24.95	25.08	25.05
	30.05	30.11	30.05
	35.01	35.08	34.98
	40.00	40.01	39.86
	45.10	45.21	45.03
	50.13	50.39	50.16
	54.92	55.24	54.98
	60.02	60.38	60.08
	64.90	65.31	64.97
	70.07	70.40	70.03
	75.04	75.42	75.01

<b>Thermocouple ID</b>	<b>m</b>	<b>b</b>	<b>s</b>
TCT-28	9.969E-01	4.563E-03	2.344E-02
TCT-29	9.938E-01	1.156E-01	1.446E-02
TCT-30	9.950E-01	5.741E-02	9.675E-03

<b>Thermocouple ID</b>	<b>m</b>	<b>b</b>	<b>s</b>
TCT-31	9.991E-01	-3.894E-02	2.151E-02
TCT-32	9.957E-01	6.759E-02	2.246E-02
TCT-33	9.949E-01	7.112E-02	1.135E-02
TCT-34	9.947E-01	1.028E-01	1.326E-02
TCT-35	9.963E-01	8.849E-03	2.282E-02
TCT-36	9.984E-01	-2.041E-02	1.501E-02
TCT-37	9.973E-01	-1.474E-02	2.603E-02
TCT-38	9.943E-01	2.783E-02	1.405E-02
TCT-39	9.959E-01	-5.375E-02	1.921E-02
TCT-40	9.952E-01	-1.218E-02	1.484E-02
TCT-41	9.989E-01	-1.588E-01	2.566E-02
TCT-42	9.960E-01	-4.542E-02	1.863E-02
TCT-43	9.964E-01	-2.754E-02	2.192E-02
TCT-44	9.934E-01	1.836E-01	1.979E-02
TCT-45	9.954E-01	1.060E-01	1.869E-02
TCT-46	9.990E-01	7.928E-02	2.754E-02
TCT-47	9.946E-01	1.941E-01	2.802E-02
TCT-48	9.994E-01	7.374E-02	2.520E-02
TCT-49	9.987E-01	5.083E-02	1.741E-02
TCT-50	9.943E-01	1.839E-01	2.644E-02

<b>Thermocouple ID</b>	<b>m</b>	<b>b</b>	<b>s</b>
TCT-51	9.952E-01	6.287E-02	2.911E-02
TCT-52	9.926E-01	2.444E-01	3.172E-02
TCT-53	9.921E-01	2.951E-01	3.337E-02
TCT-54	9.995E-01	-9.926E-02	2.307E-02
TCT-55	9.934E-01	8.591E-02	2.107E-02
TCT-56	9.990E-01	-1.036E-01	3.646E-02
TCT-57	9.943E-01	-3.766E-02	2.480E-02
TCT-58	9.993E-01	-1.453E-01	2.423E-02
TCT-59	9.981E-01	-3.694E-02	3.235E-02
TCT-60	9.952E-01	3.283E-02	1.883E-02
TCT-61	1.000E+00	-7.705E-02	1.977E-02
TCT-62	1.000E+00	-9.182E-02	1.762E-02
TCT-63	9.942E-01	1.273E-01	4.719E-02
TCT-64	9.950E-01	6.536E-02	2.901E-02
TCT-65	9.998E-01	-8.094E-02	1.923E-02
TCT-66	9.998E-01	-6.526E-02	1.932E-02
TCT-67	9.953E-01	1.595E-02	2.441E-02
TCT-68	9.961E-01	-8.617E-03	1.876E-02
TCT-69	9.999E-01	-4.792E-02	1.771E-02
TCT-70	9.950E-01	-4.941E-02	1.747E-02

<b>Thermocouple ID</b>	<b>m</b>	<b>b</b>	<b>s</b>
TCT-71	1.000E+00	-1.661E-01	1.984E-02
TCT-72	9.949E-01	1.698E-02	1.335E-02
TCT-73	9.958E-01	-9.662E-02	2.175E-02
TCT-74	9.955E-01	-4.368E-02	2.396E-02
TCT-75	9.956E-01	-6.352E-02	3.078E-02
TCT-76	9.946E-01	1.232E-01	3.286E-02
TCT-77	9.949E-01	1.253E-01	3.519E-02
TCT-78	9.950E-01	1.113E-01	2.125E-02
TCT-79	9.947E-01	1.670E-01	4.351E-02
TCT-80	9.881E-01	6.171E-01	1.692E-01
TCT-81	9.944E-01	1.485E-01	4.236E-02
TCT-82	9.949E-01	1.075E-01	2.518E-02
TCT-83	9.952E-01	1.263E-01	3.755E-02
TCT-84	9.955E-01	9.535E-02	3.008E-02
TCT-85	9.817E-01	8.649E-01	2.306E-01
TCT-86	9.949E-01	3.399E-02	4.093E-02
TCT-87	9.923E-01	1.652E-01	7.537E-02



**CERTIFICATE OF CALIBRATION**

Certificate Number: 014365270718  
 Calibration Date: 07/13/18  
 Order Number: 200779  
 FS Code: 12294

Customer: McMaster University  
 Address: 1280 Main Street West  
 Hamilton ON L8s4L8  
 Phone: N/A  
 Contact Name: N/A

Meter Type: Coriolis Mass Meter  
 Model Number: TCM 1550-FA-TGSS-HZZS  
 Serial Number: 01436527  
 Max. Rated Flow (lb/min): 57

Electronics Type: Meter Mount  
 Model Number: TCE 8001-W-SDSH  
 Serial Number: 01437527  
 Software Version: 3.43  
 Display Version: 3.42  
 Hardware Version: 2.2

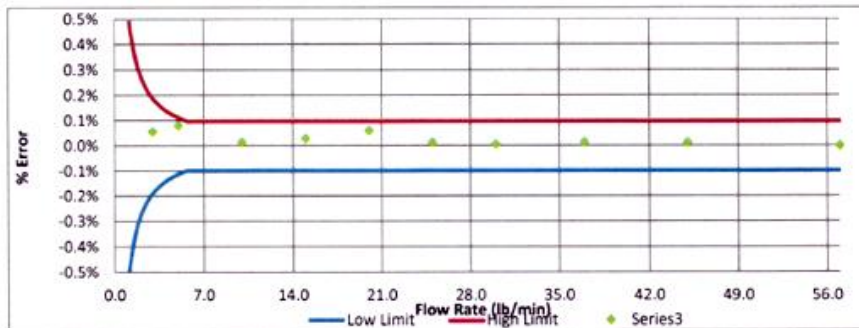
Unit Condition: New

**Calibration Results**

Meter Variable (g/s/ $\mu$ s): 10.2560

Zero Offset ( $\mu$ s): -0.0190

Flow PT.	Flow Rate (lb/min)	Flow Rate (% of Max)	Meter Total (kg)	Scale Total (kg)	% Error
1	57.00	100%	26.9510	26.9510	0.000%
2	45.00	79%	23.4780	23.4750	0.013%
3	37.00	65%	20.6590	20.6560	0.015%
4	30.00	53%	17.1670	17.1660	0.006%
5	25.00	44%	15.0970	15.0950	0.013%
6	20.00	35%	10.0780	10.0720	0.060%
7	15.00	26%	10.4370	10.4340	0.029%
8	10.00	18%	6.8580	6.8570	0.015%
9	5.00	9%	6.2510	6.2460	0.080%
10	3.00	5%	5.4070	5.4040	0.056%





**Calibration Method**

	Flow Pts.	Max Flow Rate (lb/min)	Min Flow Rate (lb/min)
Standard:	5	57	0.00
Customer Specified:	NA	NA	NA

**Calibration System Conditions**

Calibration Media: Water  
 System Temperature (°C/°F): 32.00  
 System Pressure (psi):

**Meter & Electronics Settings**

	Air Cal		Water Cal	
Tube Frequency (Hz):	128.1022		116.0843	
Tube Temperature (°C/°F):	29.27	84.68	27.85	82.13
Density (g/cc):	0.0011678		0.9963070	
Drive Current (mA):	11.57		14.06	
Amplitude, Sensor A (mV):	97		97	
Amplitude, Sensor B (mV):	103		103	

**Environmental Conditions**

Ambient Temperature (°C/°F): 32.00  
 Relative Humidity (% RH):  
 Ambient Pressure (psia):

Certificate Number: 014365270718

Calibration Technician: Jon Henningfeld  
Function Name

*Jon Henningfeld*  
Signature

This calibration is traceable to NIST. The Scale referenced is calibrated in accordance with NIST.  
 Serial Number: 01007696GM / 16199416DM; NIST Certificate #: NA2136-028-091010